UNIVERSITEIT
GENT

Faculteit Wetenschappen
Vakgroep Wiskundige Natuurkunde en Sterrenkunde

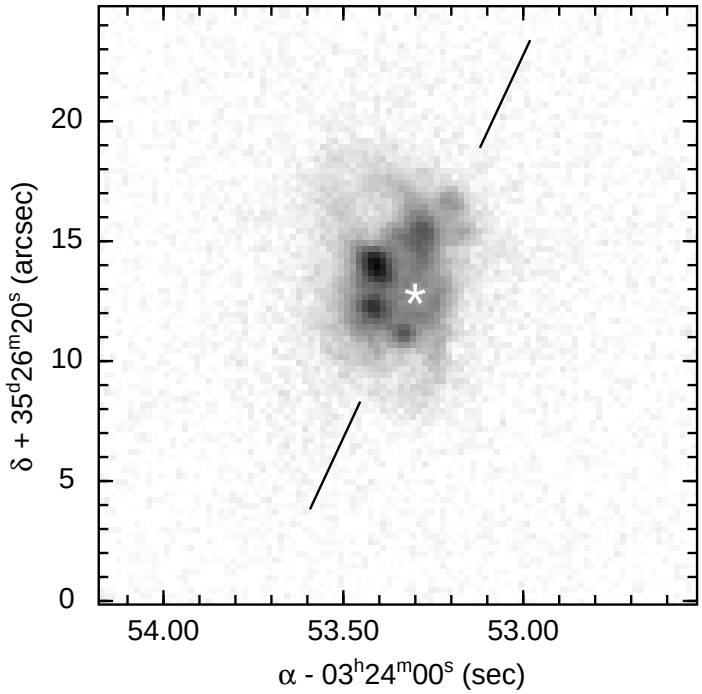

Observations and N-body/SPH simulations of the interstellar medium in dwarf elliptical galaxies

Dolf Michielsen

Proefschrift ingediend tot het behalen van de graad van Doctor in de Wetenschappen: Wiskunde
Academiejaar 2004-2005
Promotor : Prof. Dr. Herwig Dejonghe

UNIVERSITEIT
GENT

Faculteit Wetenschappen
Vakgroep Wiskundige Natuurkunde en Sterrenkunde

Observations and N-body/SPH simulations of the interstellar medium in dwarf elliptical galaxies

Dolf Michielsen

Proefschrift ingediend tot het behalen van de graad van Doctor in de Wetenschappen: Wiskunde
Academiejaar 2004-2005
Promotor : Prof. Dr. Herwig Dejonghe

Dankwoord

Hier ligt voor u het resultaat van vier jaar werk, netjes gepresenteerd. Wat er natuurlijk niet instaat zijn de moeilijke momenten. De waarnemingsvoorstellen die niet aanvaard werden door de commisies die de beschikbare tijd toekennen. De megabites aan output van simulaties die uiteindelijk tot niets dienden omdat er achterafgezien iets mis was met de code. Weken werk die plotseling in rook opgaan. Gelukkig waren er een heleboel mensen waarbij ik terecht kon voor een opbeurend woord of een schouderklop. Mensen die me er steeds bovenop hielpen en mee enthousiast waren als er resultaten kwamen. Daarom is een dankwoord vooraf zeker wel gepast.

Vooreerst wil ik mijn promotor, Prof. Herwig Dejonghe, bedanken om me de mogelijkheid te bieden een doctoraat in de sterrenkunde te maken. Al van kindsbeen af wilde ik iets met sterrenkunde doen, dus dit is een van mijn jongensdromen die waarheid worden! Een zeker even grote merci gaat naar Dr. Sven De Rijcke die mij deze vier jaar met raad en daad bijstond, en van wie ik enorm veel geleerd heb.

Dankuwel, Veronique, Sven, Maarten, Emmanuel, Bart, Stephanie, Pieter en Sarah, mijn toffe medesterrenkundigen die altijd klaarstonden om serieuze vragen over data-reductie en programmeerproblemen te beantwoorden, om naar simulatie-filmjes te komen kijken en om op gepaste tijden te informeren naar de vorderingen van mijn werk. Dank ook aan Gerbrand om MIDAS (proberen) te installeren op een eindeloos aantal computers! Ook alle andere collega's van de vakgroep, bedankt voor de fijne sfeer en aanmoedigingen, en voor de talloze discussies. Soms over wiskunde, fysica en sterrenkunde, even vaak ook niet, maar steeds interessant!

I would like to thank my collaborators Prof. Werner Zeilinger and Dr. Philippe Prugniel for their help and the interesting discussions. I was also very pleased to talk to Stefan Kautsch, Elke Roediger, Alexandre Vazdekis, Reynier Peletier, Harald Kuntschner, Anna Pasquali, Victor Debattista, John Peacock, Gavin Pringle, Rob Thacker at various stages of my PhD. Also many thanks to the people of the MAGPOP Training Network for offering me a post-doc position before this work was completed. Of course, I met far too many interesting people to provide a detailed list here, sorry if I left someone out!

Vaak hebben ze het mij gevraagd: "*Waar zijt ge nu eigenlijk mee bezig?*" Het was niet altijd gemakkelijk om uit te leggen, maar hopelijk heb ik toch af en toe iets kunnen verhelderen. Dank u pa, ma, mijn zusjes Sarah en Els, en de rest van de familie. Dank u ook aan mijn 'nieuwe' familie, Jef, Lief, Erika!

Een dikke merci aan mijn vrienden voor de niet aflatende interesse, humor en voor de rock'n'roll!

Tenslotte bedank ik heel speciaal en met veel liefde mijn grootste steun en toeverlaat, Inger. Jij weet mij te stimuleren en geeft me de ruimte om mijn dromen waar te maken. Inger, je bent er altijd voor me, dankjewel!!!!

Dolf Michielsen
juni 2005

Contents

.

Chapter 1

Introduction

Dwarf elliptical galaxies, with blue absolute magnitudes typically fainter than $M_B = -16$, are the most numerous type of galaxy in the nearby Universe (Ferguson & Binggeli, 1994).

Over the past 10 years, numerous papers started off using this sentence, or a variation on it, to introduce new results concerning dwarf elliptical galaxies (dEs). When Ferguson and Binggeli wrote their review paper in 1994, they discussed the tremendous advances that had been achieved in the study of dEs over the preceding years. A surge of activity in the study of faint galaxies was inspired after CCD cameras and large telescopes became available in the 1980's, leading to more precise data. Also on the theoretical side, dwarf galaxies gained ever more importance because in the theory of hierarchical structure formation, based on the Cold Dark Matter model, small galaxies are the basic building blocks for larger galaxies.

Despite the many studies, both observationally and theoretically, that have been undertaken since the Ferguson & Binggeli (1994) paper, we still do not fully understand the mechanisms that govern the formation and evolution of dEs. Of course, our knowledge of the Universe is ever increasing and many new insights have been acquired over the years. In this chapter, we introduce dEs and try to summarize why they are so important in our understanding of the Universe. An introduction to population synthesis is given, and the chapter ends with an overview of the rest of this work.

1.1 Galaxies

Our galaxy, the Milky Way, is often named the Galaxy, since it was long thought to be the *only* galaxy in the Universe. In the beginning of the 20th century, a great debate raged through the astronomical community. The onset of this debate was the nature of the diffuse nebulae that had been observed all over the sky. Were these nebulae part of our Galaxy, or were they galaxies on their own right? When Hubble observed bright, variable Cepheid stars in the nearest spiral nebulae (Barnard's nebula (NGC6822), the Andromeda nebula (M31) and the Triangulum nebula (M33) Hubble (1925, 1926a)), it was recognized that the nebulae are indeed other galaxies, located far away from our Milky Way. From then on, people started looking at the nebulae with very different eyes.

1.1.1 Classification of galaxies

Hubble (1926b) observed that galaxies come in many different shapes. Some are round and featureless, while others have magnificent spiral structures. Hubble classified the galaxies according to their shapes in his famous *tuning fork diagram* (Fig. 1.1).

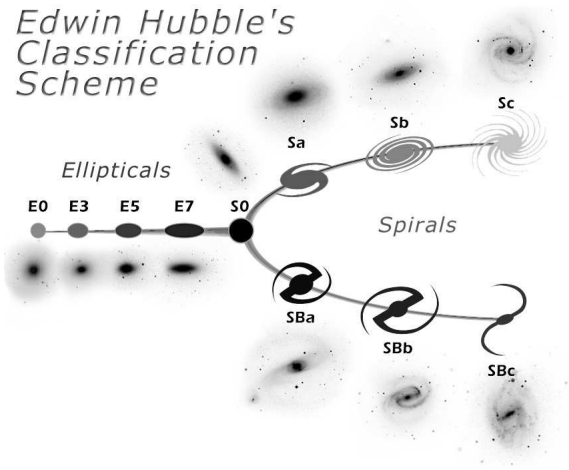

Figure 1.1: Hubble's morphological classification of galaxies (Hubble, 1926b). The elliptical (E) galaxies are ordered from round to more flattened on the left, and the spiral (S) and barred spiral (SB) galaxies come in two sequences on the right. At the junction of the elliptical, spiral and barred galaxies, the lenticular (S0) galaxies reside. Figure taken from `http://hubblesite.org/newscenter/newsdesk/archive/releases/1999/34/image/o`.

He placed the *elliptical* galaxies (Es) to the left in a series of ever increasing flattening. To quantify this, the nomenclature for Es is En, ranging from perfectly round E0 to very flattened (cigar-like) E7 galaxies. The number n is found as $n = 10\epsilon$, where the *ellipticity* $\epsilon = 1 - a/b$ is governed by the ratio of the major and minor axes (a and b) of the galaxy.
To the right of his classification scheme, Hubble placed two sequences, one for *spiral* (S) and one for *barred spiral* (SB) galaxies. Those are subclassified as a, b, c or d depending on the tightness of the spiral arms and the prominence of the bulge or bar. In between, at the junction of the E, S and SB series, the *lenticular* galaxies (S0) reside. These galaxies show a bulge/bar and a disk component, but no spiral arms. There also exists a class of *irregular* galaxies (Irr), that were not included in the tuning fork diagram. In this scheme, the Milky Way is a spiral galaxy of type Sbc (intermediate between b and c).

Hubble thought that he had found an evolutionary scheme in which galaxies move from left to right over time (going from ellipticals to spirals). Although this view is since long proved wrong, elliptical galaxies are still named *early type* galaxies, while spiral galaxies are known as *late type*.

Es are mostly devoid of interstellar gas and dust, and consist of an old stellar population, while spiral galaxies contain significant amounts of gas and are actively forming stars, mainly in the spiral arms. The bulges of spirals resemble elliptical galaxies.

1.1.2 Classification of dwarf galaxies

Over the years, the original Hubble classification scheme has been refined and expanded. In particular the classification of *dwarf galaxies* remained unsatisfactory, since Hubble had to base his scheme on observations of the apparently brightest galaxies in the sky. Due to the limited resolving power of the telescopes, only the most nearby dwarf galaxies, such as the Large and Small Magellanic Clouds, had been discovered at that time.

On the early-type branch of the tuning fork diagram, it became clear that the elliptical galaxies span an

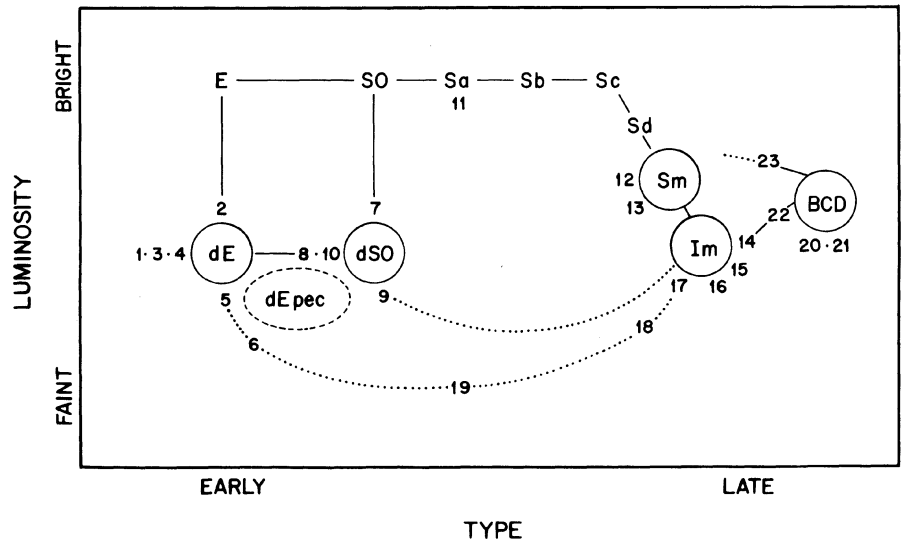

Figure 1.2: Classification of dwarf galaxies, taken from Sandage & Binggeli (1984). The early-type galaxies span a continuous range in luminosity down to dEs and dS0s. No real dwarf spiral galaxies seem to exist, but the luminosity of spirals decreases with decreasing spiral arm structure down to Sd, Sm and Im types. The BCDs (Blue Compact Dwarfs) are a class of star-forming dwarfs. Evolutionary connections between the dE, Sd, Im and BCD types have been proposed. The numbers represent panels in the classification system of Sandage & Binggeli (1984).

enormous range in intrinsic luminosities. The brightest cluster Es are a factor 10^6 more luminous than the faintest dEs discovered nearby the Milky Way. The late-type galaxy sequence was extended towards fainter luminosities, adding the Sd, Sm and Im classes (Figure 1.2). The Sm and Im are generally grouped into *dwarf irregular* galaxies (dIrrs). Apparently there are no real dwarf spiral galaxies (dSa, Figure 1.2). To form and sustain spiral arms, a galaxy should be more massive than some $5 \times 10^9\,\mathrm{M}_\odot$. Only then the circular velocity is high enough so that regular arms can form. The gap between early-type and late-type dwarf galaxies in Figure 1.2 stems from the absence of dwarf spirals and does not necessarily mean that no connections between dEs and dIrrs exist. In fact, *transition type* dwarfs have been observed that appear to fall in between the dIrr and dE class (Knezek et al., 1999; Skillman et al., 2003). A distinct class of dwarf galaxies is formed by the vigorously starforming *blue compact dwarf* (BCD) and *amorphous dwarf* galaxies. The surface brightnesses of the stellar envelopes of these galaxies suggest that they would resemble present-day dEs once the star formation has ended (Marlowe et al., 1999).

In their classification of Virgo Cluster dwarf galaxies, Sandage & Binggeli (1984) separated dEs from normal Es on morphological grounds, using surface brightness profiles to distinguish between the two classes. Elliptical galaxies have a steeply declining surface brightness profile, following an $r^{1/4}$ or de Vaucouleurs law, while dEs have nearly flat profiles, following an exponential law. The transition zone is roughly at $M_B = -18$. Later on it became clear that the surface brightness profiles of early-type galaxies can be fitted by a Sérsic $r^{1/n}$ law, with n varying continuously from $n \geqslant 4$ for normal Es to $n \leqslant 1$ for dEs. See Graham & Guzmán (2003) for a detailed discussion about the variation of the Sérsic index with elliptical galaxy luminunity. Hence, the separation between a faint E and a bright dE is not clear-cut, and might even not really exist. Mostly, galaxies with absolute blue magnitudes fainter than $M_B = -18$ will be labeled dE. A further distinction between bright and faint dEs is usually made at

$M_B = -16$. The faintest dEs ($-10 \geqslant M_B \geqslant -14$), mainly observed in the Local Group, are also called *dwarf spheroidal* galaxies (dSphs). Apparently flattened dEs, or dwarfs that show a two-component surface brightness profile, are classified as dS0. However, this class is quite small, and is generally mixed into the dE class.

Many of the brighter dEs ($M_B \leqslant -16$) have a central luminosity peak, a *nucleus*, indicated as dE.N. The nuclei are until present unresolved, but are probably dense star clusters. The formation of those nuclei, whether in situ, or from infalling globular clusters, is still a matter of debate (Oh & Lin, 2000; Lotz et al., 2004). The fraction of nucleated dEs decreases with luminosity; fainter dEs generally do not have a nucleus.

Some galaxies with $M_B > -18$ exhibit a steep de Vaucouleurs surface brightness profile, and are called *compact ellipticals* (cEs). An example of this rare galaxy class is M32, the companion of Andromeda (M31). Such galaxies are possibly not genuine dwarf galaxies, but rather Es that have been tidally stripped. A more extreme class of *ultra compact dwarfs* (UCDs) has recently been discovered in the Fornax Cluster (Mieske et al., 2002). One possible explanation for the existence of these galaxies is the *threshing* of dE.Ns by the gravitational potential of the cluster. Tidal forces near the centre of the cluster disrupt the host galaxy and only the dense nucleus can survive (Bekki et al., 2003).

1.2 Dwarf elliptical galaxies

In our current understanding, the universe is filled with only 4 per cent *baryonic matter*, i.e. stars, gas and dust. About 20 per cent is in *dark matter* (DM), which can only be observed indirectly through its gravitational interaction. The remaining 75 per cent is due to a *dark energy* that drives the expansion of the universe. What this dark energy is, remains a mystery. It is of importance to cosmologists, but will not be discussed in this work. For the DM, many forms have been suggested, like neutrinos or supersymmetric particles such as axions and fotinos, and have been given names such as *machos* and *wimps*. DM only manifests itself through its gravitational force and is needed to explain for example the rotation curves of spiral galaxies and gravitational lensing. Mostly, the DM is supposed to be *cold*, meaning that is has no internal pressure. Hot DM (in the form of massive neutrinos) is almost certainly ruled out, but a kind of *warm* DM could still be possible.

After the Big Bang, slight perturbations in the density of the universe caused the DM to collapse. Small DM halos subsequently merged to form ever larger structures, in a process of *hierarchical structure formation*. As the baryons (gas) started falling into the DM halos, the density rose, allowing the gas to cool and start forming stars and hence, galaxies.

Since the structure formation is a bottom-up process, dwarf galaxies will be among the first structures formed. Therefore they constitute the building blocks for larger galaxies. Present-day dwarf galaxies are those that survived the early assembly. If we know how these galaxies have formed and how they evolve, we gain important insights on the formation of large galaxies.

1.2.1 Observations

dEs are the numerically dominant population in nearby clusters like Virgo, where about 70 per cent of the galaxies is of the dE type. Although they carry only a few per cent of the baryonic mass, dEs are very sensitive to the environment. So they keep a fossil record of the environmental conditions over the lifetime of the cluster. However, dEs are not well studied because they are difficult to observe. Their low luminosity ($M_B > -18$), low surface brightness ($\mu_B > 23\,\mathrm{mag}/\Box''$), low metallicity ($Z < 0.1 Z_\odot$) and low intrinsic velocity dispersions ($\sigma < 50\,\mathrm{km\,s^{-1}}$) require long observing times and high spectral and spatial resolution.

Dwarf galaxies first became important in photometric studies of luminosity functions in clusters of galaxies. Based on these studies, there are more dEs per giant in denser regions than in the field (the overabundance being a factor 5-10). Moreover, dEs in groups are strongly clustered around giant galaxies, while the opposite is found for low-mass galaxies in clusters. This means that clusters of galaxies cannot form through simple mergers of galaxy groups, and that some dwarf systems must form within the cluster environment.

The dEs were believed to be simple objects, being old and metal-poor as predicted by the early models of galaxy formation. However, recent high quality observations revealed fine structures in dEs, such as embedded spirals, disks and bars (Jerjen et al., 2000; Barazza et al, 2002; De Rijcke et al., 2003a; Graham et al., 2003). Recent observational programs on dEs using long slit spectroscopy reveal the kinematic diversity of the dE population, some flattened dEs being pressure supported, while others show significant rotation (Simien & Prugniel, 2002; Pedraz et al., 2002; Geha et al., 2003; De Rijcke et al., 2001; van Zee et al., 2004; Guzmán et al., 2003). Kinematically decoupled cores (De Rijcke et al., 2003b) and off-centre nuclei were found in some dEs (Binggeli, Barazza & Jerjen, 2000; De Rijcke & Debattista, 2004).

Although first thought to be gas-less systems, a significant fraction of dEs harbours an interstellar medium (ISM). In a spectroscopic survey of the Fornax Cluster, Drinkwater et al. (2001) discovered that about 25 per cent of the dEs contain an ionized ISM. Subsequent detailed imaging of a sample of these dEs yield a variety of ionized gas morphologies (De Rijcke et al., 2003b; Michielsen et al., 2004a). In a radio survey of the Virgo Cluster, Conselice et al. (2003b) found a neutral ISM to be present in about 10 per cent of the dEs. Recently, we also detected neutral gas in two Fornax dEs (Buyle et al, 2005). In chapter 4 we describe these observations and their consequences in more detail.

Stellar population studies show that dwarf galaxies have either young/metal rich or old/metal poor stellar populations. Fainter galaxies seem to be more heterogeneous, with large scatter from the colour-magnitude relation for galaxies (Conselice et al., 2001; Rakos et al., 2001). This trend can be explained by different dwarfs having mixtures of ages and metallicities. There is no obvious difference between rotationally and non-rotationally supported dEs in terms of morphology or chemical abundances, although the samples are still small. Spectroscopic studies hint at a bimodal distribution of dEs, a metal-poor and a metal-rich one (Poggianti et al., 2001; Michielsen et al., 2003b), in the Coma and Fornax cluster respectively, suggesting that the dE population has multiple origins. In chapter 3 we present the results from our CaT measurements for 15 Fornax dEs.

1.2.2 Formation scenarios

There are three main formation scenarios for dEs currently in vogue; the wind model, the harassment model and the fading model. The present-day dEs are probably a mixed population, originating through different evolutionary paths. However, we don't know which of the scenarios, if any, is the most common.

The *wind model* predicts that dEs are primordial objects. In the standard Cold Dark Matter (CDM) paradigm of hierarchical structure formation, dwarf galaxies are the first galaxy type formed. Gas flows into the dark matter haloes, cools and star formation starts. The feedback from star formation may have a particularly strong influence on the evolution of low-mass galaxies. Owing to their low escape velocity, Larson (1974) suggested that the loss of supernova-heated gas would carry away a large fraction of their initial gas in a *galactic wind*. More recent numerical simulations of isolated galaxy formation show how the wind model can reproduce primordial, low-metallicity and diffuse dEs (Mori et al., 1999). Chemical evolution models have also taken galactic winds into account to explain a number of peculiarities about dwarf galaxies. Moreover, dynamical response to starburst-induced gas removal needs to be taken into account in order to explain the luminosity-velocity dispersion relation observed in dwarf galaxies (Nagashima & Yoshii, 2004).

However, the CDM model predicts that dEs are more common in low density environments, while the direct opposite is observed. dEs are amongst the most clustered galaxy types, being abundant in groups and clusters of galaxies, but scarce in the field. This relation between dwarf morphology and environmental density favours environmental effects in shaping dEs. Moreover, there are hints that dEs are recent additions to clusters, because they appear to form a broader distribution, both spatially and in radial velocity, than the normal galaxies (Conselice et al., 2001). Observations of rotating dEs, of dEs with embedded disks and of dEs with an ISM suggest that some dEs stem from small spiral or irregular galaxies that have been transformed into dEs through interactions with giant cluster members.

In the *harassment model*, a late-type spiral galaxy (type Sd-Im) that enters a group or cluster environment loses its ISM due to *ram pressure stripping* by the intracluster medium (ICM) (Mori & Burkert, 2000; Marcolini et al., 2003; Michielsen et al., 2004b). Then, tidal harassment due to distant and repeated encounters with other cluster members dynamically heat the stellar disk and a diffuse, gas-poor dEs remains (Moore et al, 1998). In galaxy groups, dEs are mostly bound to a giant host galaxy. Tidal interactions of satellites with potential of giant host can transform a dIrr into a dE or dSph galaxy (Mayer et al., 2001; Pasetto et al., 2003).

Some dwarf galaxies appear to be in a transient stage between a dIrr and a dE, having smooth, elliptical isophotes, but containing a significant amount of gas and showing evidence for star formation. The *fading model* considers fading of gas-rich and starforming dIrrs or BCDs into dEs after the starburst has consumed or blown out the ISM (Marlowe et al., 1999; van Zee et al., 2004). However, present-day dIrrs have, on average, lower surface brightnesses than present-day dEs. Hence simple fading of the stellar population of dIrrs cannot reproduce all dEs, unless the properties of dIrrs were different at earlier times. It has also been argued that the underlying stellar envelope of BCDs resembles a dE, but some controversy still remains (Drinkwater & Hardy, 1991).

Finally it should be mentioned that some dEs could be formed from the debris after the merger of two gas-rich giant spirals. Such *tidal dwarfs* would not be as dark matter dominated as the primordial dEs (Duc et al., 2004). This scenario is most likely not the main possibility for dE formation because it predicts very low-luminosity dEs. Moreover, during each merger event at most a few tidal dwarfs are formed and therefore this scenario cannot account for the abundance of dEs in clusters.

1.3 Stellar population synthesis

On a clear night, about 5000 stars can be distinguished with the naked eye. These all belong to the Milky Way and have been arranged and re-arranged in *stellar constellations* by almost every human civilization that walked our Earth. With a little help (e.g. using binoculars or a small telescope), several beautiful gas complexes can be observed, such as the Orion and the Horsehead nebulae. Dust can be beautiful also, as in the reflection nebula around the young stars in the Pleiades. But apart from having an aesthetic value that fills our hearts with wonder and provides pretty pictures to fill magazines and books, the stars, gas and dust observed in galaxies can tell us something about its present and its past, what it is and how it became to be that way.

From the luminosity, the colors and the spectral *absorption lines* of a star, we can deduce the surface temperature, the surface gravity and the chemical composition of the star. These quantities allow us to calculate the age and the mass of the star in question. Stars are not randomly distributed in a color-magnitude diagram (or, equivalently, a temperature-luminosity diagram, or Hertzsprung-Russel diagram), as can be seen in Fig. 1.3.

Most of the stars lie in a diagonal band going from blue (hot), bright stars to red (cool), dim stars. This band is called the *main sequence* and consists of normal stars that are burning hydrogen in their cores. There are also red (cool), bright stars, the *red giants*, these are stars that have ended hydrogen

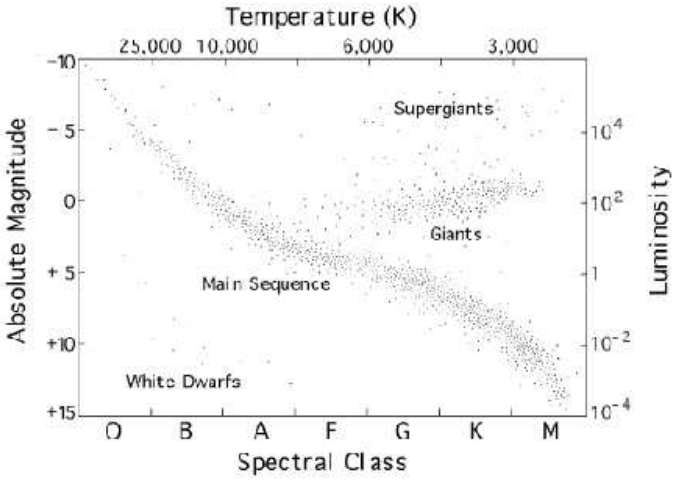

Figure 1.3: The Hertzsprung-Russel diagram. Taken from `http://calspace.ucsd.edu/virtualmuseum/images/hertzsprungrussel.html`.

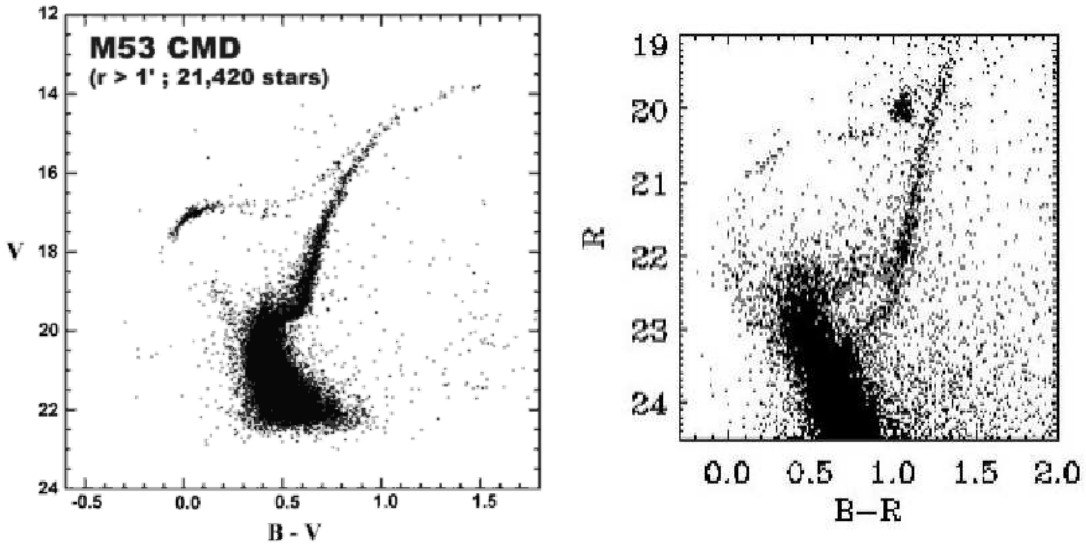

Figure 1.4: Color-magnitude diagrams of the globular cluster M53 (left) and the Carina dwarf spheroidal galaxy (right). While the globular cluster resembles a simple stellar population, the dSph has a composite stellar population. Taken from `http://www.astro.virginia.edu/s̃s5fb/research/m53/m53.html` and `http://www.ps.uci.edu/physics/facrec/img005.jpg`, respectively.

burning and are going towards the end-phase of their lives. The hot (blue), dim stars are *white dwarfs*, the remnants of low-mass stars. The remnants of more massive stars, black holes and neutron stars, are not represented in the temperature-luminosity diagram.

During most of its lifetime, a star will reside on the main sequence. When a main-sequence star exhausts its hydrogen fuel, it will leave the main sequence. In the temperature-luminosity diagram, a star will *turn off* the main sequence to the cooler and brighter regions. More massive stars exhaust their hydrogen more quickly than low-mass stars. The evolutionary paths that stars of different mass and chemical composition follow in a temperature-luminosity diagram are named *stellar tracks*.

The globular clusters and some dwarf galaxies around the Milky Way are close enough so that we can resolve their individual stars. The positions of the observed stars in a temperature-luminosity or color-magnitude diagram reveal important information about the star formation history (SFH) of the stellar population (Figure 1.4). The most simple stellar populations are found in globular clusters. These systems consist of stars that essentially formed at the same time and with the same chemical composition, so that they all have the same age and the same metallicity. The temperature-luminosity diagram of such a single-age and single-metallicity population (SSP) shows one turn-off point on the main sequence. The dwarf spheroidal satellite galaxies of the Milky Way exhibit more complex SFHs. Some appear to have formed in one single burst of star formation and have stellar populations that resemble those of globular clusters, while other show different distinct turn-off points on their main sequence, indicating stellar populations of different age. Their SFH is characterized by recurrent bursts, followed by more quiescent periods. The reproduction of synthetic temperature-luminosity diagrams from stellar evolutionary tracks is called *population synthesis*.

Since galaxies are generally so far away that we cannot resolve their individual stars, we receive the *integrated light* from the whole stellar population of the galaxy. Hence it is not possible to construct the temperature-luminosity diagram of the galaxy. However, stars at different locations in the diagram also have different colors and different spectral features. Therefore, the colors and spectra of galaxies will contain information on the stellar populations of those galaxies. The light of a young population will be dominated by hot, blue main-sequence stars, while the light of an old population will be dominated by cool, red giant stars. The spectra of young stars show prominent hydrogen Balmer absorption lines, while old stars have stronger metal features. Over the years, various theoretical and observational stellar libraries have been compiled, in order to extract observable quantities from synthetic populations. Most work has concentrated on colors and spectral features of SSPs, since these are the simplest populations to model. By comparing the observed colors and spectral indices of galaxies to those of SSPs, one can estimate the age and metallicity of the galaxy in question.

1.4 Purpose of this work

My first interest in dwarf elliptical galaxies was raised when I studied their photometry during my Master's thesis. The data I used came from an ESO Large Programme on dEs that was spearheaded by the astronomy group in Ghent. During this Large Programme, deep optical photometric and near-infrared spectroscopic data of 15 dEs in the Fornax Cluster and in three Southern Groups was collected. The structural and kinematical properties of our sample of 15 dEs were put together with those of recently published dE samples of similar size, and compared to the properties of normal Es (chapter 2). Predictions made by the wind model and the harassment model are confronted with the data. Although dynamical response to mass loss following a galactic wind phase can well explain the position of dEs and Es in the structural parameter diagrams, various observational features also point to harassment as a possible mechanism for dE formation.

Also pointing to different formation scenarios for dEs are the Calcium II Triplet (CaT) absorption strengths (chapter 3). Using recently compiled synthetic spectra in this wavelength regime, we found

that, while three of our dEs have CaT values corresponding to old metal-poor populations, the other twelve have CaT values that are too large to be explained by the population synthesis models. Moreover, these large CaT values continue the anti-correlation of CaT with velocity dispersion σ observed in normal ellipticals and bulges of spiral galaxies.

Although dEs are generally thought of as gas-less systems, recent surveys have found that a significant fraction of dE-classified dwarf galaxies do contain an interstellar medium (Drinkwater et al., 2001; Conselice et al., 2003a). Two dEs in the Large Programme sample were known to exhibit Hα emission. Detailed narrow-band imaging revealed evidence for recent star-formation in FCC046, a result that was corroborated by the high hydrogen Paschen absorption found in this dE. In order to study the ISM in dEs in more detail, three more Fornax dEs were imaged in Hα with the VLT. In section 4.2, these observations are described and discussed. We also obtained 20 cm radio observations of two Fornax dEs in order to search for a neutral interstellar medium. In section 4.3, H I detections in both dEs are reported.

Clearly, not all dEs are simple gas-less systems. Since most dEs are found in clusters and groups of galaxies, and since dEs with an ISM are found predominantly in the outskirts of clusters, the environment appears to play an important role in the evolution of dEs. Ram pressure stripping by the intracluster medium is supposed to efficiently remove the ISM from a dwarf galaxy. On the other hand, primordial dEs are supposed to rapidly lose their ISM though a galactic wind. Are then all dEs with an ISM transformed dIrrs or small spirals? To shed some light on this question, we use N-body/SPH simulations to follow the evolution of the ISM in dEs. The details of the code are described in chapter 5.

In chapter 6, we consider the evolution of a gas-rich dE in a cluster environment. It is found that small dEs (dSphs) lose their ISM almost immediately, but larger dEs can retain part of their ISM over quite long timescales. In this kind of simulations, the choice of the initial conditions for the ISM seems to play an important role.

The formation of an isolated dE is simulated in chapter 7. Star formation, stellar feedback and chemical evolution are implemented in the N-body/SPH code. The influence of the different parameters involved is investigated and discussed. Since dEs have shallow gravitational potentials, they are very sensitive to feedback processes and thus constitute an ideal testbed for refining star formation and feedback prescriptions. It is shown that the galactic wind generated by the first starburst is not always that efficient in removing the ISM from the primordial dE, a significant part of the gas still being present after several gigayears.

The results are summarized in chapters 8 (in Dutch) and 9. Future projects, both observationally and theoretically, are outlined in chapter 10.

Finally, the Fast Fourier Transform used in the N-body/SPH code to calculate the gravitational forces, is explained in detail in appendix A, followed by the bibliography and my publication list.

Part I

Observations

Chapter 2

Structural and kinematical properties of dEs

This chapter is devoted to the first results of an ESO Large Program on the kinematics and internal dynamics of dwarf elliptical galaxies (dEs), in which our research group in Ghent was involved. Deep major and minor axis spectra of 15 dEs and broad-band imaging of 22 dEs were obtained.

Here, we investigate the relations between the parameters that quantify the structure (B-band luminosity L_B, half-light radius R_e, and mean surface brightness within the half-light radius $I_\mathrm{e} = L_B/2\pi R_\mathrm{e}^2$) and internal dynamics (velocity dispersion σ) of dEs. We confront predictions of the currently popular theories for dE formation and evolution with the observed position of dEs in $\log L_B$ vs. $\log\sigma$, $\log L_B$ vs. $\log R_\mathrm{e}$, $\log L_B$ vs. $\log I_\mathrm{e}$, and $\log R_\mathrm{e}$ vs. $\log I_\mathrm{e}$ diagrams and in the $(\log\sigma, \log R_\mathrm{e}, \log I_\mathrm{e})$ parameter space in which bright and intermediate-luminosity elliptical galaxies and bulges of spirals define a Fundamental Plane (FP). In order to achieve statistical significance and to cover a parameter interval that is large enough for reliable inferences to be made, we merge our data set with two other recently published, equally large data sets. We show that the dE sequences in the various univariate diagrams are disjunct from those traced by bright and intermediate-luminosity elliptical galaxies and bulges of spirals. It appears that semi-analytical models (SAMs) that incorporate quiescent star formation with an essentially z-independent star formation efficiency, combined with post-merger starbursts and the dynamical response after supernova-driven gas-loss, are able to reproduce the position of the dEs in the various univariate diagrams. SAMs with star formation efficiencies that rise as a function of redshift are excluded since they leave the observed sequences traced by dEs virtually unpopulated. dEs tend to lie above the FP and the FP residual declines as a function of luminosity. Again, models that take into account the response after supernova-driven mass-loss correctly predict the position of dEs in the $(\log\sigma, \log R_\mathrm{e}, \log I_\mathrm{e})$ parameter space as well as the trend of the FP residual as a function of luminosity.

While these findings are clearly a success for the hierarchical-merging picture of galaxy formation, they do not necessarily invalidate the alternative *harassment* scenario, which posits that dEs stem from perturbed and stripped late-type disk galaxies that entered clusters and groups of galaxies about 5 Gyr ago.

2.1 Introduction

It is known for almost two decades now that dynamically hot galaxies (elliptical galaxies and bulges of spiral galaxies) are not scattered randomly in the three-dimensional space spanned by B-band luminosity

($\log L_B$, expressed in solar B-band luminosities), half-light radius ($\log R_\mathrm{e}$, expressed in kiloparsecs), and velocity dispersion ($\log \sigma$, expressed in $\mathrm{km\,s^{-1}}$) but that instead they occupy a slender plane: the Fundamental Plane (FP) (Djorgovski & Davis, 1987; Dressler et al., 1987; Bender et al., 1992).
Projections of the FP onto the coordinate planes, in combination with the particular way in which galaxies are distributed within the FP, produce the univariate relations between luminosity and velocity dispersion ($\log L_B = \mathrm{const.} + 3.739 \log \sigma$, (Faber & Jackson, 1976)), luminosity and half-light radius ($\log L_B = \mathrm{const.} + 1.187 \log R_\mathrm{e}$, (Fish, 1963)), surface brightness (expressed in solar B-band luminosities per square parsec) and half-light radius ($\log I_\mathrm{e} = \mathrm{const.} - 0.813 \log R_\mathrm{e}$, (Kormendy, 1977)), and luminosity and surface brightness ($\log L_B = \mathrm{const.} - 1.460 \log I_\mathrm{e}$, (Binggeli et al., 1984)). See Guzmán et al. (1993) for a compilation of these so-called fundamental relations.

Dwarf elliptical galaxies (dEs) are small, low-luminosity galaxies ($M_B \gtrsim -18\,\mathrm{mag}$) (Ferguson & Binggeli, 1994). They are among the most numerous galaxy species in the universe and are found abundantly in groups and clusters of galaxies. Their diffuse, approximately exponentially declining surface-brightness profiles set them apart from the compact ellipticals (cEs) which, while occupying the same luminosity range as the dEs, have much higher central surface brightnesses and a de Vaucouleurs-like surface-brightness profile. We distinguish dwarf lenticular galaxies (dS0s) from dEs by their highly flattened appearance (E6/E7) and their disky isophotes. The locus of the dEs and dS0s in the $(\log \sigma, \log R_\mathrm{e}, \log I_\mathrm{e})$ space and in the univariate diagrams that require kinematical information (such as the Faber-Jackson relation, hereafter FJR) was up to now rather uncertain. After the early work by Nieto et al. (1990), Bender et al. (1992), and Guzmán et al. (1993), relatively little attention has been paid to the relations between the internal kinematics and the structural parameters of these faint, small elliptical galaxies and, particularly, to what we can learn from such relations regarding the origin and evolution of dEs. This is in part due to their low surface brightness, which makes spectroscopy, required for the extraction of stellar kinematics, very time-consuming. This also limits the size of the individual data sets and consequently compromises the statistical significance of the results. Still, explaining the scaling relations among the structural parameters of dwarf galaxies, which are believed to be the building blocks of more massive galaxies, is a crucial test for theories of cosmological structure formation. A comparison of theoretical predictions with observations can put strong constraints on the cosmological star formation history and help to refine prescriptions for e.g. star formation and energy feedback from supernova explosions, which play a crucial role in low-mass dwarf galaxies (see chapter 7).

We explore the relations between the various structural parameters of dEs and compare them with theoretical predictions. This chapter is organised as follows: we briefly discuss the observations and data reduction procedures in section 2.2. In section 2.3, the theoretical models with which we compare our data are presented. The univariate relations between the different structural parameters are discussed in section 2.4. The position of the dEs with respect to the Fundamental Plane is presented in section 2.5. We end with a discussion of the results in section 2.6.

2.2 Observations and data reduction

Within the framework of an ESO Large Program, we observed deep major and minor axis spectra with unprecedented spatial and spectral resolution of a sample of 15 dEs and dS0s, both in group (NGC5044, NGC5898, and NGC3258 groups) and cluster environments (Fornax cluster). We also collected Bessel VRI-band images of 22 dEs and dS0s (including the 15 dEs/dS0s of the spectroscopic sample). The targets were selected because they were faint galaxies with elliptical isophotes (with absolute magnitudes in the range $-13.3 \geq M_B \geq -18\,\mathrm{mag}$ in order to distinguish them from the brighter ellipticals and the fainter dwarf spheroidals (dSphs)) and had a high enough surface brightness ($\mu_\mathrm{e,B} \leq 23.5\,\mathrm{mag}$, with $\mu_\mathrm{e,B}$ the mean B-band surface brightness within the half-light radius) to make the extraction of reliable kinematics out to roughly $1.5 - 2\,R_\mathrm{e}$ feasible. In order to obtain a good spatial sampling of

the kinematics, the seeing FWHM should be much smaller than a galaxy's half-light radius so galaxies with a half-light radius smaller than $R_{\rm e} \approx 4''$ were rejected as possible targets. There was no direct kinematical selection criterion.

The data were obtained with the FORS2 imaging spectrograph mounted on the unit telescopes Kueyen and Yepun of the VLT. The images were bias-subtracted and flatfielded using skyflats taken during twilight of the same night as the science frames. The sky background was removed by fitting a tilted plane to regions of the images free of stars or other objects and subtracting it. The photometric zeropoints in each band were measured using photometric standard stars observed during the same night as the science frames. The images were corrected for airmass and for interstellar extinction, using the Galactic extinction estimates from Schlegel et al. (1998). We measured the surface-brightness profile, position angle, and ellipticity as a function of the geometric mean of major and minor axis distance, denoted by a and b respectively, using our own software. Basically, the code fits an ellipse through a set of positions where a given surface brightness level is reached (cosmics, hot pixels, and foreground stars were masked and not used in the fit). The shape of an isophote, relative to the best fitting ellipse, is quantified by expanding the intensity variation along this ellipse in a fourth order Fourier series with coefficients S_3, S_4, C_3 and C_4 :

$$I(a,\theta) = I_0(a)\left[1 + C_3(a)\cos(3\theta) + C_4(a)\cos(4\theta)) + S_3(a)\sin(3\theta)) + S_4(a)\sin(4\theta)\right]. \qquad (2.1)$$

Here, $I_0(a)$ is the average intensity of an isophote with semi-major axis a and the angle θ is measured from the major axis. The basic photometric parameters of the galaxies are presented in Table 2.1. This smooth representation of a galaxy's surface-brightness profile, $I(a,\theta)$, was integrated over circular apertures out to the last isophote we could reliably measure in order to calculate its total magnitude. We did not wish to extrapolate the surface brightness profile or the growth curve beyond the region covered by the data (e.g. by using a Sérsic profile) because of the uncertainties inherent to this procedure. However, our images go down at least 8 mag. Cutting off an exponential surface brightness profile 8 mag below its central value results in an underestimate of the total luminosity by less than one per cent (a cut-off at 6 mag below the central surface brightness, as in a few less deep images, results in an underestimate of the total luminosity by about 2.5 per cent for an exponential profile).

The spectra were obtained within typical exposure times of $5-8$ h per position angle and have a seeing in the range $0.3-1.0''$ FWHM. They cover the wavelength region around the strong Ca II triplet absorption lines (~ 8600 Å). All standard data reduction procedures (bias-subtraction, flatfielding, cosmic removal, wavelength-calibration, sky-subtraction, flux-calibration) were carried out with ESO-MIDAS (developed and maintained by the European Southern Observatory), IRAF (distributed by the National Optical Astronomy Observatories, which are operated by the Association of Universities for Research in Astronomy, Inc., under cooperative agreement with the National Science Foundation) and our own software. We fitted the dispersion relation with a cubic spline, which rectified the lines of the arc spectra to an accuracy of $1-2$ km s^{-1} FWHM. We extracted the stellar kinematical information by fitting a weighted mix of late G to late K giant stars, broadened with a parameterised line-of-sight velocity distribution (LOSVD) to the galaxy spectra. We approximated the LOSVD by a fourth-order Gauss-Hermite series (Gerhard, 1993; van der Marel & Franx, 1993). (For those interested, the kinematics of the full sample and a complete discussion of the data acquisition and analysis will be presented in De Rijcke et al., in prep.) The strong Ca II lines, which contain most of the kinematical information, are rather insensitive to the age and metallicity of an old stellar population (see chapter 3 and Michielsen et al. (2003b); Falcón-Barroso et al. (2003); Saglia et al. (2002)), so template mismatch does not significantly affect our results. The spectra contain useful kinematical information out to $1.5-2\,R_{\rm e}$.

Table 2.1: Structural properties of the observed dEs. The FCC dEs are members of the Fornax Cluster (Ferguson, 1989), the FS dEs belong to the NGC5044 and NGC3258 groups and are cataloged by Ferguson & Sandage (1990). NGC5898_DW1 and NGC5898_DW2 are two previously uncatalogued dEs in the NGC5898 group (where DW stands for DWARF). For each galaxy, the equatorial coordinates, the B-band apparent magnitude m_B (taken from Ferguson (1989) and Ferguson & Sandage (1990), except for FCC046 and FCC207 for which we have obtained B-band images), the luminosity-weighted ellipticity $\epsilon = 1 - q$, with q the isophotal axis ratio, outside the inner 1 arcsec where the ellipticity measurement is affected by seeing, the luminosity-weighted velocity dispersion $\sigma\,\mathrm{km\,s^{-1}}$, see equation (2.2) for a precise definition of σ), the half-light radius R_e arcsec, this is the radius of the circular aperture that encloses half of the light, derived from the R-band images, and the B-band mean surface brightness within one half-light radius $\mu_{\mathrm{e},B}$ are listed. We used our R-band R_e to calculate $\mu_{\mathrm{e},B}$. This does not influence our results in any way since we found R_e not to differ between R, B, and V-band images. For 7 dEs, only photometry is available.

name	α (J2000)	δ (J2000)	m_B	ϵ	σ	R_e	$\mu_{\mathrm{e},B}$
FCC043	03 26 02.2	-32 53 40	13.91	0.26	56.4±3.7	16.9	22.05
FCC046	03 26 25.0	-37 07 41	15.99	0.36	61.4±5.0	6.7	22.12
FCC100	03 31 47.6	-35 03 07	15.30	0.28	/	11.7	22.63
FCC136	03 34 29.5	-35 32 47	14.81	0.21	64.3±3.8	14.2	22.57
FCC150	03 35 24.1	-36 21 50	15.70	0.19	63.8±3.9	5.7	21.48
FCC188	03 37 04.5	-35 35 26	16.10	0.06	/	9.3	22.94
FCC204	03 38 13.6	-33 07 38	14.76	0.61	67.2±4.4	11.5	22.06
FCC207	03 38 19.3	-35 07 45	16.19	0.15	60.9±6.6	8.4	22.81
FCC245	03 40 33.9	-35 01 23	16.00	0.11	39.5±4.2	11.4	23.28
FCC252	03 40 50.4	-35 44 54	16.00	0.08	/	7.9	22.47
FCC266	03 41 41.4	-35 10 12	15.90	0.11	42.4±3.4	7.1	22.15
FCC288	03 43 22.6	-33 56 25	15.10	0.72	48.5±3.3	9.5	21.99
FCC303	03 45 14.1	-36 56 12	15.50	0.09	/	11.6	22.81
FCC316	03 47 01.4	-36 26 15	16.30	0.26	/	9.0	23.06
FCC318	03 47 08.2	-36 19 36	16.10	0.18	/	10.6	23.22
FS029	13 13 56.2	-16 16 24	15.70	0.54	59.6±3.6	8.9	22.44
FS075	13 15 04.1	-16 23 40	16.87	0.10	/	6.8	23.03
FS076	13 15 05.9	-16 20 51	16.10	0.07	56.8±3.8	4.4	21.41
FS131	13 16 49.0	-16 19 42	15.30	0.54	87.0±3.2	8.1	21.83
FS373	10 37 22.9	-35 21 37	15.60	0.23	73.1±3.1	7.9	22.03
NGC5898_DW1	15 18 13.0	-24 11 47	15.66	0.34	43.5±3.0	8.7	22.35
NGC5898_DW2	15 18 44.7	-24 10 51	16.10	0.57	44.2±3.4	5.9	21.95

2.3 Theoretical models for dE formation

Here, we discuss the models for dE formation and evolution which in the following sections will be compared with the data. First, three different calculations are introduced that are all based on the idea that dEs are primordial objects that lost their gas in a supernova-driven galactic wind (also known as the *wind model*) and second, we discuss model predictions based on the *harassment* scenario.

2.3.1 The wind model

The first detailed models of the evolution of galaxies taking into account the dynamical response after a supernova-driven galactic wind (hence the name of this class of models) were presented by Yoshii & Arimoto (1987) (hereafter YA87). These models follow the evolution of stellar systems using one-zone models without internal structure and with masses between $10^5\,\mathrm{M}_\odot$ and $2\times10^{12}\,\mathrm{M}_\odot$. They assume an empirical scaling law between the gravitational binding energy Ω and total mass M: $\Omega\propto M^{1.45}$ (Fish, 1964; Saito, 1979). This translates into a mass-gravitational radius relation of the form $R_G\propto M^2/\Omega\propto M^{0.55}$, a mass-density relation $\rho\propto M/R^3\propto M^{-0.65}$, and a velocity dispersion-mass relation $\sigma\propto\sqrt{\Omega/M}\propto M^{0.225}$ *before* any mass-loss has occurred. The star formation timescale t_{SF} is proportional to the minimum of the collision time of molecular clouds and the free-fall time of individual clouds. In both cases, $t_{\mathrm{SF}}\propto1/\sqrt{\rho}$ with the proportionality constant chosen such that the present-day color-magnitude relation, from giant ellipticals down to globular clusters, is reproduced. The structure of these models is altered as they expand in response to the loss of a mass-fraction f in the form of supernova-driven galactic winds. The value of f is determined by the timing of the galactic winds, with later winds expelling a smaller gas fraction than earlier ones. In these models, the time-scales on which all physical processes operate are determined by M, making f also a function of M. The crux is, of course, for f to have the correct behaviour as a function of M in order to reproduce the observed relations between the different structural parameters of spheroidal galaxies. Since R_G is roughly proportional to R_{e} in a constant-M/L model, and the precise value of the radius does not affect the physics of the models anyway, we scaled the mass-radius relation such that the present-day half-light radii of ellipticals with a luminosity $\log L_B=10.4$ ($M_B=-20.5\,\mathrm{mag}$) are reproduced. This is the boundary between, roughly speaking, the disky, cuspy, isotropic intermediate-brightness ellipticals and the boxy, anisotropic bright ellipticals with a core (Bender et al., 1989; Graham & Guzmán, 2003).

More recent semi-analytical models (SAMs) (Somerville et al., 2001; Nagashima & Yoshii, 2004) take into account the hierarchical merger tree that leads up to the formation of a galaxy of a given mass in a ΛCDM cosmology ($\Omega_{\mathrm{baryon}}\approx0.02$, $\Omega_{\mathrm{matter}}=0.3$, $\Omega_\Lambda=0.7$, $H_0=70\,\mathrm{km\,s^{-1}\,Mpc^{-1}}$). SAMs make use of prescriptions for star formation, energy feedback from supernova explosions, gas cooling, tidal stripping, dust extinction, and the dynamical response to starburst-induced gas ejection and, despite the inevitable oversimplifications in the description of immensely complex processes such as star formation, they are able to account pretty well for many observed properties of galaxies. E.g., Somerville et al. (2001) compare their SAMs with the comoving number density of galaxies, the evolution of the galaxy luminosity function and the H I content of the universe as a function of redshift, and the star formation history of the universe (the *Madau diagram*). Based on this comparison, these authors favor the idea that merger-induced starbursts have played an important role in enhancing the star formation efficiency at high redshift. Nagashima & Yoshii (2004) (NY04) moreover take into account the gas ejection and the ensuing dynamical response of a galaxy after a merger-induced star-burst. These authors compare the galaxies formed in their SAMs with the observed properties of dynamically hot galaxies (from the faint Local Group dSphs up to the very brightest elliptical galaxies) and come to roughly the same conclusions as Somerville et al. (2001). Despite their simplicity, the YA87 models already capture a lot of the physics of galaxy formation, at least in the mass-regime of the dEs, which apparently formed while their progenitors were still largely gaseous. In all ../figures, we will use them as an instructive proxy for the physically more motivated SAMs of e.g. Somerville et al. (2001) and NY04. Using the tables given in YA87, we fitted cubic splines to all relevant parameters as functions of M in order to be able to plot them as continuous sequences in the ../figures in the following sections.

In Chiosi & Carraro (2002) (hereafter CC02), the evolution of spherical elliptical galaxies in a standard CDM universe ($\Omega_{\mathrm{baryon}}=0.1$, $\Omega_{\mathrm{dark}}=0.9$, $\Omega_\Lambda=0$) is followed using N-body/SPH simulations with prescriptions for star formation, feedback, cooling, and chemical evolution. A protogalaxy is assumed to virialize at a redshift $z=5$, when it had an overdensity $1+\delta\sim200$, after which star

formation ensues. Two series of models, with masses between 10^8 and $10^{13}\,\mathrm{M}_\odot$ and with different initial densities, are presented. Models of series A have a high initial density (they virialized at redshift $z = 5$, when the universe was still very dense), models of series B have low initial densities (they virialized at much lower redshift). These models allow for a more realistic description of the galactic wind as compared to YA87: only gas particles with velocities above the local escape speed are blown away. This reduces the amount of mass that is lost and leads to a much milder structural evolution compared to the YA87 models. Contrary to the YA87 models, dwarf galaxies are found to have the longest star formation histories. Massive ellipticals hold on very strongly to their gas reservoirs, allowing the gas to be converted almost completely into stars in a single burst. In dwarf galaxies, on the other hand, supernova explosions disperse the gas, switching off further star formation. Gas cools, sinks back in and the star formation efficiency goes up again after which subsequent supernova explosions disperse the gas and so on. This gives rise to very inefficient, oscillating but long-lived star formation. As aforementioned, the way star formation is implemented in the YA87 models causes the star formation efficiency to be highest in low-mass galaxies, they simply do not continue forming stars for very long. By the time a galactic wind sets off, most of the gas has been converted into stars. Very massive galaxies form stars most slowly but they hang onto their gas very strongly, leaving enough time for most of the gas to be converted into stars. Hence, galaxies around $\log(L_B) = 7$ ($M_B = -12\,\mathrm{mag}$) experience the most drastic mass-loss while more and less luminous galaxies are less affected by gas ejection. This effect is most likely due to the extreme simplicity of the models. The more complex models, with more realistic star formation histories, do not show this behaviour.

Both the YA87 and CC02 models do not take into account mergers. As a consequence, they will underestimate the velocity dispersions and half-light radii and overestimate the surface brightnesses of massive ellipticals (see e.g. Hernquist (1992) and Dantas et al. (2003) for the effects of dissipationless mergers and Hernquist et al. (1993) and Bekki (1998) for merger simulations taking into account the presence of gas). SAMs (e.g. NY04) follow the merger tree leading up to a galaxy (including dissipationless mergers) and hence do a much better job at reproducing the characteristics of massive galaxies. Hence, the failure of the YA87 and CC02 models for bright galaxies does not signal a problem with CDM. These models simply lack the physics necessary to explain the properties of bright ellipticals.

The N-body/SPH models presented by Kawata (1999) and Kawata (2001) (K01) are based roughly on the same premises as those of CC02, although the details differ. Using an N-body/SPH code, the evolution of a slowly rotating (spin parameter $\lambda = 0.02$) region in a standard CDM universe, on which small-scale density fluctuations are laid out, is followed from $z = 40$ up to the present. Overdense clumps within this region collapse, merge, and finally form a single elliptical galaxy. Regions with masses between 10^{11} and $8 \times 10^{12}\,\mathrm{M}_\odot$ are modeled. E.g., for a region with a total mass $M = 8 \times 10^{11}\,\mathrm{M}_\odot$, star formation starts in merging clumps at $z \approx 3.5$ and the final galaxy is in place at $z \approx 1.9$. No merging takes place after $z \approx 0.8$. The influence of the energy feedback efficiency of supernova explosions (SN II and SN Ia) on the evolution of elliptical galaxies and bright dEs is explored. The more efficient the supernovae inject kinetic energy into the interstellar medium, the sooner the gas is blown away. This results in more expelled gas and more structural evolution in low-mass galaxies. Two series of models are calculated: a series with very efficient kinetic feedback, which is able to reproduce the observed color-magnitude relation of elliptical galaxies, and one with minimal feedback. As an example: a bright dwarf galaxy with an initial total mass $M = 10^{11}\,\mathrm{M}_\odot$ and with a high feedback efficiency develops a galactic wind at $z \approx 1.7$. By $z \approx 1.2$, most of the gas has been blown out. For these models, only photometric quantities are calculated.

It should be noted that CC02 and K01 use a CDM cosmology whereas NY04 use ΛCDM. This is probably not a major concern. CC02 follow the evolution of an isolated galaxy, disconnected from the universal expansion. The only cosmological parameter that goes into these calculations is the density of the universe at the virialization redshift of the galaxy. However, at $z \sim 5$, a CDM universe very much resembles a ΛCDM universe since Ω_Λ started to dominate Ω_{matter} only at $z \sim 0.3$. In K01, most

of the merging activity, which is influenced by the dynamics of the universe, has ended around $z = 2$. So, hierarchical merging takes place at a cosmic time when CDM and ΛCDM universes do not differ much. The YA87 models, due to their simplicity, are essentially devoid of cosmological considerations. Moreover, slight effects due to cosmology can probably be offset by using slightly different star formation or feedback efficiencies. This makes us confident that the different cosmologies do not yield significantly different predictions for the properties of individual galaxies.

2.3.2 The harassment scenario

Alternatively, dEs could stem from late-type disk galaxies that entered the clusters and groups of galaxies about 5 Gyr ago ($z \sim 0.5$). N-body simulations show that gravitational interactions trigger bar-formation in any small late-type disk galaxy (Scd-Irr) orbiting in a cluster (Moore et al., 1996; Moore et al, 1998) or around a massive galaxy in a group environment (Mayer et al., 2001) and strip large amounts of stars, gas, and dark matter from it by tidal forces. Internal dynamical processes (such as the buckling of the bar) subsequently transform a disk galaxy into a dynamically hot spheroidal dE within a timespan of a few Gyr (Mastropietro et al., 2004). Gas (if it is not stripped off by the ram pressure of the intergalactic medium, see e.g. Marcolini et al. (2003)) is funneled inwards by the non-axisymmetric force field of the bar (Mayer et al., 2001). If this gas is converted into stars, the resulting galaxy is likely to have a higher central surface brightness than its progenitor and would probably resemble a nucleated dE. Purely stellar dynamical processes such as bar formation and buckling lead to a more shallow central density enhancement. The dEs formed in these simulations rotate quite rapidly and some still display some memory of their former state. Examples are dEs with embedded stellar disks (Barazza et al, 2002; De Rijcke et al., 2003a; Graham et al., 2003) or kinematically decoupled cores (De Rijcke & Debattista, 2004). This model explicitly takes into account the fact that dEs are found predominantly in clusters and groups of galaxies. It also offers a natural explanation for the Butcher-Oemler effect (Butcher & Oemler, 1978): at $z \sim 0.4$, a population of blue, distorted galaxies is present in clusters of galaxies while no such objects reside in present-day clusters. The former could be late-type galaxies caught in the predicament of being harassed and transformed into more spheroidal objects.

Clearly, the parameter space that should be explored to make firm predictions based on this scenario is huge. One should start with gas-rich late-type galaxies of various masses and with different scale-lengths, placed on different orbits in a variety of cluster and group environments, using realistic prescriptions for star formation, energy feedback, gas cooling, and ram-pressure stripping by the intra-cluster medium. As long as this formidable task has not been performed, we will have to settle with what can be gleaned from the few calculations that have been published up to now. These show that, harassment being a stochastic process whose effects depend in a very complicated way on the orbit of a progenitor galaxy through a cluster, it is rather unlikely that dEs end up close to a slender plane like the FP. The half-light radius of a dE formed through harassment is about half that of its progenitor, with the central surface brightness about two to three times higher than the original value (Mayer et al., 2001). The velocity dispersion has also roughly doubled. Moreover, it is very likely that interactions induce star-bursts and hence that dEs formed through harassment harbor stellar populations of different ages, further adding to the expected scatter about the FP (Forbes et al., 1998). Although more simulations are needed to converge on a coherent picture of the effects of harassment, two predictions can already be made: (1) some dEs should still contain some memory of their disky, gaseous past and (2) only weak correlations with large scatter are expected between structural parameters. The latter is due to the stochastic nature of harassment and, if the Butcher-Oemler galaxies at $z \sim 0.4$ are anything like the present-day Scd-Irr galaxies, due to the large scatter of the progenitor galaxies in the FP (Burstein et al., 1997).

Yet another possible way to produce dwarf galaxies is described by Kroupa (1998) or Duc et al. (2004). The hundreds of young compact massive star clusters formed during the merger of two gaseous disk galaxies may coalesce within a few 100 Myr to form a small number of objects, with masses of or-

der $10^9\,M_\odot$, with negligible dark-matter content, and with a half-mass radius of a few 100 parsec. However, simulations have thus far not been able to make predictions for the present-day properties of these so-called tidal dwarf galaxies. Also, major mergers cannot have produced a significant fraction of the dE population since each merger only yields one or two tidal dwarf galaxies. For these reasons, and since the objects formed this way are less massive than the dEs considered here and in many respects are more like the Local Group dSphs, we will not discuss this formation mechanism here.

2.4 Univariate relations

In the following, we confront the predictions of the models discussed in section 2.3, with the observed relations between the structural and kinematical parameters of dynamically hot galaxies. The most massive representatives of this family of galaxies are the giant ellipticals (B-band luminosity $\log L_B \sim 11.5$ or $M_B = -23.3$ mag); the least massive systems are the Local Group dwarf spheroidals ($\log L_B \sim 6$ or $M_B = -9.5$ mag). Three data sets of kinematics of dEs in the luminosity range $\log L_B \approx 8 - 9.2$ or $M_B = -14.5$ to -17.4 mag) are currently available: our sample of 15 group and cluster dEs/dS0s (DR04), the sample of 17 Virgo cluster dEs observed by Geha et al. (2003) (G03) and the 16 Virgo cluster dEs from van Zee et al. (2004) (vZ04) (which has an overlap of 5 objects with the G03 sample). Since none of the three datasets on its own can boast statistical significance or cover a parameter interval large enough for reliable inferences to be made, it is natural to combine them, bringing the total number of dEs with spatially resolved kinematics to 43. For completeness, we also compare our results with the central velocity dispersions of nucleated dEs measured by Peterson & Caldwell (1993) (PC93).

In diagrams relating only photometrical parameters, we have included the sample of 25 Virgo cluster dEs and dS0s of Barazza et al. (2003) (Ba03), which was used for the determination of surface-brightness fluctuation (SBF) distances, the Fornax dEs presented in Michielsen et al. (2004a) (M04, see also chapter 4), and the 18 Coma dEs analysed in Graham & Guzmán (2003) (Gr03). The dwarf galaxies in the Ba03 sample were selected because they have large half-light radii and yield as many independent SBF measurements as possible. Hence, the Ba03 sample traces the dE sequences in the photometric univariate diagrams in regions as yet unexplored by spectroscopic samples. The relevant data for giant ellipticals, intermediate-luminosity ellipticals, bulges, dwarf spheroidals and a handful of dEs come from Bender et al. (1992) (B92). Where necessary, all datasets have been converted to B-band luminosities assuming $B - V = 0.7$ and to a Hubble parameter $H_0 = 70\,\mathrm{km\,s^{-1}\,Mpc^{-1}}$ (Freedman et al., 2001). This places the Fornax cluster at a distance of 19.7 Mpc ($v_{\rm sys} = 1379\,\mathrm{km\,s^{-1}}$). and the Virgo cluster at 15.4 Mpc ($v_{\rm sys} = 1079\,\mathrm{km\,s^{-1}}$), both in good agreement with SBF distances: Jerjen (2003) and Jerjen et al. (2004) find a Fornax distance of 20.3 ± 0.7 Mpc and a distance of 15.8 ± 1.4 Mpc for the Virgo M87-subcluster, with the main uncertainty being the depth of the Virgo cluster. Using this H_0 value, the NGC5044 group distance is estimated at 35.1 Mpc ($v_{\rm sys} = 2459\,\mathrm{km\,s^{-1}}$), that of NGC3258 at 40.7 Mpc ($v_{\rm sys} = 2848\,\mathrm{km\,s^{-1}}$), and NGC5898 at 30.3 Mpc ($v_{\rm sys} = 122\,\mathrm{km\,s^{-1}}$). Using SBF, these groups or their dominant elliptical galaxy are placed at 31.2 ± 4.0 Mpc (NGC5044), 32.1 ± 4.0 Mpc (NGC3258), and 29.1 ± 3.5 Mpc (NGC5898) (Tonry et al., 2001). Hence, with the exception of the NGC3258 group, Hubble-distances and SBF-distances agree within the errorbars.

Below, we discuss the position of the dEs in the (mutually dependent) $\sigma - L_B$, $R_{\rm e} - L_B$, $I_{\rm e} - L_B$, and $I_{\rm e} - R_{\rm e}$ diagrams. Since the quantities plotted on the ordinate and abscissa are not necessarily independent (e.g. $I_{\rm e}$ and $R_{\rm e}$), their errors can also be correlated. We estimated the systematic and statistical (measurement) uncertainties on all quantities for a typical galaxy in our sample by assuming the values $\sigma = 50 \pm 3\,\mathrm{km\,s^{-1}}$ (assumed to be a 1σ Gaussian error), $R_{\rm e} = 1.25 \pm 0.06$ kpc, $L_B = (8 \pm 0.8) \times 10^8\,L_{\odot,B}$. Using a Gaussian random-number generator, a data-point can be generated that is afflicted only by measurement errors. For each such new data-point, a distance estimate was generated,

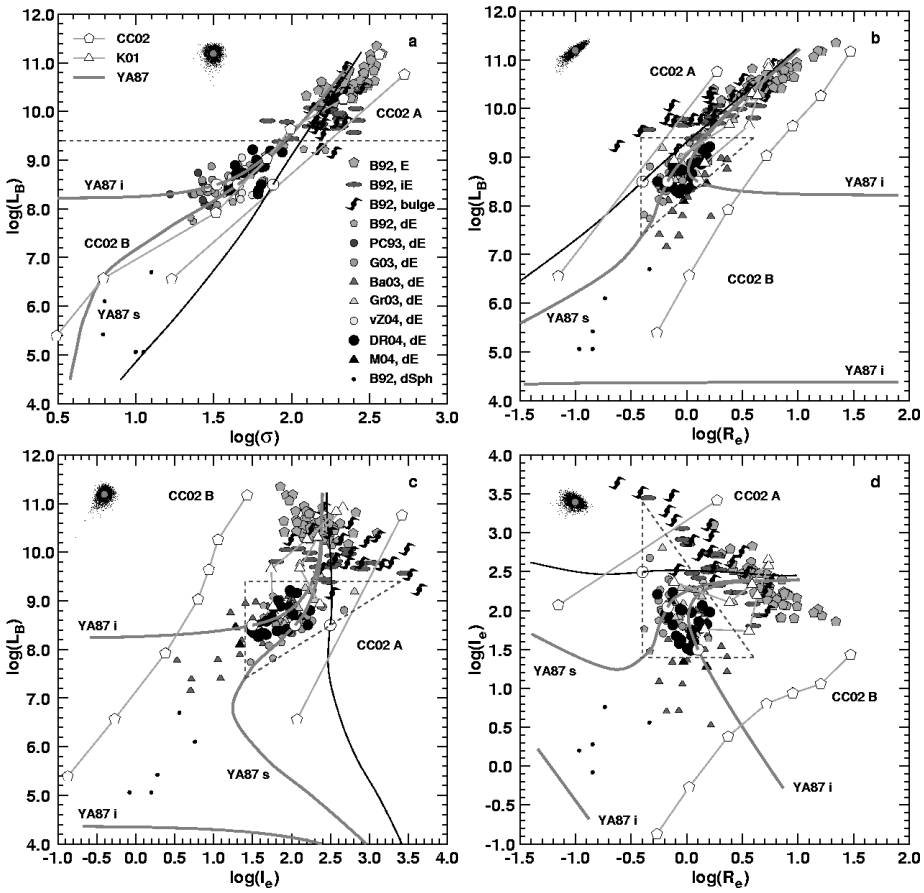

Figure 2.1: Panel **a**: the $\sigma - L_B$ relation; panel **b**: the $R_\mathrm{e} - L_B$ relation; panel **c**: the $I_\mathrm{e} - L_B$ relation; panel **d**: the $R_\mathrm{e} - I_\mathrm{e}$ relation. The regions in these diagrams that satisfy our selection criteria are delineated by dotted lines. L_B is expressed in solar B-band luminosities, σ in $\mathrm{km\,s^{-1}}$, R_e in kiloparsecs, and I_e in solar B-band luminosities per square parsec. The symbols representing the various datasets, galaxy types (bright ellipticals: E, intermediate-luminosity ellipticals: iE, bulges of spiral galaxies: bulge, dwarf ellipticals: dE, dwarf spheroidals: dSph), and theoretical models are indicated in panel **a**. The black line traces the zero mass-loss relation of the YA87 models. The thick grey lines trace the relations after slow (YA87 s) or instantaneous (YA87 i) gas removal. The position of a typical dE with apparent magnitude $m_B = 16\,\mathrm{mag}$ at the distance of Fornax before and after supernova-driven mass-loss is indicated with white circles. The CC02 models (white pentagons) of series A (CC02 A) collapse to a final state with a very small half-light radius and a large velocity dispersion. The models of series B (CC02 B) on the other hand reproduce the observed $\sigma - L_B$ relation but have half-light radii that are too large. On the whole, the CC02 models are able to reproduce the observed slopes of the several structural relations. The photometric properties of the K01 models (white triangles) roughly agree with the observations and the YA87 models. For a given mass, the trend for K01 models as a function of feedback efficiency parallels that of the YA87 models as a function of mass-loss timescale. In the upper left corner of each panel, a cloud of 3000 simulated data points gives an idea of the systematic and statistical uncertainty on a typical DR04 data point (indicated by a grey dot).

assuming a distance of 30 ± 3 Mpc (1σ-error), which, even in the absence of other measurement errors, would introduce a correlated uncertainty on distance-dependent quantities. Each new data-point was then shifted according to its distance. We calculated 10000 new data-points for this typical galaxy, each one affected randomly by measurement errors and a distance-dependent shift. This way, the Monte-Carlo procedure properly adds the random measurement errors and the systematic distance-dependent errors. In the corner of each panel of Fig. 2.1, a dark grey data point is indicated, surrounded by 3000 of these simulated data points (small black dots). These give an idea of the typical systematic and statistical (correlated) errors on our data. They over-estimate the true scatter between the individual data points since all galaxies belonging to the same group or cluster will be affected in the same way by the distance uncertainty.

2.4.1 The $\sigma - L_B$ or Faber-Jackson relation (FJR)

Bright and intermediate-luminosity ellipticals and bulges of spiral galaxies adhere closely to the FJR: $L_B \propto \sigma^{\alpha}$, with $\alpha \sim 4$ (Faber & Jackson, 1976). Held et al. (1992) fitted a straight line through data of 4 dEs (three Local Group dEs and one Virgo dE) and 4 Local Group dSphs and found $L_B \propto \sigma^{2.5}$. They however omitted one dE from their original dataset of five and two dSphs from an original sample of six. All three deviate significantly from the relation fitted to the eight galaxies that were used, casting serious doubts on the slope of the fitted relations. PC93 fitted a straight line to the then available dE and dSph data and found $L_V \propto \sigma^{5.6\pm0.9}$. Guzmán et al. (1993) connected the B92 dE data with that of the dSphs and found a similar slope to the FJR of the bright ellipticals but with a different zero-point. In both attempts to measure the dE FJR, the region of about 5 magnitudes in luminosity between the dEs and the dSphs, for which no data was available, had to be bridged.

We are now for the first time in the situation that kinematical data of enough dEs are available to measure the dE FJR without the need of extrapolating towards the dSphs. Many dEs contain a central brightness peak, called the nucleus. Hence, the central velocity dispersion does not necessarily reflect the dynamics of the whole galaxy and cannot be expected to be a good measure for a galaxy's kinetic energy budget. To account for this, we instead use the luminosity-weighted mean velocity dispersion

$$\sigma = \frac{\int_0^{a_{\max}} \sigma_{\rm maj}(a) I(a) a \, da}{\int_0^{a_{\max}} I(a) a \, da}, \tag{2.2}$$

with $\sigma_{\rm maj}(a)$ and $I(a)$ the major-axis velocity dispersion and the surface brightness, respectively, at a major-axis distance a and $a_{\max}$ the major-axis distance of the last kinematical data-point. Since the velocity dispersion can be strongly influenced by the nucleus and hence show a pronounced central depression, the luminosity-weighted mean velocity dispersion can differ from the central dispersion by as much as 100% of the central value. However, for $a_{\max}$ larger than $1\,R_{\rm e}$, σ changes very little by integrating farther out so we are sure that we have defined a robust quantity. For the other galaxies, we had to settle for the mean (G03) and the median (vZ04) of the dispersion profile, measured along the major axis.

As is obvious from the panel **a** in Fig. 2.1, the FJR becomes noticeably flatter below $\log(L_B) \sim 9.5$ or $M_B \sim -18.3$ mag (here and in the following, L_B is expressed using the solar B-band luminosity as unit and σ is expressed in units of km s^{-1}). We fitted a straight line to the available data, taking into account the errors on the luminosities and the velocity dispersions. For the luminosities, we used $\delta_{\log L_B} = 0.1$. The velocity-dispersion errors $\delta_{\log \sigma}$ of our data can be found in Table 2.1. For the other data sets, we of course used the errors stated by the various authors. We minimized the non-linear quantity

$$\chi^2 = \frac{1}{N-2} \sum_{i=1}^{N} \frac{(a + b \log \sigma_i - \log L_{Bi})^2}{b^2 \, \delta^2_{\log \sigma_i} + \delta^2_{\log L_{B\,i}}}, \tag{2.3}$$

with $\log \sigma_i$ and $\log L_{Bi}$ observed data-points and $\delta_{\log \sigma_i}$ and $\delta_{\log L_{Bi}}$ the corresponding errorbars, using the routine `fitexy` of Press et al. (1992) in order to obtain the zeropoint a and the slope b. N is the number of data points. The diagonal elements of the estimated covariance matrix were used as approximations to the variances of the regression coefficients a and b. A straight-line fit to the DR04, vZ04, G03, and B92 dEs yields

$$\log L_B = 6.02^{\pm 0.31} + 1.57^{\pm 0.19} \log \sigma \tag{2.4}$$

with a regression coefficient $r = 0.68$ and $\chi^2 = 4.9$. If the B92 dSphs are included in the fit, one obtains

$$\log L_B = 4.39^{\pm 0.37} + 2.55^{\pm 0.22} \log \sigma \tag{2.5}$$

with a regression coefficient $r = 0.85$ and $\chi^2 = 9.2$. The linear trend becomes more significant since a much larger data-interval is covered but the χ^2 is much higher, quantifying what the eye sees immediately: the $\sigma - L_B$ relation does not have a constant slope when going from the dEs to the dSphs. A dE FJR that is steeper than the FJR of bright ellipticals is definitely excluded by these data. This clearly shows the need of combining the available data-sets of dE kinematics and the dangers involved with extrapolating each of these data-sets separately towards the dSphs. Moreover, these results contradict the universality of the $\sigma - L_B$ relation, which was suggested by Guzmán et al. (1993). A currently running project on the properties of faint early-type galaxies ($-22 < M_R < -17.5$) in the central $1\,\mathrm{deg}$ of the Coma cluster yields FJR $L \propto \sigma^{2.01}$ at the faint end, which is consistent with our results (Matković & Guzmán, private communication).

According to the YA87 models, if a mass-fraction f is blown away, a galaxy evolves to a new virial equilibrium with a velocity dispersion that is offset from the initial value by

$$\Delta \log \sigma = \log(1 - f) \tag{2.6}$$

for slow, and

$$\Delta \log \sigma = 0.5 \log(1 - 2f), \tag{2.7}$$

for instantaneous mass-loss.

Hence, the expansion following the galactic wind drives more low-mass dEs, that lose a larger mass-fraction than more massive objects, progressively towards lower velocity dispersions, leading to a flatter FJR in the luminosity regime of the dEs (cf. the shift with respect to the zero mass-loss curve of the evolutionary endpoints of a typical $m_B = 16\,\mathrm{mag}$ Fornax dE, indicated by white circles in Fig. 2.1). Galaxies with luminosities in the range $\log L_B \approx 4.4 - 8.2$ or $M_B = -5.5$ to $-15.0\,\mathrm{mag}$ are disrupted by the instantaneous ejection of more than half of their initial mass which causes the velocity dispersion to drop to zero at $\log L_B \approx 8.2$ or $M_B = -15.0\,\mathrm{mag}$. The locus of the dEs in a $\log L_B$ versus $\log \sigma$ diagram is bracketed nicely by the lines corresponding to slow and instantaneous mass-loss. The zero mass-loss YA87 $\sigma - L_B$ relation has a slope similar to that of the bright ellipticals although it underestimates the velocity dispersion of the very brightest ellipticals (most likely due to the fact that mergers are not taken into account). The CC02 models A collapse to rather centrally concentrated systems with velocity dispersions that are about a factor two too high. The CC02 models B agree with the YA87 models for slow mass-loss and also reproduce the observations fairly well, from the dSphs up to the brightest ellipticals. For a comparison of the FJR with SAM-predictions, with and without dynamical response to mass loss, see Figs. 12 and 14, respectively, of NY04.

2.4.2 The $R_\mathrm{e} - L_B$ relation or Fish's law

According to the YA87 models, galaxies experiencing mass-loss are expected to evolve towards larger half-light radii at fixed luminosity, i.e. to the right in panel **b** of Fig. 2.1, which relates the half-light

radius (in kpc) to luminosity, by an amount

$$\Delta \log R_{\rm e} = -\log(1-f) \tag{2.8}$$

for slow, and

$$\Delta \log R_{\rm e} = \log(1-f) - \log(1-2f), \tag{2.9}$$

for instantaneous loss of a mass-fraction f. Galaxies in the luminosity range $\log L_B \approx 4.4 - 8.2$ or $M_B \approx -5.5$ to -15.5 mag are disrupted by the instantaneous loss of more than half of their initial mass. This causes their half-light radius to diverge at $\log L_B \approx 8.2$ or $M_B \approx -15$ mag. The zero mass-loss $L_B - R_{\rm e}$ relation predicted by YA87 (i.e. the sequence that galaxies would trace if the dynamical response to the mass loss is not taken into account) is slightly steeper than that of the bright elliptical galaxies and the very brightest elliptical galaxies have larger half-light radii than is expected. The slope of the zero mass-loss relation in combination with the dynamical response to the galactic wind result in a dE L_B–$R_{\rm e}$ relation that is much steeper than that of the brighter galaxy species, as is actually observed. For bulges, intermediate-luminosity and bright ellipticals, the best fitting straight line is given by $L_B \propto R_{\rm e}^{1.19}$ (Guzmán et al., 1993).

For the dEs, we used the same non-linear least-squares technique as in the previous section, assuming an error of 5% on the DR04 effective radii. This error takes into account the error on the measurement of the total magnitude and photon-shot noise. It should be noted that not all authors measure effective radii the same way. In DR04, $R_{\rm e}$ is the radius $R_{\rm e,\,circ}$ of the circular aperture that encloses half the light. Ba03 and Gr03 use the geometric mean radius $R_{\rm e,\,mean}$ (which is not expected to deviate much from $R_{\rm e,\,circ}$). G03 uses the major-axis distance $R_{\rm e,\,maj}$ as radius. We derived geometric mean half-light radii from the G03 data using the relation $R_{\rm e,\,mean} = \sqrt{1-\epsilon} R_{\rm e,\,maj}$, with ϵ the ellipticity. The B92 are a mix of $R_{\rm e,\,circ}$ and $R_{\rm e,\,mean}$ measurements. A fit to the DR04, G03, and B92 dEs yields

$$\log L_B = 8.72^{\pm 0.04} + 2.07^{\pm 0.26} \log R_{\rm e} \tag{2.10}$$

with a regression coefficient $r = 0.68$ and $\chi^2 = 5.1$. Taking the dSphs together with these dEs makes the slope even steeper:

$$\log L_B = 8.50^{\pm 0.05} + 3.71^{\pm 0.20} \log R_{\rm e} \tag{2.11}$$

with a regression coefficient $r = 0.90$ and $\chi^2 = 8.2$. One should be very cautious about these results since adding the Ba03 dEs clearly destroys the impression of a strong linear relation. Also, the YA87 models do not predict that a tight $L_B - R_{\rm e}$ relation should exist, given the spread between the models with slow and instantaneous mass-ejection (unlike in the case of the $\sigma - L_{\rm B}$ relation where slow and instantaneous mass-loss models almost coincide in the dE-regime). The slope of the dE/dSph $L_B - R_{\rm e}$ relation is reproduced very nicely by the CC02 models, although the models of series A, that virialized at high redshift, are too compact while the models of series B, that virialized at low redshift, are too extended. This however does not necessarily invalidate these calculations nor the wind model since the initial density of the models, and hence the present-day half-light radius to which they collapse, depends on the virialization redshift which was arbitrarily fixed at $z = 5$ by CC02. These authors argue that, interpolating between the CC02 models A and B, models that virialized at $z \sim 2$ would be able to reproduce the position of dEs in this diagram.

The locus of the observed dEs is bracketed by the YA87 models for slow and instantaneous gas removal. The K01 models roughly agree with the observations and with the YA87 models. SAMs (like NY04) predict some cosmic scatter on structural scaling relations because of the different merger trees that lead up to a galaxy with a given present-day luminosity. K01 only calculated one model per mass per feedback efficiency. It is therefore not possible to assess the uncertainty on (or the scatter about) the

predicted model properties. Still, it is encouraging that the models with minimal feedback efficiency approximate the zero or slow mass-loss models of YA87 while the models with high feedback efficiency expand towards larger half-light radii, reproducing the onset of the dE sequence. For a comparison of the $L_B - R_\mathrm{e}$ relation with SAM-predictions see Fig. 10 of NY04.

2.4.3 The $I_\mathrm{e} - L_B$ relation

The YA87 models predict that galaxies should expand after the galactic-wind phase and evolve towards a more diffuse state, characterised by a much lower surface brightness. Hence, they should move to the left in panel **c** of Fig. 2.1, which relates surface brightness to total luminosity, by an amount

$$\Delta \log I_\mathrm{e} = 2 \log(1 - f) \tag{2.12}$$

for slow, and

$$\Delta \log I_\mathrm{e} = 2 \log(1 - 2f) - 2 \log(1 - f), \tag{2.13}$$

for instantaneous mass-loss. Galaxies in the luminosity range $\log L_B \approx 4.4 - 8.2$ or $M_B \approx -5.5$ to -15.5 mag become unbound after the instantaneous loss of more than half of their initial mass and consequently evolve towards zero surface brightness. In the range $\log L_B = 7 - 11$ or $M_B = -12$ to -22 mag, the zero mass-loss $I_\mathrm{e} - L_B$ relation runs almost vertically in this diagram, predicting that $\log I_e \approx 2.5$ for all elliptical galaxies. While most intermediate-luminosity ellipticals indeed scatter around this value, bright elliptical galaxies tend to be more diffuse, with surface brightnesses in the range $\log I_e \approx 2.0 - 2.5$. Since less massive galaxies are expected to lose a larger mass-fraction than more massive objects, they move progressively towards lower surface brightnesses, changing the slope of the $I_\mathrm{e} - L_B$ relation. The YA87 models for slow and instantaneous mass-loss are able to reproduce the observed trend in the $I_\mathrm{e} - L_B$ diagram, with the dE-sequence running almost perpendicular to that of the bright galaxies. The faintest K01 models also coincide with the observed locus of the dEs. The CC02, being either too diffuse or too compact depending on the virialization redshift, end up having too high or too low surface brightness (see the discussion in subsection 2.4.2). However, they roughly reproduce the slope of the observed dE sequence. For a comparison of the $L_B - I_\mathrm{e}$ relation with SAM-predictions see Fig. 9 of NY04.

2.4.4 The $R_\mathrm{e} - I_\mathrm{e}$ or Kormendy relation

The 12 dEs in the B92 sample suggest a R_e-I_e relation that runs almost perpendicular to that of the bright ellipticals and bulges (Guzmán et al., 1993). However, this picture changes completely when more data, especially of faint galaxies, are added, as is obvious from panel **d** in Fig. 2.1. This result was already derived by e.g. Capaccioli et al. (1992) and Graham & Guzmán (2003). Mass-loss moves galaxies towards larger half-light radii and towards much lower surface brightnesses, i.e. slightly to the right and steeply downward with respect to the initial $\log R_\mathrm{e}$-$\log I_\mathrm{e}$ relation, by an amount given by equations (2.8) and (2.12) for slow, and equations (2.9) and (2.13) for instantaneous loss of a mass-fraction f. The region occupied by models that are disrupted by instantaneous gas ejection is bounded by the leftmost and rightmost thick grey lines in panel **d** of Fig. 2.1. The position of a typical $m_B = 16$ mag Fornax dE before and after slow or fast gas removal is indicated by white circles in Fig. 2.1, showing the direction in which dEs are expected to evolve in this diagram. The slope of the dE $R_\mathrm{e} - I_\mathrm{e}$ relation (if it can be called such, given the large scatter) is nicely reproduced by these models. The R_e-I_e relation predicted by YA87 becomes much flatter in the regime of the intermediate-luminosity and bright elliptical galaxies. However, the very brightest elliptical galaxies have larger half-light radii and hence lower surface brightnesses than accounted for by the YA87 relation, due to not taking into

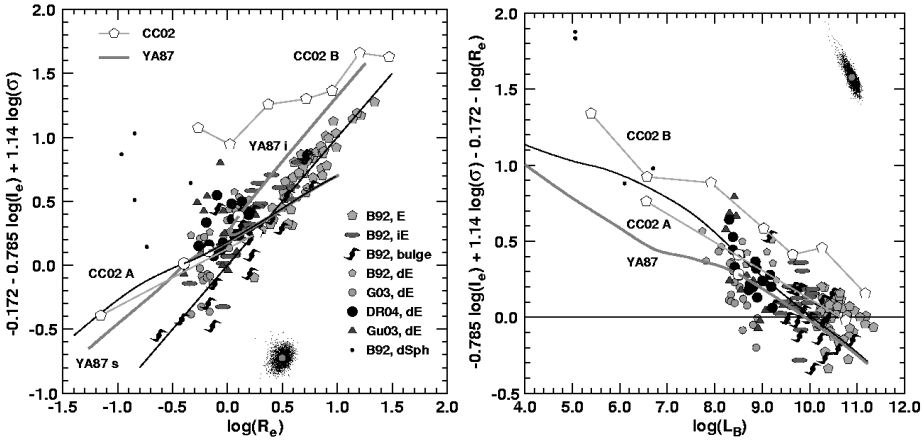

Figure 2.2: Left panel: an edge-on view onto the FP of the bulges, bright and intermediate-luminosity ellipticals in $(\log R_{\rm e}, \log I_{\rm e}, \log \sigma)$ space. All symbols have the same meaning as in Fig. 2.1. The straight black line traces the $\log R_{\rm e} = -0.172 - 0.785 \log I_{\rm e} + 1.14 \log \sigma$ relation that defines the FP. The dEs observed by Guzmán et al. (2003) (Gu03) have been added to the DR04, G03, and B92 data sets. The curved black line traces the FP of the zero mass-loss YA87 models. The thick grey lines give the locus of the YA87 models after slow (bottom thick grey line) or fast (top thick grey line) gas removal. The white circles show the expected evolution of a $m_B = 16\,$mag Fornax dE: most of the evolution happens almost parallel to the FP so that, given the slope of the zero mass-loss YA87 FP, one would expect dEs to lie slightly above the FP defined by the bright ellipticals in this projection. Right panel: vertical deviation of the FP as a function of luminosity. All models predict less massive galaxies to lie progressively higher above the FP in this projection, as is observed. The YA87 curves for slow and instantaneous winds coincide in this diagram. In each panel, a cloud of 3000 simulated data points is plotted to give an idea of the systematic and statistical uncertainty on a typical DR04 data point (indicated by a grey dot).

account the fact that mergers played an important role in shaping bright ellipticals. Again, the CC02 models are either too compact or too extended. They roughly reproduce the trend going from dEs towards dSphs. The photometric properties of the K01 models agree rather well with the observations. The effect of the kinetic feedback efficiency of supernova explosions is clear: models with a low feedback efficiency (top sequence of K01 models in panel **d** of Fig. 2.1) experience a late galactic wind and lose little gas. Consequently, the dynamic response is rather mild and they scatter about the YA87 zero mass-loss curve. Models with a high feedback efficiency (bottom sequence in panel **d** of Fig. 2.1) lose much more gas and expand towards much larger $R_{\rm e}$ and lower $I_{\rm e}$. At fixed mass but for different feedback efficiencies, the trend is in the same direction as the observed $R_{\rm e}$-$I_{\rm e}$ relation and as the YA87 models (with feedback efficiency replaced with mass-loss timescale). For a comparison of the Kormendy relation with SAM-predictions see Fig. 11 of NY04.

2.5 Bivariate relations

2.5.1 The Fundamental Plane (FP)

The FP of the bulges and the bright and intermediate-luminosity ellipticals is given by the equation

$$\log R_{\rm e} = {\rm const.} + 1.14 \log \sigma - 0.785 \log I_{\rm e}, \tag{2.14}$$

(Guzmán et al., 1993). The FP can be seen as an emanation of the virial theorem, relating the potential energy $\mathcal{PE}$ and kinetic energy $\mathcal{KE}$ budgets of a galaxy in equilibrium. More specifically, with $\mathcal{PE} = GM^2/R_G$ and $\mathcal{KE} = \frac{1}{2} M \langle v^2 \rangle$, where M is the mass of the galaxy, R_G its gravitational radius, and $\langle v^2 \rangle$ the mass-weighted mean-square stellar velocity (Binney & Tremaine, 1987), one finds that $\mathcal{PE} + 2\mathcal{KE} = 0$ or that $M \propto R_G \langle v^2 \rangle$. Hence, one expects that $M = c\, R_{\rm e} \sigma^2$, with c a proportionality parameter that (hopefully) transforms the mass-weighted theoretical parameters (R_G, $\sqrt{\langle v^2 \rangle}$) to the luminosity-weighted observed ones ($R_{\rm e}$, σ). This, together with the relation $L_B = 2\pi I_{\rm e} R_{\rm e}^2$, leads to the theoretical FP relation

$$\log R_{\rm e} = {\rm const.} + \log c - \log \frac{M}{L} + 2 \log \sigma - \log I_{\rm e}. \tag{2.15}$$

Variations of c (structural non-homology) and/or the mass-to-light ratio M/L along the mass sequence of dynamically hot galaxies, exacerbated by an imperfect correspondence between σ and $\sqrt{\langle v^2 \rangle}$ due to rotation and anisotropy, slightly change the tilt of the FP to the observed value and introduce some scatter (see e.g. Trujillo et al. (2004)).

The positions of the various galaxy species in a side view of the FP are plotted in Fig. 2.2. We did not correct our velocity dispersions for aperture effects in this plot since applying the prescriptions given by Blakeslee et al (2002) leads to corrections of order $\Delta \log \sigma = 0.02$ and are clearly negligibly small. In both panels of Fig. 2.2, a cloud of 3000 simulated data points, calculated along the lines discussed in section 2.4, is plotted to give an idea of the systematic and statistical uncertainty on a typical DR04 data point (indicated by a grey dot). Here and in the following, we have also made use of the FP-data of 14 Coma cluster dEs presented by Guzmán et al. (2003) (Gu03). By and large, dEs show a tendency to lie above the FP in this projection. The Local Group dSphs deviate even more extremely from the FP. The dynamical response after the loss of a mass-fraction f, given by

$$\begin{aligned} \Delta \left(-0.785 \log I_{\rm e} + 1.14 \log \sigma \right) &= -0.43 \log(1-f), \\ \Delta \log R_{\rm e} &= -\log(1-f), \end{aligned} \tag{2.16}$$

for slow removal and

$$\begin{aligned} \Delta \left(-0.785 \log I_{\rm e} + 1.14 \log \sigma \right) &= 1.57 \log(1-f) - \log(1-2f), \\ \Delta \log R_{\rm e} &= \log(1-f) - \log(1-2f), \end{aligned} \tag{2.17}$$

for instantaneous mass-loss, moves dEs almost parallel to the FP in the direction of larger half-light radii (see e.g. the typical $m_B = 16$ mag Fornax dE which moves from left to right, as shown by the white circles in Fig. 2.2). Since the zero mass-loss FP has a much flatter slope than the observed one, fainter galaxies are indeed expected to lie progressively above the FP in this projection. The CC02 models A agree very well with the YA87 models and with the observations. The surface brightness of the CC02 models B however is much lower than observed, placing them well above the observed FP in this projection.

In the right panel of Fig. 2.2, the deviations of the different galaxy species from the FP are plotted as a function of luminosity. The expected change of the FP residual after the ejection of a mass fraction

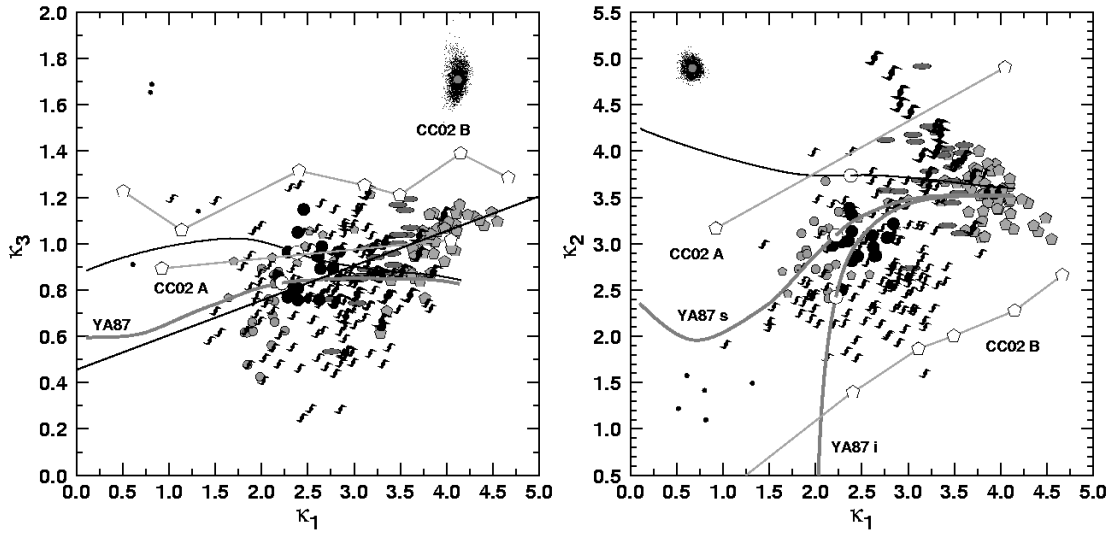

Figure 2.3: The FP in κ-space. Left panel: edge-on view of the FP, the black straight line traces the $\kappa_3 = 0.46 + 0.15\kappa_1$ relation. All symbols have the same meaning as in Fig. 2.1. The Sc/Sd/Irr galaxies taken from Burstein et al. (1997) are plotted as small spirals. According to the YA87 models, the evolution in the (κ_1, κ_3) plane does not depend on the time-scale on which mass is lost as a galactic wind. The predicted tendency for faint dwarf galaxies to lie above the FP in this projection is borne out by the observations. Right panel: face-on view onto the FP (equivalent to panel **c** of Fig. 2.1). The evolution within the FP is much more outspoken: the mass-loss suffered by the dwarf galaxies makes them expand, shifting them towards lower κ_2 values. The dEs and dSphs end up forming a sequence almost parallel to that of the bulges and the bright and intermediate-luminosity ellipticals. The CC02 models A reproduce the slope of the dE FP but are somewhat too compact and as a consequence have too high κ_2 values. The CC02 models B on the contrary are too extended lie below the dE sequence in the (κ_1, κ_2) plane. Still, all models predict the same slope of the dE sequence in the (κ_1, κ_2) plane. In each panel, a cloud of 3000 simulated data points is plotted to give an idea of the systematic and statistical uncertainty on a typical DR04 data point (indicated by a grey dot).

f is given by

$$\Delta\left((-0.785\log I_{\rm e} + 1.14\log\sigma) - \log R_{\rm e}\right) = 0.57\log(1-f), \tag{2.18}$$

i.e. slightly downwards with respect to the YA87 zero mass-loss sequence, which itself is a steep function of luminosity. This expression is valid both for slow and instantaneous winds although in the latter case galaxies in the luminosity range $\log L_B \approx 4.4 - 8.2$ or $M_B \approx -5.5$ to -15.5 mag cease to exist. Hence, according to the YA87 calculations, the dynamical response after mass-loss in fact reduces the FP residual. Still, dEs are expected to lie above the FP in this projection. The YA87 and the CC02 models A roughly reproduce the observed trend as a function of $\log L_B$. The CC02 models of series B show approximately the same trend but lie systematically above the FP in this projection.

2.5.2 The FP in κ-space

Another way to view the FP is in the so-called κ-space (Bender et al., 1992) defined by

$$\begin{aligned}\kappa_1 &= \frac{1}{\sqrt{2}}\log\left(R_{\rm e}\sigma^2\right),\\ \kappa_2 &= \frac{1}{\sqrt{6}}\log\left(\frac{I_{\rm e}^2\sigma^2}{R_{\rm e}}\right),\\ \kappa_3 &= \frac{1}{\sqrt{3}}\log\left(\frac{\sigma^2}{I_{\rm e}R_{\rm e}}\right).\end{aligned} \tag{2.19}$$

Using these definitions and the virial theorem, κ_1 is expected to be a measure for the mass of a galaxy, κ_2 is sensitive mostly to surface brightness and κ_3 depends on the mass-to-light ratio. A galaxy is shifted in κ-space by an amount

$$\begin{aligned}\Delta\kappa_1 &= \frac{1}{\sqrt{2}}\log(1-f),\\ \Delta\kappa_2 &= \frac{7}{\sqrt{6}}\log(1-f),\\ \Delta\kappa_3 &= \frac{1}{\sqrt{3}}\log(1-f)\end{aligned} \tag{2.20}$$

if a mass-fraction f is blown away in a slow wind. An instantaneous wind engenders a dynamical response given by

$$\begin{aligned}\Delta\kappa_1 &= \frac{1}{\sqrt{2}}\log(1-f),\\ \Delta\kappa_2 &= \frac{1}{\sqrt{6}}\left(6\log(1-2f)-5\log(1-f)\right),\\ \Delta\kappa_3 &= \frac{1}{\sqrt{3}}\log(1-f).\end{aligned} \tag{2.21}$$

Since a galaxy's luminosity is not affected by the ejection of gas, $I_{\rm e}\propto R_{\rm e}^{-2}$, and

$$\Delta\kappa_1\propto\Delta\kappa_3\propto\Delta\log M. \tag{2.22}$$

Galaxies are therefore expected to evolve downwards and to the left in the (κ_1,κ_3)-projection of the FP (left panel of Fig. 2.3). In both panels of Fig. 2.3, a cloud of 3000 simulated data points, calculated along the lines discussed in section 2.4, is plotted to give an idea of the systematic and statistical uncertainty on a typical DR04 data point (indicated by a grey dot). The YA87 zero mass-loss FP however has a much flatter slope than the observed FP, which tends to position dEs slightly above the FP in this projection. As in the right panel of Fig. 2.2, the dynamical response to the galactic wind moves galaxies away from the zero mass-loss FP towards the FP of the bright galaxies.

The sensitivity of κ_2 to surface brightness, which drops significantly as a galaxy expands after the wind phase, leads to a strong downward evolution in the (κ_1,κ_2)-projection of the FP (right panel of Fig. 2.3). The models undergoing an instantaneous wind are disheveled most severely by the suffered mass-loss and show the most pronounced evolution in the (κ_1,κ_2) plane. The YA87 models and the CC02 models A are able to reproduce the position of the dEs in the (κ_1,κ_3)-projection of the FP. The CC02 models B are too extended and consequently lie above the observed FP in this projection. In the (κ_1,κ_2)-projection, which is a nearly face-on view onto the FP, the dEs define a sequence running

almost perpendicular to that of the bulges and the bright and intermediate-luminosity ellipticals. Within the context of the YA87 models, this is in part due to the zero mass-loss sequence which runs almost horizontally across the (κ_1, κ_2)-plane and to the evolution induced by the mass-loss during the galactic-wind phase, which shifts galaxies downwards. Both the YA87 and the CC02 models reproduce the observed slope of the dE sequence in the (κ_1, κ_2)-plane.

The present-day Sc/Sd/Irr galaxies are probably the stellar systems that best resemble the dE progenitors as envisaged by the harassment scenario. Their position in κ-space, with the maximum rotation velocity $v_{\rm max}$ used as a substitute for the theoretical quantity $\sqrt{\langle v^2 \rangle}$ in the virial theorem, is indicated in Fig. 2.3 by small spiral symbols. This population of late-type galaxies has a much larger scatter in κ-space than the dEs. It is not clear how harassment, which is by nature a stochastic process whose effects depend in a very complicated way on the orbit of a progenitor galaxy through a given galaxy cluster or group, could transform the scatter cloud of late-types into the much tighter dE sequence.

2.6 Discussion and conclusions

We have presented the sequences traced by dEs in the $\log L_B$ vs. $\log \sigma$, $\log L_B$ vs. $\log R_{\rm e}$, $\log L_B$ vs. $\log I_{\rm e}$, and $\log R_{\rm e}$ vs. $\log I_{\rm e}$ diagrams and in the $(\log \sigma, \log R_{\rm e}, \log I_{\rm e})$ parameter space in which bright and intermediate-luminosity elliptical galaxies and bulges of spirals define a Fundamental Plane (FP). These results are based on three equally large kinematical data-sets: the data presented in this paper (DR04), G03, and vZ04. This brings the number of dEs with resolved kinematics to 43. More data were added when studying correlations involving only photometric data (Ba03 and Gr03) or the FP (Gu03). We also used the kinematical and photometric data presented in B92. Our main conclusions are the following.

We have shown that the $\sigma - L_{\rm B}$ or Faber-Jackson relation does *not* have a constant slope when going from the bright ellipticals, over the dEs, down to the dSphs, contrary to previous claims. The $L_B \propto \sigma^{3.7}$ relation of the bright galaxies changes into a $L_B \propto \sigma^{1.6 \pm 0.2}$ relation below $L_B \approx 9.4$ or $M_B \approx -18$ mag. A dE FJR as steep as or even steeper than that of the bright ellipticals is definitely excluded by these data. A flatter slope is predicted by all models presented here (YA87, CC02) as a consequence of the dynamical response to the supernova-driven gas ejection. More sophisticated SAMs that simulate the hierarchical merger tree that leads up to the formation of a galaxy show that post-merger starbursts are absolutely necessary to bring the models in agreement with a whole host of observations and that a significant flattening of the FJR in the dE-regime is a direct consequence of the dynamical response to starburst-induced gas ejections (Somerville et al., 2001; Nagashima & Yoshii, 2004). As a consequence, dEs and their progenitors, being low-mass, fragile objects, are the ideal objects to study if one aims at further refining prescriptions for star formation, supernova feedback and the response to galactic winds in semi-analytical or numerical simulations of cosmological structure growth.

The simple fact that these diffuse, low surface-brightness, low velocity-dispersion dEs exist puts strong constraints on the redshift dependence of the cosmic star formation rate. Nagashima & Yoshii (2004) have shown convincingly that structure-formation models in a ΛCDM universe with a short star formation timescale at high z fail to produce such inflated dEs. In such a universe, dEs are assembled from progenitors that have already converted most of their gas into stars, and they are expected to trace the same sequences in the panels of Fig. 2.1 as the giant ellipticals (which are formed further down the merger tree from almost purely stellar progenitors, independent of the cosmic star formation rate). Only models that have long enough star formation timescales at high z, such that dEs can be formed by the mergers of gaseous progenitors, agree with these observations (e.g. the models of NY04 with a redshift independent star formation time scale $\tau_* = 1.3$ Gyr, where the star formation rate is given by $M_{\rm gas}/\tau_*$ with $M_{\rm gas}$ the H I mass). The starburst triggered by each merger and the

ensuing supernova-explosions eject gas and thus lead to a population of diffuse dwarf galaxies with low velocity dispersions, as observed. This also explains the success of the YA87 and CC02 models, which do not take into account mergers but rather assume galaxies to originate from a single gas cloud, for dEs while they fail to reproduce the properties of massive ellipticals. However, all this needs to be reconciled with the observation that the stellar mass density of the universe at redshift $z > 2$, contained in massive galaxies, is larger than can be accounted for by SAMs (Fontana et al., 2003; Somerville et al., 2004). Still, the distribution of the dEs in the various univariate diagrams can, if enough dwarf galaxies have been observed for statistically sound statements to be made, put very stringent limits on the redshift dependence of the star formation timescale in semi-analytical or numerical simulations of galaxy evolution.

Models for the evolution of dwarf and intermediate-luminosity elliptical galaxies, based on the idea that these stellar systems grow from collapsing primordial density fluctuations, are able to reproduce the observed relations between parameters that quantify their structure (L_B, R_e, I_e) and internal dynamics (σ) quite well. Despite their simplicity, the YA87 models account very well for the behaviour of dEs in the ($\log\sigma, \log R_\mathrm{e}, \log I_\mathrm{e}$) parameter space. Although numerically and physically much more sophisticated and with a more sound cosmological footing, the predictions of the models presented by K01 and Nagashima & Yoshii (2004) agree with the YA87 models. The CC02 models, in which the virialization redshift of the models is set "by hand", fail to get the zeropoints correctly but nonetheless are able to reproduce the slopes of the various relations. All this suggests that little merging took place in the life of a dE *after* it started forming stars.

Low-mass systems such as dEs and dSphs lie above the FP in the projection used in Figs. 2.2 and 2.3 defined by the bright ellipticals, with fainter galaxies lying progressively higher above the FP. It is well known that the remnant of the merger of two galaxies is more diffuse than its progenitors (see e.g. Held et al. (1992) and Dantas et al. (2003) for dissipationless mergers and Hernquist et al. (1993) and Bekki (1998) for merger simulations taking into account the presence of gas). Hence, the structural properties of the brightest elliptical galaxies, including the slope of the FP, can be explained quite well if late mergers (with progenitors that had already converted a significant fraction of their gas into stars) played an important role in their formation and evolution. This is much less the case for less massive systems such as dEs, which formed higher up the hierarchical merging tree from more dissipative mergers.

While dEs follow well-defined sequences in the various univariate diagrams, the correlations are not as tight as in the case of bright ellipticals. This cannot only be due to measurement uncertainties (e.g. very deep photometry is now available that allows to determine L_B and R_e with very small errors, still the scatter on the dE $\log R_\mathrm{e}$-$\log I_\mathrm{e}$ relation is large). This cosmic scatter may be a consequence of the sensitivity of these low-mass systems to both internal (supernova explosions, feedback efficiency, the details of galactic winds, ...) and external processes (gravitational interactions, tidal stripping of stars and ram-pressure stripping of gas, ...) in group and cluster environments. Hence, these objects are ideal laboratories to study these physical processes to which bright ellipticals seem to be quite insensitive.

The wind model has passed this test. However, these findings do not necessarily falsify the harassment scenario. The dEs observed so far overlap in κ-space (see Fig. 2.3) with the present-day analogs of possible dE progenitors (the Scd and Irr galaxies). This overlap leaves open the possibility that we have observed dEs that formed via hierarchical merging *and* dEs that formed via harassment. Especially since some of the dEs observed during the Large Program provide us with very strong evidence (such as embedded stellar disks or kinematically decoupled cores) that harassment has indeed played an important role in their past evolution.

Hence, judging from the photometric and kinematical data that are now available, dEs are most likely a mixed population, with primordial and more recently (trans)formed objects co-existing in the present-day universe. More spectroscopic age and metallicity estimates and kinematical data are required in

order to allow the importance of the evolutionary avenues to be constrained, especially of faint, low surface-brightness dEs in order to fill the gap between the dEs and the dSphs in the FJR (the faintest dEs with resolved kinematics are still ~ 20 times brighter than the brightest Local Group dSph) and to determine the position of such faint dEs in the other uni- and bivariate diagrams.

Chapter 3

The puzzlingly large Ca II triplet absorption in dwarf elliptical galaxies

3.1 Introduction

In this chapter, we present central CaT, PaT and CaT* indices for the fifteen dwarf elliptical galaxies (dEs) for which spectra were obtained during the Large Program (see chapter 2). Twelve of these have CaT* ~ 7 Å and extend the negative correlation between the CaT* index and central velocity dispersion σ, which was derived for bright ellipticals (Es), down to $20 < \sigma < 55\,\mathrm{km\,s^{-1}}$. For five dEs we have independent age and metallicity estimates. Four of these have CaT* ~ 7 Å, much higher than expected from their low metallicities ($-1.5 < [\mathrm{Z/H}] < -0.5$). The observed anti-correlation of CaT* as a function of σ or Z is in flagrant disagreement with theory. We discuss some of the amendments that have been proposed to bring the theoretical predictions into agreement with the observed CaT*-values of bright Es and how they can be extended to incorporate also the observed CaT*-values of dEs. Moreover, 3 dEs in our sample have CaT* ~ 5 Å, as would be expected for metal-poor stellar systems. Any theory for dE evolution will have to be able to explain the co-existence of low-CaT* and high-CaT* dEs at a given mean metallicity. This could be the first direct evidence that the dE population is not homogeneous, and that different evolutionary paths led to morphologically and kinematically similar but chemically distinct objects.

3.2 The low CaT-value of high-mass galaxies

The Ca II triplet (8498, 8542, 8662 Å) is a prominent absorption-line feature in the near-infrared spectrum of cool stars. Theoretical and empirical population synthesis modeling of the Ca II triplet showed that it is a good tracer of the metallicity of stellar systems (Idiart et al., 1997; García-Vargas et al., 1998). This is indeed observed to be the case for Galactic globular clusters (Armandroff & Zinn, 1988; Rutledge et al., 1997). However, in early type galaxies only a small spread of Ca II strengths was measured (Cohen, 1979; Bica & Alloin, 1987; Terlevich, Diaz & Terlevich, 1990). Recently, Cenarro et al. (2001) defined new line-strength indices for the strength of the Ca II triplet (CaT) and for the combined strength of the P12, P14, and P17 H Paschen lines (PaT). The Ca II index corrected for the contamination by the Paschen P13, P15, and P16 lines is denoted by CaT* (CaT* = CaT $- 0.93 \times$ PaT). These authors compiled a large library of stellar spectra and produced fitting functions (Cenarro et al., 2002) that can be employed to predict index-values for single-age, single-metallicity stellar populations

(SSPs) using population synthesis models (Vazdekis et al., 2003). These models predict that for low metallicities, CaT* should be sensitive to metallicity but virtually independent of age.

However, Saglia et al. (2002) (SAG) and Cenarro et al. (2003) (CEN) present CaT* indices for bright ellipticals and show that CaT* and central velocity dispersion σ anticorrelate. Falcón-Barroso et al. (2003) (FAL) arrive at the same conclusion based on a sample of bulges of spirals. On a linear σ-scale, all samples yield essentially the same slope and zeropoint. These results provide the first evidence for an anti-correlation between a metal-line index and σ while other metallicity indicators such as Mg_2 increase with σ (Terlevich, Diaz & Terlevich, 1990). Moreover, the CaT* values of the Es in the SAG-sample scatter around 6.9 Å, about 0.5 Å lower than expected by SSP models, given their ages and metallicities (determined independently from optical Lick indices). CEN do not give independent metallicities for their sample but find that the measured CaT* values, with the exception of those of a few low-mass Es, are lower than any model prediction using a Salpeter IMF.

3.3 Observations and data reduction

We collected long-slit spectra of 15 dEs in the Fornax Cluster and in the NGC5044, NGC5898, and Antlia Groups in the wavelength region $\lambda\lambda$ 7900–9300 Å. These observations were carried out at the ESO-VLT with FORS2 during 5 observing runs in 2001 and 2002. We used the FORS2 grism GRIS_1028z+29, which, with a 0.7″ slit, yields an instrumental broadening of $\sigma_{\rm instr} \simeq 30\,{\rm km\,s^{-1}}$. Seeing conditions were typically 0.7–1.0″ FWHM. Total integration times varied between 5 and 8 hours. We obtained spectra of late G to early M giant stars as velocity templates. The standard data reduction procedures were performed with ESO-MIDAS[1]. The spectra for each galaxy were bias-subtracted, flatfielded, corrected for cosmic-ray events, rebinned to a linear wavelength scale (rectifying the emission lines of the arc spectra to an accuracy of $\approx 1\,{\rm km\,s^{-1}}$ FWHM) and co-added. After sky-subtraction, the spectra were flux calibrated using spectrophotometric standard stars observed in the same instrumental setup. Since our spectral resolution is close to that of the stellar library of Cenarro et al. (2001) and the galactic velocity dispersions were always well below $100\,{\rm km\,s^{-1}}$, no corrections for resolution effects or Doppler broadening were necessary. This was confirmed by comparing the values of the indices for the template stars in common with the library. We measured the CaT, PaT and CaT* indices, averaged over an aperture of radius $R_{\rm e}/8$ (or 1″ for galaxies with $R_{\rm e} < 8''$), using the definitions given in Cenarro et al. (2001), and extracted kinematics out to 1–2 $R_{\rm e}$ (De Rijcke et al., 2001, 2003a).

3.4 Results

The CaT, PaT and CaT* indices of our sample dEs versus central velocity dispersion σ are presented in Fig. 3.1. The majority of the dEs scatter around CaT* ~ 7 Å and form the low-σ extension of the CaT* $-\,\sigma$ relation of bright Es and bulges of spirals. Three out of fifteen dEs have a discrepantly low CaT* ~ 5 Å value. FCC046 has CaT $= 8.3 \pm 0.3$ Å but a very high PaT $= 3.3 \pm 0.2$ Å, in agreement with the fact that this is an actively star-forming dE and contains a very young stellar population (De Rijcke et al., 2003b). FCC245 and NGC5898_dE2 (a dE in the NGC5898 group) have normal PaT values but very low CaT ≈ 5.5 Å. Excluding these three galaxies, we find that CaT, PaT and CaT* remain nearly constant over the range $\sigma = 20 - 55\,{\rm km\,s^{-1}}$. In Fig. 3.2, we present our results together with those of SAG, CEN and FAL. CEN and FAL broadened their spectra to 370 and $300\,{\rm km\,s^{-1}}$respectively. In order to compare their data with ours, we used the broadening corrections given by Vazdekis et al. (2003) for an old population with solar metallicity and a Salpeter IMF. These corrections are model-dependent, but the maximum error introduced is ~ 0.2 Å. Clearly, except for the three outliers, dEs populate the

[1]ESO-MIDAS is developed and maintained by the European Southern Observatory

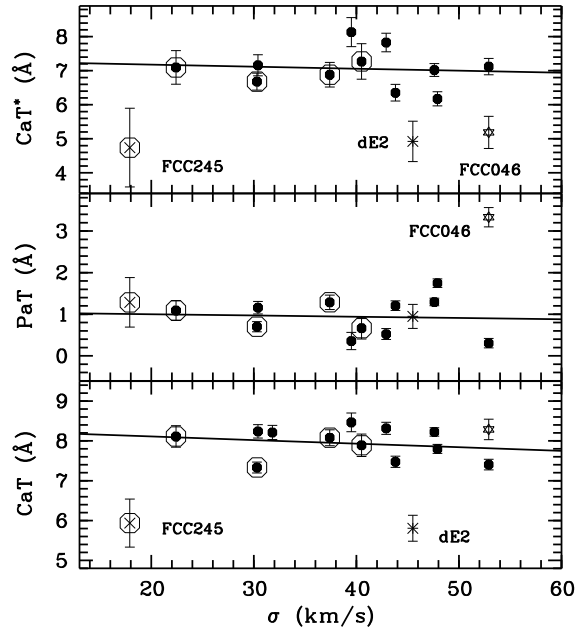

Figure 3.1: CaT, PaT and CaT* values versus central velocity dispersion σ for our 15 dEs with a least-squares fits to the data, showing a mild anti-correlation. Three galaxies were excluded from the fit: FCC245 and NGC5898_dE2 show a very low CaT value; FCC046 has a very high PaT absorption, due to recent starformation. Galaxies appearing in Fig. 3.3 are marked with a circle.

low-σ extension of the CaT* $-\ \sigma$ relation of bright Es and bulges. All datasets yield approximately the same slight CaT* $-\ \sigma$ anti-correlation. SAG find PaT to anti-correlate with σ, while the CEN data scatter around PaT ≈ 1 Å, and FAL find PaT ≈ 1.4 Å. The same trend is found for CaT where SAG find a stronger anti-correlation and the Es of CEN are slightly offset with respect to the bulges of FAL. These differences could be due in part to flux calibration differences and to the different ways of correcting the spectra to the system defined by the models (as discussed in FAL).

In Fig. 3.3, we show model predictions for CaT, PaT and CaT* as functions of age (between 1 and 18 Gyr) and metallicity ($-1.68 < [\mathrm{Z/H}] < 0.2$). The SSP models (Salpeter IMF) are safe for all ages in the metallicity range $-0.7 \leq [\mathrm{Z/H}] \leq 0.2$, while for lower metallicities the age range 10–13 Gyr, which is of most interest to us, is safe (Vazdekis et al., 2003). The predicted CaT and CaT* values are strong functions of metallicity for $[\mathrm{Z/H}] \leq -0.4$ and nicely reproduce the observed behavior of these indices in globular clusters (Armandroff & Zinn, 1988), which, for all practical purposes, are genuine SSPs. However, the bright ellipticals in the SAG sample have CaT* values that are about 0.5 Å lower than expected by theory, given their ages and metallicities, signaling that some vital ingredient might be missing in the models. For 5 Fornax dEs in our sample, independently determined ages and metallicities can be found in the literature. The age and metallicity measurements of Rakos et al. (2001) are based on narrowband photometry employing a modified Strömgren filter system; Held & Mould (1994) use age and metallicity sensitive line-strengths in the $\lambda\lambda\, 4000 - 5000$ Å region. These studies find dEs to be rather old (~ 10 Gyr) and metal-poor ($-1.5 < [\mathrm{Z/H}] < -0.5$) stellar systems. Four out of these five dEs, due to the near-constancy of CaT and CaT*, lie well above the predicted values, by up to 2 Å in the case of the most metal-poor dE. In fact, FCC245 is the only galaxy in this subsample whose indices are in agreement with its low metallicity content ($[\mathrm{Z/H}] \approx -1.1$) and old age ($t \approx 10$ Gyr). FCC245 has a

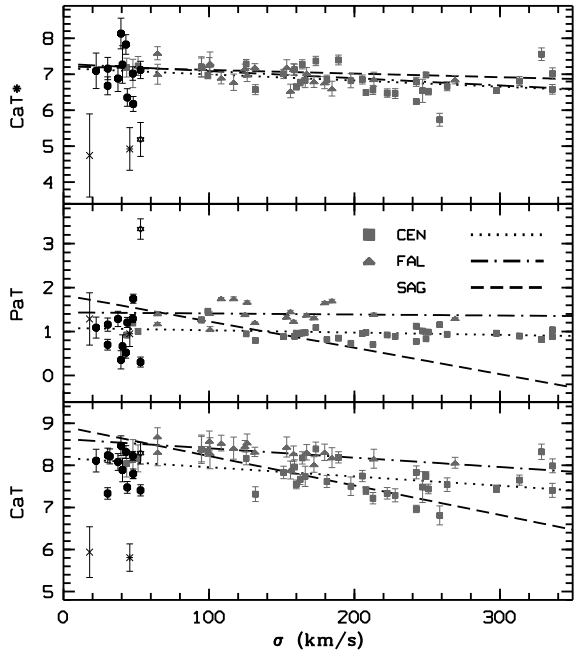

Figure 3.2: Comparison of our data with the extended relations of SAG, CEN and FAL. Data from CEN and FAL have been corrected for broadening and are shown together with linear least-squares fits to their samples and the anticorrelation found by SAG (symbols as indicated on the figure).

low surface brightness ($\langle\mu_{\rm e}\rangle_B = 23.5\,{\rm mag\,arcsec^{-2}}$) and its P14 line is affected by bright sky emission lines (influencing PaT and CaT* but not CaT), hence the somewhat larger errorbars. Although we do not have ages and metallicities for the 11 other dEs in our sample, one thing is clear; 9 have CaT* ~ 7 Å which will place them on the same sequence as the SAG ellipticals and the 4 high-CaT* dEs presented in Fig. 3.3, irrespective of their ages or metallicities. The locus of these dEs in the CaT*-Z plane is indicated in Fig. 3.3 by the upper shaded box.

Hence, the majority of the dEs in our sample follow the same CaT (or CaT*) versus σ or versus Z relations as bright ellipticals and bulges of spirals. The observed near-constancy of CaT and CaT* over a very wide range of metallicities ($-1.5 < {\rm [Z/H]} < 0.5$) is in flagrant disagreement with the prediction that these indices should be sensitive to metallicity. Three out of fifteen dEs in our sample have CaT* $\sim 5-6$ Å, in agreement with them being low-metallicity galaxies (lower shaded box in Fig. 3.3). This makes our observations even more puzzling; apparently, at a given metallicity, dEs with CaT* ~ 5 Å and with CaT* ~ 8 Å co-exist.

3.5 Discussion and conclusions

In order to interpret their low CaT and CaT* in view of the current models, SAG and CEN find that model uncertainties (~ 0.5 Å) are too small to provide a solution. They consider variations of the IMF as a function of metallicity or velocity dispersion, or Ca underabundance as a possible way out. By varying the slope of a power-law IMF, CEN change the stellar dwarf/giant ratio of the population. Since CaT* depends on the surface gravity of stars, being low in dwarf stars and high in giant stars, a

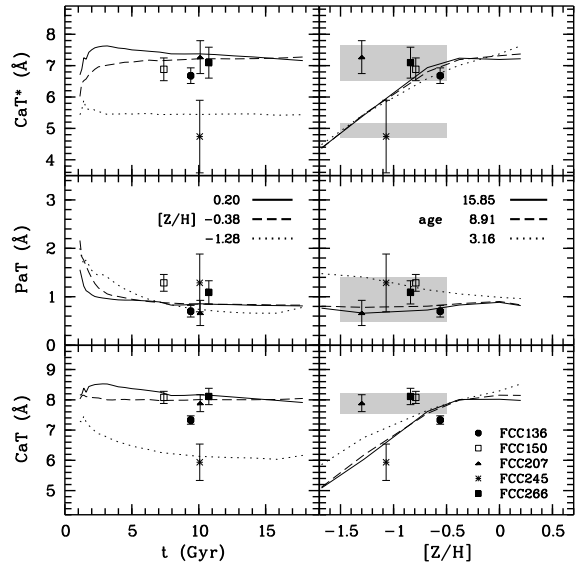

Figure 3.3: Vazdekis et al. (2003) SSP model predictions (Salpeter IMF) of CaT, PaT and CaT* versus age (left panel) and metallicity (right panel). The full, dashed and dotted lines represent different metallicities and ages as indicated on the figure. The symbols show 5 Fornax dEs of our sample with independent age and metallicity estimations (Rakos et al., 2001; Held & Mould, 1994). The shaded boxes indicate the locus of the other dEs in our sample. The metallicity range $-1.5 \leqslant [\mathrm{Z/H}] \leqslant -0.5$ is taken from Rakos et al. (2001), while the index ranges are $1\,\sigma$ deviations from the mean. While the PaT values are consistent with the model predictions, the near-constancy of CaT and CaT* for our metal-poor dEs disagrees with the model predictions. Only a few dEs have low CaT*, consistent with low metallicity (lower box in CaT* panel).

high dwarf/giant ratio in the case of a high-Z SSP and a low dwarf/giant ratio in the case of a low-Z SSP, could explain both the low CaT* observed in bright Es and the high CaT* in dEs. However, there is no sound physical basis for such variations of the slope of the IMF. Theoretical derivations show that for stellar masses above $1\,\mathrm{M}_\odot$, the IMF behaves as a Salpeter power-law and is almost insensitive to the physical conditions within star-forming molecular clouds (Padoan & Nordlund, 2002). Only in the subsolar-mass regime does the environment affect the stellar mass-distribution (e.g. low ambient densities prevent the formation of very low-mass stars). In an old stellar population the contribution of subsolar-mass stars becomes more important. Using a piecewise power-law IMF with Salpeter slope for masses above $0.6\,\mathrm{M}_\odot$ and varying slope at lower masses, SAG show that the steepening required to bring the model CaT* values in accordance with those observed in bright Es, implies higher than observed FeH $9916\,$Å index values (FeH is strong in dwarf stars but nearly absent in giants) and too high stellar mass-to-light ratios (see SAG and references therein). And if the IMF would vary with Z to explain the high CaT* in dEs, why doesn't this effect manifest itself also in low-Z, low-σ systems such as globulars?

Moreover, dEs are not composed by SSPs but can have long and complex star-formation histories (e.g. Ferrara & Tolstoy (2000)). If the IMF varies with metallicity, it will also vary in time and it remains to be seen how the use of variable IMFs in chemo-evolutionary models affects the predicted properties of dEs. Chiappini et al. (2000) explore a model for the Galaxy using a metallicity-dependent power-law IMF which steepens as the metallicity rises (slope $x = \log \mathrm{Z} + 4.05$), thus simulating also a temperature

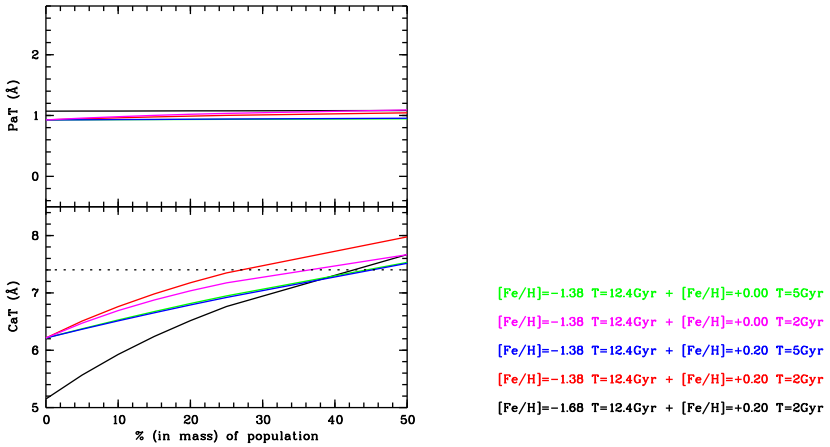

Figure 3.4: The CaT and PaT values for composite stellar populations (CSPs) in function of the mass fraction of the young, metal-rich SSP with respect to the old, metal-poor SSP. The various assumed ages and metallicities are indicated on the plot. The dotted line gives the lowest observed CaT values (apart from the two outlyers which could be genuine old populations). Because the age of the young SSPs is larger than 2 Gyr, the presence of the young SSP doesn't change the PaT values. In order to enhance the CSP CaT values to the observed onces, more than 30, and up to 50, per cent of the mass should be contained in the young population.

dependency. They find that the model predictions are in disagreement with important observational constraints and conclude that such an IMF should be rejected. Using the theoretical IMF proposed by Padoan et al. (1997) to investigate the formation of ellipticals, Chiosi et al. (1998) find that density is the leading parameter for the variations of the IMF, instead of temperature. This leads to dwarf/giant ratios that decrease with increasing galactic mass, inverse to the trend invoked by CEN. Indeed, IMFs with a low dwarf/giant ratio lead to numerous SN II explosions that rapidly recycle heavy elements into the ISM and cause α-elements such as Mg, O and Ca to be overabundant with respect to Fe. Also, such an IMF can raise the overall metallicity to above solar.

Combining SSPs, SAG find that a rather artificial stellar mix has to be invoked (consisting of a metal-rich stellar population with a small contribution of a metal-poor one) in order to lower the predicted CaT* to the one observed in bright Es and at the same time satisfy UV constraints. Adding a (more logical) young metal-rich component to explain the observed high Hβ in ellipticals only aggravates the problem, producing larger CaT* values. In dEs one could expect a small high-metallicity stellar population on top of an old low-metallicity population with the secondary star-burst triggered by e.g. gravitational interactions with giant cluster members (Moore et al., 1996; Conselice et al., 2003a). If the burst occured more than 2 Gyr ago, PaT would be essentially unaffected. We explored this scenario by adding young, high-metallicity SSPs to an old low-metallicity SSP and found that any young, metal-rich SSP must contribute more than 50 per cent of the total mass in order to raise CaT above 7.5 Å (Figure 3.4). Then, the young metal-rich population completely dominates the light, in contradiction with the low metallicities inferred from optical linestrengths.

Another suggestion to explain the low CaT* for Es is a true Ca underabundance in giant galaxies. Although the optical Ca4227 Lick index is also reported to be weaker than model predictions (e.g. Vazdekis et al. (1997)), such an underabundance is hard to combine with the observed α-element overabundance for giant Es. Also, when trying to reproduce the Ca underabundance with chemo-evolutionary models, extremely short formation timescales ($\sim 10^7$ yr), extremely flat IMFs ($x \sim 0.3$)

(Mollá & García-Vargas, 2000) or metallicity-dependent supernova yields (Worthey, 1998) are required. On the other hand, although the sensitivity of CaT* to the Ca abundance is not yet fully understood, in this scenario the high CaT* in dEs would imply a Ca overabundance at low metallicities (see Thomas et al. (2003) for a detailed discussion).

To conclude, we show that 12 out of a sample of 15 dEs follow the same sequence as bright Es and bulges of spirals in CaT or CaT* versus σ diagrams whereas 3 out of 15 have significantly lower CaT*. This could be the first direct evidence for the existence of two distinct dE populations that are morphologically and kinematically indistinguishable but have different chemical compositions. A possible explanation for this dichotomy could be that dEs evolve to their present-day state along different evolutionary paths. Two principal evolutionary sequences are galaxy harassment (Moore et al., 1996; Conselice et al., 2003b) and SN-driven galactic winds (Dekel & Silk, 1986; Arimoto & Yoshii, 1987), resulting in morphologically and kinematically similar stellar systems but with distinct chemical properties.

Variations of the IMF slope could explain the near-constancy of CaT* over a wide range of metallicities. However, the proposed drastic variations violate other observational constraints and yield contradicting results when incorporated in full-fledged chemo-evolutionary models. On the whole, it is clear that we are still far from understanding the behavior of the Ca II triplet in the integrated light of stellar systems with complex star-formation histories. Only with the aid of detailed chemo-dynamical models can one hope to explore the effects of realistic IMF variations and of complex star-formation histories on the relative elemental abundances, particularly of Ca and other α-elements, and to check how different formation scenarios reflect in the absorption-line indices of dEs.

3.6 Solving the Calcium puzzle

Cenarro et al. (2004) have shown that systematic differences exist between the Calcium absorption strengths of elliptical galaxies in the Coma cluster on the one hand and in the field on the other. What the origin of this dependence of the Calcium lines on the environment is, is not understood. To further investigate this Calcium puzzle, we will obtain optical spectra of the dEs presented in this chapter. On the one hand we will then be able to estimate the ages and the metallicities of the dEs using optical population synthesis models, which are well calibrated. Using these ages and metallicities, the chemical dichotomy suggested in Fig. 3.3 can be investigated. On the other hand we can compare the Calcium lines in the optical and in the near-infrared for dEs in the Fornax cluster and in groups.

Chapter 4

The interstellar medium in Fornax dEs

4.1 Introduction

Until recently, dEs were thought to have lost their gas and dust long ago. Several evolutionary scenarios have been proposed to explain this apparent lack of an interstellar medium (ISM) in dEs. The *wind-model* (e.g. Mori et al. (1997)) proposes that dEs are primordial objects that lost their gas after it was heated above the escape velocity by supernova explosions. Alternatively, the frequent high-speed interactions with giant cluster-members to which a small late-type disc galaxy (Sc-Sd) is subjected and the subsequent starbursts can transform it into a gasless spheroidal dE-like object. This *galaxy harassment* process (Moore et al., 1996) induces a dramatic morphological evolution on a time-span of about 3 Gyr. Moreover, hydrodynamical simulations of dwarf galaxies moving through the hot, thin intergalactic medium in clusters (Mori & Burkert, 2000; Vollmer, 2003; Michielsen et al., 2004b) or groups (Marcolini et al., 2003) show that ram-pressure stripping can completely remove the ISM of a dwarf galaxy less massive than $10^9\,\mathrm{M}_\odot$ within a few 100 Myr (see also chapter 6). If the ram pressure is strong enough, the ISM may be compressed and localised star bursts may ensue. Low-mass dwarfs ($M \sim 10^8\,\mathrm{M}_\odot$) lose their gas very rapidly, leaving virtually no time for star-formation after entering the cluster of group. Yet another possibility is that dEs are related to other dwarf galaxies such as Blue Compact Dwarfs (BCDs). The *fading model* conjectures that star-forming dwarf galaxies will fade and reach an end-state similar to present-day dEs after they have used up their gas supply and star-formation has ended (Marlowe et al., 1999), although some controversy still remains (Drinkwater & Hardy, 1991; Marlowe et al., 1999). Interactions may have sped up the gas-depletion process, explaining both the abundance of dEs and the paucity of BCDs in high-density environments (van Zee et al., 2004). These different scenarios to explain the origin of dEs are not mutually excluding. An important common point between the propositions is that they all remove the gas from dwarf galaxies. In addition, unlike massive galaxies, dEs can hardly acquire gas in collisions since their escape velocity is small compared to the velocity dispersion in galaxy clusters.

For all these reasons, dEs in dense environments were generally thought to be virtually gas-depleted systems. However, a growing amount of evidence is building up that at least some dEs have retained part of their gas. In their multi-wavelength study of the Local Group dwarf galaxies, Young & Lo presented VLA H I observations of NGC147, NGC185, and NGC205 (Young & Lo, 1996, 1997). These were the first observations that painted a detailed picture of the complex, multi-phase ISM of the most nearby representatives of the class of the dEs. While NGC147 was not detected with a 3σ mass upper

limit of $3 \times 10^3\,\mathrm{M}_\odot$ for an $8\,\mathrm{km\,s^{-1}}$ velocity width, NGC205 was found to contain $4.3 \times 10^5\,\mathrm{M}_\odot$ of neutral hydrogen and the total H I mass of NGC185 was estimated at $1.0 \times 10^5\,\mathrm{M}_\odot$. The neutral ISM of both detected galaxies turned out to be very clumpy, making a meaningful determination of their velocity fields rather difficult. Still, the stars and H I gas in NGC205 seem to have different rotation velocities while in NGC185, neither the H I or the stars show significant rotation (Simien & Prugniel, 2002). Single-dish observations of ^{12}CO emission provide evidence that the molecular and atomic gas are kinematically linked. NGC205 was not detected on Hα+[N II] narrow-band images while NGC185 contains an extended emission region, about 50 pc across (Young & Lo, 1996, 1997).

More recently, H I surveys of the Virgo Cluster dE population (see Conselice et al. (2003a) and references therein) have shown that roughly 15 per cent of the dEs contain a neutral ISM. The detected H I masses range between 0.03 and $1.22 \times 10^9\,\mathrm{M}_\odot$. Processes that remove gas, such as galaxy interactions and ram-pressure stripping, act most vigorously near the cluster center. Accordingly, the gas-rich dwarf galaxies in the Virgo cluster tend to have positions towards the outskirts of the cluster, suggesting that they are recent acquisitions of the cluster or are moving on orbits that avoid the cluster center. In a spectroscopic survey of the Fornax Cluster, Drinkwater et al. (2001) discovered Hα emission in about 25 per cent of the dEs. Again, most of these galaxies lie towards the outskirts of the cluster, while dEs near the center of the cluster are generally devoid of ionized gas suggesting an environmental effect on the gas-depletion rate of dEs (e.g. interactions or ram-pressure stripping) and strongly hinting at an (evolutionary) transition between gas-rich/star-forming dEs at the outskirts and gasless/quiescent ones in the centre of the cluster.

In section 4.2, we present R-band and Hα+[N II] narrow-band imaging of three dwarf elliptical galaxies (dEs) in the Fornax Cluster, based on observations collected at the European Southern Observatory, Chile. These dEs contain significant amounts of ionised gas. FCC032 harbours a large ionised gas complex, consisting of several individual clouds, a superbubble and a filament that extends away from the galaxy centre. The ionised gas structures observed in FCC032 bear a strong resemblance to those observed in more gas-rich and more fiercely star-forming dwarf galaxies. FCC206, a very low surface brightness dE, contains one faint extended emission region, and two compact clouds. In FCCB729, the only nucleated galaxy in this sample, one of the ionised gas clouds coincides with the stellar nucleus. We derive ionised gas masses of a few 10^2 to $10^3\,\mathrm{M}_\odot$ for these galaxies.

This brings the sample of dEs with ionised gas with Hα+[N II] narrow-band imaging observed by our group to five objects. The ionised gas morphologies in these galaxies range from pure nuclear emission peaks to extended emission complexes. This morphological diversity could also indicate a diversity in ionising processes in dEs with a warm ISM (active galactic nuclei, starbursts, post-AGB stars,...).

Moreover, inside FCC206, four star clusters appear to be on the verge of merging to form a nucleus in this presently non-nucleated dE. Understanding the formation of nuclei in dEs could give us important clues to the formation of super-massive black holes (SMBHs).

In section 4.3, we present H I 21 cm line observations, obtained with the Australia Telescope Compact Array (ATCA), of two dEs in the Fornax cluster: FCC032 and FCC336. The optical positions and velocities of these galaxies place them well within the Fornax cluster. FCC032 was detected at the 3σ significance level with a total H I flux density of $0.66 \pm 0.22\,\mathrm{Jy\,km\,s^{-1}}$ or an H I mass of $5.0 \pm 1.7 \times 10^7 h_{75}^{-2}\,\mathrm{M}_\odot$. Based on our deep H$\alpha$+[N II] narrow-band images, this dE was already known to contain ionised hydrogen. Hence, this is the first study of the complex, multi-phase ISM of a dE outside the Local Group. FCC336 was detected at the same significance level: $0.28 \pm 0.08\,\mathrm{Jy\,km\,s^{-1}}$ or a total H I mass of $2.1 \pm 0.6 \times 10^7 h_{75}^{-2}\,\mathrm{M}_\odot$. Using a compilation of H I data of dwarf galaxies, we find that the observed high H I-mass boundary of the distribution of dIrrs, BCDs, and dEs in a $\log(L_B)$ versus $\log(M_{\mathrm{H\,I}})$ diagram is in good agreement with a simple chemical evolution model with continuous star formation. The many very gas-poor dEs (undetected at 21 cm) suggest that the environment (or more particularly, a galaxy's orbit within a cluster) also plays a crucial role in determining the amount of gas in present-day dEs. E.g., FCC032 and FCC336 are located in the sparsely populated outskirts of the

Fornax cluster. This is in agreement with H I surveys of dwarf elliptical galaxies in the Virgo Cluster and an Hα survey of the Fornax Cluster, which also tend to place gas-rich dwarf galaxies in the cluster periphery.

Throughout this chapter, we use $H_0 = 75\,\mathrm{km\,s^{-1}\,Mpc^{-1}}$ and a Fornax systemic velocity $v_{\mathrm{sys}} = 1379\,\mathrm{km\,s^{-1}}$, which gives a distance of 18.4 Mpc to the Fornax Cluster. Note that this value of H_0 is slightly different from the one adopted in chapter 2.

4.2 Hα observations

4.2.1 Introduction

In De Rijcke et al. (2003b) (hereafter Paper 1) results on Hα+[N II] observations of the FCC046 and FCC207 are reported. Both dEs exhibit a central emission region that could be attributed to photo-ionization by post-AGB stars. FCC046 also harbours 6 faint emission clouds with diameters and fluxes comparable to supernova remnants. The hypothesis that FCC046 is actively forming stars, albeit at a leisurely pace, is further corroborated by its blue colour and high near-infrared Paschen absorption index (Michielsen et al., 2003b). Such dEs could be considered as the missing link between more vigorously star-forming dwarfs (such as BCDS) and traditional dEs.

Here, we present R-band and Hα+[N II] narrow-band images of three Fornax dEs (FCC032, FCC206, and FCCB729) that are expected to contain ionised gas, based on the existing spectroscopic equivalent-width (EW) estimates (Drinkwater et al., 2001). In subsection 4.2.2, we discuss the details of the observations and data reduction. The results based on the R-band and the Hα+[N II] narrow-band images are presented in subsections 4.2.3 and 4.2.4, respectively, and discussed in subsection 4.2.5. The conclusions based on this Hα survey are summarized in subsection 4.2.6.

4.2.2 Observations and data reduction

The observations were carried out on 2003 October 18 and 19 with Yepun (VLT-UT4) using FORS2 in service mode. We took 16 minute exposures with the H_Alpha/2500+60 filter centred on 6604 Å (this redshifted Hα filter gives the best overlap with the Hα emission line in galaxies at the redshift of Fornax) and with a FWHM $= 64$ Å. 130 to 160 second exposures with the R_Special−71 filter centred on 6550 Å and with a FWHM $= 1650$ Å were taken to serve as off-band images. Hα images of the spectrophotometric standard stars LB227 and LTT2415 were taken for flux-calibration. During the observations, the seeing typically was 0.5 – 0.7 arcsec FWHM (determined from the stars on the images). The standard data reduction procedures (bias subtraction, flatfielding, cosmic removal, sky subtraction) were performed with ESO-MIDAS (Munich Image Data Analysis System), which is developed and maintained by the European Southern Observatory. Before co-adding, all science images were corrected for atmospheric extinction, using the R-band extinction coefficient : $k_c = 0.068$ provided by the ESO Quality Control, and interstellar extinction, using the Galactic extinction estimates from Schlegel et al. (1998) : $A_R = 0.034$ for FCC032, $A_R = 0.038$ for FCC206 and $A_R = 0.059$ for FCCB729. The images were finally converted to units of electrons/second/pixel. In order to find the correct scaling for the R-band images we adopted the following strategy. The pure emission 'Em' can be recovered from a narrowband image 'Ha' and an R-band image 'Rb' as

$$\mathrm{Em} = \mathrm{Ha} - (c \times \mathrm{Rb} - \delta), \tag{4.1}$$

with c the proper scaling constant and δ a correction for possible faulty sky-subtraction. To find the best values for c and δ, we fitted the isophotes of the narrow-band and R-band images in an

annulus between $m_R = 24.5$ and $m_R = 26.5\,\mathrm{mag\,arcsec^{-2}}$ which in retrospect did not contain any emission (hence Em $= 0$), using the standard MIDAS FIT/ELL3 command. Thus, a smooth version of this annulus could be constructed for both images. The optimal values of c and δ can be found by minimizing the expression $|\mathrm{Ha} - (c \times \mathrm{Rb} + \delta)|$ with Ha and Rb the smoothed versions of the annulus. With these values in hand, the pure-emission image can be obtained using relation (4.1).

For all galaxies, δ was essentially zero, which makes us confident that the sky was properly subtracted from all images. Since the Hα narrowband and R-band filters overlap, subtracting an R-band image instead of a narrowband continuum image induces a partial removal of some Hα+[N II] light. The error thus introduced is of the order of the ratio of the effective widths of the filters (R-band: $W = 1650\,$Å and Hα: $W = 64\,$Å). This is less than 4 per cent which is negligible in comparison to other possible sources of error, so we did not correct for it.

A pixel-value (in electrons per second) in the pure-emission image, denoted as N, can be converted to flux units ($\mathrm{W\,m^{-2}}$), denoted by F', using the formula

$$F' = N \times \frac{\varphi_0}{N_*} \int_0^\infty \mathcal{F}_*(\lambda)\varphi_f(\lambda) d\lambda \,\mathrm{W\,m^{-2}}. \tag{4.2}$$

Here, $\mathcal{F}_*(\lambda)$ is the spectrum of a flux-calibration standard star in $\mathrm{W\,m^{-2}\,Å^{-1}}$ and N_* is the measured flux of that star, expressed in electrons per second. The function $\varphi_f(\lambda)$ is the transmission of the Hα filter and φ_0 the transmission of the optics (which is basically constant for a narrow-band filter). The prime on F' indicates that this is the flux incident on the CCD, after going through the telescope and instrument optics and the narrow-band filter. This can also be written as

$$F' = \varphi_0 \left[F_{\mathrm{H}\alpha} \varphi_f\left(\lambda_{\mathrm{H}\alpha}\right) + F_{[\mathrm{N\,II}]_1} \varphi_f\left(\lambda_{[\mathrm{N\,II}]_1}\right) + F_{[\mathrm{N\,II}]_2} \varphi_f\left(\lambda_{[\mathrm{N\,II}]_2}\right) \right], \tag{4.3}$$

with $F_{\mathrm{H}\alpha}$, $F_{[\mathrm{N\,II}]_1}$ and $F_{[\mathrm{N\,II}]_2}$ the incoming fluxes, before going through the telescope optics and the narrow-band filter, of respectively the Hα 6564 Å, the [N II] 6548 Å and the [N II] 6584 Å (redshifted) emission lines approximated as δ-functions. This allows one to obtain the true incoming flux of the Hα emission line as

$$F_{\mathrm{H}\alpha} = \frac{\frac{N}{N_*} \int_0^\infty \mathcal{F}_*(\lambda)\varphi_f(\lambda)\, d\lambda}{\varphi_f\left(\lambda_{\mathrm{H}\alpha}\right) + \left[\frac{F_{[\mathrm{N\,II}]_1}}{F_{NII_2}} \varphi_f\left(\lambda_{[\mathrm{N\,II}]_1}\right) + \varphi_f\left(\lambda_{[\mathrm{N\,II}]_2}\right) \right] \frac{F_{[\mathrm{N\,II}]_2}}{F_{\mathrm{H}\alpha}}}. \tag{4.4}$$

The total incoming Hα+[N II] flux is simply

$$F_{\mathrm{em}} = F_{\mathrm{H}\alpha} \left(1 + \frac{F_{[\mathrm{N\,II}]_1}}{F_{\mathrm{H}\alpha}} + \frac{F_{[\mathrm{N\,II}]_2}}{F_{\mathrm{H}\alpha}} \right). \tag{4.5}$$

Since the Hα filter is relatively flat-topped and the [N II] lines are well inside the filter transmission curve, the total flux is rather insensitive to the adopted relative line-strengths. In the following, we will assume the mean value $F_{[\mathrm{N\,II}]_2}/F_{[\mathrm{N\,II}]_1} = 3$ for the ratio of the line-strengths of the two N lines (Phillips et al., 1986). The ratio $F_{[\mathrm{N\,II}]_2}/F_{\mathrm{H}\alpha}$ is not known and is treated as a free parameter, though it is generally assumed that it varies between 0 and 2.

4.2.3 R-band photometry

We fitted ellipses to the isophotes of R-band images of FCC032, FCC201, FCC206, and FCCB729 (see Fig.4.1), with the semi-major axis a, the position angle (PA), the ellipticity $\epsilon = 10\,(1 - b/a)$ and the coordinates of the centre of each ellipse as free parameters. We masked hot pixels, stars, and cosmics. Masked regions were not used in the fit. For the innermost isophote, the ellipse was centred

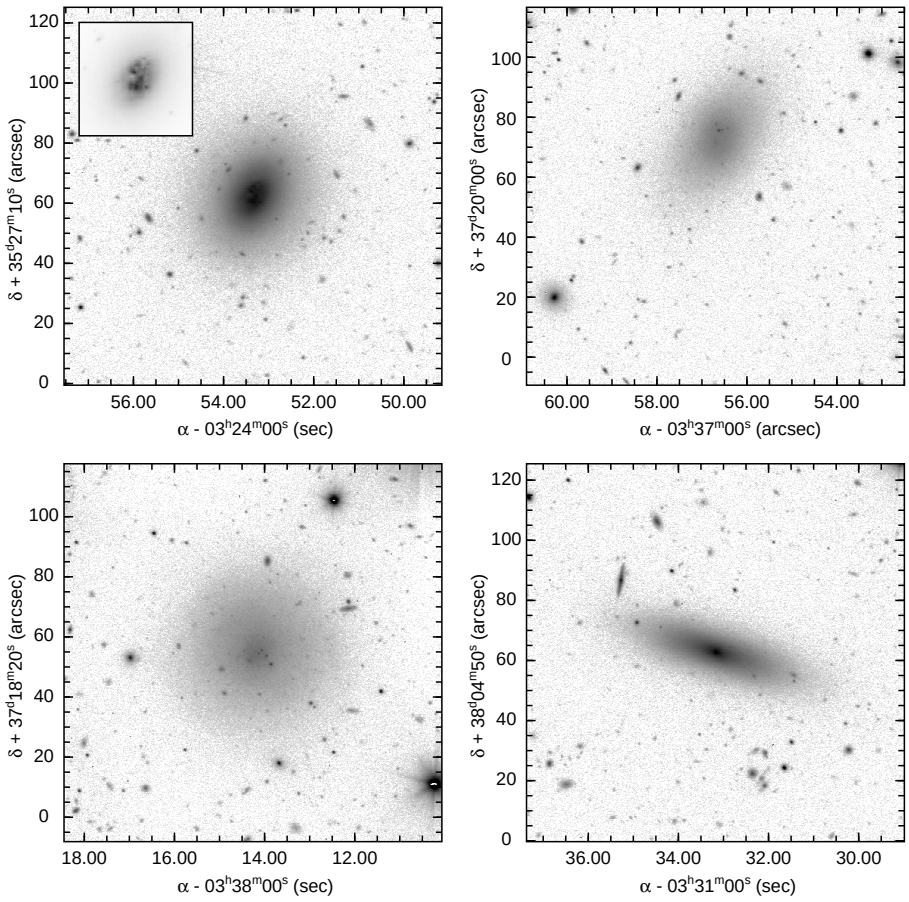

Figure 4.1: Negative R-band images of (clockwise, starting at left upper panel) FCC032, FCC201, FCC206, FCCB729. A logarithmic grayscale between 30 and 21.5 mag is adopted for all images, allowing a direct comparison of the surface brightness. *FCC032* : The inset shows the inner $25 \times 25''$ with a linear grayscale. Note the many bright knots (black) interspersed with dust patches (see also Fig. 4.4). *FCC206* : Four point sources are discernable close to the galaxy centre (see also Fig. 4.4).

on the brightest pixel, excluding the bright point sources in FCC032 and FCC206. The deviations of the isophotes from a pure elliptic shape were quantified by expanding the intensity variation along an isophotal ellipse in a fourth order Fourier series with coefficients S_4, S_3, C_4 and C_3:

$$I(\theta) = I_0 \left\{1 + C_3 \cos[3\,(\theta - \mathrm{PA})] + C_4 \cos[4\,(\theta - \mathrm{PA})] + S_3 \sin[3\,(\theta - \mathrm{PA})] + S_4 \sin[4\,(\theta - \mathrm{PA})]\right\}, \tag{4.6}$$

with $I(\theta)$ the intensity on the ellipse at an angle θ with respect to the major axis and I_0 the average intensity on the ellipse. The photometry of all four galaxies is presented in Figures 4.2 and 4.3. All photometric parameters were fitted by cubic splines as functions of the semi-major axis a of the isophotal ellipses. This allows us to reconstruct the surface brightness at any given point on the sky and hence to reconstruct the R-band image from the fitted photometric parameters. From this reconstructed

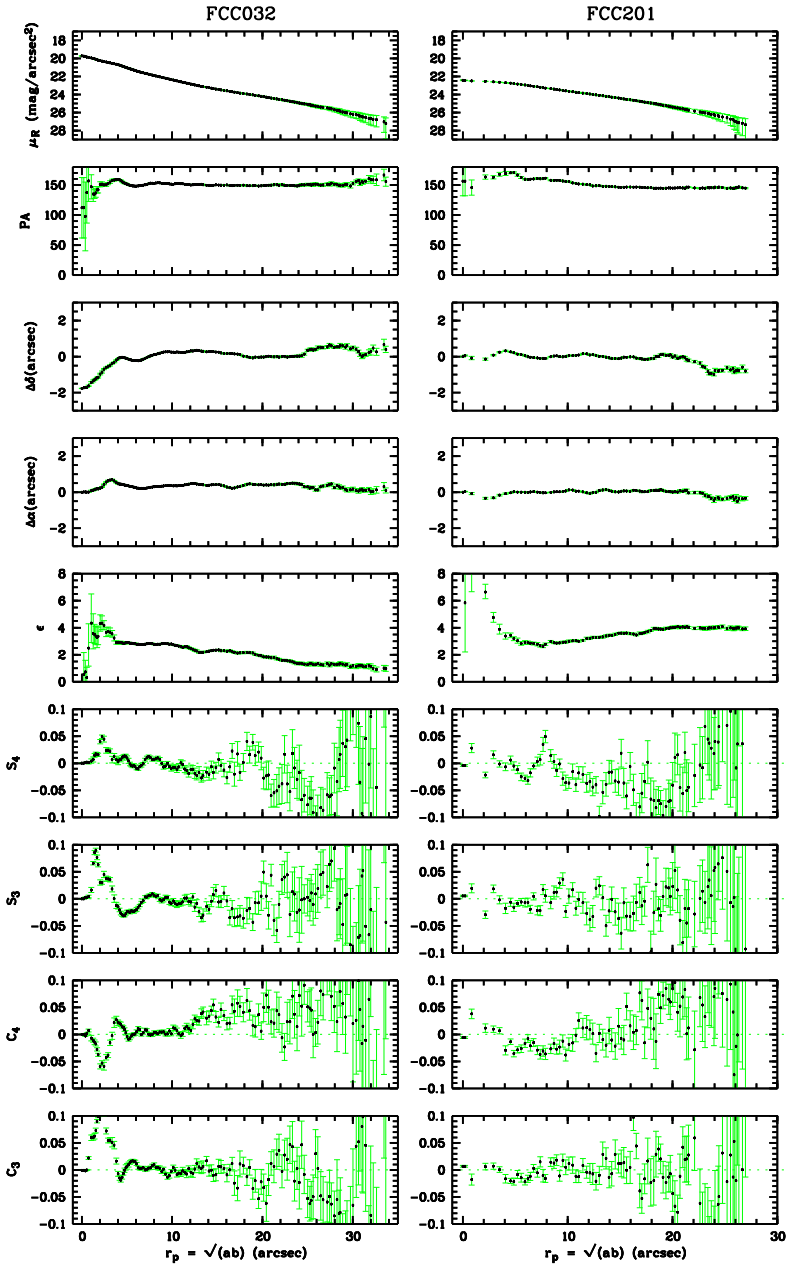

Figure 4.2: Photometric properties of FCC032 and FCC201, derived from the R-band images, versus the geometric mean of the semi-major and semi-minor distances a and b. From top to bottom: the R-band surface brightness μ_R, the deviation in declination $\Delta\delta$ and right ascension $\Delta\alpha$ of the centres of the isophotes with respect to the brightest point, the PA, the ellipticity $\epsilon = 10\,(1 - b/a)$ and the Fourier coefficients S_4, S_3, C_4 and C_3 that quantify the deviations of the isophotes from ellipses.

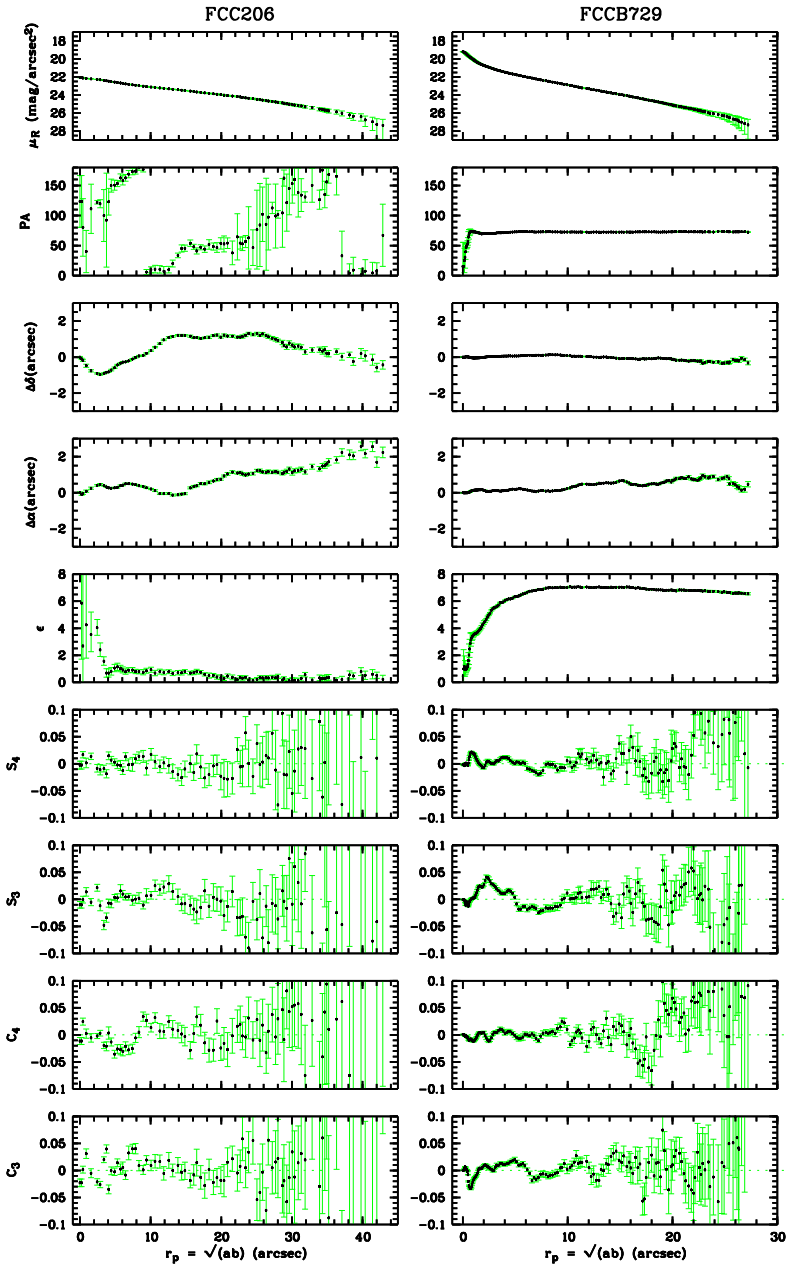

Figure 4.3: Photometric properties of FCC206 and FCCB729. Same as Figure 4.2.

image, which is obviously free of cosmics and foreground stars, we derived the total apparent R-band magnitude m_R and the model-free photometric parameters R_{eff} and $\langle\mu\rangle_{\text{eff}}$. The effective radius R_{eff} is the half-light radius of the galaxy; the effective surface brightness $\langle\mu\rangle_{\text{eff}}$ is the mean surface brightness within R_{eff} and can be derived from m_R and R_{eff} using

$$\langle\mu\rangle_{\text{eff}} = m_R + 2.5\log(2\pi R_{\text{eff}}^2). \tag{4.7}$$

The surface brightness profiles of dEs can be fitted quite well by a Sérsic profile (Sérsic, 1968), which is a generalisation of de Vaucouleurs' $r^{1/4}$ and exponential laws. Several photometric studies have used this profile to analyse dEs (see e.g. Ryden et al. (1999), Barazza et al. (2003)). We fitted the surface brightness profiles with

$$\mu(r) = \mu_0 + 1.086(r/r_0)^n, \tag{4.8}$$

with $\mu(r)$ the surface brightness at radius r (we measure radii as the geometric mean of the semi-major and semi-minor axes of the isophotes, in arcseconds), μ_0 the extrapolated central surface brightness (both in mag arcsec^{-2}) and r_0 the scale radius, in arcseconds. The Sérsic shape parameter[1] n quantifies the central concentration of the surface brightness profiles, with $n = 1/4$ corresponding to a centrally concentrated de Vaucouleurs profile and $n = 1$ to a diffuse exponential. A χ^2 fit to the profiles has been performed outside 4 arcsec and above the level of 26 mag arcsec^{-2}, to exclude the emission clouds in the centre and to avoid the outer parts of the galaxies which might be affected by flat-field and sky-subtraction uncertainties. In order to compare our results to other studies which use an exponential instead of a Sérsic law, we also fitted an exponential law to the same part of the surface profiles, deriving a central surface brightness μ_0 and a scale length r_0. All photometric parameters are listed in Table 4.1.

FCC032

Based on blue-sensitive photographic plates taken with the Las Campanas 2.5 m du Pont telescope and the UK Schmidt Telescope, Ferguson (1989) classified FCC032 as dE pec/BCD, most likely inspired by the presence of several bright knots and dust patches in the central region, which are also visible in our R-band images. We applied an unsharp masking technique to the R-band images to highlight possible small-scale structure (De Rijcke et al., 2003a). The aforementioned features stand out very clearly in the unsharp-masked image in Fig. 4.4. None of these bright knots is at the centre of the outer isophotes. We took the brightest knot (in R-band) as the reference point, but the photometry in the inner 4 arcsec is hampered by these knots, as can be seen in the rapid variation of the Fourier coefficients. FCC032's location in a cluster, its diffuse, near-exponential surface brightness profile, and its regular, elliptical isophotes argue in favour of a classification as a non-nucleated dE2.

FCC201

Cellone & Forte (1996) observed FCC201 in the Washington optical filter system and found that the colours of this galaxy are consistent with an old population, similar to Globular Clusters. This coincides with the fact that no Hα was detected in FCC201 by Drinkwater et al. (2001).

FCC206

Caldwell & Bothun (1987), in their photometric study of a sample of Fornax galaxies, noted several bright knots close to, but not actually at, the centre of FCC206. We find four unresolved sources in the

[1] Note that in some studies the Sérsic shape parameter is defined as the reciprocal $1/n$.

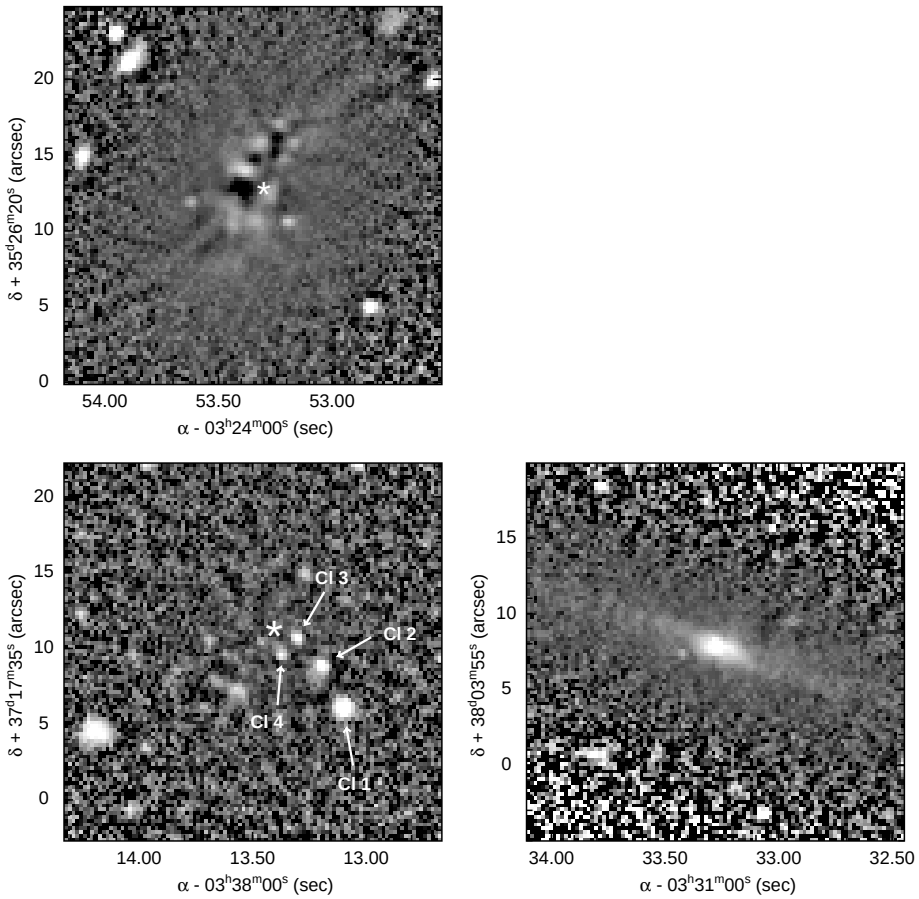

Figure 4.4: The *R*-band images of FCC032 (upper left), FCC206 (lower left) and FCCB729 (lower right) divided by their median filtered homologue (running box of $2.5 \times 2.5''$). *FCC032* : There are many bright spots (white), some of which are also visible in the Hα+[N II] image (though not all). Some of these bright spots might be foreground or background objects (although such a strong concentration of chance alignments close to the galaxy centre seems highly unlikely) while others correspond to star formation sites that ionise the surrounding gas. Also clearly visible are the dark dust patches. The asterisk marks the centre of the outer isophotes. *FCC206* : Four point sources or *star clusters* (named `Cl1` to `Cl4`) can be discerned, two of which, `Cl2` and `Cl3`, also appear in the pure emission image in Fig. 4.7. There are no traces of dust absorption. The asterisk marks the centre of the outer isophotes. *FCCB729* : A faint stellar disc can be discerned which could also be due to the high degree of flattening of this dS0,N (Fig. 4.6). The nucleus of FCCB729 appears slightly extended in the south-west direction, coincident with the extended Hα emission (Fig. 4.7).

R-band image. They show up very clearly in the unsharp masked image in Fig. 4.4. FCC206 is quite blue compared with other Fornax dEs and its $B-V=0.52$ colour is redder than would be expected from its $U-B=-0.16$ colour (assuming a single-age, single-metallicity globular-cluster like population), indicative of a composite population containing both cool stars and hot young stars. The knots are found to be even bluer and with luminosities comparable to the brightest and bluest Large Magellanic Cloud globular clusters. These authors suggest that we are witnessing the formation of a nucleus. Caldwell & Bothun (1987) estimate the absolute magnitudes of these knots at $M_V \sim -8.5$. Assuming the clusters to reside inside FCC206, we find $m_R(\texttt{C11}) = 21.7$, $M_R(\texttt{C11}) = -9.7$;$m_R(\texttt{C12}) = 23.7$, $M_R(\texttt{C12}) = -7.6$; $m_R(\texttt{C13}) = 23.8$, $M_R(\texttt{C13}) = -7.5$; and $m_R(\texttt{C14}) = 23.7$, $M_R(\texttt{C14}) = -7.6$. The values of C12 and C13 are corrected for the contribution of the Hα emission to the R-band flux. (C11 and C14 are absent in the Hα+[N II] images, see section 4.2.4). The naming of the clusters is clarified in Fig. 4.4. These absolute magnitudes are similar to those of Galactic globular clusters, the brightest of which is ωCen with $M_V = -10.6$. Due to its roundness, FCC206 has a very ill defined PA, changing continuously over more than 240 degrees. Even outside the central region, where the photometry is not affected by the bright knots, the position of the centre of the isophotes varies significantly and rapidly. We constructed surface brightness models keeping the centre coordinates fixed, but the residuals are always larger compared to the model with varying centre coordinates, thus we conclude the variation in $\Delta\delta$ and $\Delta\alpha$ is real. In the following we take the centre of the outer isophotes as the centre of the galaxy. Finally, FCC206 is non-nucleated and has a very large flat core, which is reflected in its large Sérsic shape parameter $n = 1.33$.

FCCB729

Due to its relatively high surface brightness, FCCB729 was originally classified as a background galaxy (Ferguson, 1989). However, redshift measurements by Drinkwater et al. (2001) identify FCCB729 as a true Fornax Cluster member. Moreover, FCCB729 has a nearly exponential surface brightness profile, typical of a genuine dwarf galaxy. Subtracting the best fitting Sérsic model off the surface brightness profile, we can compute the luminosity of the nucleus. We arrive at an apparent R-band magnitude $m_R = 19.64$, or absolute magnitude $M_R = -11.68$. The effect of seeing alone is not strong enough to account for the decline in ellipticity towards the centre. A simulated pure elliptical surface brightness distribution with $\epsilon = 7$ convolved with an 0.7 arcsec FWHM Gaussian point spread function would still reach $\epsilon \simeq 5$ in the centre. Thus the nucleus is significantly rounder than the galaxy itself, although overall, FCCB729 is a very flattened system. Its C_4 profile is systematically positive which indicates that the isophotes are slightly disky, especially towards the outskirts. This argues for a classification as dS0(7),N, rather than dE7,N. The dip in C_4 around $r \sim 17''$ is due to the two symmetrically opposed bright knots along the major axis, which were masked to derive the photometry. This results in a more boxy appearance at that point. With the unsharp masking technique, we detected what seems to be a faint stellar disc embedded in FCCB729 (Fig. 4.4), although some caution is needed here. We also applied the technique to the simulated pure dE7 and saw the same signature of a disc. This signature is entirely due to the high degree of flattening and the size of the filtering running box (Figs. 4.5 and 4.6).

4.2.4 Hα imaging

The Hα equivalent width

Drinkwater et al. (2001) have measured Hα EWs of 108 confirmed Fornax Cluster members, including FCC032, FCC201, FCC206 and FCCB729, with the FLAIR-II spectrograph on the UK Schmidt Telescope. The effective aperture of this system is at least 6.7 arcsec (the fiber diameter) and could be

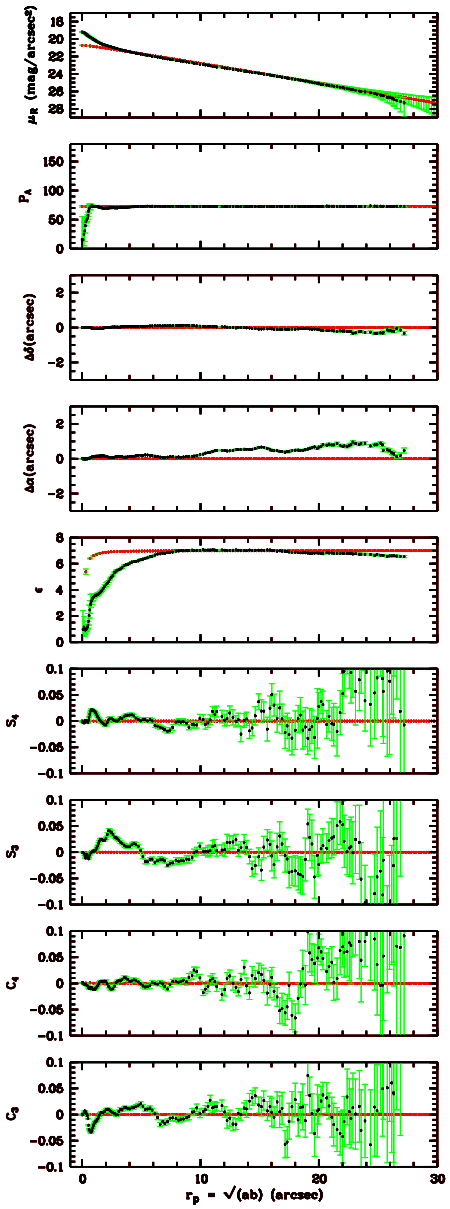

Figure 4.5: Surface photometry of a simulated *pure* dE7 galaxy (red dots) compared to the observed photometry of FCCB729. The simulated galaxy was seeing-convolved with a two-dimensional Gaussian point spread function with FWHM = 0.7″. The nucleus was not simulated as is apparant in the surface brightness profile. Although the seeing makes the galaxy look rounder towards the centre, FCCB729 becomes rounder than can be attributed by seeing alone.

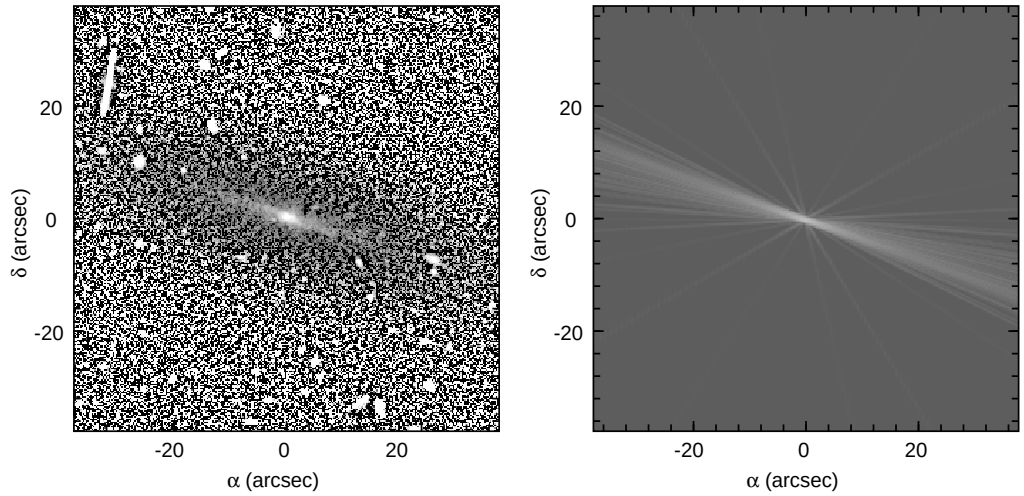

Figure 4.6: Unsharp masked images of FCCB729 (left) and a seeing-convolved pure dE7 galaxy (right). The R-band images were divided by their median filtered homologue (running box of $2.5 \times 2.5''$). Although simulated galaxy has diskyness zero, a disk-like structure appears in the unsharp-masked image.

as large as 15 arcsec because of image movements due to tracking errors and differential atmospheric refraction. These authors find:

EW(FCC032) = 9.6 Å,
EW(FCC201) = 0.7 Å,
EW(FCC206) = 14.4 Å,
EW(FCCB729) = 6.8 Å.

For comparison, we calculated the EW inside an aperture radius r from our images as :

$$\mathsf{EW} = \frac{F_{\mathsf{em}}(r)}{F_{\mathsf{cont}}(r)} \Delta\lambda, \tag{4.9}$$

with $\Delta\lambda = 64$ Å the FWHM of the Hα filter and $F_{\mathsf{em}}(r)$ and $F_{\mathsf{cont}}(r)$ the total number of counts inside a circular aperture with radius r of the narrowband and the continuum (scaled R-band) image, respectively. We find :

FCC032

$$\begin{cases} F_{\mathsf{em}}(3.5'') & = 700\,\mathsf{e}^-\,\mathsf{s}^{-1} \\ F_{\mathsf{cont}}(3.5'') & = 2340\,\mathsf{e}^-\,\mathsf{s}^{-1} \\ & \rightarrow \mathsf{EW}(3.5'') = 19.1\,\text{Å}, \\ F_{\mathsf{em}}(8'') & = 968\,\mathsf{e}^-\,\mathsf{s}^{-1} \\ F_{\mathsf{cont}}(8'') & = 5920\,\mathsf{e}^-\,\mathsf{s}^{-1} \\ & \rightarrow \mathsf{EW}(8'') = 10.5\,\text{Å}, \end{cases}$$

FCC206

$$\begin{cases} F_{\mathsf{em}}(3.5'') & = 100\,\mathsf{e}^-\,\mathsf{s}^{-1} \\ F_{\mathsf{cont}}(3.5'') & = 355\,\mathsf{e}^-\,\mathsf{s}^{-1} \\ & \rightarrow \mathsf{EW}(3.5'') = 18.0\,\text{Å}, \\ F_{\mathsf{em}}(8'') & = 308\,\mathsf{e}^-\,\mathsf{s}^{-1} \\ F_{\mathsf{cont}}(8'') & = 1300\,\mathsf{e}^-\,\mathsf{s}^{-1} \\ & \rightarrow \mathsf{EW}(8'') = 15.2\,\text{Å}, \end{cases}$$

FCCB729

$$\begin{cases} F_{\mathsf{em}}(3.5'') & = 280\,\mathsf{e}^-\,\mathsf{s}^{-1} \\ F_{\mathsf{cont}}(3.5'') & = 1383\,\mathsf{e}^-\,\mathsf{s}^{-1} \\ & \rightarrow \mathsf{EW}(3.5'') = 13.0\,\text{Å}, \\ F_{\mathsf{em}}(8'') & = 302\,\mathsf{e}^-\,\mathsf{s}^{-1} \\ F_{\mathsf{cont}}(8'') & = 3010\,\mathsf{e}^-\,\mathsf{s}^{-1} \\ & \rightarrow \mathsf{EW}(8'') = 6.4\,\text{Å}. \end{cases}$$

We did not find any emission to be present in FCC201. Indeed, based on the EW measurements of Drinkwater et al. (2001), very little emission was expected in FCC201. In all, our values are in good agreement with the EWs measured by Drinkwater et al. (2001), considering the uncertainties that affect both measurements (photon shot-noise, sky and continuum subtraction, positioning of the FLAIR-II spectrograph fiber on these faint objects, ...).

The Hα+[N II] and Hα luminosities

We present the pure Hα+[N II] images of FCC032, FCC206 and FCCB729 in Fig. 4.7. The emission fluxes are calculated using eqs. (4.4) and (4.5) and depend on the adopted value for $F_{[\mathsf{N\,II}]_2}/F_{\mathsf{H}\alpha}$. In Fig. 4.8 we show how the total emission and the Hα fluxes vary with $F_{[\mathsf{N\,II}]_2}/F_{\mathsf{H}\alpha}$ going from 0 to 2. The Hα+[N II] and Hα fluxes and luminosities are listed in columns 2 – 5 of Table 4.2. In figure 4.9, we compare the total emission luminosity with those of FCC046 and FCC207 (Paper 1) and with those found for elliptical and S0 galaxies by Phillips et al. (1986), Buson et al. (1993) and Macchetto et al. (1996). The linear correlation between emission-line luminosity L_{em} and absolute blue magnitude M_B in the large sample of galaxies studied by Phillips et al. (1986) strongly suggests that the dominant ionising source in *normal* early-type galaxies is a component of the stellar population. In these galaxies, the emission-line region is mostly concentrated in the centre, while galaxies with extended emission (Buson et al., 1993) have emission-line luminosities 10 – 100 times larger than *normal* Es and S0s. This increase in emission luminosity requires a second ionising source to be present. This can be photo-ionisation by young hot stars or shock-ionisation by supernova remnants in those galaxies in which recent star-formation is present. On the other hand, an active nucleus can also provide an extra source of ionisation. The dEs in our sample extend the correlation of L_{em} versus M_B for early-type galaxies with extended emission.

In FCC032, the emission is indeed extended and comprises several emission clouds. The total flux of FCC206 is about 3 times lower. In this galaxy, three separate emission clouds are clearly visible. Finally, the emission of FCCB729 is concentrated in the centre, with a flux comparable to that of FCC206. This is the only galaxy in which the emission coincides with the stellar nucleus; the other two show distinct emission clouds *around* the centre. Binette et al. (1994) propose photo-ionisation by post-AGB stars in an old stellar population as a source for the central emission in elliptical galaxies. Using their prescriptions, we derive central Hα luminosities of the order of 2×10^{30} W, i.e. a factor 5–10 less than what is observed here, suggesting that other ionisation mechanisms are (also) present. If, on the other hand, all Hα emission were due to photo-ionisation by young stars, we can estimate the star formation

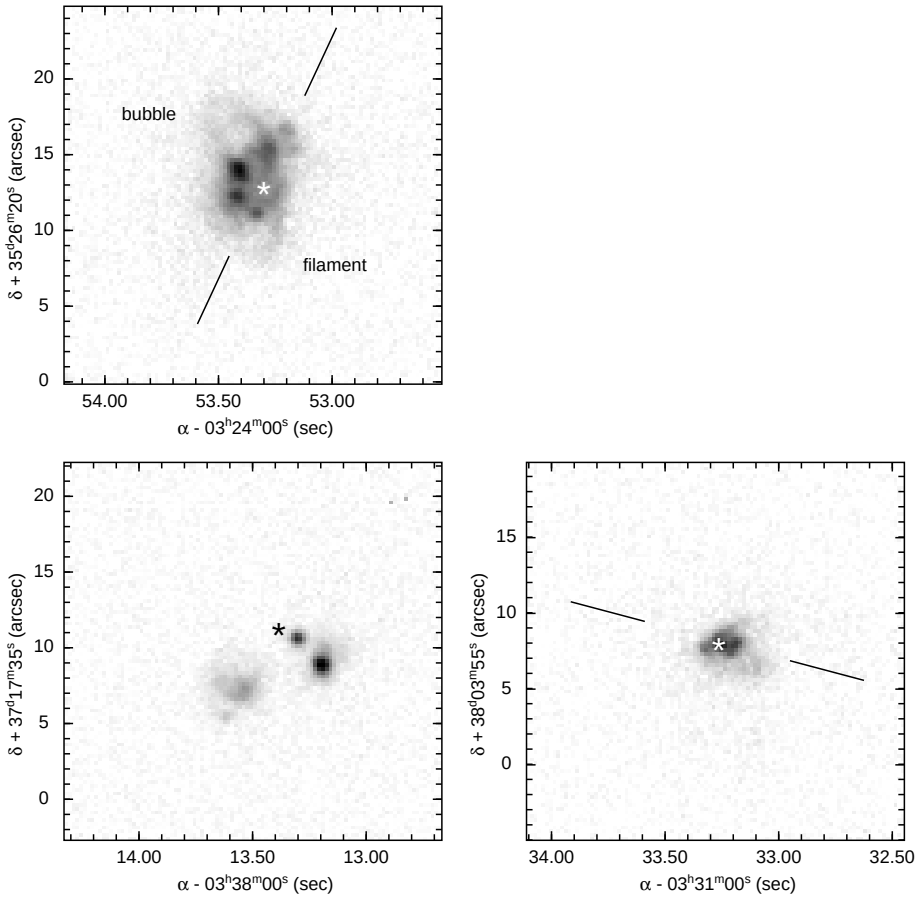

Figure 4.7: The pure Hα+[N II] emission images of FCC032, FCC206 and FCCB729. *FCC032*: Several emission clouds are visible, forming a gas complex which is elongated along the galaxy's major axis (the direction of the major axis is indicated by two black lines). Towards the north-east a superbubble is visible; towards the south, a gas filament (or bubble?), extending away from the galaxy centre, can be discerned. *FCC206*: Three separate emission regions are visible, two compact and one extended. The two compact blobs correspond to two of the bright point sources visible in the unsharp masked image (see Fig. 4.4). *FCCB729*: The central emission extends to the west, approximately along the direction of the major axis (indicated by two black lines). In all images, the asterisks mark the centres of the outer isophotes. The adopted grayscale is the same in all images.

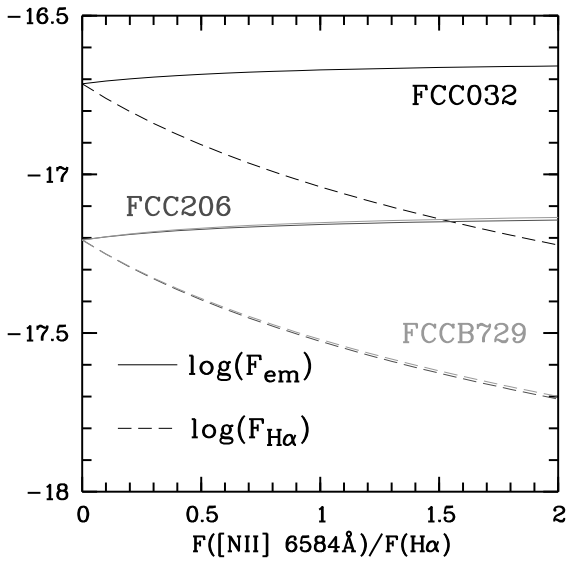

Figure 4.8: The logarithm of the total Hα+[N II] flux $F_{\rm em}$ (solid lines) and the Hα flux $F_{\rm H\alpha}$ (dashed lines) versus the ratio of the strengths of the [N II] 6584 Å and the Hα line. The total flux is virtually independent of this line-ratio. The fluxes for FCC206 and FCCB729 are almost identical.

rate (SFR) using the calibration between the total SFR and the Hα luminosity derived by Kennicutt (1983):

$$\mathrm{SFR} \simeq 8.93 \times 10^{-35} L_{\rm H\alpha} E_{\rm H\alpha}\, \mathrm{M}_\odot\, \mathrm{yr}^{-1}, \tag{4.10}$$

where $E_{\rm H\alpha} = 2.512$ is the standard 1 magnitude factor to correct for internal extinction and $L_{\rm H\alpha}$ is the Hα luminosity expressed in W. The obtained SFR varies between $\sim 10^{-3} - 10^{-2}\,\mathrm{M}_\odot\,\mathrm{yr}^{-1}$ in these galaxies (see Table 4.2, column 6).

The Hα+[N II] luminosities can also be compared with those observed in the Local Group dEs: NGC147, NGC185, and NGC205, three companions of M31. Young & Lo (1997) have detected a central emission region and several compact emission objects in NGC185 with a total Hα+[N II] luminosity $L_{\rm em} = 1.3 \times 10^{29}$ W. This is still an order of magnitude smaller than the Hα+[N II] luminosities of the dEs presented here. No extended Hα emission was detected in NGC205. NGC185 and NGC205 both contain a cold ISM while NGC147 appears to be devoid of gas (Sage et al., 1998). Hence, the Fornax dEs presented in Paper 1 and in this chapter, are comparatively rich in ionised gas. The stark contrast in environment (these dEs reside mostly in the outskirts of the Fornax cluster, see Fig. 4.10, while the M31 satellites are members of a rather compact group, orbiting a massive spiral galaxy) suggests that external factors, such as interactions, affect the gas-depletion rates of dwarf galaxies. N-body/SPH models of dwarf galaxies orbiting inside the Milky Way halo (Mayer et al., 2001) show that their gas reservoirs are depleted within a few gigayears after the first pericentre passage, due to both tidal stripping and star bursts occurring after each pericentre passage. These results for the Milky Way and its satellites should a fortiori be valid for M31 and its companions, given that they have been on bound orbits long enough.

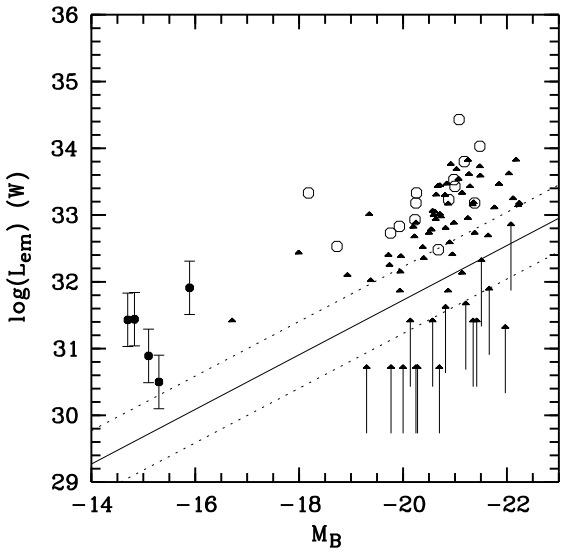

Figure 4.9: The total Hα+[N II] emission-line luminosity versus absolute blue magnitude. The black dots are our sample of dEs (this chapter and Paper 1); the circles and triangles represent the Es and S0s observed by Buson et al. (1993) and Macchetto et al. (1996), respectively. The lines indicate the linear relation and its $1-\sigma$ relation observed by Phillips et al. (1986). All observations have been corrected to the distance scale adopted in this work.

H II masses

The total mass in ionised hydrogen, $M_{\mathsf{H\,II}}$, can be written as

$$M_{\mathsf{H\,II}} = \frac{L_{\mathsf{H}\alpha}}{4\pi j_{\mathsf{H}\alpha}} m_{\mathsf{H}} N_e, \tag{4.11}$$

with $L_{\mathsf{H}\alpha}$ the total Hα luminosity, m_{H} the mass of the hydrogen atom and N_e the electron density in the gas. The hydrogen Hα emissivity $j_{\mathsf{H}\alpha}$ is given by (Osterbrock, 1989)

$$4\pi j_{\mathsf{H}\alpha} = N_e^2 \alpha_{\mathsf{H}\alpha} h\nu_{\mathsf{H}\alpha} = 3.544 \times 10^{-32} N_e^2 \,\mathsf{W\,cm^{-3}} \tag{4.12}$$

in *case B* recombination, i.e. complete re-absorption of all Lyman photons in an optically thick nebula. Each Lyman photon emitted from a level with $n \geqslant 3$ is later on converted to (a) Balmer photon(s) plus one Lyman α photon, thus raising the flux in the Balmer lines. The production coefficient $\alpha_{\mathsf{H}\alpha}$ (calculated for $T = 10^4\,\mathsf{K}$) is insensitive to the electron density (it changes by only 4 per cent if N_e is raised from $1\,\mathsf{cm^{-3}}$ to $10^6\,\mathsf{cm^{-3}}$) and varies as $T^{-0.8}$ as a function of temperature. Using equations (4.11) and (4.12), the ionised hydrogen mass can be written concisely as (Kim, 1989):

$$\begin{aligned} M_{\mathsf{H\,II}} &= 23.72 \left(\tfrac{1000\,\mathsf{cm^{-3}}}{N_e}\right) \left(\tfrac{L_{\mathsf{H}\alpha}}{10^{30}\,\mathsf{W}}\right) \mathsf{M_\odot} \\ &= 2.85 \left(\tfrac{1000\,\mathsf{cm^{-3}}}{N_e}\right) \left(\tfrac{F_{\mathsf{H}\alpha}}{10^{-19}\,\mathsf{W\,m^{-2}}}\right) \left(\tfrac{D}{10\,\mathsf{Mpc}}\right)^2 \mathsf{M_\odot}, \end{aligned} \tag{4.13}$$

with D the distance to the galaxy.

In the following, we will assume the value $N_e = 1000\,\mathsf{cm^{-3}}$ for the electron density to be in accord with most other authors and to be able to directly compare our ionised hydrogen masses with the literature

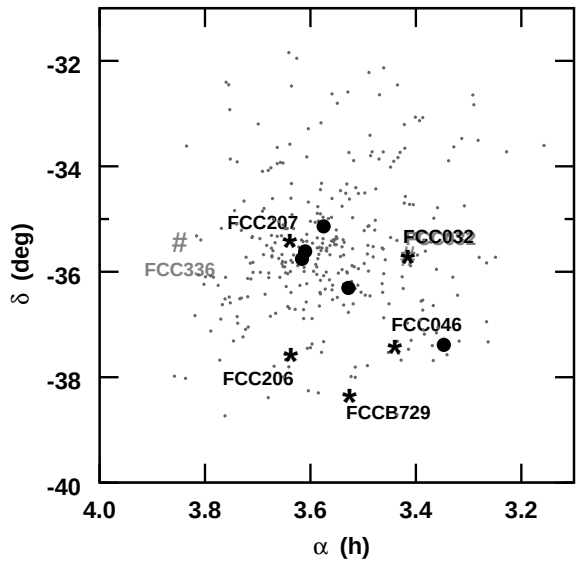

Figure 4.10: Positions of gas-rich dEs within the Fornax Cluster. Small dots indicate the positions of 340 galaxies in the Fornax Cluster Catalog. Large dots indicate the positions of galaxies brighter than $M_B < -20$ mag. Asterisks indicate the positions of FCC032, FCC046, FCC206, FCC207, and FCCB729. These dEs contain an ionised ISM (De Rijcke et al., 2003b; Michielsen et al., 2004a) (see also section 4.2). The positions of the H I detected Fornax dEs FCC032 and FCC336 (Buyle et al, 2005), are indicated with a grey hash. Except for FCC207, which has a projected position close the cluster centre, these dEs appear to populate the less densely populated outskirts of the cluster.

(however, Spitzer (1978) advocates $N_e = 100\,\mathrm{cm}^{-3}$ as a typical value for both Galactic H II regions with diameters of the order of 100 pc and for supernova remnants). Using equation (4.13), we derived ionised hydrogen gas masses between 10^2 and $10^3\,\mathrm{M}_\odot$ (see column 7 of Table 4.2).

4.2.5 Discussion

FCC032

FCC032 is the most gas-rich galaxy in our sample and contains an extended ionised gas complex, about $10''(\approx 850\,\mathrm{pc})$ across. The bulk of the Hα emission in FCC032 is distributed over 4 different emission clouds, 2 of which are clearly visible in the R-band. The other 2 are only visible in the pure-emission images. These clouds appear to lie on a semi-ellipse around the centre of the outer isophotes, with its major axis along the major axis of the galaxy. To the north of the centre, a superbubble is visible, with a diameter of 350 pc, capped with a ~ 90 pc thick shell. Towards the south, a gaseous filament (or bubble?) is extending ~ 260 pc away from the galaxy centre. A comparison of Fig. 4.7 with Fig. 4.4 shows that the low-surface brightness cavities in Fig. 4.7 cannot be due to dust-absorption. This image bears a very strong resemblance to Fig. 1, panel b, in Calzetti et al. (2004), which shows a high-resolution HST narrow-band image of the Hα emission in the starbursting dwarf galaxy NGC3077. The diameter of the bubble in FCC032 is comparable to those found in hydrodynamical simulations of supernova remnants (SNRs) (de Avillez & Berry, 2001) and those observed in irregular dwarf galaxies by Martin (1998), who measures (super)bubble diameters of ~ 100 to 2000 pc.

Such shells of ionised gas are quite common in more gas-rich and star-forming dwarf galaxies such as dwarf irregulars. Usually, these shells consist of gas that is shock-ionised by the supernova explosions and stellar winds leaving the starburst regions. In all, there appears to be a very strong energy feedback of the starburst into the ISM. The strong resemblance between the shells in starbursting dwarf galaxies such as NGC3077 and the ones observed in FCC032, are strong evidence for recent or ongoing star-formation in this dE.

FCC206

The emission in FCC206 comes from 3 separated emission clouds. The two brightest clouds are unresolved. There is also an extended emission region, about $4''(\approx 350\,\mathrm{pc})$ across, to the south-east of the centre. `C12` and `C13` are the only point sources in the R-band image that coincide with an emission region. `C11` and `C14` could either be foreground stars or young globular clusters inside FCC206. Their blue colours, similar to the bluest Large Magellanic Cloud globular clusters, as reported by Caldwell & Bothun (1987), seem to argue for the latter interpretation although, clearly, only via spectroscopy can one shed light on the true nature of these point sources.

FCCB729

FCCB729 has an extended emission region in the centre, with faint extensions towards the west, along the galaxy's major axis, and towards the north, along its minor axis. The emission peak coincides with the galaxy's central nucleus.

4.2.6 Conclusions

Ionisation mechanisms

Combining the results of this chapter and Paper 1, we find different ionised gas morphologies in these galaxies. This morphological diversity could also indicate a diversity in ionising processes. All nucleated dEs in our sample, i.e. FCC046, FCC207 (Paper 1) and FCCB729 have an emission peak coinciding with their central nucleus, while the non-nucleated dEs lack such a bright central emission, suggesting a physical connection between the central emission and the presence of a nucleus. We are planning follow-up spectroscopy for these objects in order to identify the ionisation mechanism in the central regions (active galactic nucleus (AGN), starburst, post-AGB stars,...). The discovery of an AGN in a bona-fide dE would be of considerable interest for theories of the formation and evolution of dEs and their nuclei. Up to now, only one AGN in a dE has been reported: Barth et al. (2004) show evidence for a Seyfert 1 nucleus in the bright dE/faint E POX 52, its classification as either a dE or E made uncertain by its low Sérsic shape parameter $n = 0.28$, which means the galaxy is well described by a de Vaucouleurs profile, and its high luminosity. On the other hand, its position in the Fundamental Plane argues for a dE classification.

In three dEs of our sample (FCC032, FCC046 and FCC206) the emission comprises several emission clouds that argue for recent or ongoing star formation (H II clouds, SNRs,...). In particular the ionised gas complex in FCC032 is similar to those observed in star-forming dwarf irregulars. Such dEs could be descendants of more fiercely star-forming dwarf galaxies, such as Blue Compact Dwarfs, which are not (or no longer) present in the Fornax Cluster. The fact that the number density of dEs with Hα or H I emission declines as a function of radius within their host cluster (Drinkwater et al., 2001; Conselice et al., 2003a), indicates that environmental agents, such as ram-pressure stripping or gravitational interactions, play a very important role in the gas-depletion process.

Formation of the central nucleus

FCC206 is a non-nucleated dE but it contains 4 non-resolved star clusters, two of which show Hα emission. These knots have blue colours and luminosities comparable to globular clusters, which tempted Caldwell & Bothun (1987) to suggest we are witnessing the formation of a nucleus. This corroborates one currently popular hypothesis concerning the formation of nuclei in dEs, namely the merger of globular clusters that have been driven inward by dynamical friction (Oh & Lin (2000), Lotz et al. (2001)). Mouri & Taniguchi (2003) have estimated the orbital decay timescale of a typical globular cluster of mass $M \sim 10^6\,\mathrm{M}_\odot$, starting at a radius of about 1 kpc in a dwarf galaxy with a circular velocity of order $50 - 100\,\mathrm{km\,s}^{-1}$ at $1 - 5 \times 10^9$ yr. The tidal disruption timescale is much longer so a globular cluster would not dissolve before reaching the galaxy centre where it adds its stars to the nucleus. If the point sources near the centre of FCC206 are truly globular clusters belonging to this dE, their projected distances of the order of 100 pc would imply the formation of a nucleus within the next 10^8 yr. Nucleated dEs, after being stripped from their stellar envelope by tidal forces during gravitational interactions, have been suggested as possible progenitors of both the recently discovered ultra compact dwarfs (Phillips et al., 2001) and of massive globular clusters like ωCen (Gnedin et al., 2002) and G1 in M31 (Meylan et al., 2001).

Intermediate-mass black holes (IMBHs), with masses of the order $M_\bullet \sim 10^3\,\mathrm{M}_\odot$, are predicted to grow in dense star clusters (Portegies Zwart & McMillan, 2002). According to this scenario, a massive black hole will grow in the nucleus of the host dE by the coalescence of several globular cluster IMBHs. If globular clusters contain massive black holes (e.g. Gebhardt et al. (2002), Gerssen et al. (2002)), which is still debated, and the nuclei in dE,Ns form from merging globular clusters, these nuclei could be expected to contain super-massive black holes (SMBHs). Thus understanding how the nuclei of dE,Ns form may also help us understand how SMBHs grow.

Table 4.1: Photometric parameters of FCC032, FCC201, FCC206 and FCCB729

name	Type	m_R (mag)	$R_{\rm eff}$ (arcsec)	$\langle\mu\rangle_{\rm eff}$ (mag arcsec^{-2})	r_0 (1) (arcsec)	μ_0 (1) (mag arcsec^{-2})	n (1)	r_0 (2) (arcsec)	μ_0 (2) (mag arcsec^{-2})
FCC032	dE2	14.52	7.59	20.92	1.41	18.69	0.64	5.52	20.28
FCC201	dE4	16.04	9.82	23.00	9.15	22.36	1.32	6.20	21.87
FCC206	dE0	15.02	15.86	23.01	15.33	22.43	1.33	10.64	22.02
FCCB729	S0(7),N	15.15	7.21	21.44	5.19	20.71	1.04	4.84	20.62

Galaxy type as classified by us, total de-reddened R-band magnitude m_R, half-light radius $R_{\rm eff}$, and effective surface brightness $\langle\mu\rangle_{\rm eff}$. (1): parameters of the Sérsic profile that best fits the surface brightness profile: scale-length r_0, extrapolated central R-band surface brightness μ_0, and shape-parameter n; (2): parameters of the best fitting exponential profile: scale-length r_0 and extrapolated central R-band surface brightness μ_0.

Table 4.2: Emission properties of FCC032, FCC206 and FCCB729.

name	$F_{\rm em}$ $10^{-18}\,{\rm W\,m^{-2}}$	$L_{\rm em}$ $h_{75}^{-2}\times10^{31}\,{\rm W}$	$F_{\rm H\alpha}$ $10^{-18}\,{\rm W\,m^{-2}}$	$L_{\rm H\alpha}$ $h_{75}^{-2}\times10^{31}\,{\rm W}$	SFR $h_{75}^{-3}\times10^{-3}\,{\rm M_\odot\,yr^{-1}}$	$M_{\rm H\,II}$ $h_{75}^{-2}\,{\rm M_\odot}$
FCC032	19.3 – 22.0	7.81 – 8.90	19.3 – 6.00	2.43 – 7.81	17.5 – 5.5	570 – 1850
FCC206	6.17 – 7.17	2.50 – 2.90	1.96 – 6.17	0.79 – 2.50	1.8 – 5.6	190 – 590
FCCB729	6.21 – 7.33	2.51 – 2.96	2.00 – 6.21	0.81 – 2.51	1.8 – 5.6	190 – 600

4.3 H I observations

4.3.1 Introduction

In this section, we present new H I 21 cm line observations of two Fornax dEs, obtained with the Australia Telescope Compact Array (ATCA). With optical systemic velocities $v_{\rm sys} = 1318 \pm 26\,{\rm km\,s^{-1}}$ (FCC032) and $v_{\rm sys} = 1956 \pm 67\,{\rm km\,s^{-1}}$ (FCC336) (Drinkwater et al., 2001), these dEs are bona fide members of the Fornax Cluster, located in the sparsely populated outskirts of the cluster (see Fig. 4.10). In subsection 4.3.2, we present our H I observations, followed by a discussion of our results in subsection 4.3.3. We summarize our conclusions in subsection 4.3.4.

4.3.2 H I observations

We first observed FCC032 with the Australia Telescope Compact Array (ATCA) in May 2003 for a total of ≈ 4 hours. The array configuration used was the EW352, and an 8 MHz-wide band was centered upon 1413 MHz. The number of channels used was 512, giving a frequency resolution of 15.6 kHz, equivalent to 3.3 ${\rm km\,s^{-1}}$per channel. Sources 1934-638 and 0438-436 were also observed, the former for flux and bandpass calibration, and the latter for phase and gain calibration. All data reduction was carried out using MIRIAD. We detected no H I gas in FCC032 and derived an upper H I mass limit for the galaxy using:

$$M_{\rm HI} = 2.356 \times 10^5 D^2 \int S(v)\,dv\,{\rm M_\odot}, \tag{4.14}$$

where $M_{\rm HI}$ is the H I mass, D is the distance to the galaxy in Mpc, and $\int S(v)\,dv$ is the integrated flux in Jy ${\rm km\,s^{-1}}$. Assuming a velocity width of the galaxy of 50 ${\rm km\,s^{-1}}$, a 3σ detection would have an upper H I mass limit of $7.1 \times 10^7\,{\rm M_\odot}$.

We therefore used the Australia Telescope Compact Array on 20 and 23 December 2004 to observe FCC032 and FCC336, another Fornax Cluster dE. We preferred interferometry observations above single-dish observations to avoid confusion with other galaxies that can be located within the large beam, which is a common nuisance in crowded environments such as the Fornax Cluster. The observations were made during night time to avoid solar interference. We used the ATCA in the 1.5D configuration, with baselines ranging from 107 m to 4439 m. To be able to detect H I emission in three independent channels and since both sources had an estimated velocity width of about 50 ${\rm km\,s^{-1}}$, we selected a correlator setup that yielded 512 channels of width 15.6 kHz. To increase the signal-to-noise ratio the data were on-line Hanning smoothed which resulted in a velocity resolution of $6.6\,{\rm km\,s^{-1}}$. At the start of each observation we observed the source 1934-638 as primary calibrator for 15 minutes. The source 0332-403 was observed every 40 minutes for 5 minutes as a secondary calibrator. The total integration time (including calibration) for each galaxy was 12 hours. The usual data reduction steps (phase, amplitude and bandpass calibration) were performed with the MIRIAD package (Sault et al., 1995), the standard ATCA data analysis program. We subtracted the continuum by performing a first order fit to the visibilities over the line-free channels which were not affected by the edge effects of the band (selected in advance by eye). The data cubes were created by using natural weighting and were subsequently tapered with a Gaussian beam of $1' \times 1'$ (which corresponds to the optical spatial radius of our sources) and off-line Hanning smoothed to increase the signal-to-noise. The final data cubes had a spectral resolution of $13.3\,{\rm km\,s^{-1}}$. Due to the faintness of these objects, we did not attempt a deconvolution of our images.

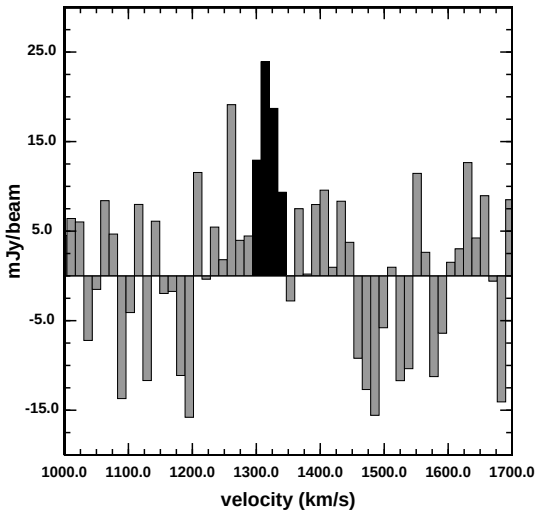

Figure 4.11: H I profile of FCC032, obtained by summing the flux within a $2' \times 2'$ box around the optical center of the galaxy. The channels containing the 21 cm emission of FCC032 are colored in black.

FCC032

FCC032 was selected as a suitable target because it was known to contain a sizable ionised ISM (see Section 4.2). This galaxy harbours a large ionised gas complex, about 850 pc across, containing star-formation regions and bubble-shaped gaseous filaments, probably supernova remnants. This offers strong evidence for recent or ongoing star formation in this dE.

Our final data cube had a synthesised beam of $87.56'' \times 55.55''$ due to the Gaussian tapering, resulting in a noise of 4 mJy/beam. To derive a spectrum, we summed the flux within a $2' \times 2'$ box entered on the optical position of FCC032. This resulted in a detection of the galaxy near the optical systemic velocity of $1318\,\mathrm{km\,s^{-1}}$, spread over 4 channels (see Fig. 4.11).

We fitted a Gaussian to the global H I profile and adopted the method of Verheijen & Sancisi (2001) to measure the systemic velocity and line widths at the 20% and 50% levels (corrected for broadening and random motions). We applied the instrumental correction given by the formulae

$$W_{20} = W_{20,\mathrm{obs}} - 35.8\left[\sqrt{1+(R/23.5)^2}-1\right], \quad (4.15)$$

$$W_{50} = W_{50,\mathrm{obs}} - 23.5\left[\sqrt{1+(R/23.5)^2}-1\right], \quad (4.16)$$

with R the velocity resolution or $13.3\,\mathrm{km\,s^{-1}}$ in our case. This correction is based on approximating the edges of the global profile, which are mostly due to turbulent motion, with a Gaussian of dispersion $10\,\mathrm{km\,s^{-1}}$. The results show a maximum flux of 0.314 Jy/beam at a velocity of $1318\,\mathrm{km\,s^{-1}}$, which we adopt as the radio systemic velocity of FCC032 and which is in excellent agreement with the optically derived systemic velocity (Drinkwater et al., 2001). For the widths at 20% and 50% we found respectively $52\,\mathrm{km\,s^{-1}}$ and $34\,\mathrm{km\,s^{-1}}$.

By summing the flux within the 4 channels that contain the 21 cm emission of FCC032, we created a total H I intensity map (see Fig. 4.12). The noise at a certain position in the total intensity map can

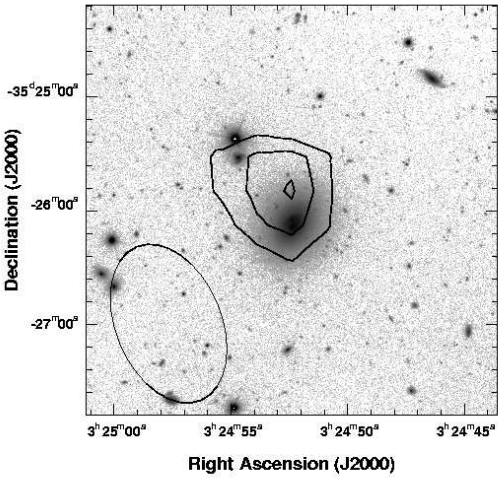

Figure 4.12: Total H I intensity map (contours) of FCC032 on top of an R-band grey-scale image (obtained with FORS2, VLT). The contours correspond to the $2\sigma_N^h$, $2.33\sigma_N^h$, $2.66\sigma_N^h$ and $3\sigma_N^h$ levels with $\sigma_N^h = 0.11\,\mathrm{Jy/beam\,km\,s^{-1}}$ (see eq. (4.17)). The beam is plotted in the lower-left corner.

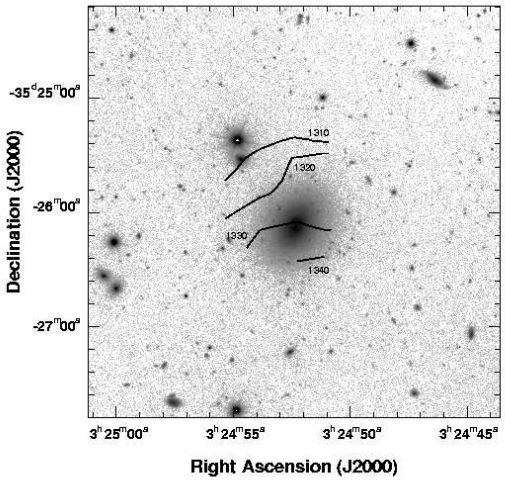

Figure 4.13: H I intensity-weighted velocity field of FCC032 (contours) on top of an R-band grey-scale image (obtained with FORS2, VLT). The contours are labeled with the velocity in $\mathrm{km\,s^{-1}}$.

be calculated by means of the formula (Verheijen & Sancisi, 2001)

$$\sigma_N^h = \left(\frac{N}{2} - \frac{1}{8}\right)^{\frac{1}{2}} \frac{4}{\sqrt{6}} \sigma^h \tag{4.17}$$

where N stands for the number of channels that have been added at that position (typically, $N = 3$ in this case) and with σ^h the noise in the Hanning smoothed channel maps (4 mJy/beam or 53.2 mJy/beam km s^{-1}). This yields $\sigma_N^h \approx 0.11$ Jy/beam km s^{-1}. We rebinned the channels plotted in Fig. 4.11 by taking together 4 adjacent channels, such that all the 21 cm flux of FCC032 ends up in one single bin, 53.2 km s^{-1} wide, and then calculated the rms noise from the other bins. This way, we find a total velocity integrated H I flux density of 0.66 ± 0.22 Jy km s^{-1} and calculated a total estimated H I mass of $5.2 \pm 1.8 \times 10^7 h_{75}^{-2}$ M$_\odot$, based on the W$_{20}$ velocity width by means of the formula:

$$M_{\rm H\,I} = 2.36 \times 10^5 \, D^2 \int S(v) dv \, \mathrm{M}_\odot \tag{4.18}$$

with $D = 18.4\, h_{75}^{-2}$ Mpc the distance to the Fornax cluster and $\int S(v)dv$ the total flux density in units of Jy km s^{-1}. Note that this mass estimate is slightly different than in Buyle et al (2005) because they used a distance of 18 Mpc. The H I intensity-weighted velocity field of FCC032 is presented in Fig. 4.13.

FCC336

FCC336 was selected according to its position in the outskirts of the Fornax cluster and thus, in accordance with the ram-pressure stripping theory, could be expected to harbor a relatively large amount of neutral hydrogen. Gaussian tapering was again applied to the data cube to increase the signal-to-noise ratio, resulting in a synthesised beam of $110.60'' \times 82.13''$ and a noise of 4 mJy/beam. We summed the flux within a $2' \times 2'$ box centered on the optical position of the galaxy in order to create a global H I profile of the galaxy. We found a strong intensity peak of 0.469 Jy/beam at a velocity of 2003 km s^{-1} (see Fig. 4.14), which is in fair agreement with the optical systemic velocity of 1956 ± 67 km s^{-1} (Drinkwater et al., 2001). A total H I intensity map shows that the emission, allowing for the coarse resolution of the H I map, coincides spatially with the optical image of the galaxy (see Fig. 4.15). We fit a Gaussian to the global H I profile and find a velocity width of 31 km s^{-1} and 20 km s^{-1} at respectively the 20% and 50% levels. We measure a total H I flux density of 0.28 ± 0.08 Jy km s^{-1}, which, by means of formula (4.18), corresponds to an estimated total H I mass of $2.1 \pm 0.6 \times 10^7 h_{75}^{-2}$ M$_\odot$. Here, we use the summed rms of 0.14 Jy/beam within the $2' \times 2'$ box and the W$_{20}$ velocity width. Due to our velocity resolution of 13.3 km s^{-1} and the very small velocity width of FCC336, we did not attempt constructing an H I intensity-weighted velocity field.

4.3.3 Discussion

In Fig. 4.16, we plot the B-band luminosities of FCC032 and FCC336 versus their H I masses, along with the Virgo dEs compiled by Conselice et al. (2003a), the Local Group dEs NGC185 and NGC205 (Young & Lo, 1996, 1997), the Local Group dwarf spheroidals (dSphs) and dwarf irregulars (dIrrs), taken from Mateo (1998), and Virgo Cluster BCDs and late-type dwarf galaxies (Sd-Sm-Im), taken from Gavazzi et al. (2005). We included only those galaxies in this diagram that were actually detected at 21 cm. Clearly, BCDs and dIrrs seem to trace a sequence, defined roughly by the relation $\log(L_B) \approx \log(M_{\rm H\,I})$. The Local Group dSphs and the Local Group dEs NGC185 and NGC205 (both are satellites of M31) deviate from this sequence by being gas deficient. Non-detections at 21 cm were not plotted in this figure. Hence, many undetected gas-poor dwarf galaxies (like NGC147, with a 3σ upper limit of 3×10^3 M$_\odot$

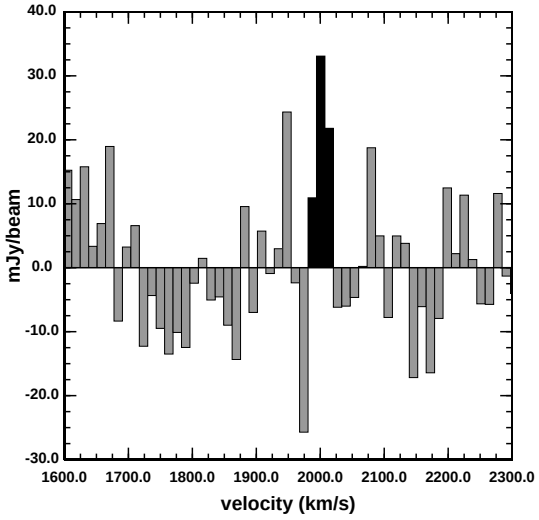

Figure 4.14: H I profile of FCC336, obtained by summing the flux within a $2' \times 2'$ box around the optical center of the galaxy. The channels containing the 21 cm emission of FCC336 are colored in black.

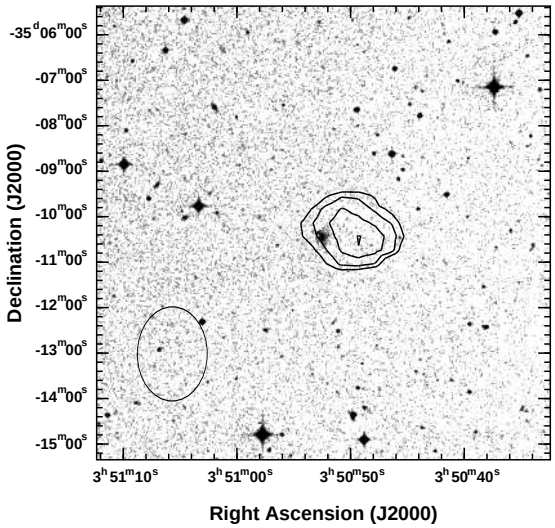

Figure 4.15: Total H I intensity map (contours) of FCC336 on top of an optical SDSS image (grey-scale). The contours correspond to the $2\sigma_N^h$, $2.33\sigma_N^h$, $2.66\sigma_N^h$, $3\sigma_N^h$ and $3.33\sigma_N^h$ levels, with $\sigma_N^h = 0.11\,\mathrm{Jy/beam\,km\,s^{-1}}$ (see eq. (4.17)). The beam is plotted in the top-left corner.

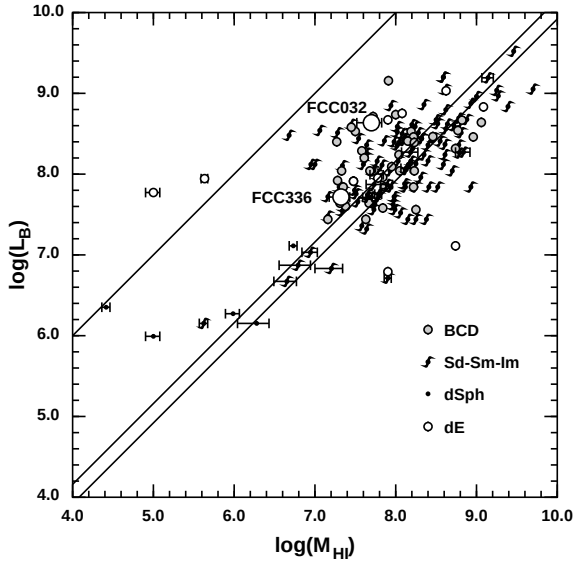

Figure 4.16: B-band luminosity (in $L_{\odot,B}$) versus H I mass (in $\mathrm{M}_{\odot}$). Large white circles indicate FCC032 and FCC336; small white circles correspond to Virgo dwarf ellipticals, except for the two leftmost white circles, which are NGC185 and NGC205. The small grey dots are Virgo Cluster BCDs. Late-type dwarfs (Sd-Sm-Im) in the Local Group and the Virgo Cluster are indicated by spiral symbols. Black dots correspond to Local group dwarf spheroidals. Full lines trace the sequences predicted by simple chemical evolution models for various star-formation efficiencies (see text).

for $M_{\mathrm{H\,I}}$ (Young & Lo, 1997), or the 20 Virgo dEs that were not detected by Conselice et al. (2003a), with mass upper limits of $\sim 8\times10^6\,\mathrm{M}_{\odot}$) are expected to occupy the left part of the diagram. Therefore, the L_B vs. $M_{\mathrm{H\,I}}$ sequence of gas-rich dwarf galaxies in Fig. 4.16 is best seen as a boundary, enclosing the most H I-rich galaxies while many gas-poor dwarfs (like dEs and dSphs) lie significantly to the left of this sequence.

Chemical evolution of dwarf galaxies

In order to interpret this diagram, we overplotted the observed data points with theoretical predictions for the $\log(L_B)$ vs. $\log(M)$ relation, based on the analytical models of Pagel & Tautvaišienė (1998) for the chemical evolution of the Large and Small Magellanic Clouds. In the formalism of these models, galaxies are formed by the infall of pristine gas. Stars are born at a rate proportional to the gas mass and supernova explosions eject gas at a rate proportional to the star-formation rate (SFR). The build-up of the elemental abundances is calculated using the delayed-recycling approximation in order to include the contribution of SNIa. We used the B-band mass-to-light ratios of single-age t, single-metallicity Z stellar populations (or SSPs), denoted by $\Upsilon^*_B(Z,t)$, presented by Vazdekis et al. (1996), in order to calculate the present-day $L_B/M_{\mathrm{H\,I}}$ ratio as

$$\frac{L_B}{M_{\mathrm{H\,I}}}(T) = \frac{1}{g(T)}\int_0^T \frac{\omega g(T-t)}{\Upsilon^*_B(Z(T-t),t)}dt \tag{4.19}$$

with $T = 13\,\mathrm{Gyr}$ the assumed age of the galaxies, $g(t)$ the gas mass at time t, and ω the star-formation efficiency (or the inverse time-scale for star formation). The time-dependence of g and Z is taken

from Pagel & Tautvaišienė (1998) (their equations (6), (8), (11), and (14)). The rightmost curve in Fig. 4.16 corresponds to parameter values fine-tuned to reproduce the elemental abundances observed in the LMC; the middle curve corresponds to the SMC. Clearly, these simple models nicely reproduce the observed locus of the gas-rich dwarf late types, BCDs, and dEs. Hence, it seems that continuous, slow star formation that does not exhaust all available gas within a Hubble time is the rule for these galaxies.

Enhanced star-formation rate Using the same formalism, one can produce more gas-poor systems by raising the star-formation efficiency ω. For instance, interactions may have sped up the gas-depletion process (van Zee et al., 2004), explaining both the abundance of gas-poor dEs and the paucity of gas-rich BCDs/dIrrs in high-density environments. E.g., the leftmost curve in Fig. 4.16 corresponds to a model with a star-formation efficiency that is a factor of 3 higher than in the LMC model. This way, one can reproduce the locus of gas-poor dwarf galaxies such as the Local Group dwarf dSphs. All models presented in Fig. 4.16 have luminosity-weighted mean metallicities in the range [Fe/H]$= -0.65$ to -0.4. The models with a high SFR consume their gas reservoir in a strong starburst at an early epoch, when the gas was not yet enriched with metals, and hence do not have significantly higher mean metallicities than the low SFR models (although they do contain a sprinkling of recently formed metal-rich stars which are absent in low SFR models). As discussed in Grebel (2000), dSphs indeed have more metal-rich red giants than dIrrs and show evidence for a more vigorous early enrichment than dIrrs.

Enhanced gas-ejection efficiency Raising the gas-ejection efficiency can also enhance the $L_B/M_{\rm H\,I}$ ratio although, at the same time, it significantly lowers the mean metallicity by effectively terminating further star-formation after the first star-forming event (e.g. making the gas-ejection by supernovae 30 times as efficient as in the Magellanic Clouds leads to $L_B/M_{\rm H\,I} \approx 3.3$ and [Fe/H]≈ -1.6). However, the star-formation histories of the Local Group dSphs seem rather continuous (with the exception of the Carina dSph) and show no evidence for major starbursts which would be able to expel significant amounts of gas (Grebel, 2000). On the other hand, a centralised star-burst event in a round galaxy is much more efficient at transferring energy to the ISM (and hence at expelling gas out of a galaxy) than a similar star-burst in a disk galaxy since, in the latter case, the hot supernova-driven gas can break through the disky ISM along the minor axis (Ferrara & Tolstoy, 2000; MacLow & Ferrara, 1999; De Young & Heckman, 1994). Hence, this suggests that rotationally flattened galaxies, such as dwarf late-types, indeed have lower gas-ejection efficiencies than dEs and dSphs. The metallicity-flattening relation observed in dEs (Barazza & Binggeli, 2002), with more flattened dEs tending to be less metal-rich, seems to indicate that in flattened dEs, individual supernova-explosions or star-formation sites are better able to eject the hot, enriched gas via a chimney perpendicular to the disk, without appreciably affecting the surrounding ISM, than in round dEs. This leads to flattening as a second parameter in controlling a dE's metallicity besides total mass.

External gas-removal mechanisms Hydrodynamical simulations of dwarf galaxies moving through the hot, rarefied intracluster medium show that ram-pressure stripping can completely remove the ISM of a low-mass dwarf galaxy (Mori & Burkert, 2000; Vollmer, 2003; Marcolini et al., 2003; Michielsen et al., 2004b) (see also chapter 6). Interactions and ram-pressure stripping are most efficient at removing gas from galaxies near the cluster center. Hence, the gas-rich dwarf galaxies in the Virgo cluster tend to have positions towards the outskirts of the cluster (e.g. Conselice et al. (2003a)), suggesting that they are recent acquisitions of the cluster or are moving on orbits that avoid the cluster center. In a spectroscopic survey of the Fornax Cluster, Drinkwater et al. (2001) discovered Hα emission in about 25 per cent of the dEs. Again, most of these galaxies lie towards the cluster periphery, while dEs near

the center of the cluster are generally devoid of ionized gas. Likewise, both H I-rich dEs presented in this chapter are located in the sparsely populated outskirts of the Fornax cluster.

4.3.4 Conclusions

Based on our H I 21 cm observations of dEs in the Fornax Cluster and on H I 21 cm observations of dEs, BCDs, and late-type dwarf galaxies in the Virgo Cluster (Conselice et al., 2003a; Gavazzi et al., 2005), and the Local Group dwarfs (Mateo, 1998), we conclude that the gas-content of the most gas-rich dwarf galaxies is consistent with a continuous, slow star-formation history. After one Hubble time, these galaxies still have a large gas reservoir left and roughly trace a sequence defined by the relation $\log(L_B) \approx \log(M_{\rm H\,I})$. However, the majority of the dwarf spheroidals and dwarf ellipticals contain significantly less gas than predicted by this relation. External gas-removal mechanisms such as a star-formation rate enhanced by gravitational interactions or ram-pressure stripping can account very well for the existence of these gas-poor systems. Such external mechanisms will act most vigorously in high-density environments, offering a natural explanation for the observed morphology-density relation (Goto et al., 2003), the trend for H I mass to increase with distance from the nearest massive galaxy (Grebel, 2000), and the fact that gas-rich dEs are observed predominantly in the outskirts of clusters.

Part II

N-body/SPH simulations

Chapter 5

The N-body/SPH code

5.1 Introduction

To simulate the evolution of a dynamical system consisting of stars, gas and dark matter, we use a numerical code. Two physically equivalent, but conceptually different approaches exist to describe the gravitational and hydrodynamical forces. On the one hand, the forces can be evaluated using a Lagrangian or *particle* approach, meaning that the motion of dark matter, gas and star particles in space is followed. This is opposed to using an Eulerian or *grid* approach, where field equations for the physical quantities are solved for fixed points in space or for grid cells.

At the beginning of this work, no gravitational (N-body) or hydrodynamical code was used in our research group. However, building such a code from scratch would imply time-consuming program design and testing. Moreover, several other institutes that have long-standing expertise in developing such codes offer their programs to be used freely by the astrophysical community. The advantage is that these codes are well tested and documented and one can start simulating real problems almost at once.

Because we wanted to look more in particular to interactions between gas and star particles through star formation, supernova feedback and chemical evolution processes, a Lagrangian approach is the most natural to adopt. Moreover, the Lagrangian formalism is independent of geometrical assumptions. We chose to use the publicly available HYDRA (version 4.2)[1] code (Couchman et al., 1995) as a starting point. This is a particle (Lagrangian) code that evaluates the gravitational forces with an N-body scheme using the Adaptive Particle-Particle-Particle-Mesh algorithm (AP^3M, Hockney & Eastwood (1987); Couchman (1991)), while the hydrodynamical equations for the gas are solved using the Smoothed Particle Hydrodynamics formalism (SPH, Monaghan (1992)). The HYDRA code has been extensively tested (Couchman et al., 1995) and has been used to perform simulations similar to the ones we are interested in (Schulz & Struck, 2001). We chose this code above the Barnes-Hut Tree code (Barnes & Hut, 1986) since it includes an implementation of SPH. During the course of this work, the GADGET code (Springel et al., 2001), which is a Tree+SPH code, was also made public.

In this chapter we introduce the physics at work and their implementation in the HYDRA code.

[1] http://coho.physics.mcmaster.ca/hydra/

5.2 The equation of motion

To follow a particle system in time, we have to solve the *equation of motion* for all particles $i = 1, \ldots, N_p$

$$\frac{\mathrm{d}^2 \boldsymbol{x}_i}{\mathrm{d}t^2} = \boldsymbol{a}_i = \frac{1}{m_i}\boldsymbol{F}_i, \tag{5.1}$$

with $\boldsymbol{x}_i$, $\boldsymbol{a}_i$ and m_i the position, the acceleration and the mass of the i-th particle, and $\boldsymbol{F}_i$ the force acting on that particle. For a self-consistent system, this force can in general be a function of all particles' positions and velocities, and of time, $\boldsymbol{F}_i = \boldsymbol{F}_i(\boldsymbol{x}_j, \boldsymbol{v}_j, t);\ j = 1, \ldots, N_p$. Of course there could also be external forces acting on the system.

The equations of motion are a set of N_p coupled second-order differential equations, which can be reduced to a set of $2N_p$ coupled linear differential equations

$$\begin{aligned} \frac{\mathrm{d}\boldsymbol{v}_i}{\mathrm{d}t} &= \boldsymbol{a}_i, \\ \frac{\mathrm{d}\boldsymbol{x}_i}{\mathrm{d}t} &= \boldsymbol{v}_i. \end{aligned} \tag{5.2}$$

We will consider *gravitational forces* acting on all particles that have mass, i.e. dark matter, gas and stars. The gas particles are also subjected to *hydrodynamical forces*.

5.3 Gravitational forces

5.3.1 The gravitational force

Gravitational forces act on all objects that have mass. The velocities we encounter in simulations of galaxy formation, and even in most cosmological simulations, are low compared to the speed of light. Therefore the Newtonian description of gravity is best suited, i.e. we do not need special or general relativity. The Newtonian gravitational force $\boldsymbol{F}_{ij}$ from particle j acting on particle i is:

$$\boldsymbol{F}_{ij} = \frac{G m_i m_j (\boldsymbol{x}_j - \boldsymbol{x}_i)}{|\boldsymbol{x}_j - \boldsymbol{x}_i|^3}, \tag{5.3}$$

with G the gravitational constant, and m and $\boldsymbol{x}$ the mass and position of the particles, respectively. Note that this force only dependents on the particles' positions. Such a force is said to be *conservative*.

The *gravitational potential energy* Φ_{ij} of particle i, in the presence of particle j is given as

$$\Phi_{ij} = \frac{G m_i m_j}{|\boldsymbol{x}_j - \boldsymbol{x}_i|}. \tag{5.4}$$

Forces and potentials are additive quantities, so the total force acting on particle i (in the absence of external forces) is

$$\boldsymbol{F}_i = \sum_{j=1}^{N_p} \boldsymbol{F}_{ij}, \tag{5.5}$$

and its potential energy is

$$\Phi_i = \sum_{j=1}^{N_p} \Phi_{ij}. \tag{5.6}$$

Regarding the force and potential as *field quantities*, the gravitational potential energy field is linked to the gravitational force field in the following way

$$\boldsymbol{F}(\boldsymbol{x}) = -\boldsymbol{\nabla}\Phi(\boldsymbol{x}). \tag{5.7}$$

The gravitational potential field generated by a *density distribution* $\rho(\boldsymbol{x})$ can also be obtained from the *Poisson equation*

$$\boldsymbol{\nabla}^2\Phi(\boldsymbol{x}) = 4\pi G\rho(\boldsymbol{x}). \tag{5.8}$$

In many situations, the best way to obtain $\boldsymbol{F}$, is to calculate the gravitational potential first and then to take its gradient to obtain the force at a position $\boldsymbol{x}$.

5.3.2 N-body models

There exist several ways to implement the gravitational forces in an N-body code. The simplest is the Particle-Particle (PP) model that uses the *action at a distance* formulation of the force law. The Particle-Mesh (PM) model instead exploits the *force at a point* formulation of the force law and a field equation for the potential, approximated on a grid of mesh. The hybrid Particle-Particle-Particle-Mesh (P^3M) method combines the advantages of the two previous methods. The Adaptive P^3M (AP^3M) method uses *mesh refinements* in heavily clustered regions. Finally, there also exist Tree methods that arrange the particles in a tree structure.

The Particle-Particle method (PP)

This method is the computationally and conceptually simplest way to implement the gravitational forces (equation (5.3)) between all particle pairs. A system of N_p (equal-mass) particles is completely described by the positions and velocities of the particles. At each time t, the interaction force is calculated for each particle pair. Then, the equations of motion are used to obtain the positions and velocities for each particle at a later time $t + dt$. Repeated application of this loop is used to follow the temporal evolution of the system.

Calculating the direct forces $\boldsymbol{F}_{ij}$ for each particle pair (i, j) (with $i, j = 1, \ldots, N_p$) requires of the order of N_p^2 (denoted as $O(N_p^2)$) computations per time step, thus prohibiting the use of large numbers of particles in simulations. Several solutions to this problem are being employed. The most drastic is the design of special-purpose hardware such as GRAPE (for GRAvity PipE) which is optimized to perform direct summation of inverse-square-distance forces. GRAPE machines are being used by some supercomputing centres (Hut & Makino, 1999).

The Particle-Mesh method (PM)

Instead of using brute force, the computational cost can be reduced using special algorithms. One such algorithm is the Particle-Mesh (PM) method, that exploits the field equation for the gravitational potential (equation (5.7)). The result is a much faster, but generally less accurate, force calculation than is achieved by the PP method.

The PM force calculation consists of three steps. Firstly, a regular (Cartesian) mesh or grid is defined over the simulation box and masses are attributed to the grid cells. Secondly, the gravitational potential at the centres of the cells (mesh points) is computed. Finally, the potential and forces at the particle positions are interpolated from the mesh.

The computational cost of the first and the third step is proportional to the number of particles N_p, while the computational cost of the second step obviously depends on the number of mesh points N_m.

Generally, the number of mesh points is chosen to match the number of particles. Direct calculation of the gravitational potential in each mesh point involves all other mesh points, resulting in a computational cost of $O(N_m^2)$, which clearly isn't much of an advantage over the PP method if $N_m \approx N_p$. However, if the Poisson equation (5.8) is solved in Fourier space, we can use the *Fast Fourier Transform* (FFT) to reduce the number of computations to $O(N_m \log_2(N_m))$, provided that the cube root of the number of mesh points is a power of 2 (or $N_m = L^3$ and $L = 2^m$ for some integer m). This means an enormous speed gain over the PP method. In Appendix A, a detailed account is given on how a computational gain can be achieved by using the FFT.

However, the speed gain of the PM method is obtained at a loss of resolution in the force and potential fields. Only those potential variations that have a wavelength longer than the mesh spacing are accurately represented by mesh values. In other words, the gravitational forces on a particle $\boldsymbol{p}_i$ obtained by the PM method are only accurate if the particle density is nearly constant in the cells near to $\boldsymbol{p}_i$.

Consequently, the potential and force fields of a single point mass are poorly represented on the mesh for distances less than the mesh spacing. Making the mesh fine enough to resolve close encounters of particles would involve so many mesh points that the speed gain over the PP method would be lost. On the other hand, the inaccurate representation of a point mass on the mesh can be interpreted as an accurate representation of a finite-sized cloud with width of the order of the mesh spacing.

The Particle-Particle Particle-Mesh method (P^{3}M)

As we have seen, the PP method should only be used for small systems with long-range forces. However, it can be used for large systems, if the forces of interaction are nonzero for only a few interparticle distances. In this case the operations count will scale as $O(N_n N_p)$, with N_n the average number of particles that contribute to the force. The PM method on the other hand, is computationally fast, but can only handle smoothly varying forces. The P^{3}M method combines the advantages of both methods to enable large systems with long-range forces to be simulated.

The trick used is to split the interparticle force $\boldsymbol{F}_{ij}$ in a short-range, rapidly varying part and a long-range, smoothly varying part

$$\boldsymbol{F}_{ij} = \boldsymbol{F}_{ij}^{\mathrm{sr}} + \boldsymbol{F}_{ij}^{\mathrm{m}}. \tag{5.9}$$

The PP method is then used to compute the rapidly varying short range forces $\boldsymbol{F}_{ij}^{\mathrm{sr}}$, which are nonzero for interparticle distances $r < r_e$ for a certain radius r_e, so that only a few neighbouring particles contribute to this part. The PM method is used to compute the slowly varying part of the force $\boldsymbol{F}_{ij}^{\mathrm{m}}$, which is smooth enough so that it can be accurately represented on the mesh. The resulting P^{3}M scheme falls between the PP and PM methods in that it can represent close encounters as accurately as the PP method and calculate long-range forces as rapidly as the PM method.

The splitting of the forces can be implemented as follows. Suppose we use the Newtonian gravity law to model the forces between two unit-mass point sources. Consider the following smoothing: the point sources are approximated as spheres with uniform density and diameter b. The force between two such spheres is directed along the line joining the centres of the spheres and is given by (Hockney & Eastwood, 1987)

$$F'(r) = G \begin{cases} \frac{1}{b^2}\left(\frac{8r}{b} - \frac{9r^2}{b^2} + \frac{2r^4}{b^4}\right) & 0 \leqslant r < b \\ \frac{1}{r^2} & b \leqslant r \end{cases}. \tag{5.10}$$

Thus, one possible splitting of the force is to set r_e equal to b. The smooth part of the force, which will be represented by the mesh, is given by $F^{\mathrm{m}} = F'$ for all r, while the short-range part (nonzero only for $r < r_e$) is set to the difference between the inverse-square-law force and F'.

The operations count for the P^{3}M timestep loop consists of the part $O(N_p + N_m \log_2(N_m))$ for the PM part and integration of the equations of motion, and a part $O(N_n N_p)$ for the PP part. The number of neighbours N_n is given approximately by $4\pi b^3 n_0/3$, where n_0 is the mean particle density. Thus it is possible to reduce the computational cost to $O(N_m \log N_m + N_p(1 + N_n))$ if all particles have N_n neighbours in the short-range force calculation.

The Adaptive Particle-Particle Particle-Mesh method (AP^{3}M)

The P^{3}M method is very advantageous when the particle density throughout the simulation box remains roughly constant. However, if there are large density contrasts, the number of particles in certain cells can become very large and most of the calculation will be spent in the PP part, destroying the advantage of the fast PM calculation. This occurs, for example, in cosmological simulations under heavy clustering, or in simulations of galaxy collisions, where most of the simulation box is devoid of particles.

If we would simply increase the overall number of grid cells in order to reduce the number of particles per cell in clustered regions, the calculation for large volumes of the simulation box that are almost devoid of particles would be unneeded and exceedingly costly in computation time. Therefore it is better to refine the mesh only in those parts of the simulation box where the particle density becomes large enough. Such an *adaptive mesh* can account for clustering and large density gradients in the simulation. The resulting adaptive scheme is called the AP^{3}M method (Couchman, 1991). We will look at it in detail in Section 5.5.

The Tree method

An alternative approach to avoid direct summation of all particle pairs, is the Tree method. In this model, a particle tree is constructed by dividing the simulation box into recursively smaller cells, until each cell contains at most one particle. In this way a tree is constructed, where the leafs are represented by the particles and the branches are the nested cell centres originating from the root which is the centre of the entire simulation box. In three dimensions, each cell is divided into eight subcells, hence the particle tree is sometimes named the *octtree*.

The centre of mass of each cell is computed and the forces on the cells and particles are evaluated by direct summation. For a given particle, the nearest part of the tree will be explored in detail, while the farther branches of the tree are treated more coarsely by regarding the centre of mass of a far-away branch of particles as one massive superparticle. This method also allows the computational cost to be reduced to $O(N_p log(N_p))$ (Barnes & Hut, 1986).

The advantage of this technique is that it calculates the interparticle forces without going to the potential in Fourier space, thus it is completely gridless and allows for a more simple implementation. On the other hand, the particle tree has to be reconstructed in each timestep, which makes the method more memory- and time-consuming than the AP^{3}M approach.

5.4 Hydrodynamical forces

Apart from gravitational forces, fluids are also subjected to *hydrodynamical forces*. The state of a fluid is specified by its density ($\rho(\boldsymbol{x}, t)$), pressure ($P(\boldsymbol{x}, t)$), and velocity ($\boldsymbol{v}(\boldsymbol{x}, t)$) fields, and possibly by other thermodynamic functions such as the temperature ($T(\boldsymbol{x}, t)$), specific energy ($\epsilon(\boldsymbol{x}, t)$) or specific entropy ($s(\boldsymbol{x}, t)$).

5.4.1 Basic equations

The continuity equation

Consider an arbitrary closed volume V that is fixed in position and shape and bounded by a surface S. The fluid mass inside this volume is

$$M(t) = \int_V \rho(\boldsymbol{x}, t) d^3\boldsymbol{x}. \tag{5.11}$$

The mass $M(t)$ changes with time at a rate

$$\frac{\mathrm{d}M}{\mathrm{d}t} = \int_V \frac{\partial \rho}{\partial t} d^3\boldsymbol{x}. \tag{5.12}$$

Assuming that there are no mass sinks or sources in the volume, the rate of mass change is equal to the rate of mass flowing though the boundaries of the volume V. The mass flowing through the area element d^2S per unit time is $\rho\boldsymbol{v} \cdot \boldsymbol{n} d^2S$, where $\boldsymbol{n}$ is an outward-pointing unit vector, normal to the surface. Thus

$$\frac{\mathrm{d}M}{\mathrm{d}t} = -\int_S \rho\boldsymbol{v} \cdot \boldsymbol{n} d^2S \tag{5.13}$$

and hence

$$\int_V \frac{\partial \rho}{\partial t} d^3\boldsymbol{x} + \int_S \rho\boldsymbol{v} \cdot \boldsymbol{n} d^2S = 0. \tag{5.14}$$

Using the divergence theorem, we can write this as

$$\int_V \left[\frac{\partial \rho}{\partial t} + \boldsymbol{\nabla} \cdot (\rho\boldsymbol{v}) \right] d^3\boldsymbol{x} = 0, \tag{5.15}$$

and since this result must hold for any volume, we arrive at the *continuity equation*

$$\frac{\partial \rho}{\partial t} + \boldsymbol{\nabla} \cdot (\rho\boldsymbol{v}) = 0. \tag{5.16}$$

When mass sinks or sources are present in the volume, because of star formation, or supernova feedback, for example, these terms have to be taken into account in equation (5.16).

The equation of motion

We can write the equation of motion for the volume element V as

$$\boldsymbol{F} = \int_V \rho(\boldsymbol{x}) \frac{\mathrm{d}\boldsymbol{v}}{\mathrm{d}t} d^3\boldsymbol{x}. \tag{5.17}$$

In an inviscid and isotropic fluid, the total pressure force acting on the volume is given by

$$\boldsymbol{F} = -\int_S P(\boldsymbol{x}) \boldsymbol{n} d^2S. \tag{5.18}$$

Combining the previous two equations and applying the divergence theorem,

$$\int_V \left[\rho \frac{\mathrm{d}\boldsymbol{v}}{\mathrm{d}t} + \boldsymbol{\nabla} P \right] d^3\boldsymbol{x} = 0. \tag{5.19}$$

Considering this must hold for every volume V, and assuming that the density is nowhere zero, Newton's second law, for hydrodynamical forces only, reads

$$\frac{\mathrm{d}\boldsymbol{v}}{\mathrm{d}t} = -\frac{1}{\rho}\boldsymbol{\nabla}P. \tag{5.20}$$

In addition, there may be some external force, in particular the force resulting from a gravitational potential $\Phi(\boldsymbol{x}, t)$:

$$\frac{\mathrm{d}\boldsymbol{v}}{\mathrm{d}t} = -\frac{1}{\rho}\boldsymbol{\nabla}P - \boldsymbol{\nabla}\Phi. \tag{5.21}$$

We can now relate $d\boldsymbol{v}/dt$ to the velocity field $\boldsymbol{v}(\boldsymbol{x}, t)$. The change $d\boldsymbol{v}$ in velocity of a given particle during the interval dt is the sum of the change in velocity at a given point in space, $(\partial\boldsymbol{v}/\partial t)dt$, and the difference in velocities between two points separated by $d\boldsymbol{x} = \boldsymbol{v}dt$ at the same instant. The latter change is $(\partial\boldsymbol{v}/\partial x_i)dx_i = (d\boldsymbol{x}\cdot\boldsymbol{\nabla})\boldsymbol{v}$. Thus

$$\frac{\mathrm{d}\boldsymbol{v}}{\mathrm{d}t} = \frac{\partial\boldsymbol{v}}{\partial t} + (\boldsymbol{v}\cdot\boldsymbol{\nabla})\boldsymbol{v}, \tag{5.22}$$

the quantity $\frac{\mathrm{d}\boldsymbol{v}}{\mathrm{d}t}$ is sometimes referred to as the *Lagrangian* or convective derivative of $\boldsymbol{v}$ as opposed to the *Eulerian* derivative $\frac{\partial\boldsymbol{v}}{\partial t}$. The equation of motion can therefore also be written as

$$\frac{\partial\boldsymbol{v}}{\partial t} + (\boldsymbol{v}\cdot\boldsymbol{\nabla})\boldsymbol{v} = -\frac{1}{\rho}\boldsymbol{\nabla}P - \boldsymbol{\nabla}\Phi. \tag{5.23}$$

This equation is also known as *Euler's equation*.

We have neglected viscous forces in this derivation. In principle, the pressure term P comes from the *stress tensor* T, with elements

$$\mathsf{T}_{ij} = P\delta_{ij} + \Pi_{ij} \tag{5.24}$$

where δ_{ij} is the Kronecker δ and Π is the viscosity tensor. In the smoothed particle hydrodynamics formulation of the hydrodynamical equation, an form of *artificial viscosity* needs to be introduced in order to handle shocks.

The equation of state

In order to relate the pressure and density, we generally need an *equation of state* $P = P(\rho, s)$ or $P = P(\rho, T)$ together with an auxiliary equation determining the specific entropy or temperature. For the sake of simplicity, we consider the fluid as an *ideal gas*, whose equation of state is

$$P = \frac{\rho k_B T}{\mu m_p}, \tag{5.25}$$

where k_B is Boltzmann's constant, μ is the mean molecular weight and m_p is the proton mass. The pressure in an ideal gas is related to the velocity dispersion of the molecules in each direction by

$$P = \rho\overline{v_x^2} = \rho\overline{v_y^2} = \rho\overline{v_z^2}, \tag{5.26}$$

and thus

$$\overline{v_x^2} = \overline{v_y^2} = \overline{v_z^2} = \frac{1}{3}\overline{v^2} = \frac{k_B T}{\mu m_p}. \tag{5.27}$$

The energy equation

The *specific energy* of an ideal fluid is given by $\epsilon = \frac{3}{2}\frac{k_B T}{\mu m_p}$. The equation of state can then be written as

$$P = (\gamma - 1)\rho\epsilon, \tag{5.28}$$

with γ the ratio of specific heats, a parameter which depends on the particular gas being simulated. For mono-atomic gas, $\gamma = 5/3$, which is the value adopted everywhere.

The rate of change of specific energy under adiabatic conditions, originating from the change in pressure (the PdV work), is

$$\frac{\mathrm{d}\epsilon}{\mathrm{d}t} = -\frac{2}{3}\epsilon\,\boldsymbol{\nabla}\cdot\boldsymbol{v}, \tag{5.29}$$

which is called the *energy equation*. The change of specific energy is effected solely through the work performed by the gas in volume V on its surroundings, or vice versa. From this equation it is clear that collapsing regions ($\boldsymbol{\nabla}\cdot\boldsymbol{v} < 0$) will heat, while expanding regions ($\boldsymbol{\nabla}\cdot\boldsymbol{v} > 0$) will cool. Other processes that contribute to the energy equation, such as radiative cooling and thermal feedback from stars, should be taken explicitly into account using extra terms in the energy equation.

5.4.2 Hydrodynamical models

Smoothed Particle Hydrodynamics (SPH)

Smoothed Particle Hydrodynamics (SPH) is a Lagrangian model to describe the hydrodynamical equations. The fluid is modeled as *fluid particles* and a *smoothing kernel* is used to extend the particles in space. At each timestep, the local fluid properties are calculated by interpolation over nearby fluid particles. If the smoothing kernel has a compact support[2], this interpolation involves a finite number N_{sph} of neighbour particles. The extend of the smoothed particles is controlled by a *smooting length* h. Since the hydrodynamical equations only depend on the local fluid quantities, the SPH model is conceptually equivalent to the PP part of the P^{3}M gravity model. We will look at it in detail in Section 5.6.

The power of the SPH model is in its fully Lagrangian description and the relative ease of implementation. A particle treatment of gas in numerical simulations allows the movement of a particular gas particle to be followed over time. Moreover, it facilitates the inclusion of processes as star formation, energy feedback from supernovae and chemical evolution.

The main disadvantage of SPH is that physical quantities are smoothed out over some smoothing lengths. This means that large gradients cannot be very well represented by the SPH formalism. Especially shocks are poorly resolved by the SPH model.

Grid codes

Using the Eulerian description of the fluid equations, and the fact that all variables are in fact field quantities, the hydrodynamical equations can be solved for fixed volumes in space, on a grid. The use of a grid or mesh makes this model conceptually equivalent to the PM model. The quantities need not be smoothed over the grid cells, so that shocks can be resolved accurately. The drawback of the grid model is its dependence on the grid morphology. Similar as in PM models, adaptive refinements can be considered, resulting in AMR codes (Adaptive Mesh Refinement).

[2]Compact support means that the smoothing kernel becomes zero at a finite distance from the particle position.

Implementation of gravitational forces can be achieved by using a fluid description for gravity, as in the PM model. Star formation and feedback could in principle be modeled by introducing sinks and sources in the hydrodynamical equations, but is conceptually more difficult than in the SPH model.

5.5 The AP^{3}M algorithm

AP^{3}M is an extension of the P^{3}M algorithms, which are a class of hybrid algorithms developed by Hockney & Eastwood (1987). These algorithms allow large systems with long-range forces (e.g. gravitational forces) to be simulated in a reasonable timespan. The essence of the method is to express the interparticle force as the sum of two component parts: the short-range part $\boldsymbol{F}_{ij}^{\mathrm{sr}}$, which is non-zero for particle separations less than some cutoff radius r_e, and the smoothly varying part $\boldsymbol{F}_{ij}^{\mathrm{m}}$. The total short-range force on a particle $\boldsymbol{F}^{\mathrm{sr}}$ is computed by direct particle-particle (PP) pair force summation, while the total smoothly varying part $\boldsymbol{F}^{\mathrm{m}}$ is approximated by the particle-mesh (PM) force calculation.

Two meshes are employed in P^{3}M algorithms. The *density-potential* mesh and a coarser mesh, the *chaining mesh*. The density-potential mesh is used at different stages of the PM calculation to store in turn, mass density values, mass density Fourier transforms, potential Fourier transforms, and potential values. The chaining mesh is a regular array of cells whose sides have lengths greater than or equal to the cutoff radius r_e of the short-range force. The particles in the chaining mesh cells are arranged in a *linked list*, to locate pairs of neighbouring particles in the short-range calculation.

The force calculation proceeds as follows. First the PM force calculation is performed, by assigning densities to the density-potential mesh, then the Poisson equation is solved in Fourier space, and forces are derived from the resulting potential using a finite-difference scheme. Finally the mesh forces are interpolated on all particle positions. The PP force calculation begins with creating the linked lists of particles in the chaining mesh cells. Then the short-range force is obtained from the direct summation over all neighbouring particles. This PP part is completely separate from the PM force calculation and can be used by itself to compute interparticle forces in the absence of long-range forces (such as in Smoothed Particle Hydrodynamics, Section 5.4).

In the case of periodic boundary conditions, such as in cosmological simulations, the computationally costly problem of including periodic images that is present in direct summation methods disappears when P^{3}M is used. When the Fast Fourier Transform is used to solve for the potential, periodicity is automatically introduced into the mesh part of the force. Periodic images in the short-range part of the force are needed only for those particles within a distance r_e of the boundary of the computational box.

5.5.1 Gravitational softening

At small distances, the Newtonian gravitational force (equation (5.3)) diverges. Consequently, when two particles are very close to each other, the accelerations become very large, the velocities of point masses change rapidly, and extremely small time steps must be used in the numerical integration of the equations of motion, if this motion is to be followed accurately. This problem is known as *two-body relaxation*. To avoid large forces and accelerations, the gravitational interparticle force is *smoothed* or *softened*. This is equivalent to ascribing a finite size to the particles. At a more physical level, with the current resolution achieved in N-body simulations of galactic evolution, the individual particles have masses ranging from a few $100\,\mathrm{M}_\odot$ to $10^6\,\mathrm{M}_\odot$. Hence, the star particles should not be considered as individual stars (point masses), but rather as bunches of stars that are located in the same small volume of space with very similar velocities. Gas particles are also not point masses, but should correspond to smoothed clouds of gas. As for dark matter, we do not know what its nature is, but it seems unlikely

that it consists of point masses in this mass regime. Therefore, the optimum strategy is not to use point masses, but *softened particles*.

A straightforward method of including smoothing is to ascribe some simple density profile $S(\boldsymbol{x})$ to a particle at position $\boldsymbol{x}$. Various forms can be considered, such as a sphere with uniform or with linearly declining density, a Gaussian density distribution or a Plummer density distribution. Hockney & Eastwood (1987) investigated the shapes and chose the sphere with linearly declining density (shape $S2$) due to better accuracies in three-dimensional schemes. The radial $S2$ density distribution for a particle with diameter a and unit mass is:

$$S2 : S(r) = \begin{cases} \frac{48}{\pi a^4}\left(\frac{a}{2} - r\right) & r \leqslant a/2 \\ 0 & \text{elsewhere} \end{cases} . \tag{5.30}$$

The $S2$ particle smoothing is used in the HYDRA code.

Another much used softening shape is the Plummer density profile, used by Plummer (1911) to fit observations of globular clusters:

$$S_{\mathrm{P}} : S(r) = \frac{3}{4\pi\epsilon^3}\frac{1}{\left(1 + r^2/\epsilon^2\right)^{5/2}} \tag{5.31}$$

where the parameter ϵ controls the width of the Plummer sphere. Plummer softening is used in many Tree code implementations of the N-body problem.

The smoothing of the particles prevents the divergence of the forces. In HYDRA, the particle-particle interactions are calculated as the force of an $S2$-shaped particle (centered on $\mathbf{0}$) on an $S2$-shaped particle (centered on $\boldsymbol{x}$), or

$$\boldsymbol{F}(\boldsymbol{x}) = G\int d\boldsymbol{x}' \int d\boldsymbol{x}'' S(\boldsymbol{x}')S(\boldsymbol{x} - \boldsymbol{x}'')\frac{(\boldsymbol{x}' - \boldsymbol{x}'')}{|\boldsymbol{x}' - \boldsymbol{x}''|^3} \tag{5.32}$$

The force is directed along the $\boldsymbol{x}$ vector, and its magnitude is (Hockney & Eastwood, 1987)

$$F_{S2,a}(r) = G\begin{cases} \frac{1}{35a^2}(224\xi - 224\xi^3 + 70\xi^4 + 48\xi^5 - 21\xi^6) & 0 \leqslant \xi < 1 \\ \frac{1}{35a^2}(\frac{12}{\xi^2} - 224 + 896\xi - 840\xi^2 + 224\xi^3 + 70\xi^4 - 48\xi^5 + 7\xi^6) & 1 \leqslant \xi < 2 \\ \frac{1}{r^2} & 2 \leqslant \xi \end{cases} \tag{5.33}$$

where $\xi = 2r/a$, and r is the interparticle distance. The subscript a indicates that the diameter of the particles is a. The corresponding gravitational potential Φ equals

$$\Phi_{S2,a}(r) = G\begin{cases} \frac{1}{70a}(208 - 112\xi^2 + 56\xi^4 - 14\xi^5 - 8\xi^5 - 8\xi^6 + 3\xi^7) & 0 \leqslant \xi < 1 \\ \frac{1}{70a}(\frac{12}{\xi} + 128 + 224\xi - 448\xi^2 + 208\xi^3 - 56\xi^4 - 14\xi^5 + 8\xi^6 - \xi^7) & 1 \leqslant \xi < 2 \\ \frac{1}{r} & 2 \leqslant \xi \end{cases} . \tag{5.34}$$

On the other hand, in most Tree codes, the force on a particle is calculated as the force exerted on a point mass located at a distance r from the centre of the other particle's Plummer sphere.

$$F_{P,\epsilon}(r) = G\frac{r}{\left(\epsilon^2 + r^2\right)^{3/2}}, \tag{5.35}$$

with r the interparticle distance. The correspondent gravitational potential is given by:

$$\Phi_{P,\epsilon} = -\frac{G}{\sqrt{\epsilon^2 + r^2}}, \tag{5.36}$$

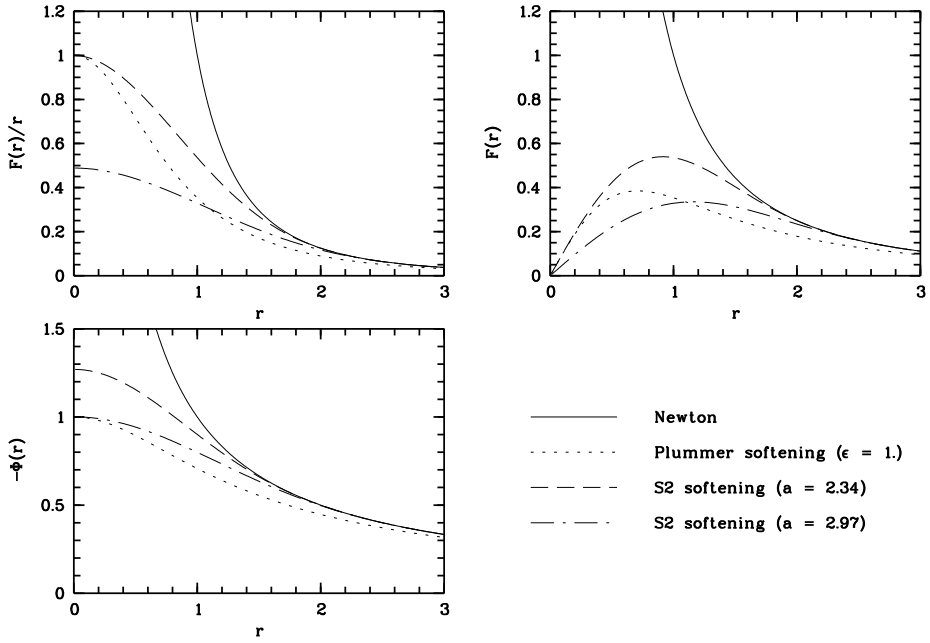

Figure 5.1: Comparison of the normalized gravitational force $F(r)$, $F(r)/r$ and gravitational potential Φ between two equal-mass particles using the Newtonian law for point masses (solid line), the Plummer softening with $\epsilon = 1$ (dotted line), the $S2$ softening with $a = 2.34\epsilon$ (dashed line) and $a = 2.97\epsilon$ (dash-dotted line).

The parameter ϵ is also called the *Plummer softening* parameter.

The way particles are smoothed is different in HYDRA and in Tree codes. In Fig. 5.1 the $S2$ and Plummer softening are compared to the exact interparticle gravitational force. Which diameter a and which Plummer softening ϵ can we use in order to compare results from codes that use the $S2$ softening to those that use the Plummer softening? The gravitational force at interparticle distance zero, is 0 in both cases. However, for computational reasons, the values $F(r)/r$ are tabulated in HYDRA. Equaling $F(r)/r$ for the $S2$ and Plummer forces results in

$$\frac{448}{35a^3} = \frac{1}{\epsilon^3} \text{ or } a = 2.34\epsilon. \tag{5.37}$$

Thus, simulations with a Plummer softening ϵ yield approximately the same accuracy as simulations with an $S2$ distribution where $a = 2.34\epsilon$. In HYDRA, the softening is entered as equivalent "Plummer softening" and internally transformed in the correspondent $S2$ shape diameter.

Another way to compare the different smoothing is to require the central gravitational potentials to be equal. In that case

$$\frac{208}{70a} = \frac{1}{\epsilon} \text{ or } a = 2.97\epsilon. \tag{5.38}$$

From Fig. 5.1 it is evident that the $S2$-shaped particles with diameter $a = 2.34\epsilon$ provide a force that most closely matches the Plummer force. It is also clear that $F_{S2,2.34\epsilon}$ is a better approximation to the Newtonian force than $F_{P,\epsilon}$. Due to the compact support of the $S2$-shape, the force is exact for interparticle distances greater than a.

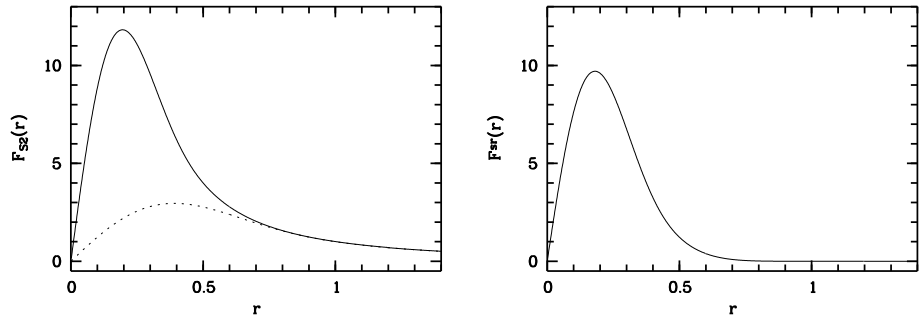

Figure 5.2: *Left panel:* The $S2$-shaped force for values $a = 0.5$ and $b = 1.0$. For $r > 1$, the forces are equal, but it can be seen that the two forces follow each other closely up to $r \approx 0.75$. *Right panel:* The short-range interparticle force $F^{\rm sr} = F_{S2,a} - F_{S2,b}$. This force is zero for all interparticle distances greater then $r \gtrsim 0.75$.

5.5.2 Force splitting

We want to split the total interparticle force in a short range part $\boldsymbol{F}_{ij}^{\rm sr}$ and a smoothly varying part $\boldsymbol{F}_{ij}^{\rm m}$. The reference force $\boldsymbol{F}_{ij}^{\rm m}$ is the interparticle force we wish to be accurately represented by the mesh calculation. To reduce the computational cost of the short-range PP loop, we require the cutoff radius r_e to be as small as possible. Therefore $\boldsymbol{F}_{ij}^{\rm m}$ should be equal to the total interparticle force down to as small a particle separation as possible. Unfortunately, we cannot make the reference and total interparticle forces identical down to arbitrarily small separations, since the mesh used in the PM part of the calculation cannot properly represent forces at a scale smaller than the mesh spacing. Hence the reference force should be smoothed, so that the point particle force law is followed beyond the cutoff radius r_e, while it goes smoothly to zero within that radius.

In practice, the reference force $\boldsymbol{F}_{ij}^{\rm m}$ is made continuous in one or more derivatives. In order to achieve a good mesh approximation for the reference force, the cutoff radius r_e should be greater than two density-potential mesh cell widths. Depending on the desired force accuracy of the PM loop, an optimal value for r_e can be calculated.

In HYDRA, the gravitational interparticle force law is approximated by $F_{S2,a}$ as in equation (5.33). If a is chosen small enough, this force is rapidly varying with respect to the density-potential mesh. Therefore the two $S2$-shaped particles are further smoothed to a diameter $b > a$. The force between two such spheres is also given by equation (5.33), with a substituted by b. This smoothed force $F_{S2,b}$ is exactly equal to the interparticle force $F_{S2,a}$ for all distances $r > b$, hence we could set $r_e = b$. However, the continuity of the derivatives of $F_{S2,b}$ at $r = b$ causes the reference force to closely follow the point particle force for radii somewhat less than b (Fig. 5.2, left panel). It was found empirically (Hockney & Eastwood, 1987) that a good measure of r_e is $0.735b$ (this can also be seen from the right panel of Figure 5.2. Once the reference interparticle force $F_{ij}^{\rm m} = F_{S2,b}(r_{ij})$ is chosen, the short-range force is computed as the difference between the total force and the reference force. In the AP^{3}M method, a new optimal mesh smoothing radius r_e is calculated for each refinement.

5.5.3 The mesh force

The mesh force is calculated in each point of the density-potential mesh. The main strength of using the mesh force is the reduction of the computational cost, compared to the PP force calculation. This reduction is achieved by using Fast Fourier Transforms, as described in Appendix A.

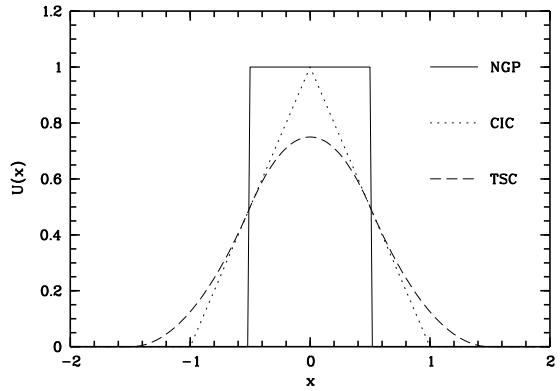

Figure 5.3: The assignment functions $u(x)$ in one dimension: the NGP, CIC and TSC schemes give increasingly smoother interpolation.

First, densities are assigned to the mesh, using the mass and positions of the N_p particles and an *assignment function* U. Then the discrete Fourier transforms of the densities are calculated. The Fourier transformed gravitational potential is computed using the Fourier transformed version of the Poisson equation (5.7). In Fourier space, the convolution of the densities with the Green's functions that occurs in the Poisson equation is reduced to a multiplication of the Fourier transforms. The potential is transformed back and is differenced to give the forces at the mesh points. Finally, these forces are interpolated on the particle's positions, using the same assignment function U.

In what follows, we assume that we have $N_m = L^3$ mesh points which are separated by unit length.

The assignment function

Once we introduce the mesh, we need to assign the particle masses to the mesh points in order to approximate the mass density. This is achieved using an assignment function $U(\boldsymbol{x})$ on a particle at position $\boldsymbol{x}$. Later on, the assignment function is also used to interpolate the mesh forces at the particles' positions. This is referred to as a *gather-scatter* operation. In order to ensure conservation of momentum, one needs to use the same assignment function for both the density and the force interpolation.

There are different possible forms for U, but as usually one has to weigh accuracy against computational cost. The assignment function in three dimensions is constructed as the product $U(\boldsymbol{x}) = u(x)u(y)u(z)$. This product construction avoids the necessity of calculating radius vectors for a spherically symmetric interpolation scheme.

Assignment functions The simplest way to interpolate the mass of a particle on the mesh is to assign it to the nearest mesh point. This scheme is called *Nearest Grid Point* (NGP). The corresponding one-dimensional assignment function is

$$u(x) = \begin{cases} 1 & |x| \leqslant \frac{1}{2} \\ 0 & \text{elsewhere .} \end{cases} \tag{5.39}$$

When this function is used to interpolate the forces, then these forces are not continuously varying over the mesh cells. Hence, the NGP interpolation scheme is a zeroth order scheme, which is not much used in practice.

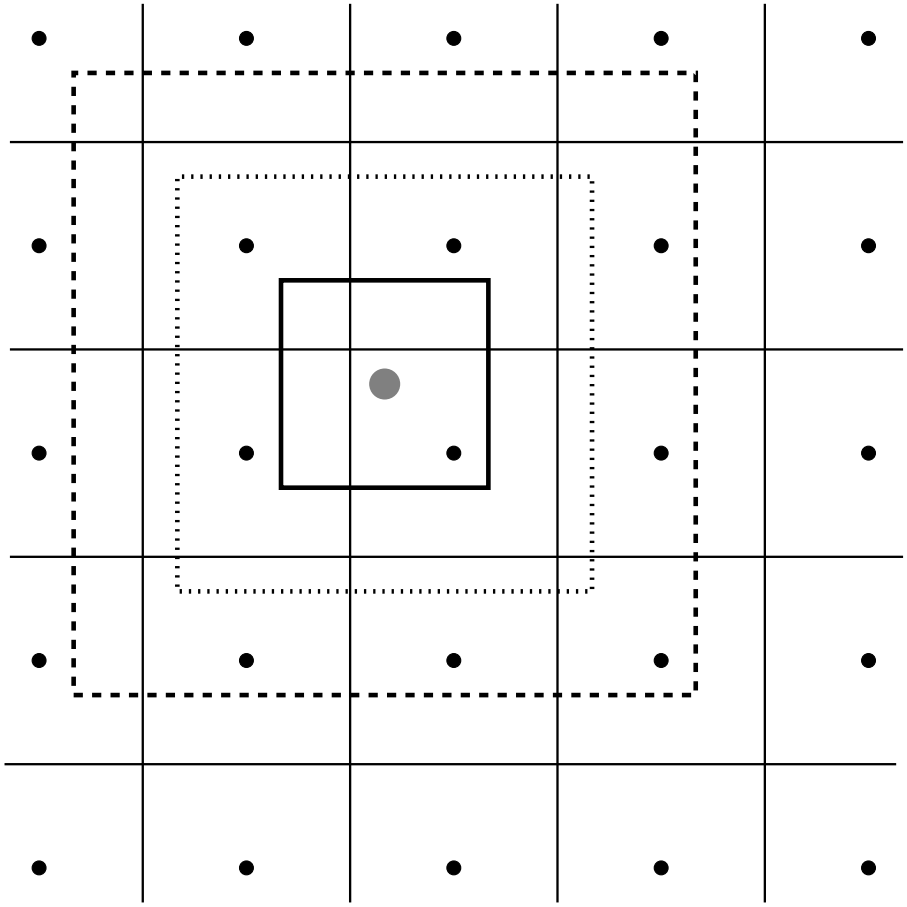

Figure 5.4: The mesh points (black dots) involved in the two dimensional mass assignment and force calculation of a particle (grey dot), for the different assignment functions NGP (solid line), CIC (dotted line) and TSC (dashed line).

A much used assignment function is the *Cloud In Cell* (CIC) scheme, which interpolates the mass of a particle linearly over the nearest 2 mesh points in each dimension. The CIC scheme in three dimensions assigns the mass of one particle to the eight nearest neighbouring mesh points. The corresponding assignment function is

$$U(x) = \begin{cases} 1 - |x| & |x| \leqslant 1 \\ 0 & \text{elsewhere} . \end{cases} \tag{5.40}$$

This function is also known as the *hat function*. Using this linear interpolation for the force assignment, the forces vary continuously over the mesh cells, but the first derivatives are discontinuous. The CIC is a first order scheme.

The assignment function used in HYDRA is the *Triangular Shaped Cloud* scheme. The TSC requires interpolation over three mesh points in each dimension, thus in three dimensions, 27 neighbour points

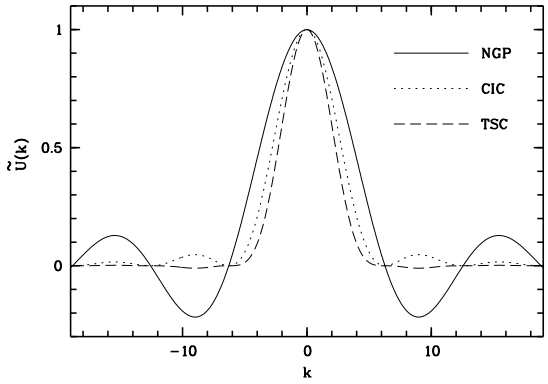

Figure 5.5: The Fourier Transform of the assignment functions $u(x)$ in one dimension: the power at large wavenumbers decreases if one goes from NGP to CIC to TSC schemes.

are used. The assignment function becomes

$$U(x) = \begin{cases} \frac{3}{4} - x^2 & |x| \leqslant \frac{1}{2} \\ \frac{1}{2}\left(\frac{3}{2} - |x|\right)^2 & \frac{1}{2} < |x| \leqslant \frac{3}{2} \\ 0 & \text{elsewhere .} \end{cases} \tag{5.41}$$

This second-order scheme ensures the continuity of the forces and their first derivatives when going from one mesh cell to the next. In Fig. 5.3 the different assignment functions NGP, CIC and TSC are shown. The corresponding assignment on the mesh is illustrated in Fig. 5.4.

Smoother, higher-order interpolation schemes provide greater accuracy, but the computational cost rises significantly. Going to the third-order scheme would require 64 mesh points per particle in three dimensions (as opposed to 27 for the TSC scheme). Since the accuracy gained does not justify the extra computational cost of higher order schemes, the TSC scheme is used.

Aliasing Because of the discreteness and of the finite size of the density-potential mesh, some Fourier modes of the continuous density distribution ρ are not represented in the discrete Fourier transform. The discrete Fourier transform of the density on a one-dimensional mesh with L mesh points, can only represent wavenumbers $k = 0, \ldots, L-1$. This range is called the *principal zone*. Hence, spatial structure on a scale finer than the mesh spacing cannot be represented on the mesh. Some of the power of this fine scale is erroneously interpreted by the mesh as belonging to longer wavelength modes which the mesh does support.

The discrete Fourier transform of the mass density is given by the sum of copies of the principal zone, each offset by a multiple of L. This means of course that the Fourier transform $\tilde{\rho}$ is periodic in k with period L. The extra contributions from the other zones to the transform in the principal zone are called *aliases*. In order to reduce the alias, the harmonic content of large wavenumbers or small wavelengths should be small. Therefore the Fourier transform of the assignment function should have low power at large wavenumbers. The smoother U, the more peaked $\tilde{U}$ becomes, and the smaller the aliases. The NGP, CIC and TSC assignment functions have continuous Fourier transforms of the form

$$\tilde{U}_{\mathsf{NGP}} = \frac{\sin(k/2)}{k/2},\ \tilde{U}_{\mathsf{CIC}} = \left(\frac{\sin(k/2)}{k/2}\right)^2 \text{ and } \tilde{U}_{\mathsf{TSC}} = \left(\frac{\sin(k/2)}{k/2}\right)^3. \tag{5.42}$$

As can be seen in Fig. 5.5, the smoother the assignment function U is, the narrower the Fourier transforms $\tilde{U}$ will be.

Solving the Poisson equation

In order to understand the way that the Poisson equation is solved on the mesh, we follow a reasoning analogous of that in Binney & Tremaine (1987), but in three dimensions. In this example, the assignment scheme U is the NGP. This zeroth order scheme is rarely used in practice, but is fine for explanatory purposes due to its simplicity. We also assume that the particles are Plummer softened, with softening parameter ϵ.

If we divide the space occupied by the particles (the simulation box) into a large number N_m of cells, we may obtain an estimate of the potential at the center of any cell by assuming that all the material in each cell lies at the center of the cell, and then evaluating

$$\Phi_\alpha = \sum_{\beta=1}^{N_m} G_{\alpha\beta} M_\beta, \tag{5.43}$$

where M_β is the mass of the particles in the β^{th} cell and $G_{\alpha\beta}$ is defined to be the potential at the center of the α^{th} cell that is generated by unit mass at the center of the β^{th} cell. If the position vectors of the centers of the two cells are $\boldsymbol{x}_\alpha$ and $\boldsymbol{x}_\beta$, we have

$$G_{\alpha\beta} = -\frac{G}{\sqrt{\epsilon^2 + |\boldsymbol{x}_\alpha - \boldsymbol{x}_\beta|^2}}. \tag{5.44}$$

$G_{\alpha\beta} M_\beta$ will be a good estimate of the potential generated at $\boldsymbol{x}_\alpha$ by the matter in the β^{th} cell unless the two cells are nearly adjacent to one another. Hence, if the number N_m of cells becomes very large, $G_{\alpha\beta} M_\beta$ will be a good approximation to the contribution of the β^{th} cell to $\Phi(\boldsymbol{x}_\alpha)$ for the overwhelming majority of values of α.

Since the locations $\boldsymbol{x}_\alpha$ of the centres of the cells are fixed, we may store the values $G_{\alpha\beta}$ at the start of the calculation. Then at each time step, $\Phi(\boldsymbol{x}_\alpha)$ may be estimated without extracting a large number of radicals. Furthermore, since $G_{\alpha\beta}$ depends only on the difference $(\boldsymbol{x}_\alpha - \boldsymbol{x}_\beta)$, we can evaluate the sum over cells using the Fast Fourier Transform (FFT) in order to reduce the computational effort from $O(N_m^2)$ to $O(N_m \log_2(N_m))$.

The $N_m = L^3$ cells of the density-potential mesh are assumed to be cubic, and the units chosen such that the side lengths of the cells correspond to unit length and the gravitational constant G is unity. The cell centres may then be at $\boldsymbol{x}_{klm} = (k, l, m)$ with $k, l, m = 0, \ldots, L-1$. Hence we have

$$\Phi_{klm} = \sum_{k=0}^{L-1} \sum_{l=0}^{L-1} \sum_{m=0}^{L-1} G(k-k', l-l', m-m') M_{k'l'm'}, \tag{5.45}$$

where

$$G(k-k', l-l', m-m') = \frac{-1}{\sqrt{\epsilon^2 + (k-k')^2 + (l-l')^2 + (m-m')^2}}, \tag{5.46}$$

which depends only on the differences $(k-k')$, $(l-l')$ and $(m-m')$.

The sums are almost of the same form as those for a discrete Fourier transform. However, the functions $G(p, q, r)$ and $M_{k'l'm'}$ are not periodic. In the case we want to perform large cosmological simulations, we can make these functions continuous by simply repeating them cyclicly, with period $2L$ for p, q and

r, and with period L in k', l' and m'. If we want to investigate an isolated part of the universe, we can extend the sums to the range $0, 2L-1$ and define $M_{k'l'm'}$ to be zero whenever either k', l' or m' is in the range $L, 2L-1$ without affecting any of the values of Φ_{klm}. Then we can make $M_{k'l'm'}$ periodic since the sum does not involve any values of k', l' or m' outside the first period. We are also free to make G periodic by defining it to be the periodic function that agrees with its definition for the differences $(k-k')$, $(l-l')$ and $(m-m')$ in the range $0, 2L-1$. We can do this because the only values of the indices k, l and m that are of interest are in the range $0, L-1$ since we only need the potential where we have particles. Thus the only values of the differences $(k-k')$, $(l-l')$ and $(m-m')$ that are of interest and for which the coefficient of G is non-zero lie in the range $0, 2L-1$. Finally, we come to the Fourier transformed Poisson equation

$$\tilde{\Phi}_{pqr} = \frac{1}{\sqrt{N_m}} \tilde{G}_{pqr} \tilde{M}_{pqr}. \tag{5.47}$$

If we chose $L = 2^p$ for some integer p, we can apply the FFT to obtain the values for $\tilde{\Phi}_{pqr}$.

The implementation in HYDRA follows the same reasoning, but using the TSC as the assignment function, and Green's functions corresponding to the S2 softening. For a full account hereof, see (Hockney & Eastwood, 1987).

Differencing the potential

The gravitational force at a mesh point is obtained by taking the divergence of the gravitational potential. In order to do so, a *finite difference* scheme is used, using the potential values in neighbouring mesh points in order to estimate the gradient of the potential in different directions. To see this, in the one-dimensional case, at mesh cell i, the force can be estimated as

$$F_x(i) = \frac{\partial \Phi(i)}{\partial x} = \frac{1}{2}\left(\Phi(i-1) - \Phi(i+1)\right). \tag{5.48}$$

In three dimensions, this becomes a 10-point differencing scheme in order to take into account the gradients in the other dimensions. The x component of the mesh force, $F_x(ijk)$, at mesh point (i,j,k) is given by

$$\begin{aligned} F_x(i,j,k) \quad = \quad & \frac{1}{6}(\Phi_{i-1,j,k} - \Phi_{i+1,j,k}) + \\ & \frac{1}{12}(\Phi_{i-1,j-1,k} - \Phi_{i+1,j-1,k} + \Phi_{i-1,j+1,k} - \Phi_{i+1,j+1,k} + \\ & \quad \Phi_{i-1,j,k-1} - \Phi_{i+1,j,k-1} + \Phi_{i-1,j,k+1} - \Phi_{i+1,j,k+1}) \end{aligned} \tag{5.49}$$

where $\Phi_{i,j,k}$ is the potential at grid point (i,j,k). This is the difference scheme used by HYDRA. One could always consider higher-order difference schemes at the cost of increased computational efforts.

5.5.4 The short-range force

The total short-range part of the force on a particle at position $\boldsymbol{x}$, is given by the sum of the interparticle short-range forces:

$$\boldsymbol{F}^{\mathrm{sr}} = \sum_{j=1}^{N_p} \boldsymbol{F}_{ij}^{\mathrm{sr}}. \tag{5.50}$$

The elementary method of evaluating $\boldsymbol{F}^{\rm sr}$ is to sweep through all particles $j = 1, \ldots, N_p$, test whether the separation is smaller then r_e and, if so, compute $\boldsymbol{F}^{\rm sr}_{ij}$ and add it to $\boldsymbol{F}^{\rm sr}$. Such an approach is clearly impractical, since for each of the N_p values of i one would have to test $N_p - 1$ separations r_{ij} giving an operations count scaling as $O(N_p^2)$.

The computational cost of locating those particles j which contribute to the short-range force on particle i is greatly reduced if the particle coordinates are ordered such that the tests for locating particles j with $r_{ij} \leqslant r_e$ need only be performed over a small subset N_n of the total number of particles N_p. It is for this reason that the *chaining mesh* is introduced. The chaining mesh (in three dimensions) is a regular lattice of $N_c = L_c^3$ cells, covering the computational box of size L^3 in much the same manner as the $(N_m = L_m^3)$ cells of the much finer density-potential mesh. The number of chaining mesh cells L_c in one dimension is given by the largest integer less than or equal to L/r_e. Consequently, the lengths of the sides of the cells of the chaining mesh are always greater than or equal to the cutoff radius r_e. The pairwise force accuracy required dictates the softness b of the mesh force, which in turn sets the chaining-mesh cell size necessary to reproduce the required total force. Typically, the side lengths of the chaining mesh cells are between two and four times greater than the side lengths of the cells of the density-potential mesh.

For each particle i in chaining cell $\boldsymbol{q}$, the particles j that have nonzero contributions to the short-range force, must either lie in the same cell $\boldsymbol{q}$ or in one of the twenty-six neighbouring cells (in three dimensions). Thus by sorting the particles into linked lists associated with the chaining mesh cells, one can save a considerable amount of time. Due to Newton's third law (action=reaction), particle pairs have to be evaluated only once. In order to avoid double computation, the interparticle forces are calculated for all pairs in the current cell, and for all pairs with one member i in the current cell and one member in one of thirteen of the neighbouring cells. The same thirteen neighbour cells are used for each current cell. Of course, the cells at the boundaries should have some empty neighbour cells (if isolated boundary conditions are implied) or some mirror cells (if periodic boundary conditions are implied).

The short-range force calculation can be summarized as follows: for all chaining cells, compute for all pairs in a certain subset of neighbour cells (in order to avoid double computation) the interparticle distance and interpolate the force from a force look-up table. Considerable computational savings are made in this loop by tabulating the values $F^{\rm sr}(r_{ij})/r_{ij}$ at uniform intervals of r^2, thus avoiding the computation of square roots in the pairwise summation loop. The tabulated values are

$$\mathcal{F}(r) = \frac{f^{\rm sr}(r)}{r} = \frac{F_{S2,a}(r) - F_{S2,b}(r)}{r}. \tag{5.51}$$

5.5.5 Adaptive refinements

Under heavy gravitational clustering, the range of the short-range sum may enclose a large number of neighbours, thus largely increasing the computational cost of the PP loop. To overcome this problem, the long range-short range force splitting can be exploited by refining the short-range part in regions where it is computationally expensive. The effect of this is to split the gravitational force due to near neighbours into a new mesh part, with $a'_{\rm m} < a_{\rm m}$, followed by a further direct neighbour sum over a reduced search radius $r'_e < r_e$, enclosing close to the number of neighbours optimal for efficient operation of the P^{3}M algorithm. In very high density regions a series of refined meshes may be used which accumulate the forces on particles within the refinements to successively higher resolution.

In practice, the basic idea is to find those cells in the chaining mesh of the parent P^{3}M which carry a high operations count due to a high particle content, and to further process them with a finer potential mesh before the direct sum is performed. These cells are organized into non-overlapping cubic refinements containing an integral number of chaining cells (remember, $L_c \approx 2 - 4L_m$). Each refinement, including

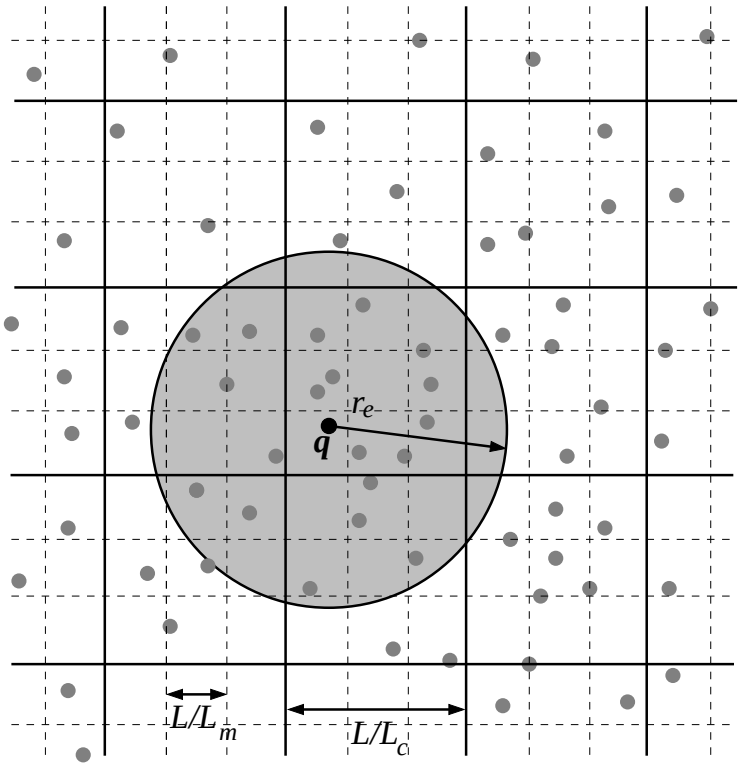

Figure 5.6: The chaining mesh used to find the neighbour particles for the direct sum part of the force calculation. The size of the chaining mesh cells, L/L_c is greater than or equal to the cutoff radius r_e. Hence all particles that contribute to the short-range force calculation of a particle $\boldsymbol{q}$ in a certain cell lie within the 26 neighbour cells (in three dimensions). Typically, the chaining mesh is about 2-4 times as coarse as the density-potential mesh, which has cell sizes L/L_m.

the original region, is solved as an independent set of particles with the appropriate boundary conditions. This proceeds along the following three steps. Firstly, the long-range force is solved for as in the normal PM code and the particle accelerations are updated with this force. Then the regions within the current refinement which need to be treated with a further refined mesh are identified. The selected chaining mesh cells are labeled with the new refinement's index number and the refinements' numbers are arranged into a list. Finally, the short-range direct sums over all pairs of neighbouring chaining mesh cells is performed, *excluding* those pairs of cells that reside in the *same* new refinement. This sequence of steps fully updates the force on all particles for pairs which do not both lie in the same new refinement.

Pairs within a refinement require an extra force component beyond that added by the parent's mesh calculation. These three steps are then followed recursively to allow several levels of refinement. All levels of refinement, save the zeroth, require isolated boundary conditions. The zeroth may require isolated or periodic boundary conditions depending on the problem under investigation. The HYDRA code used in this work allows up to six refinement levels.

Choosing the refinements to be cubic, to cover an integral number of chaining mesh cells, and not allowing refinements to overlap inevitably reduces the theoretical efficiency. However, the gain is in simplicity and in the great reduction of bookkeeping overhead that would be necessary otherwise.

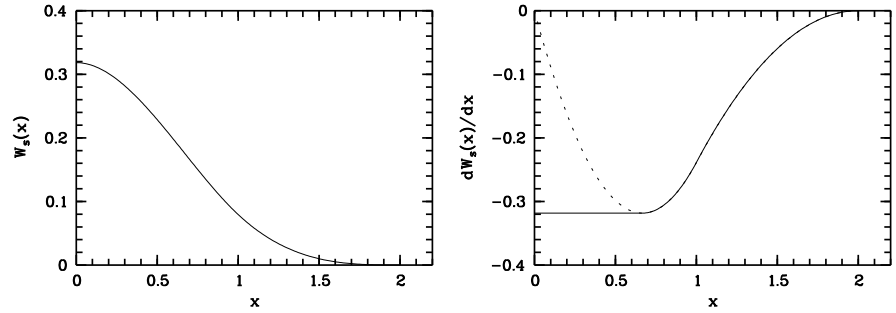

Figure 5.7: *Left panel*: The normalized SPH smoothing kernel $W_s(x)$ in function of $x = r/h$. *Right panel*: The modified derivative $\frac{\mathrm{d}W_s(x)}{\mathrm{d}x}$ (full line) and the unmodified derivative (dotted line). The derivative is made to rise monotonically, to give a small repulsive force at small distances (Thomas & Couchman, 1992), as is clear in the resulting $|\nabla W_s(x)| = \frac{1}{x}\frac{\mathrm{d}W_s(x)}{\mathrm{d}x}$.

5.6 The SPH algorithm

The hydrodynamical equations are solved using the Smoothed Particle Hydrodynamics method (SPH) which uses a particle representation of the fluid. The particles are smoothed with an interpolation kernel to approximate the local hydrodynamic quantities from a sample of neighbouring fluid particles. All relevant physical quantities are interpolated in the following way:

$$\langle f(\boldsymbol{r})\rangle = \int W(\boldsymbol{r}-\boldsymbol{r}',h) f(\boldsymbol{r}')\mathrm{d}\boldsymbol{r}', \tag{5.52}$$

where the integral is extended over the whole space and W is a function generally referred to as the *interpolation kernel*, h is the *smoothing length* that determines the spatial region within which variables are smoothed, and thus it governs the spatial resolution of the method. For a finite number of particles, this becomes

$$\langle f(\boldsymbol{r})\rangle = \sum_j m_j \frac{f_j}{\rho_j} W(\boldsymbol{r}-\boldsymbol{r}_j,h), \tag{5.53}$$

where the volume element $\mathrm{d}\boldsymbol{r}_j$ is substituted by m_j/ρ_j. The spatial derivative of a quantity reads

$$\langle \boldsymbol{\nabla}_{\boldsymbol{r}} f(\boldsymbol{r})\rangle = \sum_j m_j \frac{f_j}{\rho_j} \boldsymbol{\nabla}_{\boldsymbol{r}} W(\boldsymbol{r}-\boldsymbol{r}_j,h), \tag{5.54}$$

where $\boldsymbol{\nabla}_{\boldsymbol{r}}$ denotes the spatial derivative with respect to $\boldsymbol{r}$.

5.6.1 The smoothing kernel W

The interpolation kernel W should be normalized and has to approach a Dirac δ distribution in the limit of small smoothing lengths ($h \to 0$)

$$\int W(\boldsymbol{r}-\boldsymbol{r}',h)\mathrm{d}\boldsymbol{r}' = 1, \tag{5.55}$$

and

$$\lim_{h\to 0} W(\boldsymbol{r}-\boldsymbol{r}',h) = \delta(\boldsymbol{r}-\boldsymbol{r}'). \tag{5.56}$$

Several forms of the interpolation kernel are possible and have been extensively tested (Carraro et al., 1998). The interpolation kernel used in HYDRA is a *spline kernel* (Monaghan, 1992), which is defined on a compact support with radius $2h$ (Figure 5.7, left panel)

$$W(\boldsymbol{r},h) = \frac{W_s(r/h)}{h^3}, \tag{5.57}$$

where, if $x = r/h$

$$W_s(x) = \frac{1}{4\pi}\begin{cases} 4-6x^2+3x^3, & 0 \leqslant x < 1, \\ (2-x)^3, & 1 \leqslant x < 2, \\ 0, & \text{elsewhere.} \end{cases} \tag{5.58}$$

The first derivative of the kernel is made to rise monotonically, to give a small repulsive force at small distances (Figure 5.7, right panel)

$$\frac{\mathrm{d}W_s}{\mathrm{d}x}(x) = -\frac{1}{4\pi}\begin{cases} 4, & 0 \leqslant x < 2/3, \\ 3x(4-3x), & 2/3 \leqslant x < 1, \\ 3(2-x)^2, & 1 \leqslant x < 2, \\ 0, & \text{elsewhere.} \end{cases} \tag{5.59}$$

The primary reason for having a non-zero gradient at the origin is to avoid artificial clustering (Thomas & Couchman, 1992; Thacker et al., 2000).

In order to avoid calculating the kernel for all particles at each timestep, the normalized kernel $W_s(x)$ and its first derivative $\frac{1}{x}\frac{\mathrm{d}W_s(x)}{\mathrm{d}x}$ are stored as lookup tables W_s and $\frac{1}{x}\frac{\mathrm{d}W_s}{\mathrm{d}x}$, in function of $x = r/h$. The correct values for $W(\boldsymbol{r},h)$ and $\boldsymbol{\nabla}_{\boldsymbol{r}}W(\boldsymbol{r},h)$ are then calculated from the interpolated table values, multiplied by h^{-3} and $\boldsymbol{r}h^{-5}$ respectively.

5.6.2 The smoothing length h

If the smoothing length h is held constant for all particles, the spatial resolution is fixed, as in the gravitational PP loop. However, in the hydrodynamical equations only local quantities are evaluated. To ensure a good approximation of these quantities, the smoothing length should be large enough so that even in low-density regions sufficient neighbouring particles contribute to the sum in equation (5.53). In that case, the smoothing kernel of particles in high-density regions will enclose a large number of neighbours, hence leading to a significant slow-down in the calculation time.

Therefore, each gas particle has an individual smoothing length h_i, chosen such that the number of neighbours is constant (or approximately constant) for all particles. This leads to a spatial resolution that depends on the local particle number density. It also removes the slow-down of the calculation time. At each timestep, a new smoothing length is computed for each particle, to ensure that the number of neighbours is kept around $N_{\mathrm{SPH}} \sim 30-50$.

A minimum value of h could be set by requiring that the SPH resolution should not fall below that of the gravity solver. The minimum resolution of the SPH kernel is the diameter of the smallest smoothing sphere, $4h_{\min}$. The gravity resolution is defined to be twice the $S2$ softening diameter a, as at this radius, the force is closely equivalent to the $1/r^2$ law. Equating these two resolutions yields

$$4h_{\min} = 2a. \tag{5.60}$$

Once this minimum smoothing length is reached by a particle, smoothing should occur over all neighbouring particles within a radius of $h_{\rm min}$. In HYDRA however, an option exists to smooth the SPH quantities over an exact number $N_{\rm SPH}$, of neighbour particles. In that case the minimum h constraint is not set. A number of $N_{\rm SPH} = 32$ ensures that the fluid variables are well approximated, while keeping the computational cost low in clustered regions.

5.6.3 Gather-Scatter interpretation

Since each particle has its own smoothing length h_i, it is possible to interpret the hydrodynamical equations in two ways: the *gather* and *scatter* interpretation (Hernquist & Katz, 1989). The gather method evaluates the equations for $\boldsymbol{p}_i$ by summing over all particles $\boldsymbol{p}_j$ that lie within $2h_i$, while the scatter method sums over all particles $\boldsymbol{p}_j$ that have $\boldsymbol{p}_i$ within their compact support $2h_j$. The question of which smoothing method to use may be circumvented by using a hybrid formalism based upon the average of the smoothing length h (Springel & Hernquist, 2002). In that case, an estimate of the density is given by

$$\langle \rho(\boldsymbol{r}_i) \rangle = \sum_{j=1}^{N_{\rm SPH}} m_j W(\boldsymbol{r}_i - \boldsymbol{r}_j, h_{ij}), \tag{5.61}$$

with h_{ij} the arithmetical mean ($(h_i + h_j)/2$) or the geometrical mean ($\sqrt{h_i h_j}$) of h_i and h_j.
An alternative approach to the gather/scatter interpretations is to combine them into a hybrid framework by averaging the kernels. In this case, an estimate for the density is given by

$$\langle \rho(\boldsymbol{r}_i) \rangle = \sum_{j=1}^{N_{\rm SPH}} m_j W_{ij}, \tag{5.62}$$

with

$$W_{ij} = \frac{W(\boldsymbol{r}_i - \boldsymbol{r}_j, h_i) + W(\boldsymbol{r}_i - \boldsymbol{r}_j, h_j)}{2}. \tag{5.63}$$

In HYDRA, the gather interpretation is used to approximate the smoothed density associated with the i-th particle

$$\rho_i = \rho(\boldsymbol{x}_i) = \sum_j m_j W(r_{ij}, h_i), \tag{5.64}$$

where $r_{ij} = |\boldsymbol{x}_i - \boldsymbol{x}_j|$ and the sum j runs over all neighbour particles for which $r_{ij} < 2h_i$. In the case that exact $N_{\rm SPH}$ neighbour particles are required, the sum is retained to the $N_{\rm SPH}$ nearest neighbours.

5.6.4 The force calculation

The forces are computed from the hydrodynamical equation of motion derived in Section 5.4

$$\frac{\mathrm{d}\boldsymbol{v}}{\mathrm{d}t} = -\frac{1}{\rho}\boldsymbol{\nabla} P. \tag{5.65}$$

In order to ensure conservation of momentum, particles should be treated on the same footing, so some sort of hybrid gather/scatter interpretation has to be applied to the force calculation. In SPH this is achieved by re-writing equation (5.65) using equation (5.54) and the identity

$$\frac{\boldsymbol{\nabla} P}{\rho} = \boldsymbol{\nabla}\frac{P}{\rho} + \frac{P}{\rho^2}\boldsymbol{\nabla}\rho, \tag{5.66}$$

the SPH equation of motion with kernel averaging becomes

$$\frac{\mathrm{d}\boldsymbol{v}}{\mathrm{d}t} = -\sum_j \frac{P_j}{\rho_j}\frac{m_j}{\rho_j}\boldsymbol{\nabla}_i W_{ij} - \frac{P_i}{\rho_i^2}\sum_j \frac{m_j}{\rho_j}\boldsymbol{\nabla}_i W_{ij} \tag{5.67}$$

$$= -\sum_j m_j \left(\frac{P_i}{\rho_i^2} + \frac{P_j}{\rho_j^2}\right)\boldsymbol{\nabla}_i W_{ij}, \tag{5.68}$$

where $\boldsymbol{\nabla}_i$ means that the derivative is taken with respect to $\boldsymbol{r}_i$.

However, this scheme requires the SPH loop to be processed twice over all particles. The first time to calculate the density, pressure gradient and velocity dispersion of each particle, and the second time to apply equal and opposite SPH forces to the particle and each of its neighbours. This increases the computational cost considerably. Therefore the approximation

$$\boldsymbol{\nabla}_i W(r_{ij}, h_i) \simeq -\boldsymbol{\nabla}_j W(r_{ij}, h_j) \tag{5.69}$$

is used to arrive at (Thomas & Couchman, 1992)

$$\frac{\mathrm{d}\boldsymbol{v}}{\mathrm{d}t} = -\sum_{j:\ r_{ij}<h_i} m_j \frac{P_i}{\rho_i^2}\boldsymbol{\nabla}_i W(r_{ij}, h_i) + \sum_{j:\ r_{ij}<h_j} m_j \frac{P_j}{\rho_j^2}\boldsymbol{\nabla}_j W(r_{ij}, h_j). \tag{5.70}$$

Although somewhat less accurate, this scheme is extremely efficient since the forces can be calculated in one loop over all particles.

5.6.5 Artificial viscosity

An *artificial viscosity* is necessary in SPH in order to dissipate convergent motion and hence prevent interpenetration of the gas clouds. Several formulations of artificial viscosity are possible and they all involve adding an artificial viscosity term Π_{ij} to the P/ρ^2 sum in the force:

$$\frac{\mathrm{d}\boldsymbol{v}}{\mathrm{d}t} = \sum_j m_j \left(\frac{P_i}{\rho_i^2} + \frac{P_j}{\rho_j^2} + \Pi_{ij}\right)\boldsymbol{\nabla}_i W_{ij}. \tag{5.71}$$

An excellent review on different implementations of artificial viscosity is given by Thacker et al. (2000). The standard Monaghan artificial viscosity (Monaghan, 1992) has an explicit $i-j$ particle symmetry which is again motivated by Newton's third law:

$$\Pi_{ij} = \frac{-\alpha\mu_{ij}\bar{c}_{ij} + \beta\mu_{ij}^2}{\bar{\rho}_{ij}}, \tag{5.72}$$

where

$$\mu_{ij} = \begin{cases} \frac{\bar{h}_{ij}\boldsymbol{r}_{ij}\cdot\boldsymbol{v}_{ij}}{r_{ij}^2+\nu^2} & \boldsymbol{r}_{ij}\cdot\boldsymbol{v}_{ij} < 0 \\ 0 & \boldsymbol{r}_{ij}\cdot\boldsymbol{v}_{ij} \geqslant 0. \end{cases} \tag{5.73}$$

The bar denotes arithmetic averaging of the quantities and $\nu^2 = 0.01\bar{h}_{ij}^2$ is a term included to prevent numerical divergences. The sound speed c_i of a gas particle is calculated from $c_i = \sqrt{10/9\epsilon_i}$ with ϵ_i the specific thermal energy. Typical values for the viscosity coefficients α and β are estimated from shock tube experiments and yield $\alpha = 1$ and $\beta = 2$ (Monaghan, 1992).

In HYDRA, the artificial viscosity is implemented in the following way

$$\frac{\mathrm{d}\boldsymbol{v}}{\mathrm{d}t} = -\sum_{j:\ r_{ij}<h_i} m_j \left(\frac{P_i}{\rho_i^2} + \Pi'_{ij}\right) \boldsymbol{\nabla}_i W(r_{ij}, h_i) + \sum_{j:\ r_{ij}<h_j} m_j \left(\frac{P_j}{\rho_j^2} + \Pi'_{ji}\right) \boldsymbol{\nabla}_j W_{r_{ij},h_j}. \quad (5.74)$$

Note that in the second sum, the subindices ji are switched. The modified artificial viscosity term is

$$\Pi'_{ij} = \frac{2}{3}\frac{\bar{\epsilon}_{ij}}{\bar{c}_{ij}^2}\frac{-\alpha'\bar{c}_{ij}\mu'_{ij} + \beta'{\mu'_{ij}}^2}{\rho_i}, \quad (5.75)$$

where

$$\mu'_{ij} = \begin{cases} \frac{h_i \boldsymbol{r}_{ij}\cdot\boldsymbol{v}_{ij}}{r_{ij}^2 + 0.01h_i^2} & \boldsymbol{r}_{ij}\cdot\boldsymbol{v}_{ij} < 0 \\ 0 & \boldsymbol{r}_{ij}\cdot\boldsymbol{v}_{ij} \geqslant 0. \end{cases} \quad (5.76)$$

This modified artificial viscosity scheme is approximately equivalent to the Monaghan standard scheme, but it has the advantage that the SPH loop needs to be evaluated only once. It has been made explicitly symmetric in the specific energy terms. The values $\alpha' = 5/6$ and $\beta' = 5/3$ are used to yield a scheme that approximates the Monaghan viscosity scheme with parameters $\alpha = 1$ and $\beta = 2$.

5.6.6 The energy equation

The evolution of the specific internal energy ϵ is determined by the energy equation (see also Section 5.4)

$$\frac{\mathrm{d}\epsilon}{\mathrm{d}t} = -\frac{P}{\rho}\boldsymbol{\nabla}\cdot\boldsymbol{v} = -\frac{2}{3}\epsilon\boldsymbol{\nabla}\cdot\boldsymbol{v}, \quad (5.77)$$

where we have used the equation of state

$$P = \frac{2}{3}\epsilon\rho. \quad (5.78)$$

The SPH estimate for $\boldsymbol{\nabla}\cdot\boldsymbol{v}$ can be used directly to calculate $d\epsilon_i/dt$ of the i-th particle

$$\frac{\mathrm{d}\epsilon_i}{\mathrm{d}t} = -\frac{P_i}{\rho_i}\boldsymbol{\nabla}_i\cdot\boldsymbol{v}_i. \quad (5.79)$$

In order to calculate the SPH estimate for the velocity divergence, the following identity is used

$$\boldsymbol{\nabla}\cdot\boldsymbol{v} = \frac{\boldsymbol{\nabla}\cdot(\rho\boldsymbol{v}) - \boldsymbol{v}\cdot\boldsymbol{\nabla}\rho}{\rho}, \quad (5.80)$$

so that we can write

$$\boldsymbol{\nabla}_i\cdot\boldsymbol{v}_i = \frac{1}{\rho_i}\sum_j m_j(\boldsymbol{v}_j - \boldsymbol{v}_i)\cdot\boldsymbol{\nabla}_i W_{ij} \quad (5.81)$$

$$= -\sum_j m_j \frac{\boldsymbol{v}_{ij}}{\rho_i}\cdot\boldsymbol{\nabla}_i W_{ij}, \quad (5.82)$$

with $\boldsymbol{v}_{ij} = \boldsymbol{v}_i - \boldsymbol{v}_j$. Explicitly writing the summation for the SPH estimate gives

$$\frac{\mathrm{d}\epsilon_i}{\mathrm{d}t} = \sum_j m_j \frac{P_i}{\rho_i^2}\boldsymbol{v}_{ij}\cdot\boldsymbol{\nabla}_i W_{ij}. \quad (5.83)$$

The term P/ρ^2 is augmented by an artificial viscosity term Π as shown in the force calculation. In principle, this equation could be symmetrised along the same line of reasoning as used in the SPH force (Thomas & Couchman, 1992). However, although ensuring very good energy conservation, the entropy is not well conserved when using such a symmetrised scheme (Couchman et al., 1995). Thus, in HYDRA, the energy change is summed in the following way

$$\frac{\mathrm{d}\epsilon_i}{\mathrm{d}t} = \sum_j m_j \left(\frac{P_i}{\rho_i^2} + \Pi'_{ij} \right) \boldsymbol{v}_{ij} \cdot \boldsymbol{\nabla}_i W_{ij}. \tag{5.84}$$

5.6.7 The specific entropy

The specific entropy s_i of a gas particle i is given by

$$s_i = \frac{\epsilon_i}{\rho_i^{2/3}} \tag{5.85}$$

In order to conserve the total entropy, one has to take into account the spatial variation of the smoothing length in time. The $P\mathrm{d}V$ work is modified by a correction factor f_h, as outlined in Springel & Hernquist (2002), which vastly improves entropy conservation (see HYDRA documentation). Exact entropy can be achieved by integrating the specific entropy rather than the specific energy. However, in this case energy conservation is no longer guaranteed. Conservation of entropy is important to correctly simulate cooling and heating processes in SPH simulations.

5.6.8 Neighbour search

The neighbour search for the SPH forces is equivalent to the neighbour search for the short-range gravitational forces. Calculating the pairwise separation for each particle pair and comparing it to the smoothing lengths of both particles requires $O(N_p^2)$ computations, which becomes quickly too large. Therefore it is best to introduce a chaining mesh for the gas-particles only. If the smoothing lengths were constant for all particles, and if the gas resolution were equal to the gravitational resolution ($a = 2h$), the same chaining mesh could be used for the gravitational and hydrodynamical forces and the SPH loop could be fully integrated in the PP part of the gravitational force calculation. In fact one could consider using the $S2$ shape as a smoothing kernel for the hydrodynamical particles, or the SPH spline kernel as a smoothing shape for the gravitational forces.

Since the hydrodynamical forces are local forces only, one has to ensure that each gas particle has about N_{SPH} neighbours within the smoothing length, to ensure a good sampling. In gravity this is not needed as particles with no direct neighbours still feel the other particles via the mesh force. On the other hand, no matching between short-range and long-range forces is needed, so that the size of the gas chaining mesh cells need not be an integer multiple of the density-potential mesh cell size. One could set the chaining mesh cell size to be equal to two times the largest smoothing length. With this choice, the SPH neighbours for all gas particles lie within the nearest twenty-six cells (in three dimensions).

It is immediately clear that such a choice would lead to a very coarse chaining mesh if the simulation contains a low-density region. Therefore it is better to use a kind of adaptive refinement implementation of the chaining mesh. First the SPH loop is performed for particles with large h, on a very coarse mesh. Then the SPH loop is computed for a range of smaller h on a finer mesh and so on until all gas particles have been processed.

5.7 Timestepping

5.7.1 Integration schemes

In numerical simulations, the equation of motion is solved in discrete time steps dt. At a certain timestep n (at time $t = n\,dt$), we denote the array of the positions, velocities, forces, ... for all particles, as $\boldsymbol{x}_n$, $\boldsymbol{v}_n$, $\boldsymbol{F}_n$, ... Several possible schemes can be used to perform timestepping. When choosing a particular scheme, one has to think about accuracy, stability, computational cost and memory constraints.

Suppose for simplicity that we are dealing with a conservative system, i.e. the forces only depend on the particle positions. Moreover we suppose that all particles have unit mass, so that $\boldsymbol{a} = \boldsymbol{F}$. Couchman et al. (1995) considered three different time integration schemes; Runge-Kutta, Leapfrog and a Predict-Evaluate-Correct (PEC) scheme.

The Leapfrog scheme is a popular integration scheme that uses the velocity array at intermediate timesteps

$$\begin{aligned} \boldsymbol{r}_n &= \boldsymbol{r}_{n-1} + \boldsymbol{v}_{n-1/2}dt, \\ \boldsymbol{v}_{n+1/2} &= \boldsymbol{v}_{n-1/2} + \boldsymbol{F}(\boldsymbol{r}_n)dt. \end{aligned} \tag{5.86}$$

This scheme is especially useful in systems with conservative forces, as is the case for purely gravitational systems. However, if the forces also depend on the velocities, as in hydrodynamics, then $\boldsymbol{v}_n$ must be also evaluated, since the use of $\boldsymbol{v}_{n-\frac{1}{2}}$ in the hydrodynamical force calculation significantly reduces the accuracy (Couchman et al., 1995).

An alternative, related scheme is the *Prediction-Evaluation-Correction* scheme (PEC). In this scheme the positions are predicted first,

$$\boldsymbol{r}'_n = \boldsymbol{r}_{n-1} + \boldsymbol{v}_{n-1}dt + \boldsymbol{F}(\boldsymbol{r}'_{n-1})\frac{dt^2}{2}. \tag{5.87}$$

Then the forces are evaluated at the predicted positions, and finally the positions and the velocities are corrected as follows:

$$\begin{aligned} \boldsymbol{r}_n &= \boldsymbol{r}_{n-1} + \boldsymbol{v}_{n-1}dt + \boldsymbol{F}(\boldsymbol{r}'_{n-1})\frac{dt^2}{2}, \\ \boldsymbol{v}_n &= \boldsymbol{v}_{n-1} + \frac{1}{2}[\boldsymbol{F}(\boldsymbol{r}'_{n-1}) + \boldsymbol{F}(\boldsymbol{r}'_n)]dt. \end{aligned} \tag{5.88}$$

(5.89)

To start the integration, a first evaluation of the forces is required.

From the tests presented in Couchman et al. (1995), the PEC scheme comes out best in terms of accuracy, energy and entropy conservation, stability and performance. Therefore, this scheme is used in the HYDRA code.

5.7.2 The timestep dt

Now, how do we choose the timestep dt? On the one hand, the timestep should be large enough, so that the number of timesteps needed to cover the desired timespan to be simulated is as small as possible. On the other hand, it should be small enough, in order to achieve a given accuracy.

In order to optimize the timestepping, a variable timestep can be used. For gravitational systems, the optimal timestep is determined by the accelerations. If the accelerations are small, large timesteps can

be used, while smaller timesteps are needed if accelerations become large. The acceleration timestep dt_a is defined as

$$dt_a = \min_i \left(\sqrt{\frac{\epsilon}{|a_i|}} \right), \tag{5.90}$$

where i ranges over all the particles, ϵ is the equivalent Plummer softening used in the simulation and $|a_i|$ is the magnitude of the acceleration of particle i.

Similarly, for the gas particles, a velocity timestep dt_v is defined as

$$dt_v = \min_{ij} \left(\sqrt{\frac{h_i^2}{v_{ij}^2 + \epsilon_i}} \right) \tag{5.91}$$

where i and j range over all the gas particles, h_i is the SPH smoothing length of particle i, ϵ_i is its specific energy and v_{ij} is the relative velocity of gas particles i and j. The relative velocity condition keeps control of the force in regions where the velocities change abruptly, such as in shocks, while the specific energy condition makes sure that the *Courant condition* is satisfied. The Courant condition states that the timestep dt must be small enough that the fastest soundwaves do not outrun the spatial resolution h, and the sound speed in a gas particle is given by $c_s = \sqrt{10/9\epsilon}$.

Finally, the overall temporal timestep dt is set to

$$dt = min(0.25dt_a, 0.4dt_v). \tag{5.92}$$

Some codes also consider *spatially* variable timesteps to further optimize the simulations. However this is not implemented in HYDRA.

5.8 Using the HYDRA code

This is a general introduction and some remarks to the use of the HYDRA code. For a more complete account of the program structure and it's usage, see the `DOCUMENTATION` file which comes with the public HYDRA distribution. What follows refers to version 4.2 of HYDRA, and can differ slightly from other versions.

5.8.1 Input and output

The initial setup for the simulation is presented to the code in binary files. The final endstate and temporary snapshots are also written to binary files, which can be used as input files for subsequent runs.

A HYDRA input file consists of two parts: a header and a data part. The header contains three information blocks. The first block holds information on parameters such as time, timestep and potential, kinetic and thermal energy. The second block holds start values of the total number of particles. Finally the last block are the times at which an output file needs to be produced. The header information is shared in the program via common blocks which are grouped in the include file `pinfo.inc`.

The initial data for the particles are read next. First come the particle types (none, dark, gas, star). Then come the masses, the positions and the velocities. In case of gas particles, the smoothing lengths, the specific energies and the densities are also specified. It is possible to also store the accelerations (after the velocities), if one wants identical startup conditions. Else, the accelerations will be calculated,

which can yield slightly different results. Also the metallicities of the gas and star particles can be stored. The data arrays are shared in common blocks that are grouped in the `rvarrays.inc` file.

The output data files are named d*irun*.*itime*, with *irun* the number of the simulation run and *itime* the output timestep. At fixed intervals, backup files are stored, alternatively in d*irun*.data and d*irun*.back.

5.8.2 Units

The initial conditions data given to HYDRA contain values with respect to certain physical units. The units are shared in a common units block in the include file `units.inc` and are initialized in the `inunits` subroutine. By setting the length unit `lunit` (in cm), the time unit `tunit` (in s) and the mass unit `munit` (in $M_\odot$), all other units are fixed. Beware of the fact that by choosing e.g. the length unit `lunit` $= 1$ kpc and the time unit `tunit` $= 1$ Gyr, the velocity unit `vunit` becomes $0.977\,\mathrm{km\,s^{-1}}$. At startup, HYDRA displays the units in which it is currently compiled, so one has to make sure that the units in which the data of the initial conditions file are stored, and the units with which HYDRA is compiled, are the same.

HYDRA can be compiled with periodic and with isolated boundary conditions. In case of periodic conditions, the simulation box axes are always $[0, 1]$ in length units.

5.8.3 Array sizes

In FORTRAN, the size of an array at declaration should be a fixed number. By choosing a maximum number for the amount of dark matter and gas particles (and perhaps star particles), the maximum optimal number of density-potential mesh cells can be estimated. Also the maximal number of chaining mesh cells, the maximum length of linked lists, etc. needs to be fixed. All these parameters are set and shared in the include file `psize.inc`.

5.8.4 Starting a simulation

To start a simulation, some last parameters need to set. These are read in from the file `prun.dat`. This file contains the initial conditions input file name, the number of the simulation, the timestep interval for backup file dumps, the softening parameter, etc...

As the simulation proceeds, the total kinetic, thermal and potential energy at every timestep is written in the file pr*irun*.log.

Chapter 6

Ram-pressure stripping in a cluster environment

6.1 Introduction

Dwarf elliptical galaxies (dEs) are commonly known as gas-less systems, having lost their interstellar medium (ISM) either through a galactic wind or through ram-pressure stripping by the intragroup or intracluster medium (ICM for both). In this chapter we investigate numerically the effect of ram pressure on low-mass systems, using the N-body/SPH code described in chapter 5, which we adapted to perform such simulations.

The ram-pressure hypothesis leans on the abundance of dEs in clusters of galaxies whereas they appear to be much less abundant in the field (Ferguson & Binggeli, 1994). In general, a morphology-density relation for galaxies exists; the fraction of early-type to late-type galaxies increases with galaxy density or decreases with cluster-centric radius (Dressler, 1980; Goto et al., 2003), indicating that the environment plays an important role in the evolution of galaxies in general, and of dwarf galaxies in particular. Apart from being ram-pressure stripped by the ICM, dwarf galaxies are also expected to be *harassed* due to interactions with giant cluster members (Moore et al, 1998) and *threshed* due to tidal disruption forces in the very center of clusters (Bekki et al., 2001; Trujillo et al., 2002).

Satellite X-ray observations reveal that most groups and clusters of galaxies contain a hot, dilute ICM (Forman & Jones, 1982; Jones & Forman, 1999; Mulchaey, 2000), hence galaxies moving around in groups and clusters will experience a ram pressure

$$P_{\rm ram} = \rho_{\rm ICM} v_{\rm gal}^2, \tag{6.1}$$

which depends on the density $\rho_{\rm ICM}$ of the ICM and the relative velocity of the galaxy with respect to the ICM $v_{\rm gal}$. In a study of 17 bright spiral galaxies, Cayatte et al. (1994) found these galaxies to have rather normal stellar disks and normal molecular gas structures, while being deficient in H I. This points to ram pressure stripping as the main gas-removal mechanism, as opposed to tidal interactions which would also distort the structure of the molecular gas and the stars (Moore et al, 1998). Moreover, Cayatte et al. (1994) find a trend of increasing H I deficiency with distance to the centre of the Virgo cluster. From a compilation of H I observations of dEs in the Virgo cluster, Conselice et al. (2003a) also find that dEs with an H I detection lie preferentially towards the outskirts of the cluster. Finally, the dEs with an Hα detection in the Fornax cluster survey of Drinkwater et al. (2001) tend to reside in the outskirts. These trends suggest that galaxies on radial orbits through the cluster will get stripped of their

ISM while galaxies on more circular orbits in the outskirts of the cluster can retain their ISM over much longer timescales. On the other hand, galaxies residing in the cluster for a long time will have lost their gas while recent acquired galaxies will still contain an ISM. Observations of several individual galaxies that are undergoing ram pressure stripping can be found in the literature: e.g. NGC4479 (Lucero et al., 2005), NGC4522 (Kenney et al., 2004), NGC4569 (Vollmer et al., 2004), NGC4654 (Vollmer, 2003). Moreover, the compression of the ISM due to the ram pressure can lead to a burst of star formation in galaxies that are infalling onto a cluster, as observed by Gavazzi et al. (2003). Analytical calculations show that the star formation rate can increase by a factor of two as a galaxy falls into a cluster (Fujita & Nagashima, 1999). N-body/SPH simulations of individual galactic molecular clouds confirm that the combined thermal and ram pressure of the ICM can induce a starburst (Bekki & Couch, 2003).

Simulations of ram pressure stripping have thus far mostly concentrated on giant galaxies. The lack of an ISM in cluster giant ellipticals was numerically studied by Lea & De Young (1976) and Gisler (1976) who performed 2D hydrodynamical simulations of ram pressure stripping from elliptical galaxies. They showed that substantial stripping occurs and that ram pressure stripping is more effective than galactic winds in removing the ISM from an elliptical galaxy. Later, 2D hydrodynamical simulations by Takeda et al. (1984) showed that ram pressure stripping occurs in two different processes, namely sudden stripping of the ISM on the one hand and continuous stripping on the other. Gaetz et al. (1987) investigate the effect of including a galactic dark matter halo and of cooling and star formation in their simulations of ram pressure stripping. Recently, high resolution simulations of ellipticals falling into a cluster have been performed by Acreman et al. (2003), focusing on the X-ray properties of the wake that forms behind the galaxy as it plows through the cluster medium.

Ram pressure stripping has also been invoked as a mechanism to transform spiral galaxies into S0s. Farouki & Shapiro (1980) ran 3D particle simulations of disk galaxies subjected to ram pressure and found that the number of stripped ISM particles depended on the ICM properties. However, their simulations had a low resolution (1000 star particles, 100 gas particles) due to the limited computing resources at that time. More recent simulations of ram pressure on spiral galaxies, using 3D N-body/SPH codes (Abadi et al., 1999; Schulz & Struck, 2001) show that the inclination of the disk with respect to the motion of the galaxy is an important parameter in the stripping. Spirals that enter the ICM face-on lose much more of their ISM than spirals that move edge-on through the ICM. High resolution 3D hydrodynamical simulations by Quilis et al. (2000), show that ram pressure stripping could account for the transformation of spirals to S0s within a few 100 Myr. Finally, Roediger & Hensler (2005) present a very nice study of the dependence of ram pressure stripping in disk galaxies on a variety of ICM and galaxy parameters using 2D hydrodynamical simulations.

In order to explain the observed H I deficiency observed in Virgo cluster spiral galaxies, Vollmer et al. (2001) and Vollmer (2003) use a sticky particle code to simulate the passing of a disk galaxy through the Virgo cluster. Taking explicitly into account the time-dependence of the ram pressure, which depends on the orbit of the galaxy in the cluster, they where able to reproduce the observed features of on-going stripping in disk galaxies.

Due to their shallow potential wells and low escape velocities, dwarf galaxies are expected to be more susceptible to stripping than their giant counterparts. A 2D hydrodynamical study of dEs in a cluster environment was conducted by Mori & Burkert (2000), who found that small dEs are instantaneously stripped of their ISM, while more massive dEs lose their ISM over longer timescales, mainly via Kevin-Helmholtz instabilities. Marcolini et al. (2003) simulated disky dwarf galaxies in groups, where the ram pressure is lower. Their 3D hydrodynamical simulations show that the ISM of dwarfs can still be stripped in groups and in the outskirts of clusters. Moreover, they show that the outflow of metal-enriched gas in supernova-driven galactic winds can be significantly reduced due to the presence of an ICM. The thermal pressure of the ICM pushes part of the gas lost by the galactic wind back on to the galaxy, thereby prohibiting the escape of metal-enriched gas (Marcolini et al., 2004).

In this chapter, we want to model a gas-rich dwarf elliptical galaxy moving through an ICM. Typical

velocities of galaxies are comparable to the three-dimensional velocity dispersion of galaxies in a cluster, ranging from a few $100\,\mathrm{km\,s^{-1}}$ in groups, $\sim 1000\,\mathrm{km\,s^{-1}}$ in intermediate-mass clusters like the Virgo cluster and up to a few $1000\,\mathrm{km\,s^{-1}}$ in rich clusters like the Coma cluster. The density of the ICM ranges from about $10^{-5}\,\mathrm{cm^{-3}}$ in groups and in cluster outskirts, to some $10^{-3}\,\mathrm{cm^{-3}}$ in the centre of the Coma cluster. Typical temperatures of the ICM measured from X-ray observations range from $1-4\,\mathrm{keV}$ ($0.23-1.0\times10^{7}\,\mathrm{K}$) in early cluster systems such as the Virgo cluster, up to 10 keV ($2.3\times10^{7}\,\mathrm{K}$) in evolved cluster systems such as the Coma cluster (Forman & Jones, 1982). Generally, the temperature of the ICM in simulations is chosen to give a sound speed,

$$c_{\mathrm{ICM}} = \sqrt{\frac{\gamma k_B T_{\mathrm{ICM}}}{\mu m_p}}, \tag{6.2}$$

that is less than the velocity of the galaxy relative to the ICM, or in other words, to have a supersonic ICM flow. This is done to prevent the upstream propagation of sound waves and numerical perturbations, which could interfere with the inflow boundary conditions at the beginning of the simulation box (Marcolini et al., 2003). The galaxy's velocity through the ICM is mostly set to the galaxy-galaxy velocity dispersion of the cluster under consideration. Although the effects of stripping are also slightly dependent on the Mach number of the ICM wind

$$M = \frac{v_{\mathrm{gal}}}{c_{\mathrm{ICM}}}, \tag{6.3}$$

the main parameter for stripping is the ram pressure (Roediger & Hensler, 2005).

In most simulations the ICM is modelled as a single fluid, whereas in reality the highly ionized ICM consists of an ion and an electron fluid. The ram pressure of the ICM should thus be split into an electron and an ion fluid contribution

$$P_{\mathrm{ram}} = \rho_{\mathrm{ICM}} v_{\mathrm{gal}}^2 = (\rho_i + \rho_e) v_{\mathrm{gal}}^2 = P_i + P_e \approx P_i, \tag{6.4}$$

where ρ_i and ρ_e are, respectively, the ion and electron densities of the ICM. Keeping in mind that the electron mass is about 2000 times smaller than the proton mass, the electron contribution to the ram pressure will be negligible. The decoupling of the electron and ion fluids could in principle be modelled using the SPH technique, by including Coulomb forces between electron and ion particles. However, the resolution at which these forces play a role is so small compared to the resolution of the phenomena we want to describe here, that such an approach is not justified (each particle would represent an electron and ion cloud, smoothed over several parsecs). Therefore, the ICM is modelled as a single fluid with mean molecular weight $\mu = 60$, corresponding to an ionized hydrogen-helium gas with a number density ratio $n_{\mathrm{He}} = 0.1 n_{\mathrm{H}}$. Moreover, Portnoy et al. (1993) studied the difference between the single-fluid and the two-fluid description for a spherical galaxy, and found no difference for the amount of gas remaining inside the galaxy. Hence, we can safely adopt the one-fluid approximation.

Finally, numerical simulations of ram pressure stripping are usually performed in the galaxy's rest frame, because we are especially interested in the effect of ram pressure on the galaxy. The relative motion of the galaxy through the ICM is then translated into an ICM wind. This has the advantage that one can restrict the simulation to a box centered around the galaxy, so that not the cluster as a whole needs to be modeled. The ISM stripped from a galaxy will eventually become part of the ICM. Ram pressure stripping can thus be invoked as a mechanism to enrich the ICM (see e.g. Aguirre et al. (2001) for an account on the various mechanisms for ICM metal enrichment).

6.2 Analytical estimates of ram pressure stripping

6.2.1 Instantaneous stripping

Gunn & Gott (1972) were the first to appreciate the effect of a hot, dilute ICM on a galaxy moving through a cluster. Based on the simple estimate that the ISM of a spiral galaxy that falls face-on into the ICM is completely stripped if the ram pressure exceeds the gravitational binding force, Gunn & Gott (1972) concluded that ram pressure stripping is a very effective means of removing the ISM from spiral galaxies that move through the core regions of a typical cluster. Their analysis allows to analytically estimate the truncation radius for the ISM. Consider cylindrical coordinates (R, z) centered on the disk galaxy, which is falling face-on through the ICM. The z-axis is then the direction of the ICM wind, perpendicular to the disk. Given a model for the galaxy components (dark matter, stellar disk and bulge and gas disk), one can calculate the radial binding force per unit area $\frac{\partial \Phi}{\partial z}(R, z)\Sigma_{\rm ISM}(R, z)$, which depends on the gradient of the galactic gravitational potential Φ in the z-direction (equal to the z-component of the gravitational acceleration), and the surface density $\Sigma_{\rm ISM}$ of the gas disk. The stripping radius is then the radius $R_{\rm strip}$ where the gravitational binding force equals the ram pressure force. However, as the acceleration vector due to the gravitational potential in the central plane of the galaxy is perpendicular to the wind direction, the binding force is zero. Hence, the ISM is displaced from the galactic plane. The maximum restoring force is found at some distance behind the galactic plane and depends on both the extraplanar distance z, behind the original disk, and the galactocentric distance R. As mentioned by Schulz & Struck (2001) and Roediger & Hensler (2005), the effective potential well has been displaced by the addition of the ram pressure force, so that even if the ISM remains bound, it is displaced with respect to the original disk and it is not clear where the value of $R_{\rm strip}$ should be calculated (Roediger & Hensler, 2005).

Another analytic estimate for instantaneous stripping is due to Mori & Burkert (2000) and compares the ram pressure to the central gas pressure in the ISM. If the ram pressure exceeds the central thermal pressure of the galaxy, the ISM is immediately stripped. In all other cases, the stripping radius can be estimated as the radius at which the thermal pressure equals the ram pressure. The stripping radius derived using this criterion is always smaller than that derived from the Gunn & Gott (1972) criterion (see Roediger & Hensler (2005)).

The timescale for the instantaneous stripping can be estimated from the time needed to displace the ISM over a distance z relative to the host galaxy. Initially starting with $z = 0$ and $v_z = 0$, we can write

$$z = \frac{1}{2} a_z t_{\rm strip}^2, \tag{6.5}$$

assuming a constant acceleration in the z direction due to the ram pressure,

$$a_z = \frac{P_{ram}}{\Sigma_g}, \tag{6.6}$$

with Σ_g the surface density of the ISM in the wind direction. The stripping time becomes

$$t_{\rm strip} = \sqrt{\frac{2z\Sigma_g}{P_{\rm ram}}}. \tag{6.7}$$

The stripping timescale depends on the strength of the ram pressure and on the amount of matter that needs to be displaced. The estimate does not include deceleration due to the gravitational potential, which will prolong the stripping time for large DM haloes or small ram pressures. Instantaneous stripping times range from a few 10^6 yr for small galaxies/low ram pressure, to a few 100 Myr for large galaxies/high ram pressure.

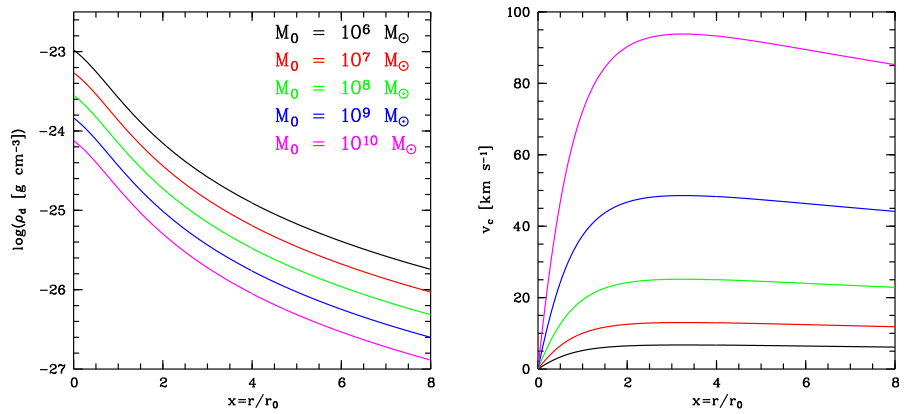

Figure 6.1: The Burkert dark matter model. *Left panel:* The dark matter density profiles for M_0 ranging from 10^6 to $10^{10}\,\mathrm{M}_\odot$, plotted against the scaled radius $x = r/r_0$. *Right panel:* The circular velocity profiles of the Burkert model for the same core mass range. The circular velocity has a maximum value at the scaled radius $x = 3.24$.

6.2.2 Continuous stripping

Continuous stripping occurs due to Kelvin-Helmholtz (KH) instabilities near the ICM-ISM interface (Nulsen, 1982; Mori & Burkert, 2000). Since the ICM is usually much hotter than the ISM (with typically $T_{\rm ICM} \geqslant 10^2 - 10^3 T_g$), continuity of pressure between the hot and cold gas means that the ISM will be considerably denser than the ICM. According to the analysis of Nulsen (1982), taking into account compressibility and viscosity, an estimate of the mass loss rate due to KH instabilities from a spherical galaxy with radius R is

$$\dot{M} = \frac{F_D}{v_{\rm gal}} = \pi R^2 \rho_{\rm ICM} v_{\rm gal}, \tag{6.8}$$

where $F_D = \pi R^2 P_{\rm ram}$ is the viscous drag force. The galaxy's gravity will only affect the stripping flow significantly if the gravitational restoring force on the gas leaving the galaxy is larger than the drag force or

$$F_D > \left(\frac{GM}{R^2}\right)\left(\dot{M}\frac{R}{v_{\rm gal}}\right), \tag{6.9}$$

which reduces to

$$\frac{GM}{R} > v_{\rm gal}^2 \tag{6.10}$$

The continuous stripping mass loss rate is quite small, but works over long timescales. Hence it can become important after the instantaneous stripping of the outer layers of a more massive galaxy.

6.3 The Burkert dark matter halo

Burkert (1995) derived an empirical density profile for the dark matter (DM) distribution from observations of the H I rotation curves of dwarf spiral galaxies. This DM halo has been used by Mori &

Burkert (2000) to simulate ram pressure stripping from spherically symmetric dEs. Also in the ram pressure simulations of Roediger & Hensler (2005), the Burkert DM halo is adopted for disk galaxies. Schulz & Struck (2001) showed that the DM halo is not affected by ram pressure. Therefore we opted to implement the DM contribution as a static DM potential in order to save computational time.

6.3.1 The density profile

Burkert (1995) tried different spherically symmetric density distributions for the dark matter. The radial DM density profile ρ_d that provided the best match between H I rotation curves observed in dwarf galaxies and rotation curves predicted by different models, is

$$\rho_d(r) = \frac{\rho_{d,0}}{(1+r/r_0)(1+(r/r_0)^2)}, \tag{6.11}$$

with $\rho_{d,0}$ the central density of the DM and r_0 a scaling radius, called the *core radius*. The Burkert density profile has a central *core*, as opposed to other galaxy density profiles that have a central *cusp* (e.g. the isothermal distribution (Binney & Tremaine, 1987) or the NFW distribution (Navarro et al., 1996)). In the right panel of Figure 6.1 we show the DM density profiles of the Burkert model for core mass M_0 ranging between 10^6 and 10^{10} $M_\odot$.

Inserting this density into the Poisson equation, we can calculate the DM gravitational potential

$$\begin{aligned}\Phi_d(r) &= -4\pi G\rho_{d,0}r_0^2\left[\frac{1}{x}\int_0^x \frac{x'^2dx'}{(1+x')(1+x'^2)} + \int_x^\infty \frac{x'dx'}{(1+x')(1+x'^2)}\right] \\ &= -4\pi G\rho_{d,0}r_0^2\left[\frac{1}{x}I_1(x) + I_2(x)\right],\end{aligned} \tag{6.12}$$

with $x = r/r_0$. The integrals I_1 and I_2 become

$$I_1(x) = \int_0^x \frac{1+x'^2-1}{(1+x')(1+x'^2)}dx' = \ln(1+x) - \int_0^x \frac{dx'}{(1+x')(1+x'^2)} \tag{6.13}$$

$$I_2(x) = \int_0^x \frac{1+x'-1}{(1+x')(1+x'^2)}dx' = \frac{\pi}{2} - \mathrm{arctg}(x) - \int_x^\infty \frac{dx'}{(1+x')(1+x'^2)}, \tag{6.14}$$

so that we have to calculate

$$\begin{aligned}I_3 = \int \frac{dx'}{(1+x')(1+x'^2)} &= \int\left(\frac{A}{1+x'} + \frac{B+Cx'}{1+x'^2}\right)dx' \\ &= \frac{1}{2}\left(\int\frac{dx'}{1+x'} + \int\frac{dx'}{1+x'^2} - \int\frac{x'dx'}{1+x'^2}\right) \\ &= \frac{1}{2}\left(\ln(1+x') + \mathrm{arctg}(x') - \frac{1}{2}\ln(1+x'^2) + C\right).\end{aligned} \tag{6.15}$$

Keeping in mind that

$$\lim_{x\to\infty}\left[\ln(1+x) - \frac{1}{2}\ln(1+x^2)\right] = \lim_{x\to\infty}\left[\ln(x) - \frac{1}{2}\ln(x^2)\right] = 0, \tag{6.16}$$

the DM potential finally reads

$$\Phi_d(r) = -\pi G\rho_{d,0}r_0^2\left\{\pi + 2\left(1+\frac{1}{x}\right)[\ln(1+x) - \mathrm{arctg}(x)] - \left(1-\frac{1}{x}\right)\ln(1+x^2)\right\}. \tag{6.17}$$

The central value of the potential is the finite value $\Phi_{d,0} = -\pi^2 G\rho_{d,0} r_0^2$.
The gravitational force $\boldsymbol{F}$ acting on a test particle at position $\boldsymbol{r}$ in this gravitational potential is

$$\begin{aligned} \boldsymbol{F}(\boldsymbol{r}) = F(r)\boldsymbol{e_r} &= -\frac{\mathrm{d}\Phi_d}{\mathrm{d}r}\boldsymbol{e_r} \\ &= \pi G\rho_{d,0} r_0 \left\{ \frac{1}{x}\left[2\,\mathrm{arctg}(x) - 2\ln(1+x) - \ln(1+x^2)\right]\right\}\boldsymbol{e_r}, \end{aligned} \tag{6.18}$$

with $\boldsymbol{e_r}$ the radial unit vector. At each timestep, the acceleration due to the DM gravitational force on a particle i is obtained from

$$\boldsymbol{a}_i(\boldsymbol{r}) = -m_i \frac{\mathrm{d}\Phi(r_i)}{\mathrm{d}r}\boldsymbol{e}_{r_i}, \tag{6.19}$$

with m_i the mass of the particle.
The DM mass distribution is given by

$$\begin{aligned} M_d(r) &= 4\pi \int_0^r \rho(r') r'^2 dr' \\ &= \pi\rho_{d,0} r_0^3 \left\{2\left[\ln(1+x) - \mathrm{arctg}(x)\right] + \ln(1+x^2)\right\}. \end{aligned} \tag{6.20}$$

The total mass of the Burkert model is logarithmically diverging. The core mass M_0 is defined as the mass within the core radius r_0:

$$M_0 = M(r_0) = \pi\rho_{d,0} r_0^3 \left[3\ln(2) - \frac{\pi}{2}\right]. \tag{6.21}$$

6.3.2 The circular velocity

The circular velocity curve generated by the Burkert DM distribution is given by

$$v_c(r) = \sqrt{\frac{GM_d(r)}{r}}. \tag{6.22}$$

Hence, the circular velocity at the core radius, v_0, is given as

$$v_0 = \sqrt{\frac{GM_0}{r_0}} \tag{6.23}$$

We can find the radius at which the maximum circular velocity is reached by numerically solving the equation $dv_c/dr = 0$ or

$$\frac{\mathrm{d}{v_c}^2}{\mathrm{d}r} = \frac{M_d(r)}{r^2} - 4\pi r\rho_d(r) = 0, \tag{6.24}$$

with respect to r, and we find that at the finite radius $r = 3.24 r_0$, the circular velocity reaches its maximum value. In the right panel of Figure 6.1 we show the circular velocity profiles of the Burkert model for core masses ranging between 10^6 and 10^{10} $\mathrm{M}_\odot$.

6.3.3 Scaling relations

The quantities $\rho_{d,0}$ and r_0 in the Burkert density equation are in principle free parameters. Burkert (1995) investigated the question whether there exists a relation between these two parameters. Instead of studying $\rho_{d,0}$, which cannot be observed directly, he chose as free parameter the rotational velocity v_0. The quantities r_0 and v_0 were determined by fitting the theoretically predicted rotation curve to the observed rotation curves of low-mass disk galaxies which are supposed to be DM dominated at r_0. The gravitational potential of the visible matter was first subtracted from the total velocity curves. A strong, linear correlation was found between r_0 and $v_0^{1.5}$. Assuming spherical symmetry, the following scaling relations were derived (Burkert, 1995)

$$\begin{aligned} v_0 &= 17.7 \left(\frac{r_0}{\mathrm{kpc}}\right)^{2/3} \mathrm{km\,s^{-1}} \\ M_0 &= 7.2 \times 10^7 \left(\frac{r_0}{\mathrm{kpc}}\right)^{7/3} \mathrm{M_\odot} \\ \rho_{d,0} &= 4.5 \times 10^{-2} \left(\frac{r_0}{\mathrm{kpc}}\right)^{-2/3} \mathrm{M_\odot\,pc^{-3}} \end{aligned} \tag{6.25}$$

which translate into

$$r_0 = 3.07 \left(\frac{M_0}{10^9\,\mathrm{M_\odot}}\right)^{3/7} \mathrm{kpc} \tag{6.26}$$

$$\rho_{d,0} = 1.46 \times 10^{-24} \left(\frac{M_0}{10^9\,\mathrm{M_\odot}}\right)^{-2/7} \mathrm{g\,cm^{-3}}, \tag{6.27}$$

so that we have a one-parameter family of models with the core mass M_0 as free parameter.

6.4 Using HYDRA for ram pressure simulations

N-body/SPH codes have been used to study ram pressure stripping of disk galaxies (Abadi et al., 1999; Schulz & Struck, 2001). In particular, Schulz & Struck (2001) (hereafter SS) used the HYDRA code to simulate the evolution of a small disk galaxy in a cluster environment. In this section, we reproduce these simulations as a first test of our implementation of ram pressure stripping.

The units used in these simulations are $10^4\,\mathrm{M_\odot}$ for `munit`, $100\,\mathrm{kpc}$ for `lunit` and $100\,\mathrm{Myr}$ for `tunit`. This gives $977\,\mathrm{km\,s^{-1}}$ as velocity unit, $6.81 \times 10^{-10}\,\mathrm{cm^{-3}}$ as density unit and $4.6 \times 10^5\,\mathrm{K}$ as temperature unit. The periodic boundaries are set at 0 and 1 `lunit` in x, y and z axes, which gives a simulation box of total volume $10^6\,\mathrm{kpc}^3$.

6.4.1 The galaxy model

The dark matter halo

In SS, the DM halo was represented by 10 000 particles, distributed according to a spherical symmetric, isothermal density distribution. However, they showed that the DM halo is not affected by ram pressure. Therefore we opted to use a static DM potential to save computing time. We adopt the DM density distribution proposed by Burkert (1995), which has been used in other ram pressure simulations as well (Mori & Burkert, 2000; Roediger & Hensler, 2005).

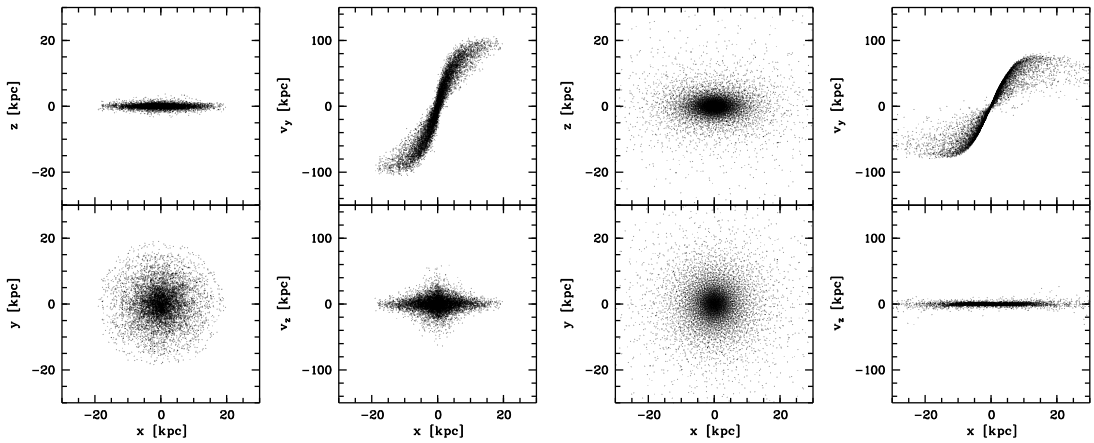

Figure 6.2: The relaxed distribution of the 9550 star and 9550 gas particles. In the leftmost panels, the $x-y$ and $x-z$ projections of the initial stellar distribution are shown, while the second panels from the left show the z and y stellar velocity component versus to the x coordinate. The stellar distribution is unaffected by the ram pressure and only contributes to the gravitational force. In the third from the left panels, the $x-y$ and $x-z$ projections of the gas distribution are shown, while the rightmost panels show the z and y gas velocity component versus to the x coordinate. Although initially distributed in the same manner as the stellar component the thermal pressure puffs up the gas distribution.

Both the isothermal and the Burkert distributions are unbound in space, so a boundary radius had to be introduced by SS in order to simulate the DM distribution. The boundary radius was $r_b = 30\,\mathrm{kpc}$, and the total mass of the DM halo inside this radius was $M_{d,\mathrm{tot}} = 6 \times 10^{10}\,\mathrm{M}_\odot$. We will use the same boundary radius and total DM halo mass as SS. In order to derive the core mass M_0 and core radius r_0 of the corresponding Burkert distribution, we numerically solve the equations

$$\begin{aligned} M_0 &= M_{d,\mathrm{tot}} \frac{3\ln(2) - \frac{\pi}{2}}{2\ln\left(1+\frac{r_b}{r_0}\right) + \ln\left(1+\frac{r_b^2}{r_0^2}\right) - 2\,\mathrm{arctg}\left(\frac{r_b}{r_0}\right)} \\ r_0 &= 3.07 \left(\frac{M_0}{10^9\,\mathrm{M}_\odot}\right)^{3/7} \mathrm{kpc}, \end{aligned} \tag{6.28}$$

which gives $r_0 = 8.0\,\mathrm{kpc}$ and $M_0 = 9.3 \times 10^9\,\mathrm{M}_\odot$. The corresponding maximum circular velocity $v_{c,\max} = 70.8\,\mathrm{km\,s^{-1}}$ is reached at a galactocentric distance of 26 kpc. These values are typical for a small disk or large dwarf galaxy.

The stars and gas particles

The 9550 gas and 9550 star particles in SS had individual masses of $3 \times 10^5\,\mathrm{M}_\odot$, summing to $5.73 \times 10^9\,\mathrm{M}_\odot$, equally divided over stars and gas, representing a relatively small, gas-rich disk galaxy. The particles were initially distributed in a rotating disk, on circular orbits, with a circular velocity implied by the DM halo, augmented by a small random three-dimensional velocity component.

In our simulations, we distributed the star and gas particles over exponential disks of mass $M_{\mathrm{disk}} =$

$2.87 \times 10^9\,\mathrm{M}_\odot$, with density profile (in cylindrical coordinates) (Abadi et al., 1999)

$$\rho_{\rm disk}(R,z) = \frac{M_{\rm disk}}{4\pi R_{\rm disk}^2 z_{\rm disk}} \exp\left(-\frac{R}{R_{\rm disk}}\right) \mathrm{sech}^2\left(\frac{z}{z_{\rm disk}}\right), \tag{6.29}$$

with disk scale-lengths $R_{\rm disk} = 4\,\mathrm{kpc}$ and $z_{\rm disk} = 1\,\mathrm{kpc}$. The rotational velocity in the disk plane is given by the Burkert circular velocity at radius R and the z component of the velocity is set to zero. The particle positions are generated using a Monte-Carlo acceptance-rejection technique. For the gas particles, we also set the initial density, temperature ($T_i = 10^4\,\mathrm{K}$) and smoothing length ($h_i = 3/\sqrt[3]{n_i}$ with $n_i = \rho_i/(\mu m_p)$).

We set up the stellar disk first and let it relax inside the Burkert DM potential for about 1000 timesteps (corresponding to about 2.5 Gyr) (Figure 6.2). Then we inserted the gas particles, which have an initial temperature of $10^4\,\mathrm{K}$. The thermal pressure makes the gas disk puff up in the z direction. The initial gas distribution of SS shows a somewhat more flattened gas disk (Figure 6.2). One possible explanation for this difference is that the density distribution of the isothermal sphere is much more centrally concentrated that the Burkert density distribution, so that the gas cannot expand so easily in the z direction due to the larger gravitational force.

The mass of the ISM gas particles is 10 times that of the ICM gas particles. The mass of the ICM particles should not be larger than that of the ISM particles, because then, they would carry too much momentum and they would punch holes in the galaxy disk (Abadi et al., 1999).

6.4.2 Setting up the ICM flow

The ICM flow was modeled by inserting 80 000 particles in 50 layers placed equidistantly along the z-axis of the simulation box. In each layer, 1600 particles are randomly distributed. This setup has the same overall resolution as a 43^3 cells grid. However, the particle nature of the SPH formalism ensures that a higher resolution is automatically achieved in regions of increased density.

Using an ICM particle mass of $3 \times 10^4\,\mathrm{M}_\odot$ results in an ICM density of $\rho_{\rm ICM} = 1.6 \times 10^{-28}\,\mathrm{g\,cm^{-3}}$ or $n_{\rm ICM} = 1.6 \times 10^{-4}\,\mathrm{cm^{-3}}$. The ICM velocity along the z-axis was set to -1 `vunit`, corresponding to $-977\,\mathrm{km\,s^{-1}}$, while the x and y velocity components were set to zero. Additionally, the temperature of the ICM was $2.3 \times 10^6\,\mathrm{K}$. These are typical values for a cluster environment.

To set up a flow, the simulations are run with periodic boundary conditions on the x, y and z axis. Moreover, all gas particles (ICM as well as ISM) that leave the simulation box at $z = 1$ are randomly played back at $z = 0$, and the gas properties (velocity, density, energy, entropy, smoothing length) are set to the ICM initial values. Hence, the ISM particles that are stripped of the galaxy and leave the simulation box become part of the ICM. Therefore we have to take care that, when a lot of ISM particles are converted to ICM particles, the increase in ICM density does not affect our results.

We let the ICM flow run for about 1000 timesteps so that it could relax from the rigid initial distribution. Actually, since the ICM flow is relaxed anyways, the ICM particles could initially be randomly distributed in the simulation box.

6.4.3 Ram pressure stripping simulations

The evolution of the ISM

Finally, the model galaxy was embedded within the ICM flow and evolved for over 1 Gyr. In Figure 6.3 we show the temporal evolution of the ISM gas particles only. Snapshots were taken at simulated times of 10^8, 2×10^8, 3.5×10^8, 5×10^8, 7.5×10^8 and 10^9 yr. The outer disk is rapidly stripped, within a few

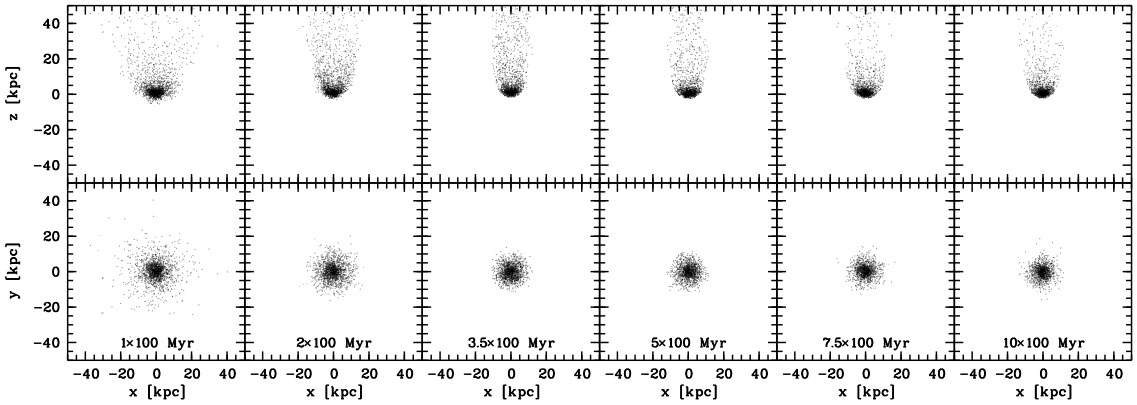

Figure 6.3: Snapshots of the evolution of the ISM in an ICM flow after 10^8, 2×10^8, 3.5×10^8, 5×10^8, 7.5×10^8 and 10×10^8 years. The upper panels show the $x - z$ plane, while the lower panels show the $x - y$ plane. In this figure, every fifth ISM gas particle is plotted.

10^8 yr. Thereafter, stripping occurs at a much slower rate and the ISM in the inner ~ 10 kpc remains bound to the galaxy for more than a Gyr. The evolution of the ISM can be compared to Figures 1 and 2 in SS. The evolution of the truncation of the disk is similar, but our gas disk does not develop spiral arms. This could be due to the more ellipsoidal initial gas distribution.

Meanwhile, the stellar disk is not affected at all by the ram pressure. We do not notice any offset of the stellar disk in the z-direction, and no truncation.

In Figure 6.4 the temporal evolution of the amount of ISM mass left in the simulation box, and in two boxes of different sizes centred on the DM halo of the galaxy is shown. The ISM mass inside the total grid decreases monotonically. However, the ISM mass left in the smaller boxes centred on the galaxy decreases rapidly during the first few 10^8 yr, but rises again after about 4×10^8 yr. After ~ 1 Gyr, about 45 per cent of the ISM is lost from the galactic disk.

How can the fraction of ISM inside a box around the galaxy rise again? In Figure 6.5 we follow the velocity (in the y-plane) of stripped ISM particles. During the first few 10^8 yr, the ISM particles originating from the outer disk are carried away with the ICM flow at a high velocity while later on, fewer particles are stripped from the sides of the truncated disk. Stripped ISM particles in the wake of the galactic disk have velocities that point back to the galaxy, so that the ISM mass is partly restored when gas from downstream accretes back onto the galaxy.

The evolution of the ICM

The disk galaxy moves at a relative speed of $977\,\mathrm{km\,s^{-1}}$ through the ICM, which has a temperature of 2.3×10^6 K, corresponding to a sound speed of $230\,\mathrm{km\,s^{-1}}$, hence the Mach number of the ICM flow is $M = 4.25$ (see eqns. (6.2) and (6.3)). Thus, the galaxy clearly moves supersonically through the ICM.

When the supersonic ICM flow encounters the ISM, or when a galaxy moves supersonically through the ICM, a bowshock develops in front of the galaxy The ICM particles are slowed down and forced around the ISM so that the ICM density in front of the galactic disk increases (left panels of Figure 6.6). Inside this bow shock, the ICM temperature also rises drastically, to temperatures up to 1.5×10^7 K, more than a factor of 5 higher than the original ICM temperature. (right panels of Figure 6.6). This leads to an increase of the thermal pressure inside the bowshock.

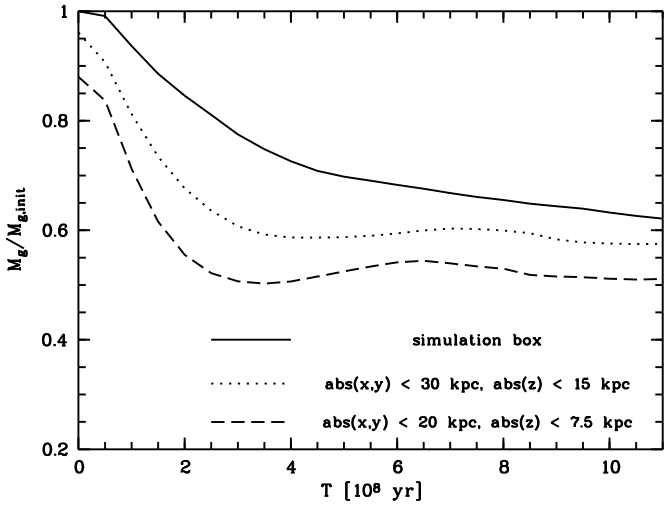

Figure 6.4: The ISM mass evolution in function of time. The fraction of ISM mass remaining in the total simulation box (full line) decreases monotonically with time. However, the remaining ISM mass fraction within a box $\mathrm{abs}(x, y) < 30\,\mathrm{kpc}$ and $\mathrm{abs}(z) < 15\,\mathrm{kpc}$ slightly rises again after about $5 \times 10^8\,\mathrm{yr}$. This effect is even stronger when considering the ISM mass fraction left in a box $\mathrm{abs}(x, y) < 20\,\mathrm{kpc}$ and $\mathrm{abs}(z) < 7.5\,\mathrm{kpc}$. Finally, after 1 Gyr of ram pressure, about 45 per cent of the ISM is stripped from the galaxy.

From the upper panels of Figure 6.6, it is also evident that the simulation box is somewhat too small for this simulation. The bow shock reaches the $x - y$ boundaries, where it is wrapped around and appears again on the other side, thereby raising the density and the temperature. Hence the thermal pressure increases in this regions. We will have to take care of this feature in future simulations, since it can introduce spurious effects (see later). After some time, when the ISM disk is sufficiently truncated, the bowshock is narrower and leaves the simulation box entirely via the z-axis (lower panels of Figure 6.6). The wrapping issue is now solved, because the particles leaving at the end of the z-axis are randomly introduced at the beginning. However, the periodic boundary conditions of the z-axis will still play a role here. In order to calculate the hydrodynamical quantities of the gas particles near the $z = 0$ edge of the simulation box, information from the $z = 1$ side is used and vice versa. Therefore, the ICM near the end of the z-axis *feels* the ICM at the beginning of the box. Clearly this could also lead to numerical problems. It is already clear that some very hot ICM particles linger in the galaxy wake, near the end of the simulation box. Although the density in the wake is very low, the increased temperature will lead to a high thermal pressure in this region. We will investigate this problem in more detail in section 6.5.2.

At the end of the simulation, 3618 ISM particles (38 per cent) have left the simulation box to become part of the ICM flow. The ICM density has thus increased by 4.5 per cent with respect to the initial density, and so has the ram pressure, since it is linearly proportional to the ICM density. This is only a small fraction, and we will see in section 6.5.2 that other numerical problems disturb the incoming ICM flow more dramatically. However, the increase in ICM density can be easily avoided by simply taking the outgoing ISM particles out of the simulation.

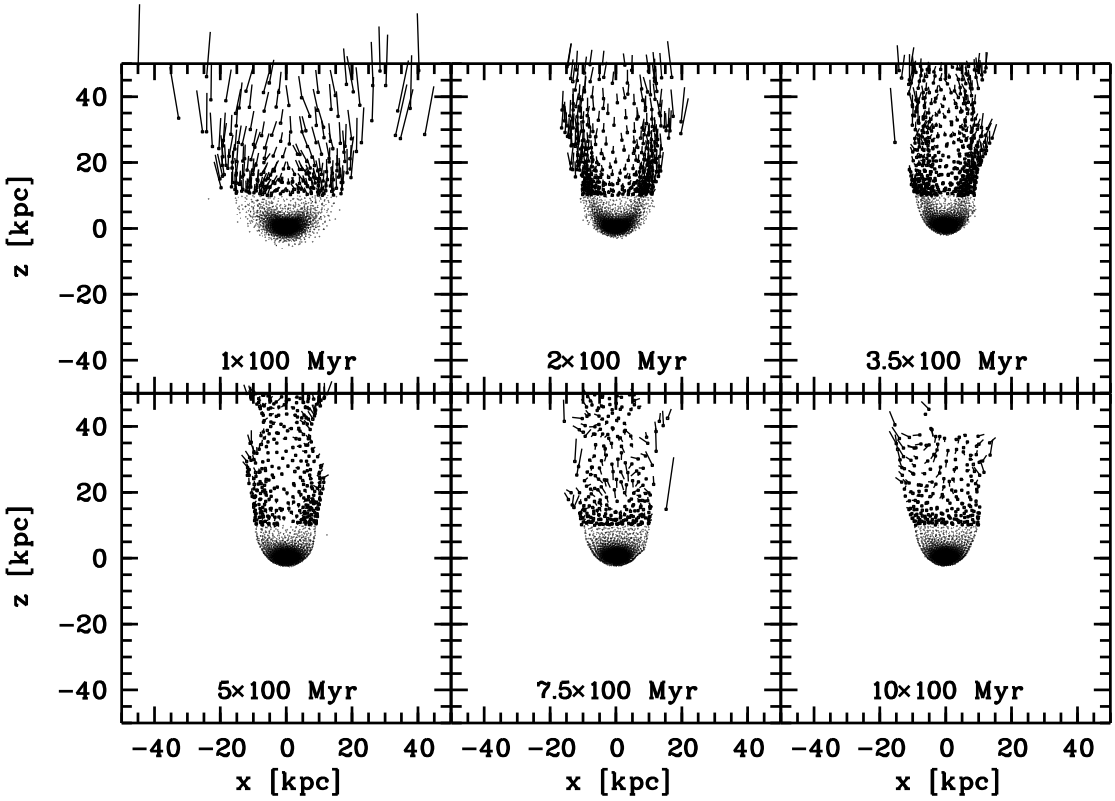

Figure 6.5: The evolution of the velocity of stripped ISM particles is followed by plotting the velocity component in the $x-z$ plane for ISM particles with $z > 10\,\mathrm{kpc}$. In the beginning, particles are carried along with the ICM flow at high velocities. At later times, ISM particles in the wake of the galaxy have negative v_z components and fall back onto the galaxy. For clarity, only the particles in a slice $\mathrm{abs}(y) < 2.5\,\mathrm{kpc}$ of the simulation box are shown.

6.4.4 Conclusions

We have modified the HYDRA code in the same way as SS in order to simulate the evolution of a small, gas-rich disk galaxy moving through a moderate cluster medium. The DM halo was included as a static gravitational potential using the Burkert density profile. The stellar disk is not affected by the ram pressure of the ICM. When the ISM is embedded in the ICM flow, the outer parts of the gas disk are rapidly stripped, on a timescale of a few $10^8\,\mathrm{yr}$. Some particles in the wake of the galaxy are able to accrete back onto the galactic disk, while a small amount of stripping continuously occurs at the edges of the truncated gas disk. Because the ICM flow is supersonic, a bowshock develops in front of the galaxy. In this bowshock, the ICM density and temperature rises. The periodic boundary conditions may lead to some unwanted results if the simulation box is too small.

Our simulations yield approximately the same results as SS, allowing for small differences due to slightly different initial conditions. The use of a static DM potential instead of a live DM halo helps reducing the computational cost of the simulation. The results make us confident that the implementation of the ICM flow is correct, although some points still need to be looked at carefully.

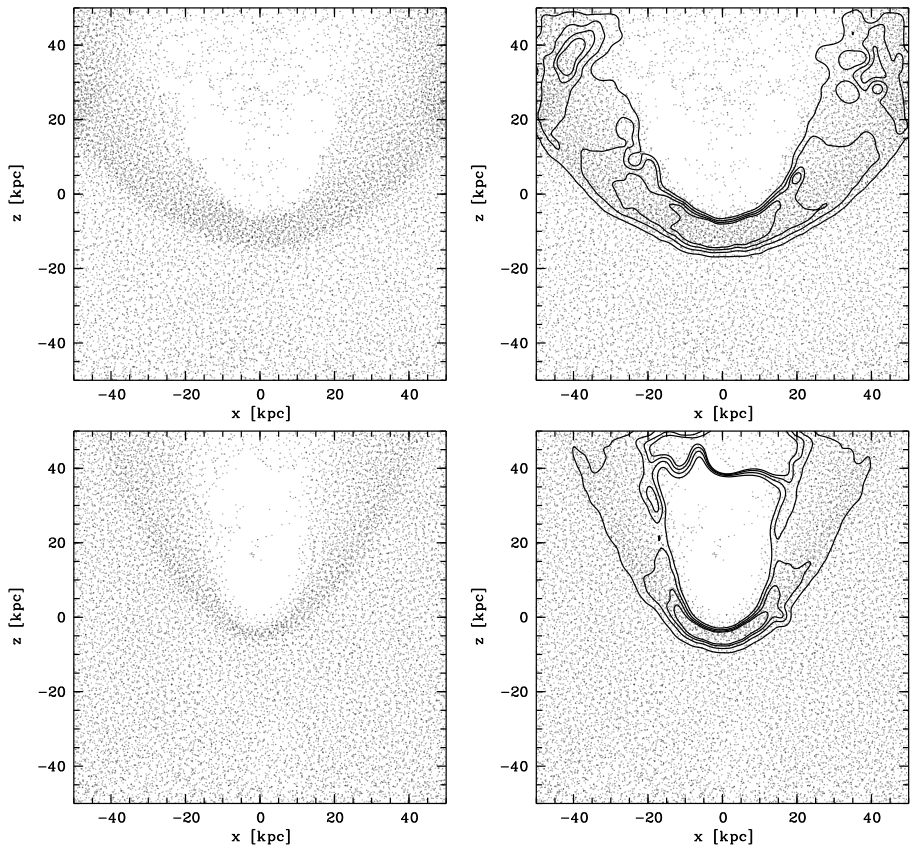

Figure 6.6: The evolution of the ICM. In the upper left panel, the ICM particles in a slice $|y| < 10\,\mathrm{kpc}$ are plotted at a simulation time of $10^8\,\mathrm{yr}$. In the upper right panel, ICM temperature contours are drawn for temperatures of 5×10^6, 7.5×10^6, 1×10^7 and $1.2 \times 10^7\,\mathrm{K}$. As the ICM encounters the ISM, a bow shock develops in the ICM. The ICM particles in the shocked region are heated. Where the bow shock encounters the $x - y$ edge of the simulation box, it is wrapped around. At those places, a density and temperature enhancement develops. In the lower panels, the same is shown but for a simulated time of $10^9\,\mathrm{yr}$. Because the ISM disk is much reduced in size, the bow shock is less extended and leaves the simulation box entirely at the z axes. However, some spurious hot ICM particles linger near the z-boundary in the dilute wake behind the galaxy.

As a first point, the size of the simulation box should be chosen carefully, so that the ICM bowshock does not leave the simulation box at the x or y boundaries. The periodic boundary conditions applied to these sides wrap the bowshock around the simulation box, which could lead to problems due to the increased density and temperature at the edges.

Secondly, the fact that hydrodynamical quantities near the edges of the z-axis are still calculated using periodic boundary conditions could introduce problems if ICM properties in the wake of the galaxy propagate across the z-boundary and influence the incoming ICM flow.

Finally, all gas particles that reach the end of the z-axis are played back at the beginning of the simulation box. This includes ISM particles that leave the simulation box, which then become part of the ICM. If the number fraction of ISM particles that are converted into ICM particles with respect to

the total of ICM particles, is low, then this procedure poses no problem to the simulation. If however a large amount of ISM particles would be converted to ICM particles, the density of the ICM flow, and thus the ram pressure, will rise.

We shall address these problems in more detail in the next section.

6.5 Ram pressure stripping from dEs

Burkert (1995) derived a phenomenological density profile for the DM distribution from observations of the H I rotation curves of dwarf spiral galaxies. This DM halo has been used by Mori & Burkert (2000) (hereafter MB) to simulate ram pressure stripping from spherically symmetric dEs, using a 2D Eulerian grid code. We will use our 3D SPH code to reproduce the simulations of MB, in order to compare the 2D and 3D simulations. This will be a further test case for our code. Of course using 3D will imply a coarser resolution of the simulations, but on the other hand it allows for other geometries to be studied, such as the effect of flattening, inclination with respect to the galaxy motion through the ICM, rotation, etc.

6.5.1 The MB galaxy model

The dark matter halo

The DM halo is implemented as a static Burkert halo with core masses ranging from 10^6 to $10^{10}\,\mathrm{M}_\odot$ (Figure 6.1). The contribution of the stellar component to the gravitational potential can be assumed to be contained in this Burkert distribution, or to be negligible in comparison to the dark matter contribution.

The interstellar medium

The ISM is supposed to be ionized by either the UV radiation background or by supernova explosions. For simplicity's sake, the self-gravity of the gas is neglected and the ISM is supposed to be in hydrostatic equilibrium within the dark matter potential. Moreover it is assumed to be isothermal with temperature T_g. The equation of motion for the ISM becomes

$$\frac{\mathrm{d}\boldsymbol{v}_g}{\mathrm{d}t} = \mathbf{0} = -\frac{1}{\rho_g}\boldsymbol{\nabla} P_g - \boldsymbol{\nabla}\Phi_d. \tag{6.30}$$

Inserting the equation of state for an ideal gas $P_g = \frac{3}{2}\frac{k_B T_g}{\mu m_p}\rho_g$ and assuming spherical symmetry we can write

$$\frac{k_B T_g}{\mu m_p}\frac{\mathrm{d}\ln\rho_g(r)}{\mathrm{d}r} = -\frac{\mathrm{d}\Phi_d(r)}{\mathrm{d}r}, \tag{6.31}$$

which, upon integrating from 0 to r gives the radial density profile for the ISM

$$\rho_g(r) = \rho_{g,0}\exp\left\{-\frac{k_B T_g}{\mu m_p}\left[\Phi_d(r) - \Phi_d(0)\right]\right\}, \tag{6.32}$$

where $\rho_{g,0}$ is the central gas density.

M_0 $\mathrm{M}_\odot$	r_0 kpc	$\rho_{d,0}$ cm^{-3}	T_g K
10^6	0.16	10.51	666
10^7	0.43	5.44	2 480
10^8	1.14	2.82	9 260
10^9	3.07	1.46	34 500
10^{10}	8.24	0.76	129 000

Table 6.1: MB model parameters in function of core mass.

MB assume the temperature of the ISM to depend on the core mass of the dark matter, so that the whole model is a one-parameter family of DM core mass. They pose that

$$\begin{aligned} T_g &= \frac{\mu m_p}{3k_B}\frac{GM_0}{r_0} \\ &= 3.45\times 10^4 \left(\frac{M_0}{10^9\,\mathrm{M}_\odot}\right)^{4/7}\ \mathrm{K}. \end{aligned} \tag{6.33}$$

using the scaling relations found by Burkert (1995) (equations (6.26) and (6.27)).
Assuming the temperature relation of MB, the density profile of the ISM can be written as

$$\rho_g(r) = \rho_{g,0}\exp\left\{-\frac{3}{6\ln(2)-\pi}\tilde{\Phi}(x)\right\}, \tag{6.34}$$

where

$$\tilde{\Phi}(x) = 2\left(1+\frac{1}{x}\right)[\ln(1+x)-\mathrm{arctg}(x)] - \left(1-\frac{1}{x}\right)\ln(1+x^2). \tag{6.35}$$

The mass ratio between the gas and the dark matter within a core radius is defined as

$$F = \frac{M_{g,0}}{M_0}, \tag{6.36}$$

where $M_{g,0}$ is the total gas mass inside a core radius. The ratio between the central gas density $\rho_{g,0}$ and the central dark matter density $\rho_{d,0}$ follows from numerical integration of the mass ratio:

$$\frac{\rho_{g,0}}{\rho_{d,0}} = 1.40F. \tag{6.37}$$

MB assume an initial gas fraction $F = 0.1$. Consequently, the dEs are described as a one-parameter family of the DM core mass M_0. In table 6.5.1 we summarize the parameters of the MB galaxy model.

6.5.2 A first implementation

As a first test run we simulated the ram pressure stripping from dEs using the modified boundary conditions of section 6.4, for two core masses: $M_0 = 10^7\,\mathrm{M}_\odot$ and $M_0 = 10^{10}\,\mathrm{M}_\odot$. MB neglect the self-gravity of the gas, so we perform these simulations evolving the SPH equations, where the adiabatic energy equation is used, no additional heating or cooling is assumed, and the only gravitational force is that of the DM halo.

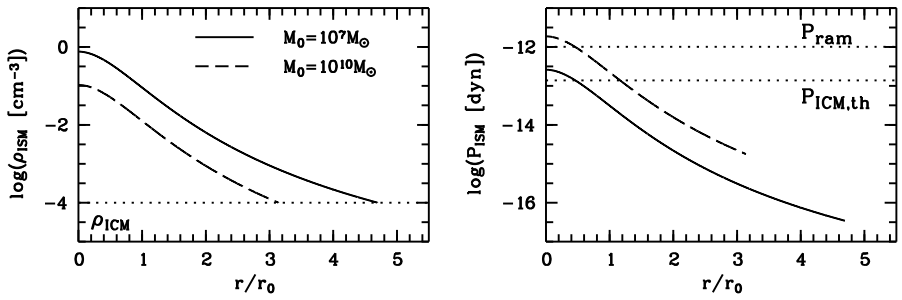

Figure 6.7: The initial density (left panel) and thermal pressure (right panel) profiles of the ISM in the $M_0 = 10^7\,\mathrm{M}_\odot$ (solid lines) and $M_0 = 10^{10}\,\mathrm{M}_\odot$ (dashed lines) DM halo. The ISM is set up so that initially, the density changes continuously at the boundary between the ISM and the ICM. This implies that there is a discontinuity in the thermal pressure; the thermal pressure in the ICM is much higher than in the outskirts of the ISM. The level of the ram pressure for a $n_{\mathrm{ICM}} = 10^{-4}\,\mathrm{cm}^{-3}$, $v_{\mathrm{gal}} = 1000\,\mathrm{km\,s}^{-1}$ ICM is also indicated. We expect that the ISM in the $10^7\,\mathrm{M}_\odot$ halo will be instantaneously stripped, while the more massive $10^{10}\,\mathrm{M}_\odot$ halo will be able to retain part of its ISM.

Because the $M_0 = 10^{10}\,\mathrm{M}_\odot$ core mass is similar to the DM core mass of the disk galaxy simulated in section 6.4, we started with the same simulation box units (`lunit` $= 100\,$kpc, `munit` $= 10^4\,\mathrm{M}_\odot$ and `tunit` $= 100\,$Myr). For the $M_0 = 10^7\,\mathrm{M}_\odot$ simulations we chose the units such that the density, velocity and energy units are the same as in the $M_0 = 10^{10}\,\mathrm{M}_\odot$ simulation (`lunit` $= 10\,$kpc, `munit` $= 10\,\mathrm{M}_\odot$ and `tunit` $= 10\,$Myr).

Setting up the ISM distribution

To set up the ISM, we initially distribute 10 000 particles according to the density profiles given by equation (6.34) for $M_0 = 10^7\,\mathrm{M}_\odot$ and $10^{10}\,\mathrm{M}_\odot$ (see Figure 6.7). The initial positions for the particles are generated with the Monte-Carlo acception-rejection technique used in section 6.4.1, while the velocities are initially set to zero. The generated distribution is then relaxed inside the static DM halo for about 1000 timesteps. The temperature of the gas particles is set to $2.48 \times 10^2\,\mathrm{K}$ for the small DM halo and $1.29 \times 10^5\,\mathrm{K}$ for the larger DM halo, as implied by equation (6.33). The corresponding initial thermal pressure profiles of the ISM is also shown in Figure 6.7. Comparing the central thermal pressure to the ram pressure of the present simulations, we expect that the small galaxy will be instantaneously stripped of its ISM, while the larger galaxy is expected to retain part of its ISM.

Setting up the ICM flow

Initially, we fill the simulation box randomly with ICM particles. Other simulations have started with particles on a regular grid (Abadi et al., 1999) or randomly distributed in planes along the z-axis (SS). However, the ICM flow is relaxed for some time, so that all particles travel several times along the simulation box. Since particles that reach the end of the simulation box are randomly played back at the beginning, they get well mixed.

The mass m_{ICM} of each ICM particle depends on the desired ICM density, ρ_{ICM}, the volume of the simulation box, V_{box}, and the number of ICM particles used, N_{ICM}, according to the relations

$$\rho_{\mathrm{ICM}} = \frac{M_{\mathrm{ICM}}}{V_{\mathrm{box}}} = \frac{N_{\mathrm{ICM}} m_{\mathrm{ICM}}}{V_{\mathrm{box}}}. \tag{6.38}$$

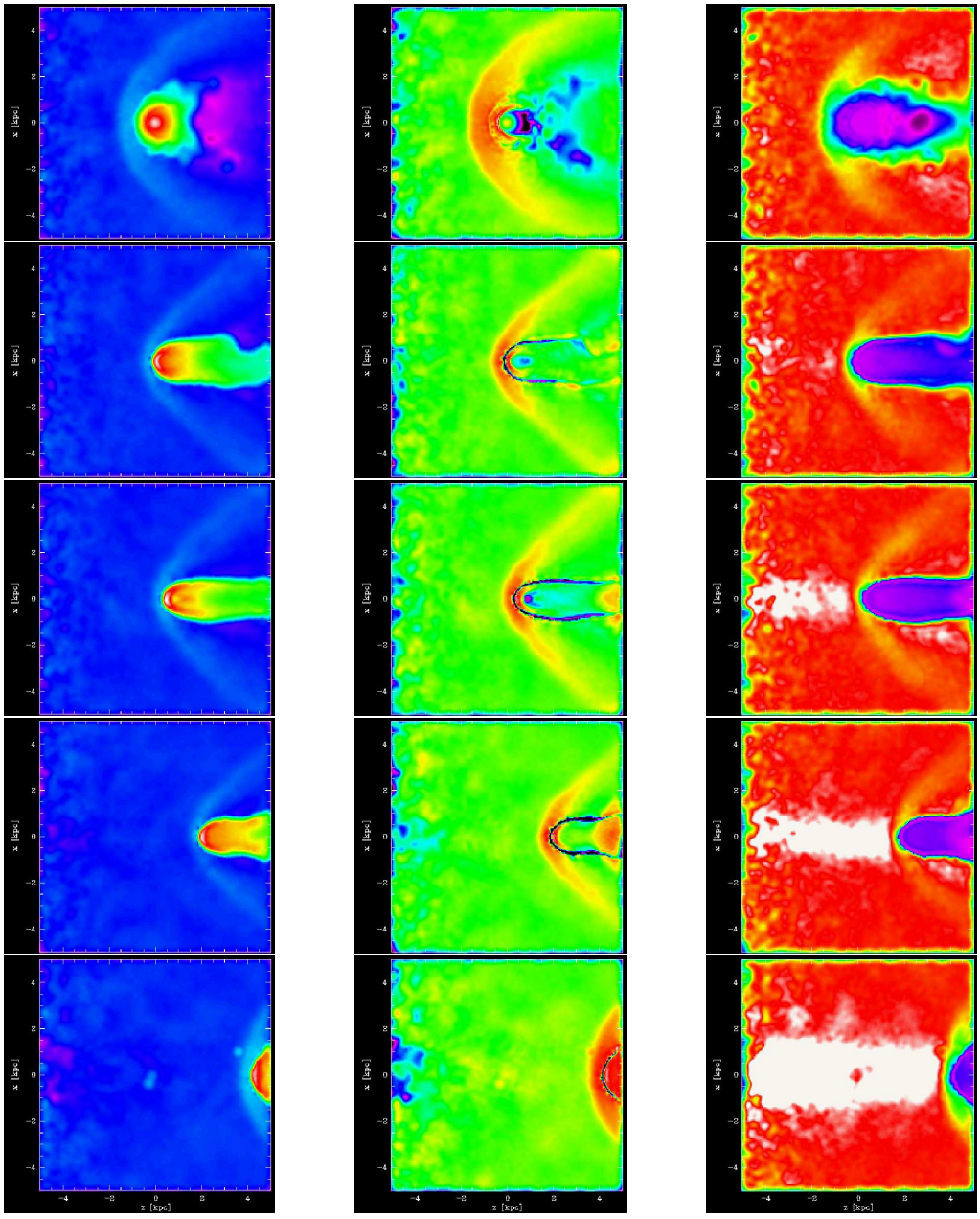

Figure 6.8: Early implementation of ram pressure simulation, for a dE with core mass $M_0 = 10^7\,\mathrm{M}_\odot$, and the initial conditions for the ISM as in MB. From top to bottom we show the logarithmic density distribution (*left panels*), the logarithmic thermal pressure (*middle panels*) and the z-velocity component (*right panels*) of the gas in the y-plane centred on the DM halo, at simulated times 6×10^6, 3×10^7, 4.5×10^7, 7.5×10^7 and 10^8 yr. Hot ICM particles raise the thermal pressure at the end of the z-axis and severely influence the velocity of the incoming ICM flow.

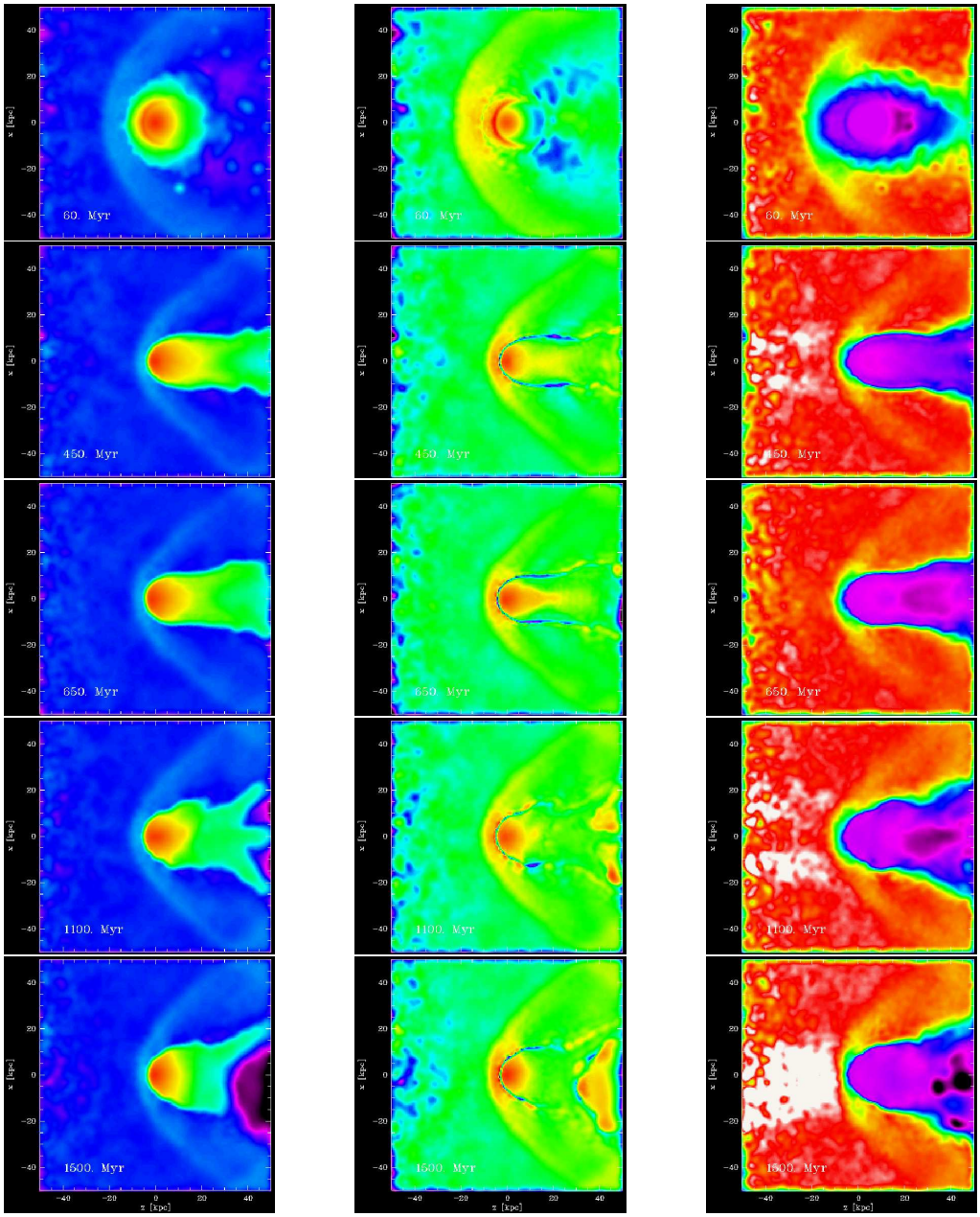

Figure 6.9: Early implementation of ram pressure simulation, for a dE with core mass $M_0 = 10^{10}\,\mathrm{M}_\odot$, and the initial conditions for the ISM as in MB. From top to bottom we show the logarithmic density distribution (*left panels*), the logarithmic thermal pressure (*middle panels*) and the z-velocity component (*right panels*) of the gas in the y-plane centred on the DM halo, at simulated times 6×10^7, 4.5×10^8, 6.5×10^8, 1.1×10^9 and $1.5 \times 10^9\,\mathrm{yr}$. A reflecting bow shock is clearly visible in the density, pressure and velocity plots. Hot ICM particles raise the thermal pressure at the end of the z-axis and influence the velocity of the incoming ICM flow.

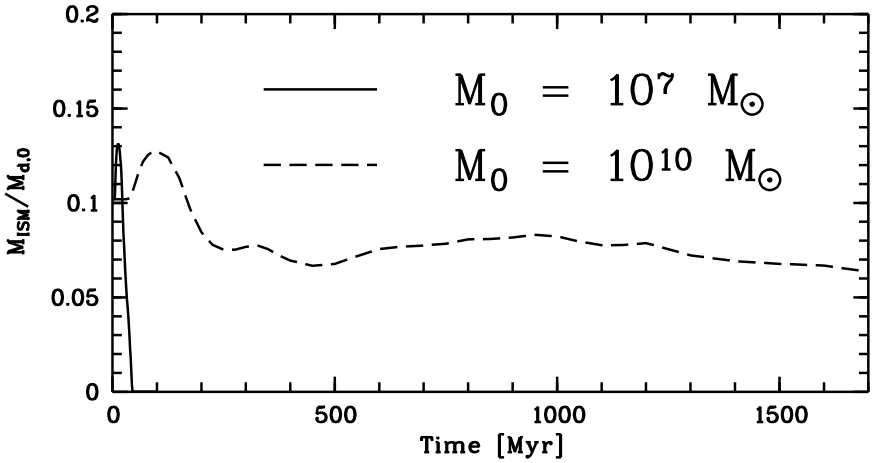

Figure 6.10: The evolution of the ISM mass fraction left within one r_0 in the first ram pressure stripping simulations. The small galaxy (solid line) is immediately stripped, while the more massive galaxy (dashed line) holds on to its ISM for much longer times.

The density of the ICM flow used in the MB simulations is $\rho_{\rm ICM} = 10^{-28}\,{\rm g\,cm^{-3}}$. To achieve this density, we set the mass of the $42^3 = 74\,088$ ICM gas particles to $m_{\rm ICM} = 2 \times 10^4\,{\rm M}_\odot$, and distribute them randomly over the simulation box. The temperature is fixed to $10^7\,{\rm K}$ and the initial velocity vector of the particles is given by $\boldsymbol{v} = (0, 0, -1000\,{\rm km\,s^{-1}})$.

Since the particles are randomly played back at the beginning of the simulation box, and their properties are reset, they will go through a relaxation phase as they travel along the z-axis. Due to this relaxation, the temperature, density and velocity of the ICM flow at the position of the galaxy could be somewhat different than the initial conditions. Therefore we tuned the properties of the incoming ICM particles so as to give the desired ICM flow at the z position of the dE.

With careful choosing of the units, we can use the same ICM flow setup for simulations at different scales. We need to scale the units such that we have the same internal velocity, density and energy units. Thus, choosing `lunit` and keeping `vunit` fixed, implies that the time unit `tunit` scales linearly with the length unit. Keeping `nunit` fixed, implies that the mass unit `munit` has to be scaled as `lunit`^{3}. With our unit choice we can use the same ICM flow for both the $M_0 = 10^7\,{\rm M}_\odot$ and $M_0 = 10^{10}\,{\rm M}_\odot$ simulations.

Ram pressure stripping

The static DM halo and the ISM gas are then embedded within the ICM flow. The ICM particles within the ISM distribution are taken away, since the ICM is not supposed to penetrate the ISM. In Figure 6.8 we follow the evolution of the density, the thermal pressure and the z-velocity component of the gas in the y-plane centred on the $10^7\,{\rm M}_\odot$ DM halo. The central pressure in the ISM is much less than the ram pressure, so that we expect the ISM to be instantaneously stripped.

We simulate the evolution of the ISM during $10^8\,{\rm yr}$. Although the ISM is indeed immediately stripped from the DM halo, we see that some hot ICM particles linger in the galaxy wake at the end of the simulation box where they raise the thermal pressure. Also the ISM particles that are stripped from the galaxy tend to linger at the end of the box, so that the density (and hence the thermal pressure)

increases. Since the hydrodynamical quantities at the beginning of the simulation box are computed using periodic boundary conditions, the increased pressure heats and accelerates the ICM flow. In the course of the simulation, more and more ISM particles accumulate at the end of the box. After 10^8 yr, only 1262 ISM particles have left the simulation box. Due to the increased pressure at the end of the box, the temperature of the incoming ICM flow increases to 1.2×10^7 K and the velocity increases up to $1500\,\mathrm{km\,s^{-1}}$ towards the end of the run. Hence, the ram pressure also increases by more than a factor of 2.

In Figure 6.9 the evolution of the density, the thermal pressure and the z-velocity component of the gas in the y-plane centred on the $10^{10}\,\mathrm{M}_\odot$ DM halo is followed. Because the central pressure in the ISM is higher than the ram pressure, we expect that the outer parts of the ISM will be stripped, while the central regions will be able to remain inside the DM halo.

The evolution of the ISM is followed for 1.5×10^9 yr. Again we see that some hot ICM particles linger at the end of the simulation box, increasing the velocity of the incoming flow. Towards the end of the simulation, a large, low-density cavity develops in the wake of the galaxy, where some very hot ICM particles lead to high thermal pressures. Moreover, we see that the bowshock leaves the simulation box at the x-axes and is wrapped around by the periodic boundary conditions. This leads to an increased density and temperature in the galaxy wake and prohibits a normal outflow at the end of the simulation box.

In Figure 6.10, the evolution of the ISM mass fraction contained within one core radius is shown. In both galaxies, the ISM is first compressed by the thermal pressure of the ICM, so that the ISM mass within one r_0 increases by up to 30 per cent. Then, the $10^7\,\mathrm{M}_\odot$ dE is rapidly stripped, while the $10^{10}\,\mathrm{M}_\odot$ dE retains more than 55 per cent of its ISM at the end of the simulation. It is also seen that, just like the spiral galaxy in the previous section, the more massive dE experiences gas replenishment from back-stream accretion.

Although we can reproduce the general features of the ram pressure stripping from dEs, namely that small dEs will have all of their ISM stripped on small timescales, while massive haloes will retain a large part of their ISM over long timescales, the behaviour of the ICM flow is still unsatisfactory. The fact that the incoming ICM flow is influenced by the conditions in the wake of the galaxy certainly needs to be looked at. Moreover we should choose the simulation box large enough so that the bowshock is not wrapped around the x and y axes.

One can also notice that the initial thermal pressure of the ICM is much larger than the thermal pressure of the ISM at the boundary between the two gas phases. Therefore, the ISM will be *compressed* by the thermal pressure, and at the same time stripped by the ram pressure.

6.5.3 Boundary conditions

As the bow-shock assumes a paraboloidal form, a wake forms behind the dE. This wake can extend to the end of the simulation box. Then, the use of periodic boundaries around the z-axis is not appropriate anymore, since the forces at the end of the simulation box lead to spurious effects in the incoming ICM flow. In particular, the velocity of the incoming ICM flow increases as the thermal pressure at the end of the simulation box increases, due to either very hot ICM particles or very dense ISM particles that cannot leave the simulation box.

To solve this problem we inserted a buffer of *ghost* ICM particles at the beginning and end of the simulation box, so that the incoming ICM particles are backed up by a smooth ICM flux. We use a slab along the flow direction from an ICM-only simulation as buffer particles. These buffer particles are included into the SPH loop, so that the real ICM particles in the simulation box feel their presence (see Figure 6.11). However, at the end of each timestep their properties (position, velocity, density, temperature, entropy, smoothing length) are *not* updated.

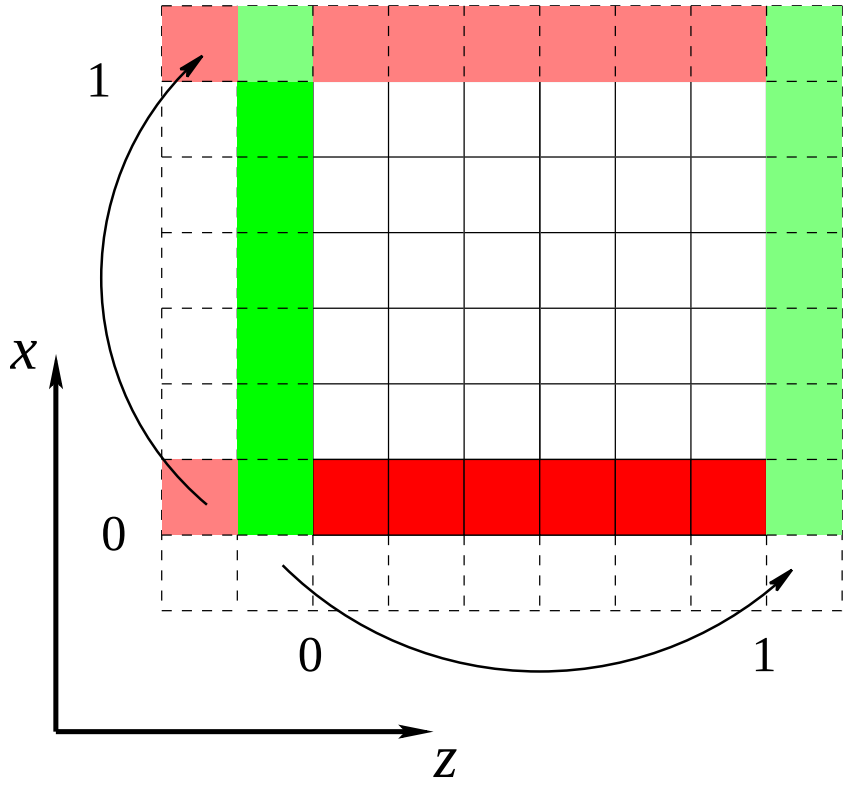

Figure 6.11: The periodic boundary conditions imply that neighbour particle search cells adjacent to the boundaries are wrapped. In this schematic picture of the $x-z$ plane this is illustrated in the case of the cells near the $x = 0$ boundary (red cells), which are wrapped around, so that they become neighbour cells to those cells at the $x = 1$ boundary. One can think about this as copying the red cells and paste them on top of the simulation box (light-red cells). In order to avoid that the conditions at the $z = 1$ boundary influence the incoming flux, we introduce an extra layer of cells (green cells), which are filled with ICM flow particles. Due to this ICM buffer, the particles in the cells at the $z = 0$ boundary are no longer influenced by those at the $z = 1$ boundary.

Because of the periodic boundary conditions, the outgoing particles also feel this buffer, as they were feeling the incoming ICM flow in the first simulations. Hot ICM or dense ISM particles could still have trouble leaving the simulation box. This problem could be solved by using pure outflow conditions at the end of the box (no wrapping conditions at the end of the simulation box). However, with such conditions, the properties of the particles near the end of the simulation box would also be incorrect. Another possible configuration could exist in copying the last part of the simulation box and placing it behind the simulation box, so that a continuation of the conditions at the end of the box is suggested. This is however computationally much more expensive. Hence we use a simulation box that is large enough so that the undesired numerical problems stay well away from the region of interest.

The size of the simulation box is also confined by the bow-shock. The box should be large enough so that the bowshock does not flow out at the x and y axes and gets wrapped around, as was the case in the $M_0 = 10^{10}\,\mathrm{M}_\odot$ simulation. However, since we work in 3 dimensions, the number of ICM particles needed to fill the box rises very rapidly if we increase the size of the simulation box and at the same time want to have a sufficiently good spatial resolution. A possible way around this could be

Table 6.2: Initial ISM boundary radius, and central gas density and pressure for the different models

		MB			PC_1			PC_2		
$M_{\rm d,0}$	r_0	$\rho_{\rm g,0}$	$P_{\rm g,0}$	x_b	$\rho_{\rm g,0}$	$P_{\rm g,0}$	x_b	$\rho_{\rm g,0}$	$P_{\rm g,0}$	x_b
$\rm M_\odot$	kpc	$\rm cm^{-3}$	$10^{-12}\,\rm dyn$	r_0	$\rm cm^{-3}$	$10^{-12}\,\rm dyn$	r_0	$\rm cm^{-3}$	$10^{-12}\,\rm dyn$	r_0
$n_{\rm ICM} = 10^5\,\rm cm^{-3}$										
10^6	0.16	1.47	0.14	9.26	1.38	0.13	1.03	0.02	0.02	3.31
10^7	0.43	0.76	0.26	7.85	0.61	0.21	1.20	0.04	0.06	2.41
10^8	1.14	0.39	0.50	6.72	0.28	0.35	1.39	0.24	0.32	1.45
10^9	3.07	0.20	0.97	5.80	0.13	0.61	1.60	1.38	1.91	0.76
10^{10}	8.24	0.11	1.88	5.03	0.06	1.10	1.83	6.33	8.74	0.40
$n_{\rm ICM} = 10^4\,\rm cm^{-3}$										
10^6	0.16	1.47	0.14	5.40	3.73	0.34	0.57	0.13	0.18	1.55
10^7	0.43	0.76	0.26	4.69	1.36	0.46	0.68	0.19	0.27	1.19
10^8	1.14	0.39	0.50	4.10	0.52	0.67	0.81	0.46	0.64	0.84
10^9	3.07	0.20	0.97	3.58	0.21	1.01	0.95	1.65	2.28	0.53
10^{10}	8.24	0.11	1.88	3.14	0.09	1.62	1.11	6.61	9.12	0.32
$n_{\rm ICM} = 10^3\,\rm cm^{-3}$										
10^6	0.16	1.47	0.14	3.35	19.75	1.82	0.29	1.09	1.51	0.73
10^7	0.43	0.76	0.26	2.94	5.99	2.05	0.35	1.26	1.74	0.58
10^8	1.14	0.39	0.50	2.57	1.90	2.42	0.43	1.73	2.39	0.44
10^9	3.07	0.20	0.97	2.24	0.63	3.01	0.52	3.22	4.45	0.32
10^{10}	8.26	0.11	1.88	1.95	0.22	3.96	0.63	8.52	11.76	0.22

achieved by grouping ICM particles into larger particles for large radii. This has been used in very large cosmological simulations where one wants to follow a small volume on a fine scale (Klypin et al., 2001). This is equivalent to the technique employed by MB, who use a grid (Eulerian) simulation with spatially varying cell sizes, taking ever larger cells going away from the galaxy. In the following simulations we will only increase the number of particles to achieve a reasonable spatial resolution.

The ISM particles that arrive at the end of the z-axis were played back as ICM particles. Although we have seen that not much ISM particles actually leave the simulation box to become part of the ICM flow, it would be more logical to keep the total number of ICM particles constant and to remove the lost ISM particles from the simulation altogether. This can be achieved by changing the type labeling in HYDRA. We subdivide the `itgas` type particles into `itism` and `iticm` particles. The hydrodynamical properties of both particle types are computed in the SPH loop as before. However, when arriving at the end of the simulation box, the `iticm` particles are played back in the incoming ICM flow, while the `itism` particles are lost from the simulation (i.e. set to `itnone`).

6.5.4 Embedding the ISM in the ICM flow

In particle codes, the ISM is embedded in the ICM by simply placing the ISM particles in the box containing the ICM particles. Hence, there will initially be ICM particles inside the ISM, and some outer ISM particles will be completely surrounded by ICM particles. In other words, there is no sharp boundary between the ISM and the ICM. In grid codes however, such a mixing of ICM and ISM is not allowed, unless a two-phase gas medium is assumed. Therefore one has to decide where to end the ISM and begin the ICM contribution to the overall gas distribution.

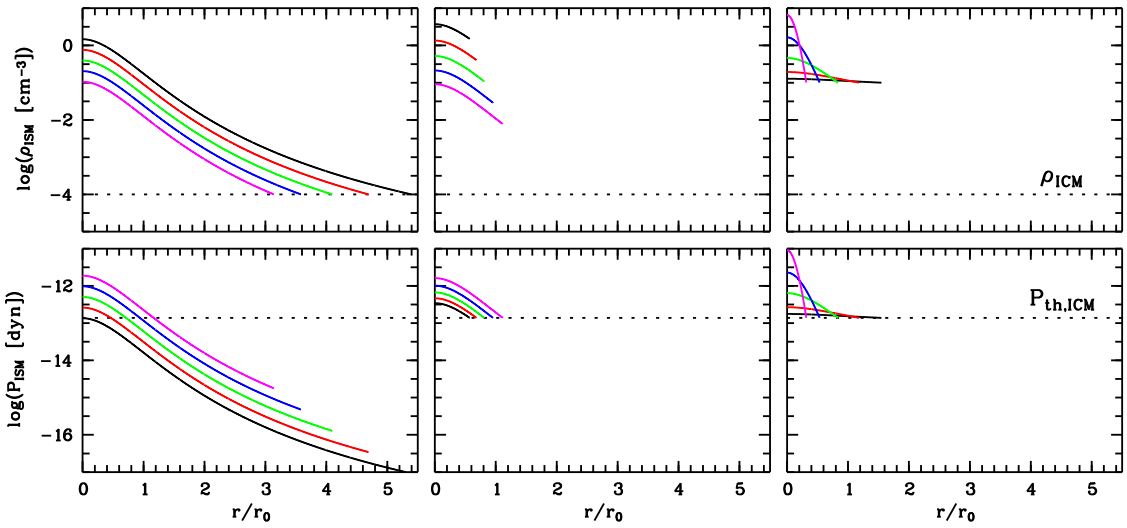

Figure 6.12: Initial ISM density and pressure profiles for the three different initial conditions models considered here. The galaxy is supposed to be embedded in an ICM of density $10^{-4}\,\mathrm{cm}^{-3}$ and temperature $10^{7}\,\mathrm{K}$, to that the thermal pressure of the ICM is $P_{\mathrm{ICM}} = 10^{-11}\,\mathrm{dyn}$. On the left panel, the original MB conditions are shown; the ISM temperature scales with dark matter halo mass and the ISM is density confined. The total gas mass inside the boundary radius is about $2FM_0$. On the middle panel, the first set of pressure confined models are shown. The temperature scales with DM halo mass, but the ISM is supposed to be pressure confined by the ICM. The total gas mass inside the boundary radius is FM_0. Although the boundary radius is much smaller than in the MB case, the initial central density and pressure are very similar. Finally, on the right panel, the ionized ISM is assumed to have a temperature of $10^{4}\,\mathrm{K}$ for all dark matter halo masses, and to be pressure confined by the surrounding ICM. The constant temperature implies that the ISM in smaller haloes is much more diffuse than in the other initial conditions, while for the most massive halo the gas is more centrally confined.

Density confinement

The ISM in MB is initially assumed to be in *density equilibrium* within the ICM, meaning that at the boundary between the ISM and ICM, the overall gas density changes continuously ($\rho_g(r_b) = \rho_{\mathrm{ICM}}$). The galaxy model is a one-parameter family of DM core mass, and is independent of the ICM conditions. Hence the values of the central density and pressure, and the shape of the radial density and pressure profiles do not depend on the density or thermal pressure of the ICM. However, the boundary radius does, as can be seen in Table 6.2, where the some parameters of the ISM models in different ICM conditions are listed. In the left panels of Figure 6.12, the radial density and thermal pressure profiles of the ISM in DM haloes from 10^{6} to $10^{10}\,\mathrm{M}_{\odot}$ are shown. The profiles are traced out to the boundary radius, assuming an ICM with density $10^{-4}\,\mathrm{cm}^{-3}$. The boundary radius is in the range $3 - 5r_0$ for all core mass haloes. Integrating the gas distribution out to these radii yields a the total ISM mass of about $2M_{g,0}$. In the following we will label these initial conditions MB.

Pressure confinement, case 1

However, the assumption that the gas density at the ISM boundary is equal to the ICM density is physically not well motivated. The high ICM temperatures lead to a discontinuity in the thermal pressure. As seen in the left panels of Figure 6.12, the thermal pressure of the ICM will be much higher than the thermal pressure in the ISM at the boundary radius. Therefore the ISM will initially experience a collapse phase that is due to the thermal pressure of the ICM, even if the galaxy were not moving through the cluster, and no ram-pressure stripping acts on it. This effect is noticeable in Figure 6.10, where the ISM mass fraction within r_0 initially *increases*, before ram pressure strips the gas of the galaxy. In order to avoid such a collapse phase, we ran a second set of simulations for which the ISM is placed in the ICM assuming *pressure equilibrium* at the boundary radius, i.e. the thermal pressure changes continuously at the boundary radius ($P_{g,\mathrm{th}}(r_b) = P_{\mathrm{ICM,th}}$). Moreover, because a galaxy will not enter the ICM at once, but will encounter a gradual increase of ICM pressure (both thermal and ram pressure), the boundary between ISM and ICM is more likely to be pressure confined. Therefore we set up a second set of initial conditions in which the ISM is assumed to be confined by the thermal pressure of the ICM. Moreover we will assume that the *total* gas fraction $F = M_g(r_b)/M_0$ within the boundary radius r_b is fixed at 0.1. We will label these initial conditions PC_1.

Because the boundary radius r_b depends on the ICM properties, assuming that the ISM mass fraction within r_b is fixed implies that the ISM density profiles are no longer independent of the ICM in which the galaxy is embedded. For each ICM density ρ_{ICM} and temperature T_{ICM}, we have to recalculate r_b and $\rho_{g,0}$ by numerically solving the equations

$$\rho_{g,0} = \frac{\rho_{\mathrm{ICM}} T_{\mathrm{ICM}}}{T_g} \exp\left\{-\frac{\mu m_p}{k_B T_g}[\Phi_d(r_b) - \Phi_d(0)]\right\} \tag{6.39}$$

$$FM_0 = 4\pi\rho_{g,0} \int_0^{r_b} r'^2 \exp\left\{-\frac{\mu m_p}{k_B T_g}[\Phi_d(r') - \Phi_d(0)]\right\} dr', \tag{6.40}$$

assuming that the ISM temperature T_g is given by equation (6.33). The initial central ISM densities, thermal pressures and boundary radii for different DM core masses and different ICM properties are listed in Table 6.2. The initial radial density and pressure profiles, assuming an ICM with density $n_{\mathrm{ICM}} = 10^{-4}\,\mathrm{cm}^{-3}$ and temperature $T_{\mathrm{ICM}} = 10^7\,\mathrm{K}$ are shown in the middle panels of Figure 6.12. It is seen that, although we no longer have a one-parameter family of models and the boundary radius for the ISM is much smaller due to the pressure confinement assumption, the density and pressure profiles of the ISM are very similar to those of the original MB profiles.

Pressure confinement, case 2

The MB simulations also assume that the ISM is isothermal with a temperature that depends on the DM halo mass (equation (6.33)). Although this relation leads to a one-parameter family of ISM models, it also implies very low and high temperatures at the extremes of the mass range (Table 6.5.1). The temperature for a galaxy with core mass $10^6\,\mathrm{M}_\odot$ is too low for an assumed ionized gas, while the temperature of a galaxy with core mass $10^{10}\,\mathrm{M}_\odot$ is higher than expected from photo-ionization by supernova feedback. Thus, the temperature of the ISM is not realistically represented in this model. Moreover, when radiative cooling would be switched on, the temperature of the ionized ISM would quickly drop to about $10^4\,\mathrm{K}$, unless a strong heating source is present (see also section 6.5.5). Therefore, we set up a third set of initial ISM conditions assuming pressure confinement and an ISM gas temperature of $10^4\,\mathrm{K}$ for all DM halo masses. We refer to these initial conditions with PC_2.

The initial boundary radii and central ISM densities and pressures follow from equations (6.39) and (6.40), assuming $T_g = 10^4\,\mathrm{K}$ and are listed in Table 6.2. The initial radial density and thermal pressure

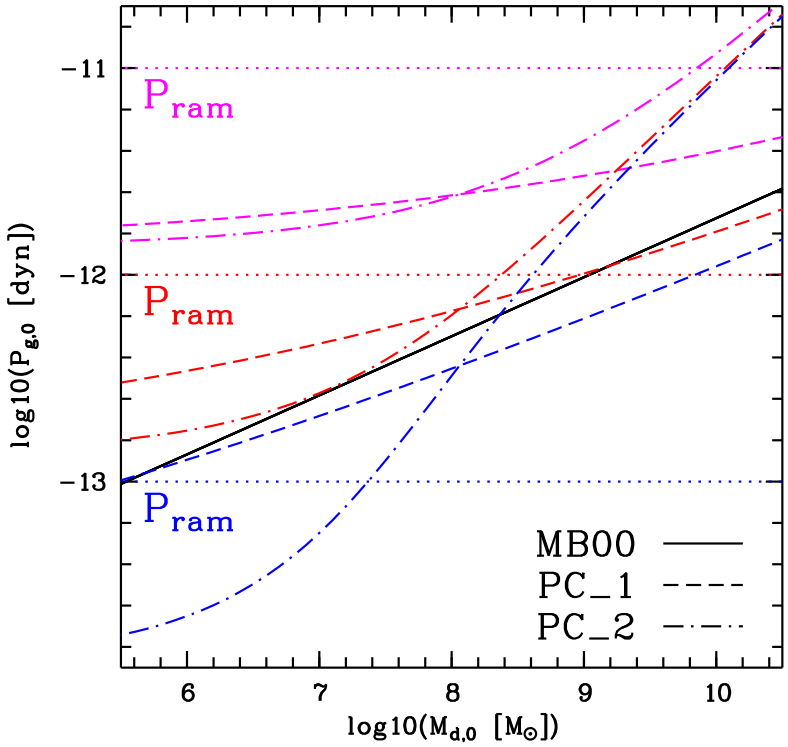

Figure 6.13: The central pressure of the ISM as a function of DM halo mass M_0, for the various initial conditions models. Instantaneous stripping occurs if the central pressure of the ISM is smaller than the ram pressure. The central pressure of the *density confined* MB models (full black line) are independent of the ICM conditions. If we assume the ISM to be *pressure confined*, then the central pressure will be dependent on the ICM density and temperature. The central pressure in models embedded in an ICM with temperature 10^7 K and density $10^{-3}\,\mathrm{cm}^{-3}$ (magenta), $10^{-4}\,\mathrm{cm}^{-3}$ (red) and $10^{-5}\,\mathrm{cm}^{-3}$ (blue) are shown, first taking the ISM temperature to vary with M_0 (PC_1, dashed lines) and second keeping the ISM temperature fixed at 10^4 K (PC_2, dash-dotted lines). The ram pressure experienced by a galaxy moving at a velocity of $1000\,\mathrm{km\,s}^{-1}$ through the ICM is also shown. See text for more details.

profiles are shown in the right panels of Figure 6.12. The profiles look very different compared to those of MB and PC_1. In small DM haloes, an ISM at a temperature of 10^4 K assumes a very extended distribution and the central density is very low. The thermal pressure of the ISM prohibits the gas from falling into the centre of the DM halo. This is in contrast to the MB and PC_1 initial conditions, where the smallest haloes have the largest initial central gas densities. The low temperatures ensure a low thermal pressure which allows the ISM to fall towards the centre of the DM halo. In the more massive haloes on the other hand, the gravitational potential well is deeper, so that the central gas density and the central gas pressure become much higher than in the previous initial conditions.

Analytic estimates

Using the analytic criterion for instantaneous stripping when the ram pressure exceeds the central ISM thermal pressure, MB arrive at an estimate of the critical DM core mass for total stripping

$$M_{0,\mathrm{crit}} = 1.27 \times 10^9 \left(\frac{F}{0.1}\right)^{-7/2} \left(\frac{n_{\mathrm{ICM}}}{10^{-4}\,\mathrm{cm}^{-3}}\right)^{7/2} \left(\frac{v_{\mathrm{gal}}}{10^3\,\mathrm{km\,s}^{-1}}\right)^{7} \mathrm{M}_\odot. \tag{6.41}$$

For the PC_1 and PC_2 initial conditions, the relation between $M_{0,\mathrm{crit}}$ and the galaxy properties is not so straightforward since the central ISM pressure depends in a complex way on the properties of the ICM. In Figure 6.13 we plot the central thermal pressure of the ISM in function of the DM core radius, for the different initial condition schemes and for different ICM conditions. The ram pressure experienced by a model galaxy moving at a velocity $v_{\mathrm{gal}} = 1000\,\mathrm{km\,s}^{-1}$ through a dense ICM ($n_{\mathrm{ICM}} = 10^{-3}\,\mathrm{g\,cm}^{-3}$; magenta dotted line), a moderately dense ICM ($n_{\mathrm{ICM}} = 10^{-4}\,\mathrm{g\,cm}^{-3}$; red dotted line) and a low-density ICM ($n_{\mathrm{ICM}} = 10^{-3}\,\mathrm{g\,cm}^{-3}$; blue dotted line) is indicated. Of course one should also consider varying the galaxy's velocity through the ICM, but this would make the figure needlessly complicated.

First let us concentrate on the MB initial conditions (black solid line). The central thermal pressure as a function of the DM core mass is

$$\begin{aligned} P_{g,0} &= \rho_{g,0} \frac{k_B T_g}{\mu m_p} \\ &= 1.40 F \rho_{d,0} \frac{G M_0}{3 r_0} \\ &= 9.6 \times 10^{-13} \left(\frac{M_0}{10^9\,\mathrm{M}_\odot}\right)^{2/7} \mathrm{dyn}. \end{aligned} \tag{6.42}$$

Assuming MB initial conditions, the ISM will be totally stripped from all DM halo masses ranging from 10^6 to $10^{10}\,\mathrm{M}_\odot$ if the ram pressure exceeds $1.85 \times 10^{-12}\,\mathrm{dyn}$. For example all MB models moving with a velocity of $v_{\mathrm{gal}} = 1000\,\mathrm{km\,s}^{-1}$ through a dense ICM will be totally stripped. On the other hand, if the ram pressure is lower than $1.33 \times 10^{-13}\,\mathrm{dyn}$, all MB models could retain some of their ISM. Hence we expect that galaxies moving through a low-density ICM are not instantaneously stripped.

When we assume that the ISM is initially pressure confined, the central ISM pressure depends on the thermal pressure of the ICM. If the ISM temperature is varied with DM halo mass we see that, for example, in a moderate cluster environment, the critical core mass is about equal to that of the MB initial conditions (dashed lines). Although the relation between the central ISM pressure and the DM core mass is somewhat different, the conclusions will be the same. In a dense ICM environment, all galaxies will be totally stripped, in a moderate ICM environment, only the most massive galaxies will retain some of their ISM and in a low-density environment no galaxies will be instantaneously stripped. Considering the PC_2 initial conditions (dash-dotted lines), the picture changes somewhat. Because of the high thermal pressure in the most massive model galaxies, they will no be totally stripped even in a dense environment, while the lowest mass model galaxies will be totally stripped even in a low-density environment.

The timescale for instantaneous stripping can be estimated using equation 6.7, assuming that the ISM is stripped when it is displaced over a distance $s = 2r_0$ and the mean surface density of the ISM is approximately $\Sigma_g = \rho_{g,0} r_0 / 4$.

$$t_{\mathrm{strip}} = \sqrt{\frac{\rho_{g,0} r_0^2}{P_{\mathrm{ram}}}} = \sqrt{\frac{\rho_{g,0}}{\rho_{\mathrm{ICM}}}} \frac{r_0}{v_{\mathrm{gal}}}. \tag{6.43}$$

Table 6.3: Units chosen for the first set of simulations.

M_0	r_0	r_b	`lunit`	`tunit`	`munit`	`lunit'`
$\mathrm{M}_\odot$	kpc	r_0	kpc	Myr	$\mathrm{M}_\odot$	kpc
10^6	0.16	5.0	4	4	0.64	5.8
10^7	0.43	4.5	10	10	10	14.4
10^8	1.14	4.0	25	25	156.25	36.1
10^9	3.07	3.5	60	60	2160	86.5
10^{10}	8.24	3.0	150	150	33750	216.3

Using the MB scaling relation between $\rho_{g,0}$, r_0 and M_0, we can write this as

$$t_{\mathrm{strip}} = 1.36 \times 10^8 \left(\frac{F}{0.1}\right)^{1/2} \left(\frac{M_0}{10^9\,\mathrm{M}_\odot}\right)^{2/7} \left(\frac{n_{\mathrm{ICM}}}{10^{-4}\,\mathrm{cm}^{-3}}\right)^{-1/2} \left(\frac{v_{\mathrm{gal}}}{10^3\,\mathrm{km\,s}^{-1}}\right)^{-1} \mathrm{yr}. \tag{6.44}$$

After the instantaneous stripping of the outer ISM halo from the more massive DM haloes or in low density ICM environments, the remaining gas will be subjected to KH instabilities, unless the gravitational restoring force is greater than the drag force (see section 6.2.2). However, the critical DM halo mass needed to retain the ISM is (see equation (6.10))

$$\begin{aligned} M_{0,\mathrm{KH}} &= \frac{v_{\mathrm{gal}}^2 r_0}{G} \\ &= 9.8 \times 10^{13} \left(\frac{v_{\mathrm{gal}}}{10^3\,\mathrm{km\,s}^{-1}}\right)^{7/2}, \end{aligned} \tag{6.45}$$

thus we expect all the model galaxies to be affected by KH stripping.

Assuming a total ISM mass FM_0 and a radius r_0 after the instantaneous stripping, KH instabilities will ablate the remaining gas on a timescale of

$$t_{\mathrm{KH}} = 2.25 \times 10^9 \left(\frac{F}{0.1}\right) \left(\frac{M_0}{10^9\,\mathrm{M}_\odot}\right)^{1/7} \left(\frac{n_{\mathrm{ICM}}}{10^{-4}\,\mathrm{cm}^{-3}}\right)^{-1} \left(\frac{v_{\mathrm{gal}}}{10^3\,\mathrm{km\,s}^{-1}}\right)^{-1} \mathrm{yr}, \tag{6.46}$$

which is several cluster crossing times. Taking into account the decrease of ISM mass and radius with time as stripping occurs, this timescale becomes somewhat shorter (Roediger & Hensler, 2005).

6.5.5 Ram pressure stripping simulations

The simulation box and the ICM flow

In order to strike a balance between computational cost (simulation time) and resolution, we settled for an ICM particle number of $N_{\mathrm{ICM}} = 60^3 = 216\,000$. This ensures roughly the same resolution as a 64^3 grid in the low-density ICM region, while allowing for about 50 000 ISM particles if we choose $64^3 = 262\,144$ sized particle arrays. The units used for the simulations of dEs with different DM halo masses are listed in Table 6.3. These units are chosen such that we can use the same ICM flow for each of the simulations. Thus, the mass of the ICM particles in HYDRA units is always the same and a factor $2 - 3$ smaller than the ISM particle masses.

To check whether the simulations are influenced by the size of the simulation box, we ran a second set of simulations using a three times larger box, but retaining the spatial resolution. Therefore we had to use three times as many particles to model the ICM. The static DM halo and the ISM particles were

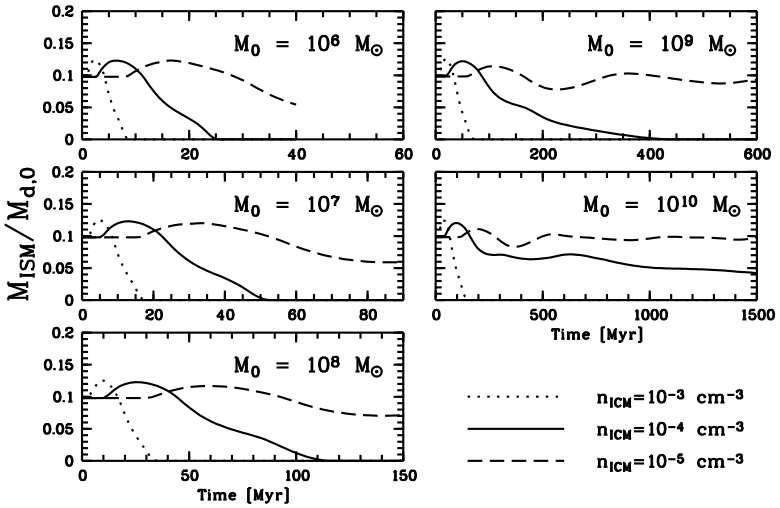

Figure 6.14: The ratio of ISM mass contained within one Burkert scale radius in function of time for the MB models moving at $v_{\rm gal} = 1000\,{\rm km\,s^{-1}}$ through cluster environments of different densities. Galaxies in a dense cluster ($n_{\rm ICM} = 10^{-3}\,{\rm cm^{-3}}$; dotted lines) are all immediately stripped, while the most massive galaxies in a moderate dense cluster ($n_{\rm ICM} = 10^{-4}\,{\rm cm^{-3}}$; solid lines) are able to hold on to their ISM over longer timescales. Finally, in a low-density environment ($n_{\rm ICM} = 10^{-5}\,{\rm cm^{-3}}$; dashed lines), all galaxies retain part of their ISM until the end of the simulation.

placed at the same distance from the beginning of the z axis. This was done to increase the distance to the end of the simulation box, where most problems are expected (see the first runs in section 6.5.2). In these simulations, we only change the size of the simulation box ($\texttt{lunit}' = \sqrt[3]{3}\texttt{lunit}$, see Table 6.3) while keeping the other units fixed.

The initial ISM distribution

The Monte Carlo realization of the ISM is not yet nicely relaxed, especially in the low-density regime where only few particles contribute to the ISM. Therefore, we first set up an extended ISM within the DM halo and let it relax for about 1000 timesteps. Then we select the ISM particles within the ISM boundary radius and place them into the ICM flow.

Varying the ICM density

We simulated the evolution of the ISM in dEs using the MB initial conditions for galaxies moving at a velocity of $1000\,{\rm km\,s^{-1}}$ through a dense ($n_{\rm ICM} = 10^{-3}\,{\rm cm^{-3}}$), a moderately dense ($n_{\rm ICM} = 10^{-4}\,{\rm cm^{-3}}$) and a low-density ($n_{\rm ICM} = 10^{-5}\,{\rm cm^{-3}}$) cluster environment. In Figure 6.14 the ISM gas fraction remaining inside the core radius r_0 is plotted against simulation time for the different DM halo masses considered. In all the simulations, there is an initial collapse phase as the thermal overpressure of the ICM compresses the ISM. The gas fraction raises by about 20 per cent and is more noticeable in the denser environments, where the pressure difference is higher. In the densest ICM conditions, the ISM is immediately stripped from all the galaxies. The analytic estimated timescales of instantaneous stripping given in Table 6.4, are in very good agreement with the simulations. In the moderate density runs, smaller galaxies also lose their ISM instantaneously, the $10^9\,{\rm M_\odot}$ galaxy is able to hold on to its

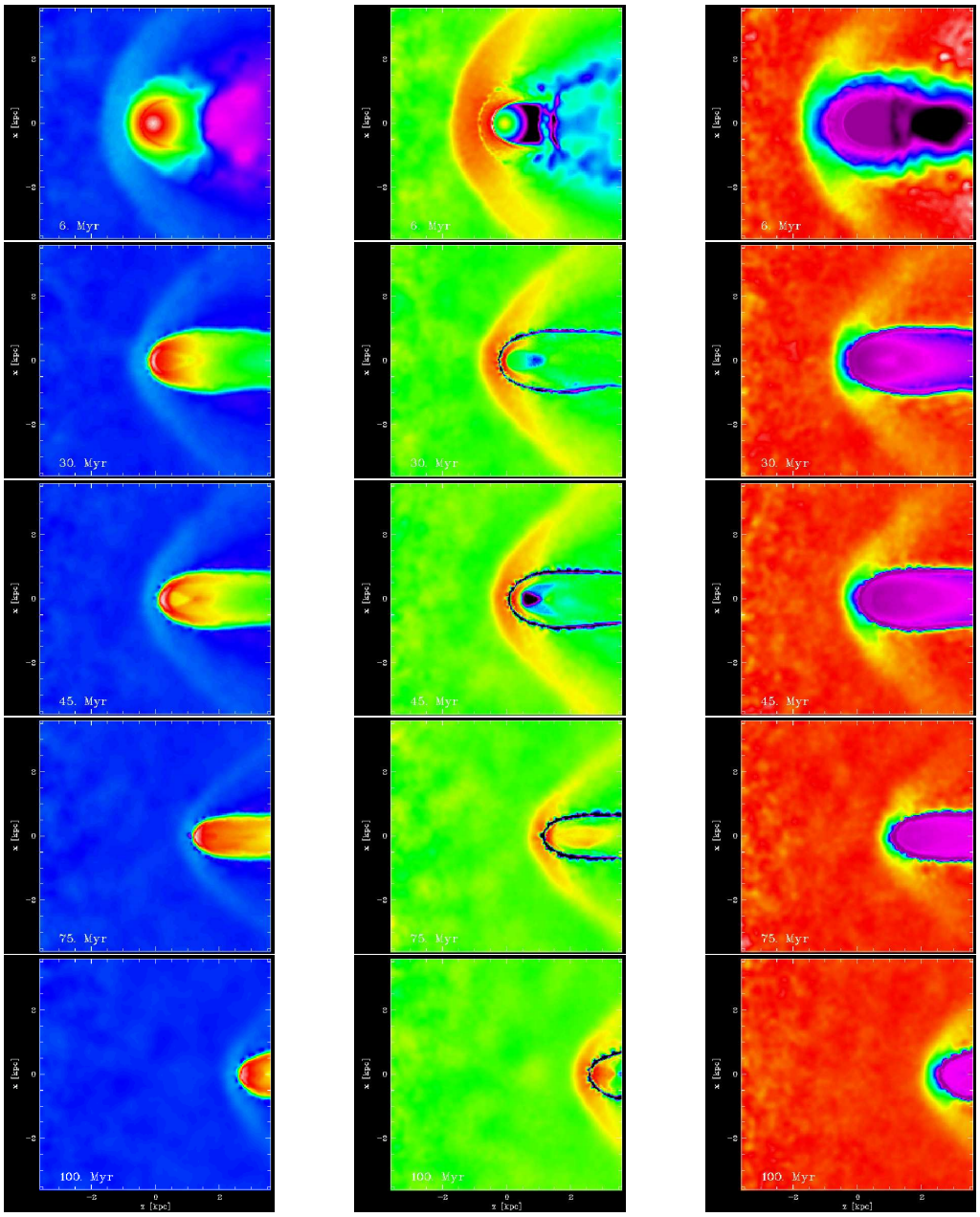

Figure 6.15: Ram pressure from a $10^7\,M_\odot$ dark halo, with MB initial conditions. In the left panel we show the logarithmic density, in the middle panel the logarithmic thermal pressure in shown and in the right panel we see the z-component of the gas velocity.

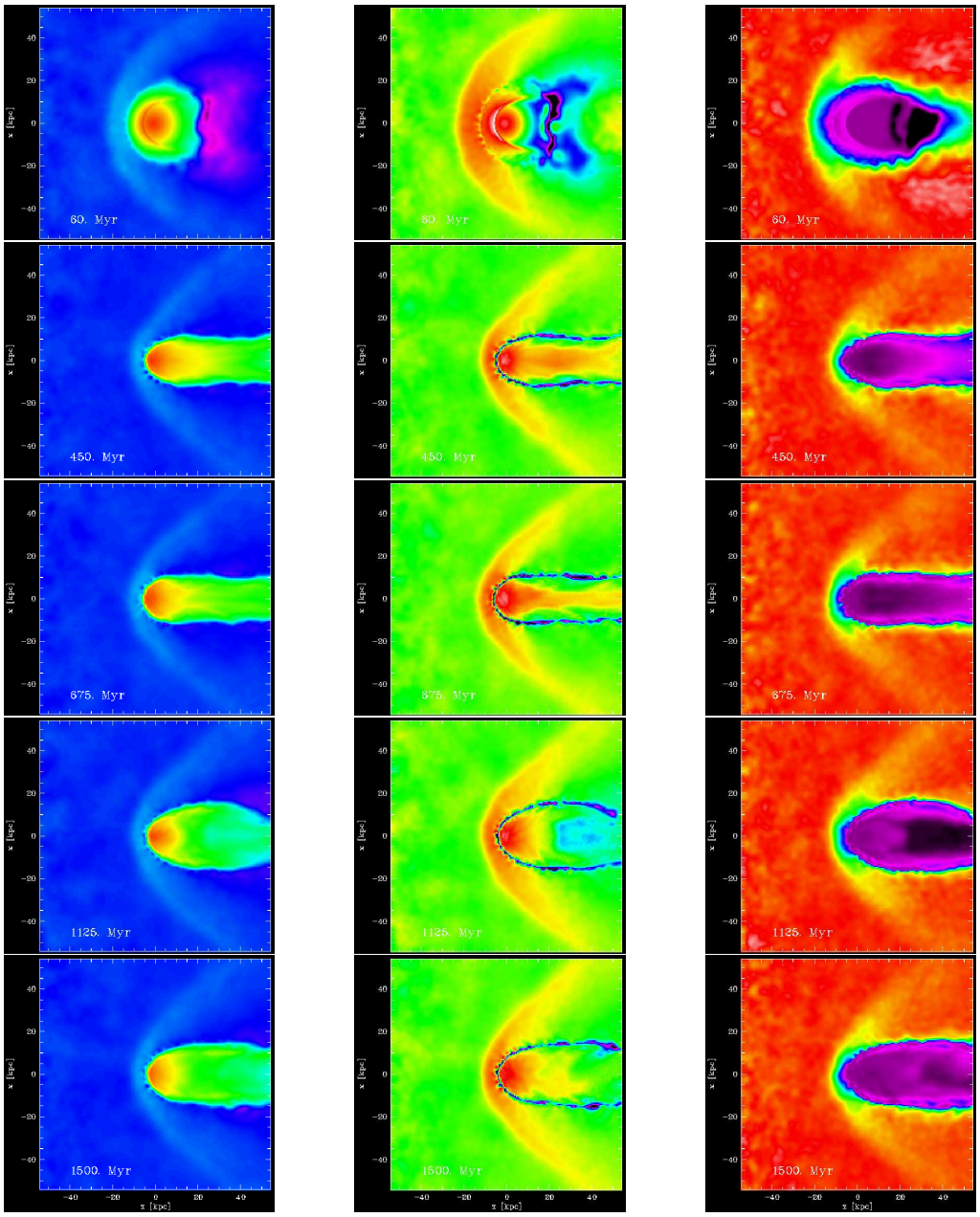

Figure 6.16: Ram pressure from a $10^{10}\,M_{\odot}$ dark halo, with MB initial conditions. In the left panel we show the logarithmic density, in the middle panel the logarithmic thermal pressure in shown and in the right panel we see the z-component of the gas velocity.

Table 6.4: Analytic estimates of the instantaneous stripping time, in Myr, for different DM halo masses and ICM densities. The velocity of the galaxy is $v_{\rm gal} = 1000\,{\rm km\,s^{-1}}$.

M_0	$n_{\rm ICM} = 10^{-3}\,{\rm cm^{-3}}$	$n_{\rm ICM} = 10^{-4}\,{\rm cm^{-3}}$	$n_{\rm ICM} = 10^{-5}\,{\rm cm^{-3}}$
$10^6\,{\rm M_\odot}$	6	19	60
$10^7\,{\rm M_\odot}$	11	36	114
$10^8\,{\rm M_\odot}$	22	70	221
$10^9\,{\rm M_\odot}$	43	70	430
$10^{10}\,{\rm M_\odot}$	83	262	828

ISM longer than predicted by the instantaneous stripping timescale, but after 4×10^8 all its ISM is lost. The most massive DM halo initially loses about $1/3$ of its ISM, but after about 6×10^8 yr, part of the ISM is replenished by accretion from downstream particles. Thereafter the galaxy undergoes continuous stripping but at a slow rate, and still retains about 45 per cent of its ISM after 1.5 Gyr. All galaxies in the low-density ICM retain part of their ISM at the end of the simulation time, but the amount of stripping is larger for smaller galaxies. The more massive dEs experience a cyclical stripping evolution, as gas that gets stripped is able to fall back again.

In Figure 6.15 snapshots of the evolution of a $10^7\,{\rm M_\odot}$ DM halo are shown. It is immediately clear that the use of the ICM buffer removes the problems we encountered with the incoming ICM flow. The simulation box is also chosen large enough that we can safely concentrate on a region around the DM halo without worrying about spurious effects due to the boundary conditions. We again see the density, thermal pressure and velocity v_z of the gas in the y plane centred on the DM halo. Initially, the thermal pressure of the ICM compresses the ISM, which is clearly seen in the wake of the galaxy where the z-component of the velocity is negative. Meanwhile, the bowshock develops in front of the ISM. Then, the ISM is quickly accelerated by the ram pressure and pushed out of the potential well. After about 4×10^7 yr, all the ISM is lost from the DM halo. The interface between the ISM and the ICM is clearly visible on the pressure plots.

In Figure 6.16 we plot the same for a $10^{10}\,{\rm M_\odot}$ DM halo. Note however that the distance and time scales are very different. Again, the ISM is initially compressed by the thermal pressure of the ICM, while a bowshock develops upstream. This more massive galaxy is able to retain its ISM over long timescales. After 6.5×10^8 yr, ISM particles that were stripped are moving back towards the DM potential well at the backside of the galaxy (in a movie of such snapshots, this churning is clearly visible).

Pressure-confined ISM

We simulated the evolution of the ISM in dEs moving at a velocity $v_{\rm gal} = 1000\,{\rm km\,s^{-1}}$ through a moderate cluster environment $n_{\rm ICM} = 10^{-4}\,{\rm cm^{-3}}$, setting up the initial conditions of the ISM assuming density confinement (MB), pressure confinement and varying ISM temperature (PC_1) and pressure confinement with $T_g = 10^4\,{\rm K}$ for all DM halo masses (PC_2). In Figure 6.17 the ISM mass fraction within one core radius in function of time is shown. The stripping timescales in the MB and PC_1 simulations are quite similar, while the PC_2 simulations behave very differently. Due to the higher initial thermal pressure, the $10^9\,{\rm M_\odot}$ PC_2 model is able to retain its ISM over much longer timescales than the MB model. Smaller DM haloes ($M_0 \leqslant 10^8$) lose their ISM instantaneously regardless of the initial conditions.

In Figure 6.18 snapshots of the evolution of a $10^7\,{\rm M_\odot}$ DM halo are shown, which can be compared to those in Figure 6.15. A low-density wake is seen to develop behind the ISM. The resolution in this low-density region is very low and some hot ICM particles are trapped in the wake, increasing the

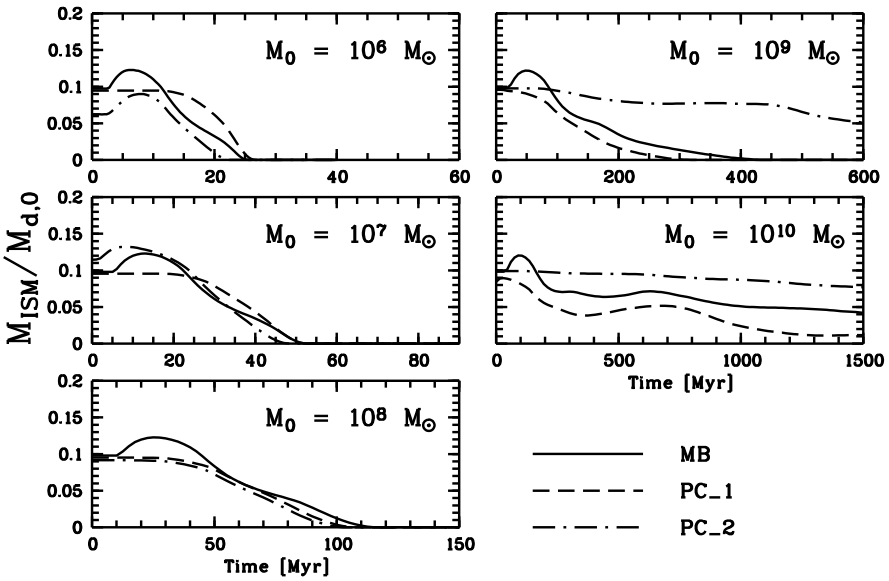

Figure 6.17: The ratio of ISM mass contained within one Burkert scale radius in function of time for the different initial conditions models: MB (full lines), PC_1 (dashed lines) and PC_2 (dash-dotted lines).

thermal pressure behind the galaxy. With the ram pressure on the front side and the increased thermal pressure on the backside, the ISM stays well confined until it is stripped from the DM halo.

In Figure 6.19 we plot the same for a $10^{10}\,\mathrm{M}_\odot$ DM halo, which can be compared to the snapshots in Figure 6.16. The boundary radius is much smaller for the PC_2 initial conditions. Although some particles from the edge of the ISM are stripped, most of the ISM remains within the DM halo, as expected. After $1.5\,\mathrm{Gyr}$, only 20 per cent of the ISM particles is lost from the DM halo.

Including radiative cooling

If radiative cooling is switched on, the ISM would cool down to about $10^4\,\mathrm{K}$ in less than $10^5\,\mathrm{yr}$. Subsequently, the thermal pressure in the ISM drops drastically and again we have thermal compression of the ISM. Just switching on the radiative cooling in the simulation results in a large and unwanted computational penalty since the ICM particles will also be cooled. However, we gave the ISM and ICM particles a different label in the simulations in order to treat them differently in the outflow conditions at the end of the z axes. We can use this labeling also to include radiative cooling in the ISM only.

Figure 6.20 shows the mass fractions contained within one core radius of the two models we considered.

In Figure 6.21, we show snapshots of the evolution of a dE with $10^{10}\,\mathrm{M}_\odot$ DM halo and an ISM with MB initial conditions. Initially the simulation is similar to that shown in Figure 6.16. However, the ISM temperature quickly drops from $1.3 \times 10^5\,\mathrm{K}$ to $10^4\,\mathrm{K}$ (the lower boundary of the cooling tables included in the HYDRA code), so that the thermal pressure also decreases. The ISM is thus even more compressed than in the previous simulations with MB initial conditions. While the outer ISM halo is stripped, the bulk of the ISM remains within the core radius of the DM halo. Clumps of stripped ISM manage to accrete back onto the galaxy from downstream. At the end of the simulation, only a small amount of stripping still occurs at the edge of the ISM.

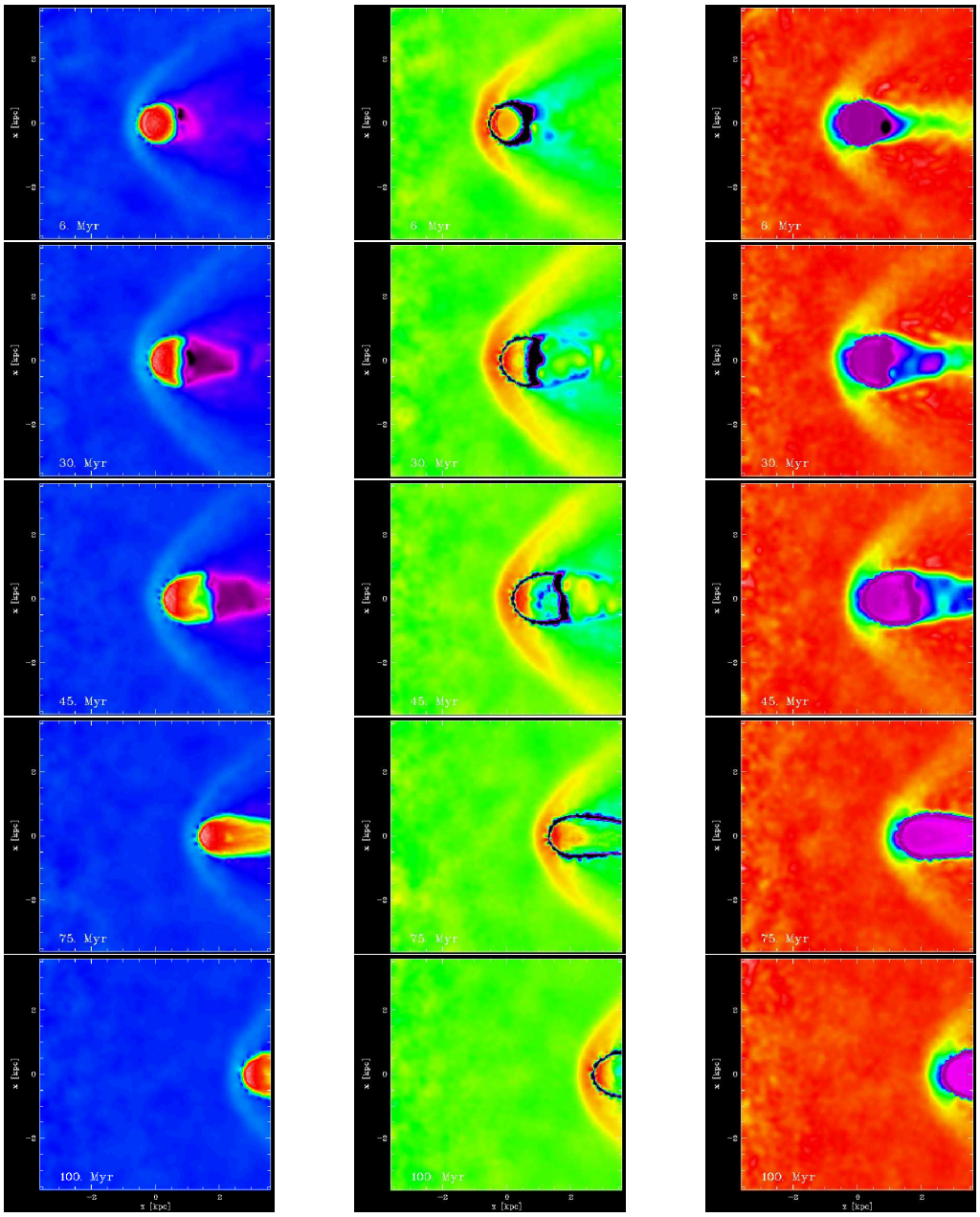

Figure 6.18: Ram pressure from a $10^7\,M_\odot$ dark halo, with pressure confinement and ISM temperature $10^4\,K$ initial conditions. In the left panel we show the logarithmic density, in the middle panel the logarithmic thermal pressure in shown and in the right panel we see the z-component of the gas velocity.

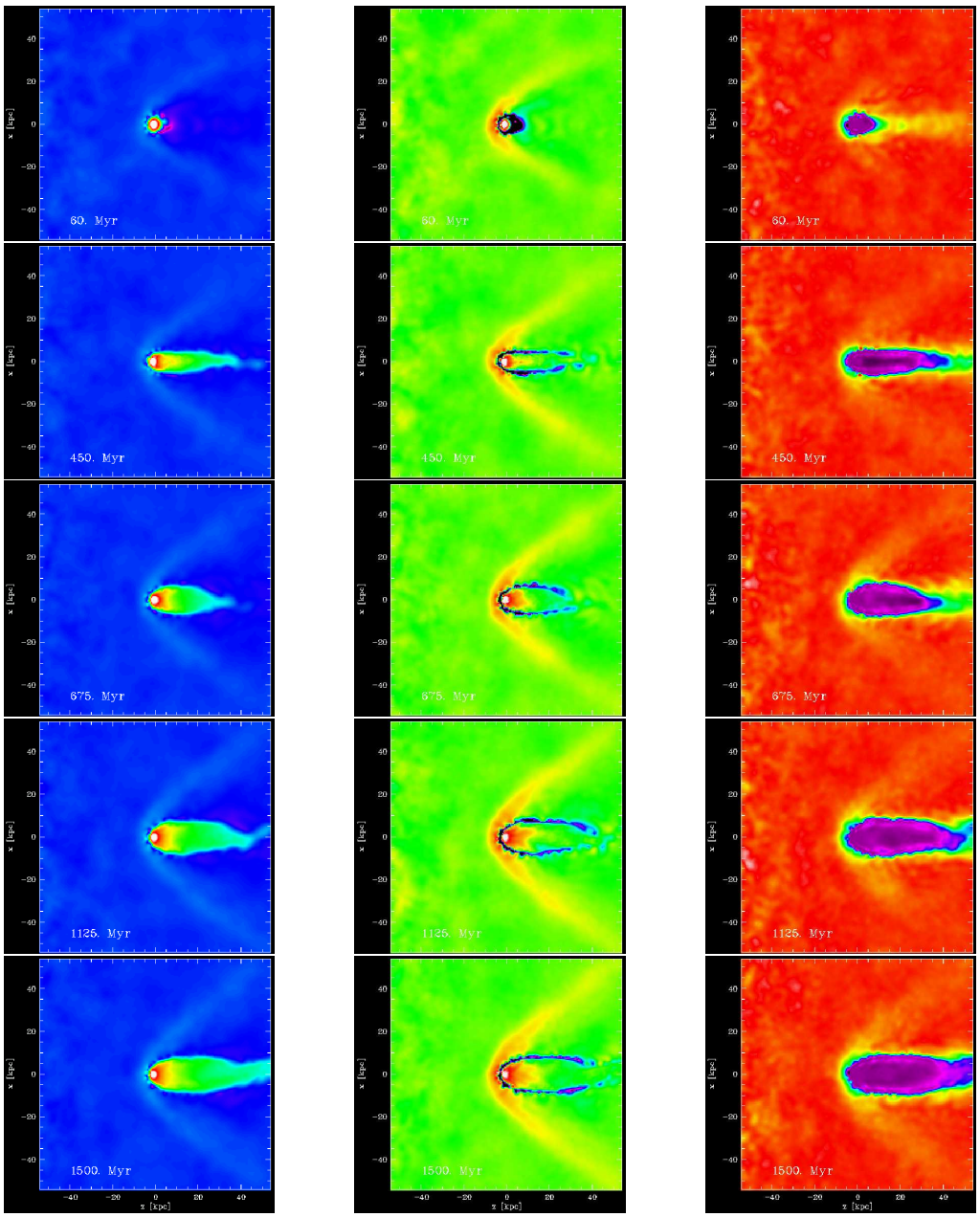

Figure 6.19: Ram pressure from a $10^{10}\,M_{\odot}$ DM halo, with PC_2 initial conditions.

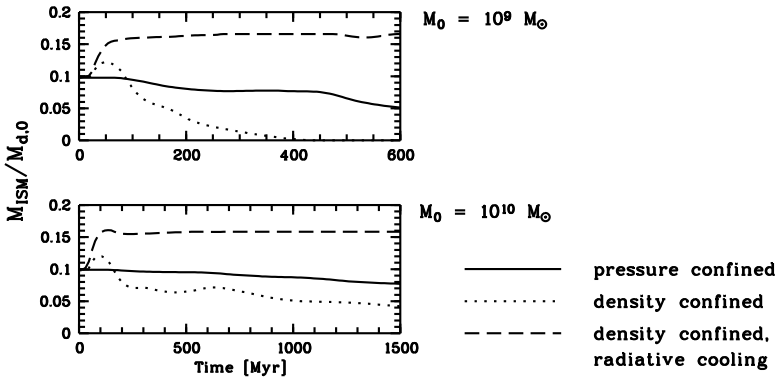

Figure 6.20: The ratio of ISM mass contained within one Burkert scale radius in function of time for the 10^9 and $10^{10}\,M_\odot$ dark matter haloes. Results for the MB run, the PC_2 run and the run including radiative cooling are compared, as indicated on the figure.

6.5.6 Conclusions

Initial conditions for the ISM

In these simulations, the ISM is modeled as a one-phase gas. Therefore the problem to choose between realistic ISM densities, temperatures and pressures is inherent to the model. In reality the volume is filled by a warm, dilute ISM at temperatures around 10^4 K, while the mass is concentrated in dense, cold molecular clouds. Trying to combine these two phases in one will lead to unphysical effects.

Comparison between hydrodynamical codes

To test the code and the prescriptions used, we compared our simulations to those of MB. They use a 2D Eulerian hydrocode to investigate ram-pressure stripping of ionized interstellar medium from dEs moving through an ICM. Since we use a 3D code and MB use a 2D code, our simulations have a significantly coarser resolution. However, the timescales and the main features of the MB simulations are nicely reproduced in our simulations. The snapshots presented in Figures 6.15 and 6.16 can be compared to Figures 2 and 3 in MB. The timescale over which the ISM is stripped depends on the mass of the DM halo.

Using a 3D code has the advantage that we can expand the spherically symmetric models considered here, to models with a more complicated geometry, e.g. including rotation or flattening (in any given direction). The advantage of an SPH code over grid codes is in the ease with which on can include self-gravity and radiative cooling of the gas. Moreover, gas processes such as star formation and feedback are difficult to implement in a grid code, whereas in the N-body/SPH formalism these processes can be included in a more natural way.

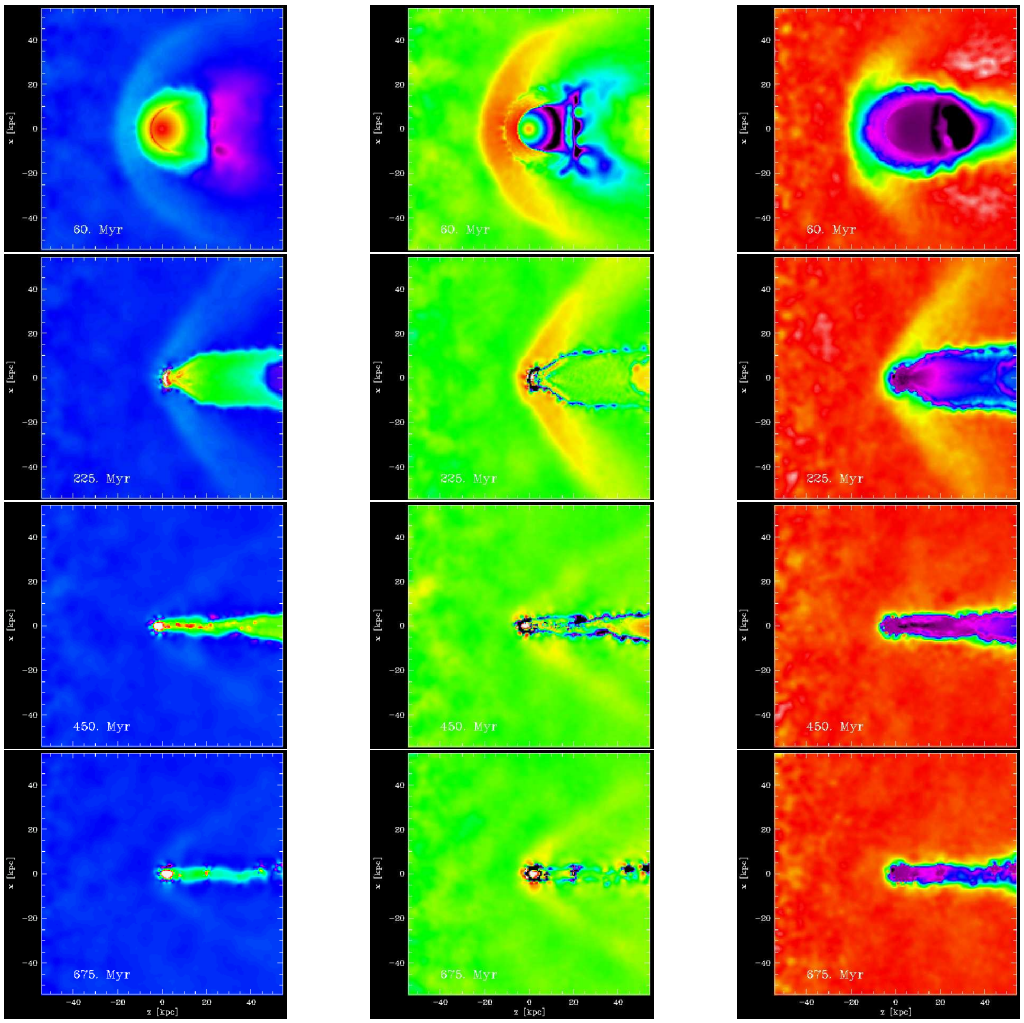

Figure 6.21: Ram pressure stripping from a $10^{10}\,M_{\odot}$ dark matter halo, with MB initial conditions, but including radiative cooling and no heating source. In the left panel we show the logarithmic density, in the middle panel the logarithmic thermal pressure in shown and in the right panel we see the z-component of the gas velocity.

6.6 Future work

6.6.1 SPH vs. hydro simulations

Future work includes a comparison between a grid and an SPH approach to ram-pressure stripping. This work will be done in collaboration with Elke Rödiger (University of Bremen, Germany), who uses a grid code to simulate ram pressure stripping in spiral galaxies. Up till now, both methods have been used to model ram-pressure stripping but no detailed comparison between the 2 methods exist. We will use exactly the same initial conditions and spatial resolution and the simulations will be analyzed in the same way.

6.6.2 Including self-gravity

Since no self-gravity of the gas is assumed, we run the code in pure SPH mode. The only gravitational force included in that of the static Burkert potential. We ran a few models including gravitational forces, but apart from slowing the code significantly, the results are the same. The main bottleneck for including gravitational forces is the ICM that fills the box, but does not actually contribute to the gravitational potential since it is assumed to be in an infinite uniform distribution. Including self-gravitation for the ISM gas particles only would be feasible, but this is not yet been attempted.

6.6.3 Including star formation

Many simulations have hinted at the possible burst of star formation caused by the compression of the ISM by the ICM (Abadi et al., 1999; Quilis et al., 2000; Schulz & Struck, 2001; Marcolini et al., 2003). However this effect has not yet been taken self-consistently taken into account. Observational evidence of a star formation burst in galaxies infalling onto a cluster has been presented by Gavazzi et al. (2003). In the following Chapter, the implementation of star formation and feedback in N-body/SPH simulations is discussed.

Chapter 7

Galactic winds in dwarf elliptical galaxies

7.1 Introduction

In this chapter, we simulate the formation of a dwarf galaxy using the HYDRA code including radiative cooling, star formation and stellar feedback. Most galaxy formation simulations concentrate on giant galaxies, but Mori et al. (1999) show that in their simulations, the formation of dwarf galaxies is quite different from that of giant ellipticals. In dwarf galaxies a galactic wind develops early on, after the first star formation burst, sweeping the gas out of the galactic potential. Star formation continues in the shell of the wind, so that an outward metallicity gradient forms. Also Chiosi & Carraro (2002) noted that the formation of elliptical galaxies depends strongly on the galaxy mass and the initial density. More precisely, massive elliptical galaxies, independent of their initial density, show a single burst of star formation, whereas the low-mass ones have a varied star formation history (SFH). An early strong starburst was observed in the high initial density systems, while in the low-density systems, the star formation was weaker and occurred in intermittent bursts. This was further investigated by Carraro et al. (2001) for the case of dwarf spheroidals (dSph). The dSphs in our Local Group are known to exhibit complicated histories of star formation ranging from a single very old episode to a series of bursts over most of the Hubble time. Carraro et al. (2001) find that in objects of the same total mass, different SFHs are possible, if the collapse phase started at different initial densities.

For the simulations we use the publicly available HYDRA code, described in chapter 5. HYDRA is a Lagrangian particle code that implements the gravitational forces via an Adaptive P^3M technique, and the hydrodynamical forces via the SPH technique. Metallicity-dependent radiative cooling tables of Sutherland & Dopita (1993), for gas temperatures in the range $10^4 - 10^8$ K are included in the HYDRA code. Cooling times quickly become very large for temperatures below 10^4 K, so we assume that gas particles cannot radiative cool below this temperature. Of course, the gas temperature can become lower due to adiabatic cooling. In Carraro et al. (2001), these cooling tables are extended to include temperatures in the range $10^2 - 10^4$ K. However, the equation of state for an ideal gas with molecular weight $\mu = 0.6$, which is assumed to be appropriate for a fully ionized plasma, may not be a good representation of cooler gas, where recombination of helium and hydrogen atoms takes place. Moreover, the cool gas condenses into dense molecular clouds so that the SPH representation of the ISM as a diffuse gas may be inadequate. Including a cool gas phase requires prescriptions for condensation of hot gas to cold clouds due to radiative cooling, star formation in cold clouds, and evaporation of clouds due to supernova feedback. The clouds could be modeled using a *sticky particles* scheme (Berczik,

1999), or a hybrid grid-particle code (Andersen & Burkert, 2000). However, such a scheme is beyond the scope of this work.

7.2 Cooling, star formation and feedback

When gas is allowed to cool, it can sink into the gravitational wells of dark matter haloes. If the gas density becomes high enough, star formation may start. The thermal feedback of supernova explosions will then heat the gas. In the previous chapter we have described the evolution of the gas in absence of cooling and heating. The change in specific energy was purely due to the $P\mathrm{d}V$ term in the hydrodynamical equations. Since the gas in an astrophysical environment will be subjected to cooling and heating, the adiabatic energy equation should be extended in order to include terms which describe these phenomena. We write the energy equation (5.77) as

$$\frac{\mathrm{d}\epsilon}{\mathrm{d}t} = -\frac{P}{\rho}\boldsymbol{\nabla}\cdot\boldsymbol{v} + \frac{\Gamma-\Lambda}{\rho}, \tag{7.1}$$

where Λ/ρ and Γ/ρ are the specific cooling and heating rates, respectively. The gas can be heated in several ways. We will study heating by stellar feedback (stellar winds, supernova explosions). Other heating sources, such as ultraviolet cosmic background radiation generated by active galactic nuclei, will not be investigated in this work.

In this section we first describe the implementation of radiative cooling in HYDRA. Then various implementations of star formation in SPH codes are reviewed. Also thermal feedback and chemical enrichment from supernova explosions are treated. Finally the detailed SPH implementation of these processes is outlined.

7.2.1 Radiative cooling

Radiative cooling is implemented using the tables of Sutherland & Dopita (1993), where the gas is assumed to be optically thin and in ionization equilibrium. The tabulated quantity is Λ_0', in units of erg s^{-1} cm^3, so that the emissivity is $\Lambda = n_e n_\mathrm{H}\Lambda_0'$, with n_e and n_H the electron and hydrogen number densities respectively. In HYDRA, the number density n of a gas particle is the *total* number density $n_\mathrm{tot} = n_e + n_i$, with n_i the ion number density. The minimum gas temperature tabulated is 10^4 K, hence hydrogen and helium atoms are assumed to be fully ionized. An assumed primordial gas composition of 75 per cent hydrogen and 25 per cent helium results in a number density ratio $n_\mathrm{He} = 0.1 n_\mathrm{H}$. Keeping in mind that each H atom contributes 1 electron and 2 particles, while each He atom contributes 2 electrons and 3 particles to the plasma, we can calculate

$$f_{\Lambda_0} = \frac{n_e n_\mathrm{H}}{n_\mathrm{tot}^2} = \frac{1.2 n_\mathrm{H}^2}{(2.3 n_\mathrm{H})^2} = 0.227. \tag{7.2}$$

The emissivity is then calculated as $\Lambda = n^2\Lambda_0 = n^2 f_{\Lambda_0}\Lambda_0'$. In HYDRA, Λ_0' is tabulated in function of temperature T within the range 10^4 and $10^{8.5}$ K and metallicity $[\mathrm{Fe/H}]$ from zero to solar metallicity. The exact value of Λ_0 for a given temperature and metallicity is found through interpolation over the tabulated values of Λ_0', multiplied by the factor f_{Λ_0}. Note that in HYDRA, $f_{\Lambda_0} = 0.229$, due to different rounding of the numerical values in equation (7.2). In Figure 7.1, Λ_0 is plotted in function of temperature for the tabulated metallicities. The temperature T_i of a particle is related to the specific energy ϵ_i via

$$\epsilon_i = \frac{3}{2}\frac{k_B T_i}{\mu m_p}, \tag{7.3}$$

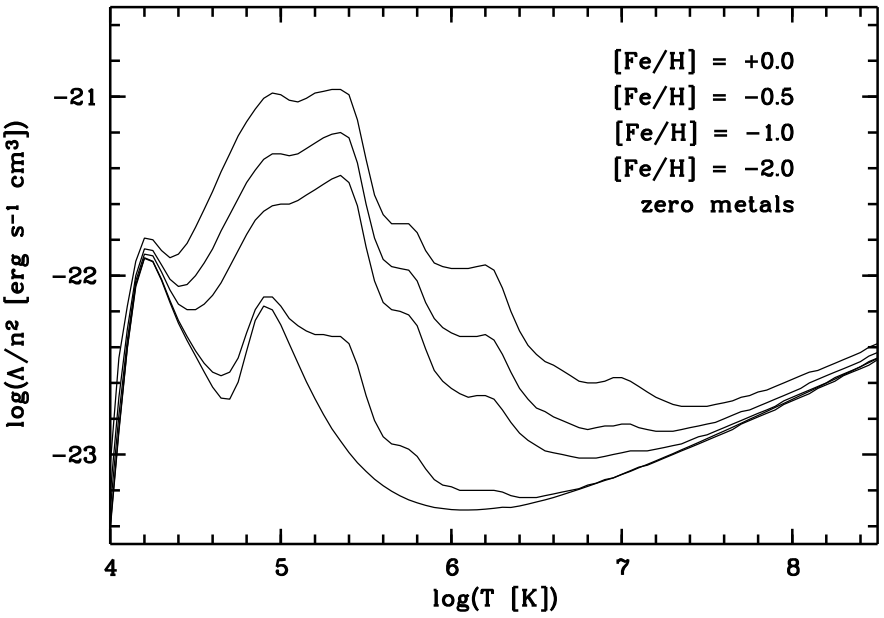

Figure 7.1: Cooling tables from Sutherland & Dopita (1993) as a function of temperature for different metallicities. The bottom curve corresponds to zero metallicity, while the top curve corresponds to solar metallicity. Intermediate curves are for the metallicity values listed in the upper right corner of the figure.

with k_B the Boltzmann constant, m_p the proton mass and μ the mean molecular weight. For simplicity, we fix $\mu = 0.6$ regardless of metallicity. This is reasonable since μ changes from 0.59 to 0.62 when going from zero to solar metallicity, for a fully ionized gas.

Since the cooling time $t_c = \epsilon\rho/\Lambda$ is often shorter than the dynamical time t_d, it is not used to constrain the HYDRA timestep. Instead, the particles are evolved adiabatically during one timestep Δt and the energy change $\Delta\epsilon$ due to radiative cooling is calculated assuming constant number density n_i and mass density ρ_i (Thomas & Couchman, 1992)

$$\int_{\epsilon}^{\epsilon+\Delta\epsilon} \frac{d\epsilon}{\Lambda_0} = -\frac{n_i^2}{\rho_i}\Delta t. \tag{7.4}$$

7.2.2 Star formation

Star formation is a very complex and still poorly understood process that is governed by the delicate interplay between stars and the interstellar medium (ISM). The local ISM consists of several components: hot intercloud medium (10^5 K), H II regions (10^4 K), warm intercloud medium (8000 K), H I clouds ($10-100$ K) and molecular H_2 clouds ($5-30$ K). The hot and warm intercloud medium occupy almost 100 per cent of the volume. On the other hand, the H I and H_2 clouds contain about 90 per cent of the mass, with the other 10 per cent in the warm intercloud medium. Star formation occurs in giant molecular clouds. These have typically masses of a few $10^5 - 10^6\,M_\odot$, temperatures around 10 K and number densities in excess of $10^3\,\mathrm{cm}^{-3}$. Giant molecular clouds do not collapse as a whole, but stars

are formed inside in smaller subclouds. The energy input from stellar winds and supernova explosions into the molecular cloud evaporates the remaining molecular gas of the cloud.

In present-day SPH simulations of galaxy formation, the precise process of star formation cannot be followed in detail due to the mass resolution of about $10^6\,\mathrm{M}_\odot$ per gas particle. Moreover, the multiphase structure of the ISM is generally not modeled, although some attempts have been made to include a multiphase ISM in particle codes. The molecular clouds are then modeled as *sticky particles* (Vollmer et al., 2001). Hence, to include star formation in a numerical code for galaxy evolution, some simplifying assumptions have to be made. We need to set two important pieces of information: first we have to set suitable conditions under which stars can form, and second, we must express the star formation rate (SFR) law governing the efficiency at which gas is converted into stars.

Another important issue is the feedback from the stars. As stars evolve and die, they eject mass, energy and heavy elements into the surrounding ISM. The energy input can slow or even halt the star formation process, while the enrichment of the ISM with heavy elements changes the chemical composition and hence affects the cooling rate of the ISM. These issues will be discussed in detail in the next section.

The first implementation of star formation and feedback in SPH codes was made by Katz (1992). Further improvements were made over the years by, amongst others, Navarro & White (1993), Mihos & Hernquist (1994), Friedli & Benz (1995), Katz et al. (1996), Gerritsen & Icke (1997), Carraro et al. (1998), Mori et al. (1999), Thacker & Couchman (2000), Mosconi et al. (2001), Kay et al. (2002), Kawata & Gibson (2003), Kobayashi (2004) ...

Star formation criteria

Several slightly different star formation criteria have been used in different SPH studies of galactic evolution. Because stars are known to form inside giant molecular clouds, the common idea of the star formation criteria is to form stars in collapsing, dense and rapidly cooling regions.

Collapsing regions are identified to be those gas particles for which $\boldsymbol{\nabla}\cdot\boldsymbol{v} < 0$. The most straightforward way to select dense and cold regions is to impose critical density and temperature criteria: $\rho > \rho_c$ and $T < T_c$ (Thacker & Couchman, 2000; Mosconi et al., 2001). The critical density is chosen such that the cooling time is always smaller than the dynamical time (see below), while the critical temperature is chosen to be the minimum temperature tabulated by the cooling tables ($T_c = 10^4\,\mathrm{K}$) (Mosconi et al., 2001) or the temperature at which the cooling time for a zero metallicity gas is the shortest ($T_c = 3\times10^4\,\mathrm{K}$) (Thacker & Couchman, 2000).

More elaborate criteria require that the gas is instable against gravitational collapse. Mostly, the Jeans instability is used (Binney & Tremaine, 1987). In a hypothetical infinite homogeneous fluid of density ρ_o, perturbations with a scale longer than $\approx c_s/\sqrt{G\rho_0}$ will be unstable, with c_s the sound speed of the perturbation. In other words, the fluid is unstable on a scale r if the dynamical time t_d is less than the time needed for a sound wave to transverse this scale, or if the sound crossing time is greater than the gravitational dynamical time.

If we take the local scale of the gas to be the SPH smoothing length h_i, the sound crossing time t_s is estimated by

$$t_\mathrm{s} = \frac{h}{c_s} = \frac{h}{\sqrt{\frac{9}{10}\epsilon}}, \tag{7.5}$$

where $c_s = \sqrt{\gamma(\gamma-1)\epsilon}$ is the local sound speed (and $\gamma = 5/3$ for an ideal gas).

The gravitational dynamical timescale has been interpreted in different ways. The definition of the dynamical time of a system with mean density ρ_0 is given by Binney & Tremaine (1987) as:

$$t_\mathrm{d} = \sqrt{\frac{3\pi}{16G\rho_0}}. \tag{7.6}$$

The dynamical time is approximately the time required for an orbiting star to travel halfway through a system with mean density ρ_0. This is the gravitational timescale proposed by Navarro & White (1993) and also used by Kawata & Gibson (2003). The free-fall time is defined as $t_{\rm ff} = t_{\rm d}/\sqrt{2}$. It is the time at which a pressureless system with mean density ρ_0 that is released at time $t = 0$ will collapse to a point. This time is used by Mori et al. (1999) as the gravitational timescale (which they call the dynamical time also). On the other hand, Katz et al. (1996) defined the dynamical time as:

$$t_{\rm d} = \frac{1}{\sqrt{4\pi G\rho_0}}, \tag{7.7}$$

which is also used by Kobayashi (2004).

Although most authors use the local gas density to estimate the dynamical timescale, Buonomo et al. (2000) argue that the total local density (gas + dark matter + stars) should be used rather than the local gas density, since the presence of dark matter accelerates the collapse of a fluid element.

Finally, the gas must be rapidly cooling, which can be expressed by requiring that the cooling timescale $t_{\rm c}$ is much less than the dynamical timescale. The cooling time is given by (Navarro & White, 1993)

$$t_c = \frac{\epsilon}{\dot{\epsilon}_c} = \frac{3}{2}\frac{k_b T}{\mu m_p}\frac{\rho}{\Lambda(n,T,Z)}, \tag{7.8}$$

where $\dot{\epsilon}_c$ is the change in specific energy due to radiative cooling. This criterion is sometimes replaced by a density constraint $\rho > \rho_c$, with $\rho_c \approx 10^{-25}\,{\rm g\,cm^{-3}}$. This density threshold is chosen such that the cooling time is significantly lower than the dynamical time for all temperatures, using the zero-metallicity cooling function. However, since the cooling function is metallicity-dependent, and chemical feedback from supernovae occurs over time, this density threshold should be adjusted over time, as the metallicity of the gas changes. Buonomo et al. (2000) compare star formation recipes using the density threshold and the cooling time criterion and conclude that the more general condition on the cooling timescale is preferred.

Carraro et al. (1998) make the cooling time also dependent on the heating rate

$$t_{\rm c} = \frac{\epsilon}{|\dot{\epsilon}_h - \dot{\epsilon}_c|}, \tag{7.9}$$

with $\dot{\epsilon}_h$ the heating rate (due to all possible sources; stellar winds, SNe, mechanical shocks) and $\dot{\epsilon}_c$ the cooling rate of the gas.

To summarize we list the conditions used in this work. We assume that star formation can take place in a gas particle when three conditions are met

$$\begin{aligned} \boldsymbol{\nabla}\cdot\boldsymbol{v} &< 0 \\ t_{\rm d} = \frac{1}{\sqrt{4\pi G\rho_t}} &< t_{\rm s} = \frac{h}{c_s} \qquad (7.10) \\ \rho_g &> \rho_c = 2\times 10^{-25}\,{\rm g\,cm^{-3}}, \qquad (7.11) \end{aligned}$$

where ρ_g is the local gas density and ρ_t is the local *total* density. There are two important remarks to be made here. Firstly, we use the *overdensity criterion* instead of a condition on the cooling time $t_{\rm c} = \frac{\epsilon}{\dot{\epsilon}_c} << t_{\rm d}$. The cooling time condition is always met for densities larger than ρ_c. Moreover the overdensity criterion is easier to implement. Secondly, it should be noted that for the dynamical timescale, the *total* density ρ_t is used, i.e. the density generated by DM+gas+stars. To estimate this total density we use a simple *tophat kernel* scheme. The mass of all particles within a distance of

$2h$ of a gas particle is summed and divided by the volume $4\pi(2h)^3/3$ to yield a total density. In the present implementation, the neighbour search is performed over all the particles. In principle this could be made much more efficient using a chaining-mesh like algorithm. For particle numbers of the order of 10^4 particles the present crude implementation is however feasible.

The star formation rate

When a gas particle is eligible to form stars, its star formation rate (SFR) is given by

$$\frac{\mathrm{d}\rho_s}{\mathrm{d}t} = -\frac{\mathrm{d}\rho_g}{\mathrm{d}t} = c_* \frac{\rho_g}{t_\mathrm{d}}, \tag{7.12}$$

with ρ_s the stellar density. Thus the SFR is proportional to the local gas density and inversely proportional to the local dynamical time, which is generally longer than the cooling timescale in star-formation regions. The dimensionless star formation efficiency parameter c_* is in most cases a free parameter, varying between 0.1 and 1. Since $t_\mathrm{d} \propto \rho_g^{-1/2}$, the SFR is proportional to $\rho_g^{1.5}$. This is in agreement with the Schmidt law, derived from observational estimations (Schmidt, 1959):

$$\frac{\mathrm{d}\rho_g}{\mathrm{d}t} \propto \rho_g^n, \tag{7.13}$$

with n usually between 1 and 2.

In a numerical simulation, the star formation will occur in discrete steps. Several different approaches have been employed to achieve this.

Equation (7.12) can be used to derive the *probability* p_* that a gas particle will form stars during a timestep Δt (Katz, 1992; Katz et al., 1996; Kobayashi, 2004). Thus the SFR can be sampled with a Monte Carlo procedure. The probability p_* that a gas particle that is eligible to form stars will actually do so, is given by

$$p_* = 1 - \exp\left(-c_* \frac{\Delta t}{t_\mathrm{d}}\right). \tag{7.14}$$

At each timestep, a random number $p \in [0, 1]$ is drawn from a uniform distribution. If $p_* > p$, a fraction ϵ_* of the gas is converted into a new, collisionless star particle (Katz, 1992; Katz et al., 1996). Hence, star particles with mass $m_s = \epsilon_* m_g$ are created, and ϵ_* is the fraction of gas in a giant molecular cloud that is converted into stars before it is evaporated. Observations of star formation in molecular clouds yield ϵ_* in the range of a few per cent to about 50 per cent. In the simulations the star formation efficiency is fixed to be $\frac{1}{3}$. If gas particles are allowed to experience unlimited recurrent star formation episodes, very many small star particles will be created.

To derive a stellar mass for the newly formed star particles, Kobayashi (2004) integrate equation (7.12) and multiply the stellar density by a volume factor

$$m_s = \pi h^3 \rho_g \left[1 - \exp\left(-c_* \frac{\Delta t}{t_\mathrm{d}}\right)\right], \tag{7.15}$$

where h is the SPH smoothing length of the parent gas particle.

Alternatively, one could rewrite equation (7.12) as (Mihos & Hernquist, 1994; Carraro et al., 1998; Thacker & Couchman, 2000)

$$\frac{\mathrm{d}m_s}{\mathrm{d}t} = -\frac{\mathrm{d}m_g}{\mathrm{d}t} = c_* \frac{m_g}{t_\mathrm{d}}. \tag{7.16}$$

Hence, during each timestep Δt, a gas particle with mass m_g that is eligible to form stars will produce a star mass m_s:

$$m_s = m_g \times \left[1 - \exp\left(-c_* \frac{\Delta t}{t_{\mathrm{d}}}\right)\right]. \tag{7.17}$$

However, this scheme leads to the spawning of a myriad of small star particles if the timestep Δt is small.

Adding a large amount of extra particles to the simulation will make the computation prohibitively expensive. In order to control the total number of newly formed particles, Mihos & Hernquist (1994) developed a scheme in which the star particles do not immediately acquire their individuality. A star-forming particle becomes a gas-star hybrid particle, which has a total mass equal to the initial gas mass, and a gas mass which decreases as star formation takes place. The total mass is used in the gravity calculation, while the gas mass only is used in the hydrodynamical equations. When the remaining gas mass falls below 5 per cent of the total mass, the particle is converted into a collisionless star particle and the remaining gas and energy are distributed amongst the gas neighbours using an SPH smoothing procedure. The advantage of this scheme is of course that the computational cost is significantly reduced, since no extra particles need to be created. Moreover, no restrictions need to be set on the stellar mass formed in one timestep. Recurrent episodes of star formation within the same gas particle are possible, so that the gas is depleted in discrete steps. On the other hand, before a star particle becomes collisionless, it is kinematically coupled to the parent gas cloud, whereas in reality they would move separately.

Thacker & Couchman (2000) consider a similar scheme, but treat the gas-star hybrid particle as an entirely gaseous particle, with a star mass as ghost variable. Each gas particle can give birth to a maximum of two star particles. First, when the star mass reaches 50 per cent of the total mass, and second, as the star mass reaches 80 per cent of the remaining gas mass. In this scheme, the total number of particles is kept under control. The main drawback is that star formation is delayed until the ghost stellar mass reaches the threshold mass.

Navarro & White (1993) remark that from equation (7.12), it follows that the gas density will decrease by a factor of 2 after a time $\tau_{1/2} \approx t_{\mathrm{dyn}}/c_* \ln 2$. Thus, in their scheme, a gas particle that becomes eligible to form stars at a time t will give birth to a star particle containing half its mass at the first timestep after $t + \tau_{1/2}$, and the mass of the gas particle is reduced accordingly. To reduce the total number of particles, each gas particle is allowed to form stars only 4 times. After the fourth parting, the remaining gas is distributed over the neighbouring gas particles using an SPH smoothing scheme.

Considering all this previous work, we came up with the following star formation scheme. Each timestep, the star formation criteria (equations (7.10)) are checked for all the gas particles. When a gas particle becomes eligible for star formation, the star formation probability p_* is computed (equation (7.14)). The star formation efficiency parameter c_* set to 1, as in Carraro et al. (2001), but we will investigate the role of c_* in section 7.4.2. If a new *star particle* is born, its mass equals $\frac{1}{3}m_g$, and the mass of the gas particle is reduced accordingly. The star particle is created at the same position and with the same velocity as the parent gas particle. Moreover, it inherits the metallicity and the smoothing length of the gas particle.

Recurrent episodes of star formation within the same gas particle are possible, but due to resolution limitations, only four bursts per gas particle are allowed. After a gas particle has experienced a fourth star burst, its gas and metal mass and its specific energy are distributed among the neighbour gas particles using the SPH smoothing scheme. This restriction in the first place prevents the creation of large numbers of star particles which would increase the computational cost of the N-body scheme.

A second reason to restrict the number of stellar bursts in the gas particles, is to introduce a lower mass limit on the star particles. With four recurrent starbursts, each consuming one third of the original gas

mass, the smallest star particle that can be formed has $m_* = \frac{8}{81} m_g$ or about one tenth of the original gas mass.

Each star particle represents a simple stellar population (SSP), with stars distributed according to an initial mass function (IMF). This IMF is assumed to be a continuous function of the stellar mass. Mass and energy feedback, and chemical evolution are then integrated over the IMF. However, if the mass of a star particle becomes too low (less than a few $100\,\mathrm{M}_\odot$), the continuous representation is no longer valid due to the actual discreteness of the IMF. Of course, one could consider sampling the IMF into discrete stars for each star particle that forms (Lia et al., 2002). Although this could be an interesting future project, we here ensure that the mass of the star particle is high enough, so that the continuous approximation of the IMF can be safely adopted.

7.2.3 Stellar feedback

Stars are born, they live and they also die, gas to gas, dust to dust. Stars inherit the properties (position, velocity, chemical composition) of the ISM from which they are born. During their lifetime the most massive stars inject thermal energy into the ISM through stellar winds. They will explode as supernovae type II (SN II), thereby injecting copious amounts of energy and synthesized elements (especially so-called α elements such as Ca, O, Si and Mg) into the ISM. Intermediate mass stars may also explode as supernovae of type Ia (SN Ia), which contribute mostly Fe to the ISM. The surrounding ISM is kinetically shocked by a SN explosion, creating a supernova remnant several parsec across. Over time, this kinetic energy is converted into thermal energy, which is radiated away. The least massive stars are long-lived and reflect the chemical composition of the ISM at the time of their birth.

The star particles in numerical simulations of galaxy formation are not individual stars, because the mass resolution that is presently achieved still exceeds the masses of individual stars by several orders of magnitude. A star particle with mass $\sim 10^4\,\mathrm{M}_\odot$ can be regarded as a population of stars that share the same properties. Such a stellar population with stars of equal age and equal metallicity is called an SSP. At birth, the stars are distributed according an IMF. In order to calculate the fraction of stars in a star particle that will contribute in the feedback loop, we have to specify the IMF and we have to specify how an SSP evolves.

Initial mass function (IMF)

Salpeter (1955) observationally derived an IMF for the stars in the solar neighbourhood. The IMF by number, $\Phi(m)$, in each mass interval dm is defined as

$$\Phi(m)dm = Am^{-(1+x)}dm, \tag{7.18}$$

where $x = 1.35$ is the Salpeter index or slope and the coefficient A is determined by the normalization in the mass range $m_l < m < m_u$, with m_l and m_u the lower and upper mass limit, respectively. The function $\Phi(m)$ can be regarded as the probability that a star with mass m is born, or as the fraction of stars with mass m present in the stellar population. Caution is needed when comparing the results from different studies that use the same symbols, but a mass normalization for the IMF.

Although the Salpeter IMF was derived for stars in the solar neighbourhood, and in the mass range $0.4\,\mathrm{M}_\odot < m < 10\,\mathrm{M}_\odot$, this IMF, extrapolated over a larger mass range, is much used in stellar population synthesis because of its mathematical simplicity.

The lower mass limit for stars is determined by the ability of a collapsing gas cloud to start hydrogen burning in its centre. Gas clouds with mass smaller than about $0.08\,\mathrm{M}_\odot$ will not reach the central density and temperature required for hydrogen fusion and thus will never shine as a star. The lower mass frequently adopted in population synthesis studies is $0.1\,\mathrm{M}_\odot$. The upper mass limit is much less

constrained, and values between 40 and $120\,\mathrm{M}_\odot$ can be found in the literature. Massive stars are quite rare and very short-lived, so that detailed observations are difficult to obtain.

If the slope of the IMF is changed, the relative fraction of dwarf and giant stars is changed. For a *top-heavy* IMF (i.e. $x > 1.35$), there will be more massive stars, and thus more supernova explosions per unit mass converted into stars. A *bottom-heavy* IMF ($x < 1.35$) will result in more mass locked away in low-mass stars.

Simply extrapolating the Salpeter IMF function might not represent the real IMF. More recent observations suggest that the IMF is flattened for masses below $0.6\,\mathrm{M}_\odot$. Based on these observations, bimodal and multimodal extensions to the Salpeter IMF have been considered (Miller & Scalo, 1979; Kroupa et al., 1993). An IMF based on physical grounds was derived by Padoan & Nordlund (2002) and provides a natural explanation for the flattening of the IMF at low stellar masses.

In this work we will follow the prescriptions of Mori et al. (1999) and adopt the Salpeter IMF with upper and lower mass limits $m_l = 0.1\,\mathrm{M}_\odot$ and $m_u = 60\,\mathrm{M}_\odot$. Then, the IMF becomes

$$\Phi(m) = 0.06 m^{-2.35}. \tag{7.19}$$

Mass feedback

Stars return part of their mass back to the ISM. Massive stars that explode as SN II are supposed to leave a neutron star or black hole. Intermediate-mass stars also expel part of their envelope in a planetary nebula, leaving a white dwarf as remnant. In principle, the detailed mass-loss rate of an SSP can be calculated using stellar evolution tracks. The main-sequence lifetime of a star with mass m can be approximated as (David et al., 1990)

$$\log(\tau(m)) = 10 - 3.42\log(m) + 0.88\log(m)^2. \tag{7.20}$$

Given the Salpeter IMF, the number of SN II can be easily calculated. Assuming that each star more massive than $m_{\mathrm{SN\,II}}$ explodes as a SN II, we obtain

$$\begin{aligned} N_{\mathrm{SN\,II}} &= \int_{m_{\mathrm{SN\,II}}}^{m_u} \Phi(m) dm \\ &= \frac{A}{x}\left(m_{\mathrm{SN\,II}}^{-x} - m_u^{-x}\right), \end{aligned} \tag{7.21}$$

if we adopt a Salpeter IMF. Because of the normalization of the IMF, $N_{\mathrm{SN\,II}}$ is actually the number fraction of stars that are SN II progenitors. This fraction is $N_{\mathrm{SN\,II}} = 2.5 \times 10^{-3}$, assuming that all stars with mass larger than $m_{\mathrm{SN\,II}} = 8\,\mathrm{M}_\odot$ are expected to go supernova. The correspondent *mass fraction* $f_{\mathrm{SN\,II}}$ of massive stars is given as

$$f_{\mathrm{SN\,II}} = \frac{\int_{m_{\mathrm{SN\,II}}}^{m_u} m\Phi(m) dm}{\int_{m_l}^{m_u} m\Phi(m) dm}, \tag{7.22}$$

or $f_{\mathrm{SN\,II}} = 0.122$, so that, of a star particle of mass m_s, the total stellar mass contributing to SN II is $0.122 m_s$.

Assuming that each SN II explosion leaves a $m_{\mathrm{rem}} = 1.4\,\mathrm{M}_\odot$ remnant (neutron star or black hole), we can now calculate the mass fraction $F_{\mathrm{SN\,II}}$ that is returned to the surrounding ISM

$$F_{\mathrm{SN\,II}} = \frac{\int_{m_{\mathrm{SN\,II}}}^{m_u} (m - m_{\mathrm{rem}})\Phi(m) dm}{\int_{m_l}^{m_u} m\Phi(m) dm} = f_{\mathrm{SN\,II}} - m_{\mathrm{rem}} N_{\mathrm{SN\,II}}, \tag{7.23}$$

or $F_{\mathrm{SN\,II}} = 0.112$. Hence, the total gas mass returned to neighbour gas particles by a star particle with mass m_s is $M_{\mathrm{SN\,II}} = 0.112 m_s$. This is done using an SPH smoothing procedure.

Chemical evolution

Heavy elements synthesized in massive stars enrich the ISM. Tsujimoto et al. (1995) tabulated the masses of 27 isotopes of 14 heavy elements synthesized in the progenitors of SN II and SN Ia and determined the number ratio of SN Ia relative to SN II that best reproduces the observed abundance pattern among heavy elements in the solar neighbourhood as $N_{\rm SN\,Ia}/N_{\rm SN\,II} = 0.15$. If the progenitor of a SN Ia is a binary system of which one star is in the mass range $3-8\,{\rm M}_\odot$, this ratio is calculated by

$$\frac{N_{\rm SN\,Ia}}{N_{\rm SN\,II}} = A_{\rm SN\,Ia}\frac{\int_{m_{\rm SN\,Ia}}^{m_{\rm SN\,II}}\Phi(m)dm}{\int_{m_{\rm SN\,II}}^{m_u}\Phi(m)dm}, \tag{7.24}$$

where $A_{\rm SN\,Ia}$ is the fraction of binary systems for stars in the SN Ia mass regime, which actually will harbour a SN Ia. Using the above numbers, one calculates that $A_{\rm SN\,Ia} = 0.051$. From nucleosynthesis yields of SN II and SN Ia for various progenitor masses, Tsujimoto et al. (1995) calculated the total yield for 14 elements produced by a stellar population.

Knowing the ith heavy element mass $M_{i,{\rm SN\,II}}(m)$ produced in a star of main-sequence mass m, the total synthesized mass fraction produced by the SN II in a stellar population can be calculated as:

$$F_{i,{\rm SN\,II}} = \frac{\int_{m_{\rm SN\,II}}^{m_u} M_{i,{\rm SN\,II}}(m)\Phi(m)dm}{\int_{m_l}^{m_u} m\Phi(m)dm}, \tag{7.25}$$

or

$$F_{i,{\rm SN\,II}} = 0.175\int_{m_{\rm SN\,II}}^{m_u} M_{i,{\rm SN\,II}}(m)m^{-(1+x)}dm\,{\rm M}_\odot{}^{0.35}. \tag{7.26}$$

The total SN II synthesized mass of an element i in a star particle of mass m_s is thus given as $M_{i,{\rm SN\,II}} = F_{i,{\rm SN\,II}}m_s$.

The same applies for SN Ia synthesized heavy element masses. Knowing the ith heavy element mass $M_{i,{\rm SN\,Ia}}$ produced in SN Ia, we can calculate the total synthesized mass fraction produced by the SN Ia in a stellar population as:

$$F_{i,{\rm SN\,Ia}} = \frac{A_{\rm SN\,Ia}\int_{m_{\rm SN\,Ia}}^{m_{\rm SN\,II}} M_{i,{\rm SN\,Ia}}\Phi(m)dm}{\int_{m_l}^{m_u} m\Phi(m)dm}, \tag{7.27}$$

or

$$F_{i,{\rm SN\,Ia}} = 0.011M_{i,{\rm SN\,Ia}}\,{\rm M}_\odot{}^{-1}. \tag{7.28}$$

The total SN Ia synthesized mass of an element i in a star particle of mass m_s is thus given as $M_{i,{\rm SN\,Ia}} = F_{i,{\rm SN\,Ia}}m_s$.

The yields of SN II, SN Ia and even intermediate-mass stars could be taken into account (Kawata & Gibson, 2003).

We use the tabulated masses of heavy elements synthesized in the progenitors of SN II (Table 2 in Tsujimoto et al. (1995)) to calculate the mass fraction of 6 elements (O, Ne, Si, Mg, Ca, Fe) produced by a whole stellar population. Cubic splines were fitted to the tabulated data points, assuming that the heavy element production of a $8-10\,{\rm M}_\odot$ SN II explosion is negligible. Then we integrated over the Salpeter IMF (equation (7.26)). Note that these mass fractions are quite dependent on the chosen IMF and mass range. Taking $m_l = 0.4\,{\rm M}_\odot$, as in Kawata (1999), results in a much smaller dwarf star fraction, so that relatively more stars will explode as SN II and the nucleosynthesis production increases by a factor of 1.75. The case of the upper mass limit is somewhat more complicated, because the SN II

Table 7.1: Nucleosynthesis products of SN II. See text for details.

Element	$F_{i,\mathrm{SN\,II}}$					
^{16}O	1.14×10^{-2}	2.00×10^{-2}	9.16×10^{-3}	1.32×10^{-2}	1.12×10^{-1}	1.21×10^{-4}
^{20}Ne	1.25×10^{-3}	2.19×10^{-3}	1.10×10^{-3}	1.40×10^{-3}	1.05×10^{-2}	1.60×10^{-5}
^{24}Mg	7.56×10^{-4}	1.33×10^{-3}	6.41×10^{-4}	8.53×10^{-4}	6.81×10^{-3}	9.00×10^{-6}
^{28}Si	6.39×10^{-4}	1.12×10^{-3}	5.48×10^{-4}	7.08×10^{-4}	5.45×10^{-3}	8.76×10^{-6}
^{40}Ca	3.56×10^{-5}	6.25×10^{-5}	3.09×10^{-5}	3.82×10^{-5}	3.05×10^{-4}	4.81×10^{-7}
^{56}Fe	4.22×10^{-4}	7.40×10^{-4}	4.20×10^{-4}	4.23×10^{-4}	2.09×10^{-3}	9.12×10^{-6}
Z	1.45×10^{-2}	2.54×10^{-2}	1.19×10^{-2}	1.66×10^{-2}	1.37×10^{-1}	1.65×10^{-4}

yields of the different heavy elements depend on the progenitor star mass. Thus, varying the IMF upper mass limit does not only change the dwarf/giant star ratio, but also the element production ratios. On the one hand, changing m_u from $50\,\mathrm{M}_\odot$ to $70\,\mathrm{M}_\odot$ will increase the O production by a factor of 1.44, while the Fe production increases by a factor of only 1.01. Finally, changing the slope of the IMF also affects the heavy element production. If the slope is smaller than $x = 1.35$, there will be more massive stars in the population (a top-heavy IMF), and the nucleosynthesis production is enhanced by a factor of about 10 for $x = 0.35$. With a steeper slope, the IMF contains many dwarf stars, thus very few SN II occur and the nucleosynthesis production is suppressed by a factor of about 100 for than $x = 2.35$. In Table 7.1, we visualize these results; the second column shows the nucleosynthesis production in case of a Salpeter IMF with $m_l = 0.1\,\mathrm{M}_\odot$, $m_u = 60\,\mathrm{M}_\odot$, in column 3 we set $m_l = 0.4\,\mathrm{M}_\odot$ (compare to Table 1 in Kawata (1999)), in columns 4 and 5 we adopted $m_u = 50\,\mathrm{M}_\odot$ and $m_u = 70\,\mathrm{M}_\odot$ respectively. Finally, in columns 6 and 7, we adjusted the slope of the IMF to $x = 0.35$ (top-heavy IMF) and $x = 2.35$ (bottom-heavy IMF) respectively.

Energy feedback

Massive stars do not only return mass to the surrounding ISM, they also inject a significant amount of energy into the gas. Before they explode as supernovae, massive stars can inject a comparable amount of energy through their stellar winds. This energy input disrupts the molecular clouds in which the stars are formed, thereby putting a halt to further star formation. Energy feedback is one of the most difficult and most critical processes to model in galaxy formation simulations. Unfortunately, there is no clear understanding of how this should be implemented.

Each supernova explosion is assumed to yield an energy $E_\mathrm{SN} = \epsilon_\mathrm{SN} 10^{51}\,\mathrm{ergs}$, where ϵ_SN is a free parameter varying between 0.1 and 1. The total energy E_tot returned by a star particle of mass m_s amounts to

$$E_\mathrm{tot} = \frac{m_s \int_{m_{\mathrm{SN\,II}}}^{m_u} E_\mathrm{SN} \Phi(m) dm}{\int_{m_l}^{m_u} m \Phi(m) dm}. \tag{7.29}$$

The energy released by a supernova explosion has two effects on the surrounding ISM. Firstly, the explosion pushes the gas away, creating a supernova remnant. Secondly, the gas inside the cavity is heated. Typical sizes for supernova remnants are in the order of a few 10 parsecs. The spatial resolution of the simulations is about the same for dwarf galaxies, and up to a few 100 parsecs for giant galaxies. Thus the detailed structure of supernova remnants is not resolved in the current simulations.

Some implementations of feedback consider returning the supernova energy as purely thermal energy E_th to the surrounding gas (Katz, 1992). However, since star formation usually takes place in dense regions, the cooling time of this gas is very short and the energy is quickly radiated away. Thacker &

Couchman (2000) investigate different variations on this feedback scheme, finding that the best results can be achieved when an adiabatic phase is included after heating has taken place. Such an adiabatic phase can be implemented in various ways. Cooling can be simply suppressed while the gas particle is heated (Mori et al., 1999; Gerritsen & Icke, 1997; Kay et al., 2002). The physical background is that supernovae remnants are hot, low-density cavities in the ISM, but on a sub-resolution scale. We will use this scheme to investigate the effect of an adiabatic cooling period in our simulations. Alternatively, since the smoothing procedure of SPH cannot represent a single low-density particle in a dense medium, the density of a heated gas particle can be artificially modified so that the cooling time becomes longer and the gas cools more slowly (Thacker & Couchman, 2000).

In order to increase the effect of energy feedback, one could assume that part of the energy is returned as kinetic feedback $E_{\rm kin}$ (Navarro & White, 1993; Kawata & Gibson, 2003). A fraction $f_v = E_{\rm kin}/E_{\rm SN}$ of the supernova energy is used to kick the surrounding gas radially away from the star particle. It is found that even for small values of f_v, the effect of kinetic feedback on the ISM is larger than the effect of thermal feedback ($E_{\rm th} = (1 - f_v)E_{\rm SN}$ in this case), which is quickly radiated away. On the other hand, given the resolution of the simulations, the claim that star particles could influence the velocity of neighbour gas particles is not physically grounded (Carraro et al., 1998). The effects of including kinetic feedback are considered in section 7.4.3.

SPH scheme for stellar feedback

The mass, heavy elements and energy feedback by the star particles is distributed over the neighbouring gas particles using the same SPH smoothing algorithm. Like the gas particles, each star particle is assigned a smoothing length h so that $N_{\rm SPH}$ neighbour gas particles are encompassed within a sphere of radius $2h$. At each timestep, the smoothing length is adjusted according to the prescriptions given in section 5.6.2, in order to account for temporal variations in the gas density. If a star particle i returns a mass $M_{{\rm ret},i}$ to the ISM, the increment of the mass of the jth neighbour gas particle is given by

$$\Delta M_{{\rm ret},j} = \frac{m_j}{\rho_{g,i}} M_{{\rm ret},i} W_{ij}, \tag{7.30}$$

where $\rho_{g,i}$ is the gas density around the star particle i, given by

$$\rho_{g,i} = \langle \rho_g(\boldsymbol{x}_i) \rangle = \sum_j m_j W_{ij}, \tag{7.31}$$

with W_{ij} the SPH smoothing kernel. Since feedback is a one-way process, the smoothing kernel does not need to be symmetrised. It is readily seen from these two equations, that total mass conservation is ensured. The return of heavy elements is implemented in the same way.

If we denote the total mass in metals in a gas particle i by $m_{Z,i}$, we can calculate the metallicity Z_i of the gas particle as

$$Z_i = \frac{m_{Z,i}}{m_i}. \tag{7.32}$$

This metallicity is subsequently used in the metallicity-dependent cooling tables to calculate the radiative cooling.

The thermal energy $E_{{\rm ret},i}$ returned by the star particle could also distributed using the SPH smoothing technique

$$\Delta E_{{\rm ret},j} = \frac{m_j}{\rho_{g,i}} E_{{\rm ret},i} W_{ij}, \tag{7.33}$$

however, we need the specific energy change $\Delta\epsilon_{\mathrm{ret},j} = \Delta E_{\mathrm{ret},j}/m_j$. Hence, the specific energy feedback is calculated as

$$\Delta\epsilon_{\mathrm{ret},j} = \frac{1}{\rho_{g,i}} E_{\mathrm{ret},i} W_{ij}. \tag{7.34}$$

If kinetic energy feedback is included, a fraction f_v of the total energy feedback is used to kick the neighbour gas particles radially away from the star particle. The amplitude of the velocity perturbation Δv is calculated from

$$\Delta E_{\mathrm{kin}_j} = \frac{m_j}{\rho_{g,i}} f_v E_{\mathrm{ret},i} W_{ij} = \frac{1}{2} m_j \Delta v_j^2, \tag{7.35}$$

or

$$\Delta v_j = \sqrt{\frac{2 f_v E_{\mathrm{ret}_i} W_{ij}}{\rho_{g,i}}}. \tag{7.36}$$

The thermal feedback is correspondingly reduced to $E_{\mathrm{th}_i} = (1 - f_v) E_{\mathrm{ret}_i}$. If f_v is equal to zero, this scheme corresponds to the purely thermal feedback scheme.

Timescale of feedback

The mass, heavy elements and energy feedback can be applied using the instantaneous recycling approximation (IRA). Feedback is then performed during the same timestep as the stars are born (Katz, 1992; Mihos & Hernquist, 1994; Katz et al., 1996). The advantage of this approximation is in simplicity. At the birth of a star particle, all feedback values are calculated and applied to the neighbouring gas particles. Thereafter, there is no interaction between star and gas particles, save gravitational forces. The IRA is especially useful if the simulation timestep is long enough (Mosconi et al., 2001), of the order of the lifetime of the least massive SN II progenitor. This lifetime is $\tau(m_{\mathrm{SN\,II}} = 8\,\mathrm{M}_\odot) = 4.3 \times 10^7$ yr.

If the timestep of the simulation is significantly smaller than 4.3×10^7 yr, the lifetime of the SN II progenitors should be taken into account. In order to do so, one can calculate the feedback rates simply by dividing the total feedback by the time during which supernova explosions occur $\tau_{\mathrm{fb}} = \tau(m_{\mathrm{SN}}) - \tau(m_u)$ (Mori et al., 1999; Kobayashi, 2004). Then, at each timestep Δt a fraction of the total feedback proportional to $\Delta t/\tau_{\mathrm{fb}}$ is applied to the neighbour gas particles.

A still more realistic way to implement feedback is to take into account the amount of SN that occur during a timestep Δt (Navarro & White, 1993; Raiteri et al., 1996). Especially if one wants to model the effects of SN Ia, whose lifetimes are of the order of $10^8 - 10^9$ yr, much longer than the integration timestep. Since the stellar lifetime $\tau(m)$ (equation (7.20)), is a monotonically rising function of stellar mass m, we can invert the function in order to know the mass the stars that turn of the main sequence at a certain lifetime τ of the stellar population. Then, the feedback FB (where FB represents mass, heavy element or energy feedback) given by a star particle of mass m_s during a timestep Δt is given by

$$\mathrm{FB} = \frac{m_s \int_{m(\tau)}^{m(\tau+\Delta t)} \mathrm{FB}(m)\Phi(m)dm}{\int_{m_l}^{m_u} m\Phi(m)dm}, \tag{7.37}$$

where $\mathrm{FB}(m)$ represents the feedback returned by a star of mass m.

7.3 The galaxy model

7.3.1 The dark matter halo

From cosmological N-body simulations, it seems clear that the dark matter distribution should have a central density cusp, although from the observational point this is not yet clear (Moore et al, 1998). A simple model that approximates the central cusps of elliptical galaxies quite well, is the *singular isothermal sphere*, which has a radial density profile given by (Binney & Tremaine, 1987)

$$\rho(r) = \frac{\sigma^2}{2\pi G r^2}, \tag{7.38}$$

with σ the one-dimensional velocity dispersion. Unfortunately, the singular isothermal sphere has infinite density at $r = 0$. Moreover the total mass of the model is linearly divergent, so that the singular isothermal sphere cannot represent a real astrophysical distribution. The *lowered isothermal models* are a family of galaxy models resembling the singular isothermal sphere, but which have a finite central density and a finite total mass. The *King model* is one of several possible modified isothermal distribution functions. Some King models were found to fit quite well the surface brightness profiles of globular clusters and elliptical galaxies. Therefore we assume that the dark matter (DM) halo is distributed according to a King model (see also Mori et al. (1999)).

The King model

This model was actually introduced by Michie (1963), but it became well-known after King (1966) used it to fit the surface density profiles of globular clusters. The distribution function (DF) is given by:

$$f_{\rm K} = \begin{cases} \rho_1 (2\pi\sigma^2)^{-\frac{3}{2}} \left(e^{\mathcal{E}/\sigma^2} - 1 \right) & \mathcal{E} > 0; \\ 0 & \mathcal{E} \leqslant 0, \end{cases} \tag{7.39}$$

where $\mathcal{E} = \Psi - \frac{1}{2}v^2$ is the relative energy which is a function of the relative potential Ψ and velocity v, ρ_1 is a scale parameter that will determine the total mass of the model, and σ is a parameter that determines the central concentration of the model.

To obtain the density at any radius, we must integrate the DF over all velocities. Since the $f_{\rm K} = 0$ for $\mathcal{E} \leqslant 0$, there is a maximum allowed velocity $v_{\rm max} = \sqrt{2\Psi}$ associated with each value of the effective potential Ψ. The density profile in function of the relative potential Ψ becomes

$$\begin{aligned} \rho_{\rm K}(\Psi) &= \frac{4\pi\rho_1}{(2\pi\sigma^2)^{\frac{3}{2}}} \int_0^{\sqrt{2\Psi}} \left[\exp\left(\frac{\Psi - \frac{1}{2}v^2}{\sigma^2} \right) - 1 \right] v^2 dv \\ &= \frac{4}{\sqrt{\pi}} \rho_1 e^{\frac{P si}{\sigma^2}} \int_0^{\sqrt{2\Psi}} \left[\exp\left(-\frac{v^2}{2\sigma^2} \right) - 1 \right] \frac{v^2}{2\sigma^2} d\frac{v}{\sqrt{2}\sigma}. \end{aligned} \tag{7.40}$$

We define the two scaled quantities $\tilde{v} = \frac{v}{\sqrt{2}\sigma}$ and $\tilde{\Psi} = \frac{\Psi}{\sigma^2}$, and substitute them in equation (7.40) so that we become

$$\begin{aligned} \rho_{\rm K}(\tilde{\Psi}) &= \frac{4}{\sqrt{\pi}} \rho_1 e^{\tilde{\Psi}} \int_0^{\sqrt{\tilde{\Psi}}} \left(e^{-\tilde{v}^2} - 1 \right) \tilde{v}^2 d\tilde{v} \\ &= \frac{4}{\sqrt{\pi}} \rho_1 e^{\tilde{\Psi}} \left(\int_0^{\sqrt{\tilde{\Psi}}} e^{-\tilde{v}^2} \tilde{v}^2 d\tilde{v} - \int_0^{\sqrt{\tilde{\Psi}}} \tilde{v}^2 d\tilde{v} \right). \end{aligned} \tag{7.41}$$

The first integral can be integrated by parts to yield

$$\int_0^{\sqrt{\tilde{\Psi}}} e^{-\tilde{v}^2}\tilde{v}^2 d\tilde{v} = -\frac{1}{2}\tilde{v}e^{-\tilde{v}^2}\Big|_0^{\sqrt{\tilde{\Psi}}} + \frac{1}{2}\int_0^{\sqrt{\tilde{\Psi}}} e^{-\tilde{v}^2} d\tilde{v}, \tag{7.42}$$

so that we finally arrive at

$$\rho_{\rm K}(\tilde{\Psi}) = \rho_1 \left[e^{\tilde{\Psi}} {\rm erf}(\sqrt{\tilde{\Psi}}) - \sqrt{\frac{4}{\pi}\tilde{\Psi}} \left(1 + \frac{2}{3}\tilde{\Psi}\right)\right]. \tag{7.43}$$

Here, we made use of the definition of the *error function*

$${\rm erf}(x) = \frac{2}{\sqrt{\pi}} \int_0^x e^{-x^2} dx. \tag{7.44}$$

We can write Poisson's equation for the relative potential Ψ as

$$\frac{d}{dr}\left(r^2 \frac{d\Psi}{dr}\right) = -4\pi G r^2 \rho(\Psi). \tag{7.45}$$

Introducing a scaled density $\tilde{\rho} = \rho_{\rm K}/\rho_0$ and a scaled radius $\tilde{r} = r/r_0$, where $\rho_0 = \rho(\tilde{\Psi}_0)$ is the central density, and

$$r_0 = \sqrt{\frac{9\sigma^2}{4\pi G \rho_0}} \tag{7.46}$$

is the *King radius*. We can thus rewrite the Poisson equation as

$$\frac{d}{d\tilde{r}}\left(\tilde{r}^2 \frac{d\tilde{\Psi}}{d\tilde{r}}\right) = 9\tilde{r}^2 \tilde{\rho}(\tilde{\Psi}), \tag{7.47}$$

or

$$\frac{d^2\tilde{\Psi}}{d\tilde{r}^2} + \frac{2}{\tilde{r}}\frac{d\tilde{\Psi}}{d\tilde{r}} + 9\tilde{\rho}(\tilde{\Psi}) = 0. \tag{7.48}$$

This is an ordinary differential equation for $\tilde{\Psi}(\tilde{r})$, which may be integrated numerically once we have chosen suitable boundary conditions. At $\tilde{r} = 0$, we have $\frac{d\tilde{\Psi}}{d\tilde{r}} = 0$, since there is no force acting at the centre $\left(F(r) = \frac{d\Psi}{dr}\right)$. In Figure 7.2, we plot the density profiles for King models with $\tilde{\Psi}_0 = 3, 6, 9$ and 12.

The value $\tilde{\Psi}_0$ from which we start the integration determines the extend of the model. When we integrate equation (7.48) outward, $\frac{d\tilde{\Psi}}{d\tilde{r}}$ decreases, because at $\tilde{r} = 0$, $\left.\frac{d^2\tilde{\Psi}}{d\tilde{r}^2}\right|_{\tilde{r}=0} = -3$, where we made use of the de l'Hôpital rule. Thus, $\tilde{\Psi}$ decreases from $\tilde{\Psi}_0$ towards zero, and the density also decreases. Eventually, at some scaled radius $\tilde{r}_t$, the density vanishes. We call $r_t = \tilde{r}_t\, r_0$ the *tidal radius* of the model. Thus, the larger we choose $\tilde{\Psi}_0$, the larger will be $\tilde{r}_t$.

We now define the *concentration* c of the model as

$$c = \log_{10}(\tilde{r}_t) = \log_{10}\left(\frac{r_t}{r_0}\right). \tag{7.49}$$

Models with c between 0.75 and 1.75 fit the surface brightness profiles of globular clusters very well, and models having $c \geqslant 2.2$ fit the observed brightness profiles of some elliptical galaxies moderately

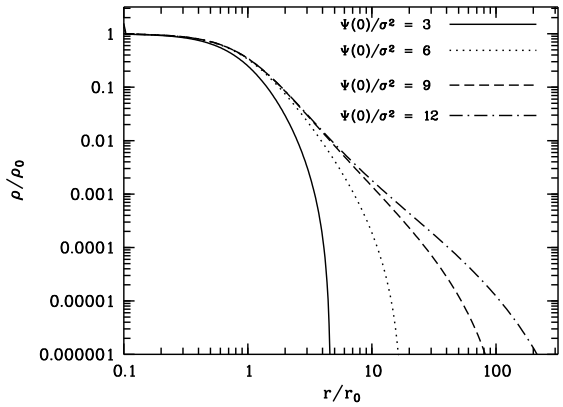

Figure 7.2: King model density profiles with $\tilde{\Psi}_0 = 3, 6, 9$ and 12

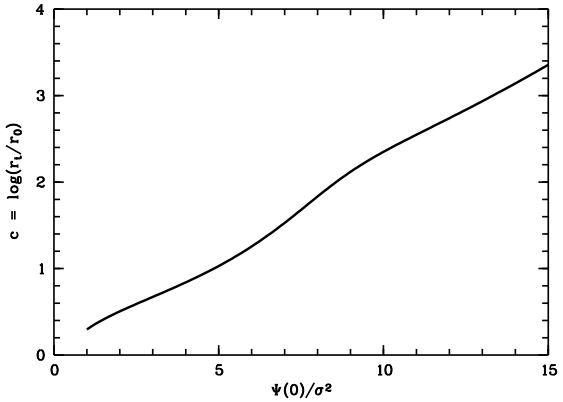

Figure 7.3: The relationship between the concentration c and the central scaled potential $\tilde{\Psi}_0$.

well (Binney & Tremaine, 1987). Because $\tilde{r}_t$ is uniquely determined by choosing $\tilde{\Psi}_0$, the King models form a simple sequence that may be parametrized in terms of either c or $\tilde{\Psi}_0$. Figure 7.3 shows the relationship between c and $\tilde{\Psi}_0$. In the limit $c \to \infty$, $\tilde{\Psi}_0 \to \infty$, the sequence of King models approaches that of the singular isothermal sphere.

The total mass of the King model is found by integrating the density over all directions, or since the King model is spherically symmetric, from $r = 0$ to $r = r_t$, the radius where the density becomes 0;

$$\begin{aligned} M_{\rm tot} &= 4\pi \int_0^{r_t} \rho(\Psi(r)) r^2 dr \\ &= 4\pi \rho_0 r_0^3 \int_0^{\tilde{r}_t} \tilde{\rho}(\tilde{\Psi}(\tilde{r})) \tilde{r}^2 d\tilde{r} \\ &= \frac{9}{G}\sigma^2 r_0 \int_0^{\tilde{r}_t} \tilde{\rho}(\tilde{\Psi}(\tilde{r})) \tilde{r}^2 d\tilde{r}, \end{aligned} \tag{7.50}$$

where we used equation (7.46). Thus, given the 3 parameters $M_{\rm tot}$, c (or $\tilde{\Psi}_0$) and r_0 (or σ), the King

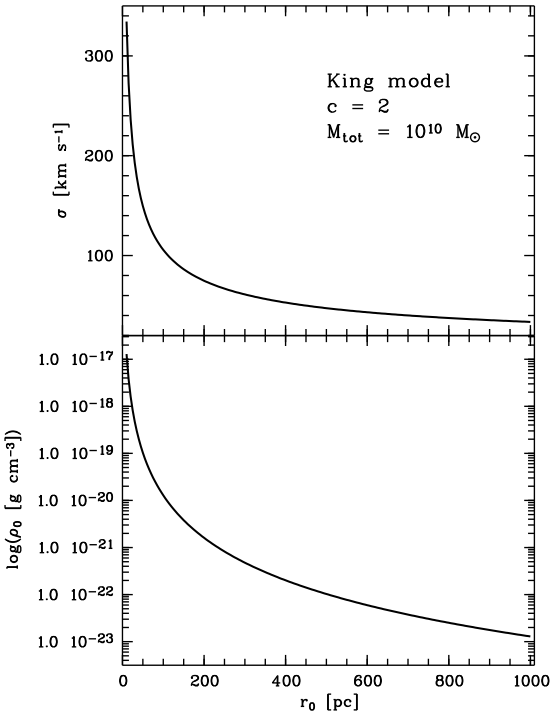

Figure 7.4: The relation between $r_0 - \rho_0$ (lover panel) and $r_0 - \sigma$ (upper panel), for a King model with concentration $c = 2$, corresponding to $\tilde{\Psi}_0. \approx 8.56$, and with a total mass of $10^{10}\,\mathrm{M}_\odot$.

parameter	value	source
c	2	given
$\tilde{\Psi}_0$	8.56	$c - \tilde{\Psi}_0$ relation (Fig. 7.3)
r_t	$8.45\,\mathrm{kpc}$	given
r_0	$0.0845\,\mathrm{kpc}$	$c = \log(r_t/r_0)$
$\tilde{M}$	4.315	$\tilde{M} = \int_0^{\tilde{r}_t} \tilde{\rho}(\tilde{r})\tilde{r}^2 d\tilde{r}$
M_{tot}	$9 \times 10^9\,\mathrm{M}_\odot$	given
ρ_0	$1.87 \times 10^{-20}\,\mathrm{g\,cm^{-3}}$	$M_{\mathrm{tot}} = 4\pi\rho_o r_0^3 \tilde{M}$
ρ_1	3.60×10^{-24}	$\rho_1 = \rho_0/[\exp(\tilde{\Psi}_0)\mathrm{erf}(\sqrt{\tilde{\Psi}_0}) - \sqrt{4\tilde{\Psi}_0/\pi}(1 + 2\tilde{\Psi}_0/3)]$
σ	$108.35\,\mathrm{km\,s^{-1}}$	$\sigma = \sqrt{4\pi G\rho_0 r_0^2/9}$

Table 7.2: Properties of the King model with $c = 2$ and $r_t = 8.45$.

model is totally defined. If we keep the total mass and the concentration c constant, it is seen from equation (7.50) that smaller King radii r_0 correspond to larger central densities ρ_0 or higher velocity-dispersion parameters σ. Figure 7.4 shows the relations between $r_0 - \rho_0$, and $r_0 - \sigma$ for a King model with concentration $c = 2$, corresponding to $\tilde{\Psi}_0. \approx 8.56$, and with a total mass of $10^{10}\,\mathrm{M}_\odot$. In table 7.2 we list the values of the parameters of the King model with mass $9 \times 10^9\,\mathrm{M}_\odot$, concentration $c = 2$ and tidal radius $r_t = 8.45$.

The parameter σ that occurs in the relations for King models must not be confused with the actual

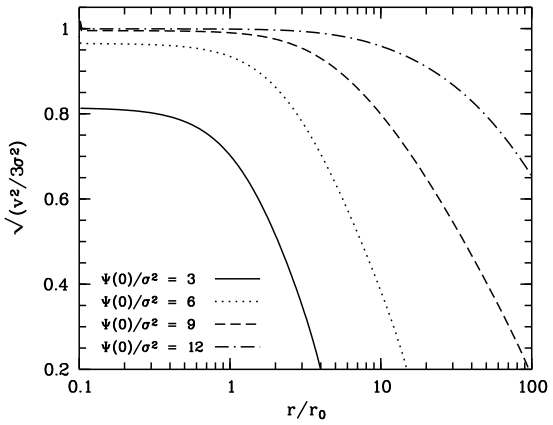

Figure 7.5: The rms velocity at a given spatial radius r for the King models shown in Figure 7.2. Velocities are given in units of $\sqrt{3}\sigma$.

velocity dispersion $(\bar{v^2})^{1/2}$ of the particles in the system. We can calculate the velocity dispersion using the DF (Binney & Tremaine, 1987)

$$\bar{v^2} = J_2/J_0, \tag{7.51}$$

where

$$J_n = \int_0^{\sqrt{2\Psi}} \left[\exp\left(\frac{\Psi - \frac{1}{2}v^2}{\sigma^2}\right) - 1\right] v^{n+2} dv, \tag{7.52}$$

with $\Psi(r)$ as a function of r. Let's calculate J_0 and J_2:

$$J_0 = \sigma^3 \left[\sqrt{\frac{\pi}{2}} e^{\tilde{\Psi}} \mathrm{erf}\left(\sqrt{\tilde{\Psi}}\right) - \sqrt{2\tilde{\Psi}}\left(1 + \frac{2}{3}\tilde{\Psi}\right)\right], \tag{7.53}$$

which is, in effect, a scaled version of the density profile,

$$J_2 = 3\sigma^5 \left\{\sqrt{\frac{\pi}{2}} e^{\tilde{\Psi}} \mathrm{erf}\left(\sqrt{\tilde{\Psi}}\right) - \sqrt{2\tilde{\Psi}}\left[1 + \frac{2}{3}\tilde{\Psi}\left(1 + \frac{2}{5}\tilde{\Psi}\right)\right]\right\}. \tag{7.54}$$

In Figure 7.5, the velocity dispersion at spatial radius r is given for different King models.

7.3.2 The interstellar medium

The initial values for the mass of DM and baryonic matter (BM, initially only gas) are in fixed proportion $M_D = 0.9M_t$ and $M_B = 0.1M_t$ to the total mass M_t. The BM inside the DM halo follows the evolution of the latter, but are only inserted once the DM has reached virial equilibrium. Following Carraro et al. (2001), the gas particles are distributed homogeneously inside the DM halo, with zero velocity field, thus mimicking the infall of primordial gas into the potential well of DM. The primordial gas has an initial temperature of 10^4 K and an initial metallicity of $Z = 10^{-4}$ ($Z_\odot = 0.02$).

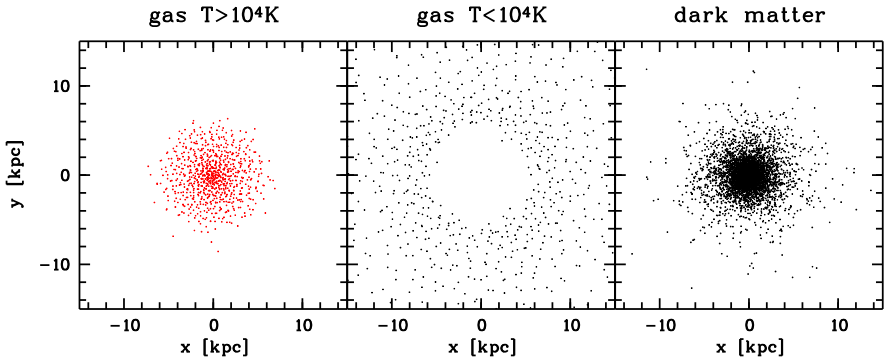

Figure 7.6: Distribution in the $x-y$ plane of the hot ($T_g > 10^4\,\mathrm{K}$) and cool ($T_g < 10^4\,\mathrm{K}$) gas and the dark matter, at a simulated time $t = 2\,\mathrm{Gyr}$. For clarity, only those particles with $|z| < 2\,\mathrm{kpc}$ are plotted. Radiative cooling is switched off, so that collapsing gas heats and expanding gas cools adiabatically. The high temperatures in the central regions of the galaxy prevent star formation.

7.3.3 The initial conditions

All the simulations presented in this chapter start from the same initial conditions. We simulate a small dwarf galaxy with total mass $M_t = 10^9\,Msol$. The DM is distributed in a King distribution with concentration parameter $c = 2$ and a tidal radius of $16\,\mathrm{kpc}$, resembling model B1 of Carraro et al. (2001).

The numerical simulations make use of the same number of particles (10^4) for both DM and BM, the mass resolution of the DM is thus $9 \times 10^4\,Msol$, while that of the gas particles is $10^4\,Msol$ initially. As star formation takes place, star particles can be formed with a minimal mass of $\sim 10^3\,Msol$. The gravitational Plummer softening adopted for DM, gas and star particles alike, is $\epsilon = 30\,pc$, roughly corresponding to the size of a molecular cloud or star cluster.

7.4 Results

7.4.1 Radiative cooling

To investigate the role of radiative cooling, we first ran a simulation with the cooling switched off. As is clear from Figures 7.6 and 7.7, gas falling towards the centre is adiabatically heated to temperatures around $10^5\,\mathrm{K}$, while the mean temperature inside the initial radius is $1.35 \times 10^4\,\mathrm{K}$. We can compare this to the *virial temperature* $T_{\rm vir}$ of the system, which is the mean temperature for which the gas cloud would satisfy the virial theorem (Binney & Tremaine, 1987)

$$T_{\rm vir} = 6.8 \times 10^5 \mu \left(\frac{M_{\rm tot}}{10^{11}\,\mathrm{M}_\odot}\right)\left(\frac{10\,\mathrm{kpc}}{r_h}\right) = 2.07 \times 10^4\,\mathrm{K}, \tag{7.55}$$

with $\mu = 0.61$ the mean molecular weight, $M_{\rm tot} = 10^9\,\mathrm{M}_\odot$ the total mass of the system and $r_h = 2\,\mathrm{kpc}$ the radius that contains half of the system's mass. The gas is thus heated to approximately the virial temperature.

At these temperatures, no star formation can take place. Part of the gas is pushed out by the thermal

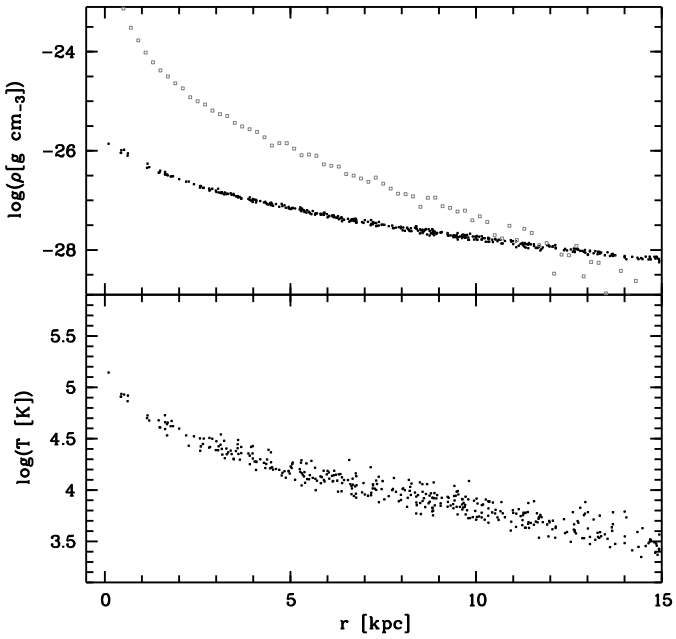

Figure 7.7: Radial density and temperature profiles of the gas (black dots) after a simulated time $t = 2\,\mathrm{Gyr}$, when radiative cooling is switched off. The high temperature in the central kpc prohibits the gas to collapse, and the threshold density for star formation is nowhere reached. Also the dark matter radial density is plotted (grey dots).

pressure of the hot central gas and cools as it expands. Due to the low densities, no stars will form in the cool outskirts either. Hence radiative cooling is a necessary ingredient in the simulations.

7.4.2 Star formation

When the gas is allowed to cool, the thermal energy gained by collapsing will be radiated away. The thermal pressure in the centre of the galaxy will be lower so that the gas continues to collapse. The gas will cool more efficiently as higher densities are reached. In these collapsing, cold and dense regions, star formation is likely to take place.

Star formation criteria

Using the local total density instead of the local gas density is crucial in these simulations. We ran also a set of simulations using the gas density to calculate the dynamical time. It was found that the sound crossing time remained larger than the dynamical time everywhere, except for a centralized region in the very nucleus, where the gas density becomes very high. This high density renders the feedback from supernovae very inefficient, since the thermal energy is quickly radiated away. Since gas keeps falling in, the star formation eventually consumes almost the whole gas reservoir and a very dense star cluster is formed.

The star formation rate

As described in section 7.2.2, each gas particle that satisfies the star formation criteria will give birth to a star particle if a randomly drawn number $p \in [0, 1]$ is smaller than the star formation probability p_*

$$p_* = 1 - exp\left(-c_* \frac{\Delta t}{t_{\rm d}}\right). \tag{7.56}$$

We also ran simulations where each gas particle eligible for star formation gives birth to a star particle with mass

$$m_* = 3\pi h(i)^3 \rho \left[1 - exp\left(-c_* \frac{\Delta t}{t_{\rm d}}\right)\right], \tag{7.57}$$

and found very little difference in the outcome of the simulations.

The star formation efficiency c_*

To investigate the effect of the star formation efficiency parameter c_*, we ran simulations with $c_* = 0.1, 0.25, 0.5, 0.75$ and 1.0 (default) including only mass feedback (no energy or metal feedback). In the left panels of Figure 7.8, the SFR during the first 2 Gyr is shown for the various simulations. On the right panels we show the time evolution of the gas mass within and outside of the initial radius (full lines) and of the mass in stars (dotted lines). Varying the star formation efficiency does not change the amount of gas converted into stars. After 2 Gyr, 68 per cent of the initial gas mass is converted into stars, while 7 per cent still remains inside the initial radius. Note that part of the gas is pushed out of the initial radius by the thermal pressure. About 30 per cent of the initial gas mass flows outwards, but some 5 per cent later falls back again, as the inner gas gets more concentrated to the centre.

Qualitatively, the SFR doesn't change much if we vary c_*. After a collapse phase of about 10^8 yr, the gas becomes dense enough to start forming stars. The starburst peaks after 5×10^8 yr and afterward follows an exponential decline. If we look closer to the SFRs, it can be noted that initially, the SFR is larger for larger c_*. On the other hand the maximum SFR is larger for smaller c_*. Moreover, for smaller c_* the SFR shows two peaks after 4.5×10^8 and 5.5×10^8 yr. For smaller c_*, the star formation proceeds in more dense regions. Initially the SFR is lower and the gas is allowed to fall deeper into the gravitational potential well. If we look at the radial stellar density profiles (Figure 7.22), it is readily seen that smaller c_* give rise to more concentrated density profiles.

7.4.3 Energy feedback

If no feedback is included, the star formation process is clearly too efficient, converting up to 70 per cent of the gas into stars. Moreover, the final stellar density profiles are very centrally concentrated. Gas particles that gave birth to a star particle quickly become eligible for star formation again. However, in a realistic molecular cloud, the UV radiation and supernova feedback from the newborn stars disrupt the parent cloud and star formation is halted for some time. Hence we need to include the effects of heating by stellar winds and supernova explosions that balance the star formation.

As said before (Section 7.2.3), energy feedback is one of the most difficult and most critical processes to model in galaxy formation simulations and several different implementations exist. First we will return the energy of the stellar winds and supernova explosions as pure thermal energy. Second we investigate the effect of including kinetic feedback. Then we include an adiabatic cooling phase after the feedback event.

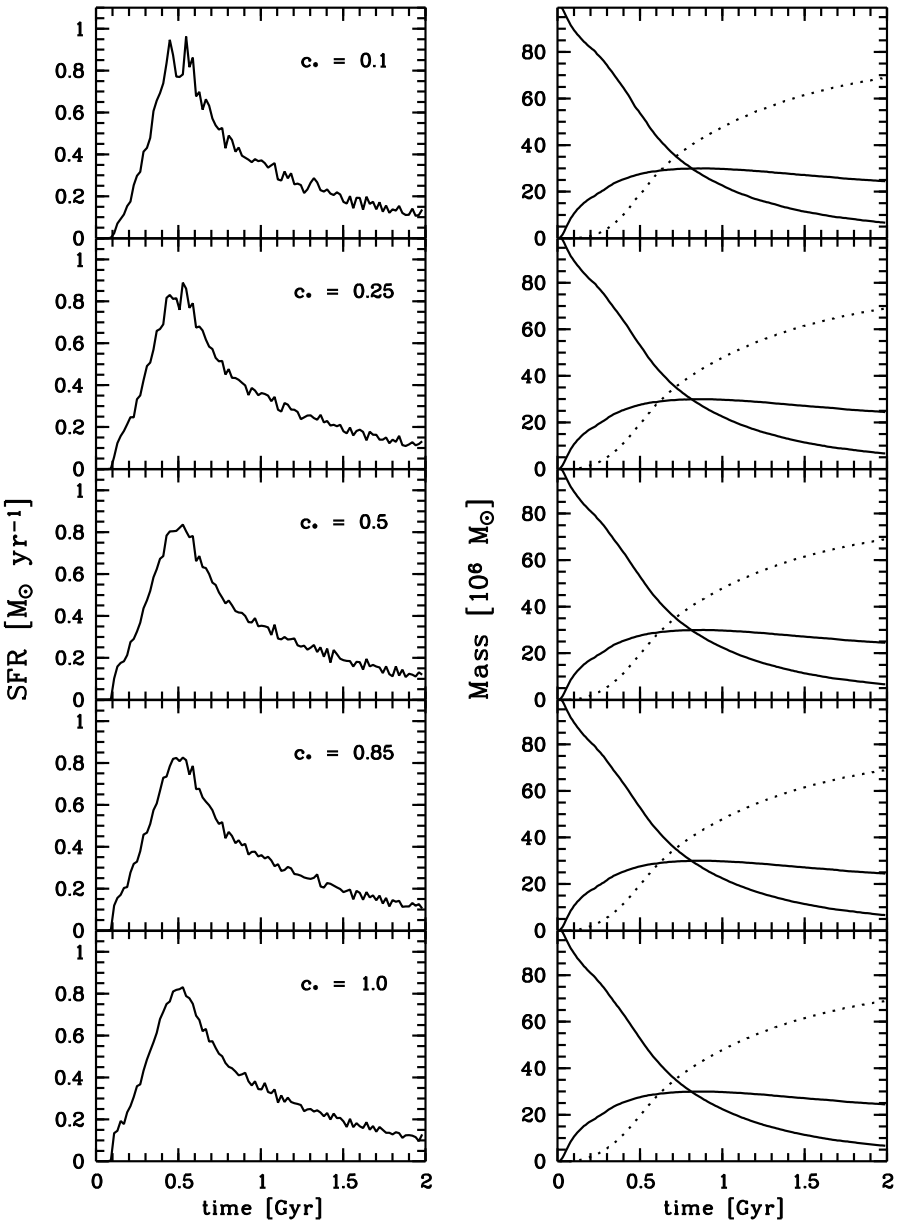

Figure 7.8: *Left panels:* The evolution of the SFR of the simulated dwarf in function of the star formation efficiency parameter c_*. *Right panels:* The time evolution of the gas (solid lines) and stellar (dotted lines) content.

Energy feedback: varying $\epsilon_{\rm SN}$

The overall energy feedback efficiency is governed by the parameter $\epsilon_{\rm SN}$. The contribution to the thermal energy budget by a massive star ($M > 8\,{\rm M}_\odot$), is $E_{\rm SW} = \epsilon_{\rm SN} 10^{50}$ ergs during its stellar wind phase, and $E_{\rm SN} = \epsilon_{\rm SN} 10^{51}$ ergs during the supernova event. Most studies adopt $\epsilon_{\rm SN} = 0.1$, following detailed one-dimensional simulations of supernova remnant evolution (Thornton et al., 1998). Here we study the effect of varying the feedback efficiency. The adopted values are $\epsilon_{\rm SN} = 0$, or no feedback, $\epsilon_{\rm SN} = 0.05$, or weak feedback, $\epsilon_{\rm SN} = 0.1$, the canonical case, $\epsilon_{\rm SN} = 0.5$, or strong feedback and $\epsilon_{\rm SN} = 1.$, or very strong feedback.

In case of weak feedback, the thermal energy returned to the gas particles is quickly radiated away, and has no influence on the SFR, or on the total gas and star content of the galaxy, as is clear from Figure 7.9. In Figure 7.10, the stellar, cold and hot gas distribution projected in the $x - y$ is shown after 5×10^8 yr and after $2\,$Gyr. Although the central gas regions are ionized as a result of the stellar feedback, the cold gas is not disturbed.

This picture changes, when 10 per cent feedback efficiency is assumed. The SFR still shows a peak around $5 \times 10^8\,$yr, but the strength of this peak is much reduced and after $7 \times 10^7\,$yr the star formation proceeds in a more discontinuous way, with short bursts and periods where star formation is virtually halted. Finally, after about $1.5\,$Gyr, the SFR settles to $\sim 0.05\,{\rm M}_\odot\,{\rm yr}^{-1}$. The total amount of gas converted into stars is smaller, about $4 \times 10^7\,{\rm M}_\odot$ after $2\,$Gyr. There is somewhat more gas present inside the galaxy's radius, than in the case of no feedback, but most of the difference between the stellar content in both cases is accounted for by gas that is blown outside the galaxy radius by a stellar wind following the star formation peak (Figure 7.9). In Figures 7.10 it can be seen that the stellar feedback has blown a superbubble in the gas. Star formation does not proceed in an exact spherically symmetric way, and stars are formed not exactly in the centre of the gas distribution. The denser gas closer to the centre is able to cool rapidly, while a hot superbubble is created in the low-density outer regions. This bubble eventually develops into a chimney, when it breaks out of the galaxy boundary. Hot gas subsequently flows out in a fountain, while on the other side cold gas continues to flow into the central region of the galaxy, fueling further star formation. Finally we are left with a more extended stellar distribution.

When strong or very strong feedback is implemented, the injected energy is not so quickly radiated away and after each star formation event, star formation is halted for several $10^7\,$yr, essentially as long as supernovae continue to explode. Consequently, very little gas is converted into stars, almost all of it is blown away in a strong galactic wind. This can be nicely seen in Figure 7.10. After $2\,$Gyr (Figure 7.11), the very strong feedback has blown out all the gas. In the case of strong feedback, some gas falls back to the centre of the galaxy, but small star formation events will eventually blow out this gas also. The strong and very strong feedback simulations are not very realistic, as the fraction of gas converted into stars is so small that we can hardly speak of galaxy formation.

In Figure 7.23, we show the radial distributions of stars, gas and dark matter at the end of the simulations (after $2\,$Gyr). Weak feedback does not affect the density profiles. The stellar density profile becomes much less centrally concentrated for stronger feedback, becoming approximately exponential. The dark matter distribution is also affected by the stellar feedback. The dynamical response to the loss of gas from the central region, in form of a galactic wind, makes the dark matter distribution less cusped. In case of very strong feedback, the stellar distribution is even more diffuse, but very few stars have formed.

Energy feedback: varying f_v

Kinetic energy feedback is included in some galaxy formation simulations (Navarro & White, 1993; Kawata & Gibson, 2003), to increase the effect of supernovae on the surrounding gas. In order to

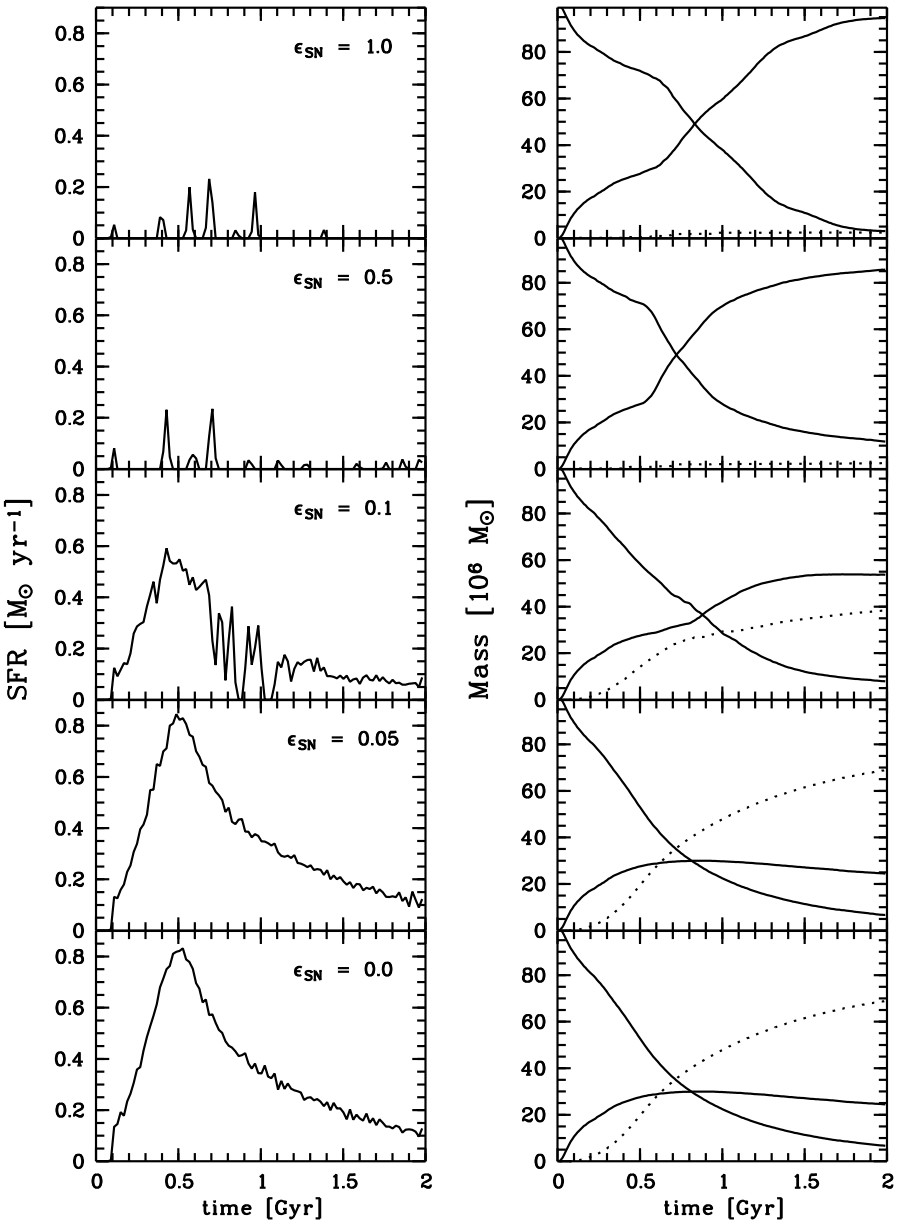

Figure 7.9: *Left panels:* The evolution of the SFR of the simulated dwarf in function of the feedback efficiency $\epsilon_{\rm SN}$. *Right panels:* The time evolution of the gas (solid lines) and stellar (dotted lines) content.

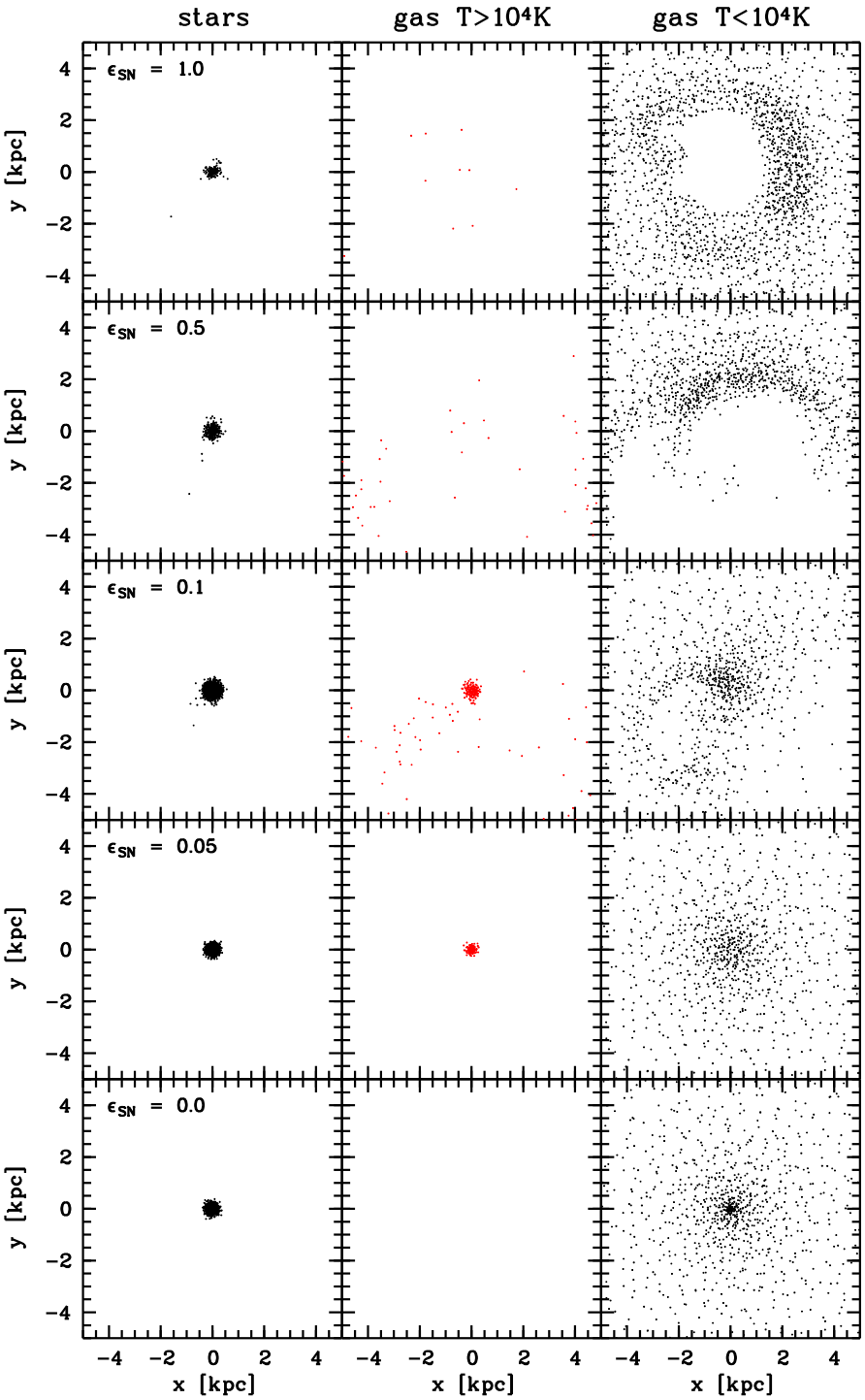

Figure 7.10: The spatial distribution of stars, hot and cool gas of the simulated dwarf after 5×10^8 yr, in function of $\epsilon_{\rm SN}$.

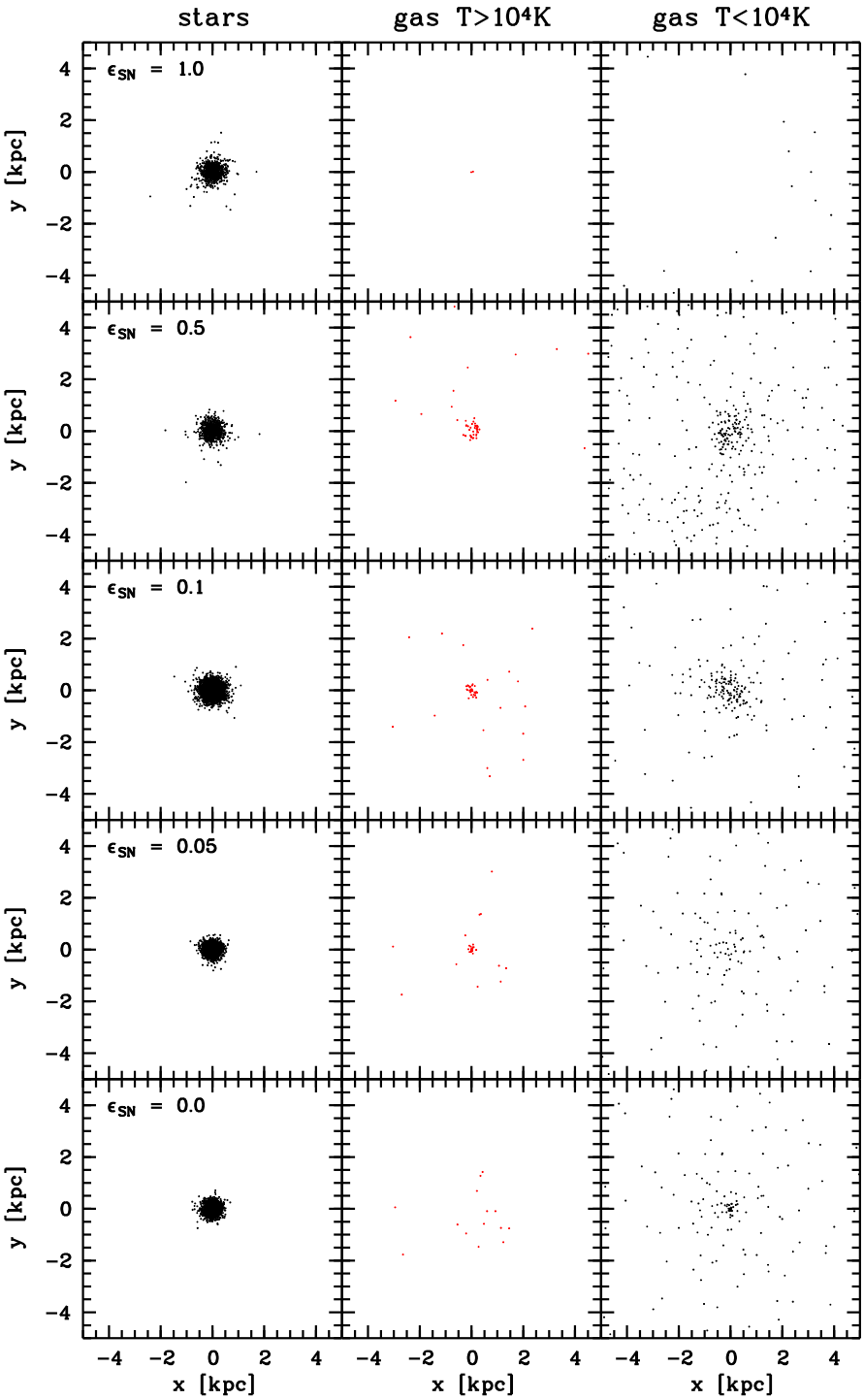

Figure 7.11: The spatial distribution of stars, hot and cool gas of the simulated dwarf after 2×10^9 yr, in function of $\epsilon_{\rm SN}$.

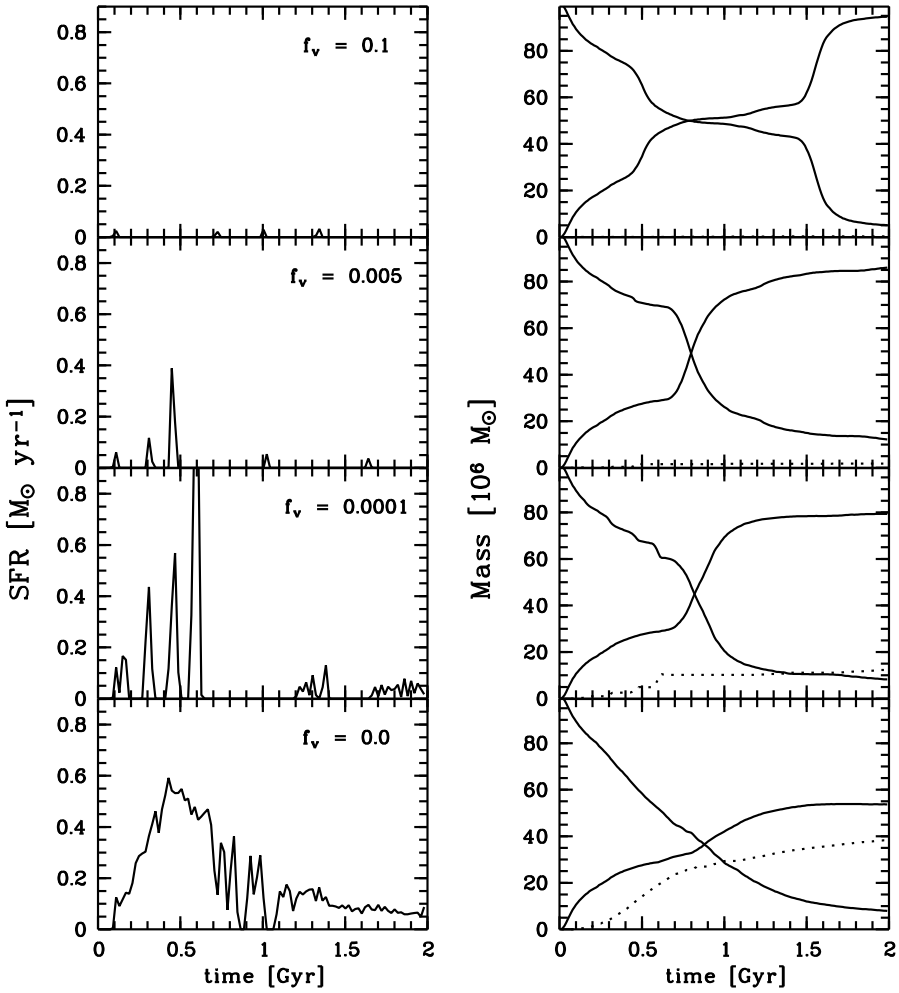

Figure 7.12: *Left panels:* The evolution of the SFR of the simulated dwarf in function of the kinetic feedback fraction f_v. The energy feedback efficiency is fixed at $\epsilon_{\rm SN}$. *Right panels:* The time evolution of the gas (solid lines) and stellar (dotted lines) content.

investigate the influence of including kinetic energy feedback, we performed a set of simulations with varying kinetic feedback efficiency f_v, and keeping $\epsilon_{\rm SN}$ fixed at 0.1.

Kinetic feedback has a very drastic effect on low-mass galaxy formation. Even when a small fraction $f_v = 10^{-4}$ of the energy is in kinetic feedback, bursts of star formation blow concentric bubbles in the gas (Figure 7.12). Although some new stars are formed in the compressed shell (Figure 7.13), star formation is halted after each burst, until the supernovae die away and gas falls back into the central regions of the galaxy, where a next star formation burst can occur. The total mass in stars formed after 2 Gyr is much smaller than without kinetic feedback, only $1.2 \times 10^7\,{\rm M}_\odot$, and the distribution is more diffuse (Figure 7.14). Most of the interstellar medium is blown out in a galactic wind. A small fraction (less than 10 per cent of the original gas mass) is still within the galaxy boundary and some of it eventually sinks down to the galactic centre where star formation can continue at a very low pace.

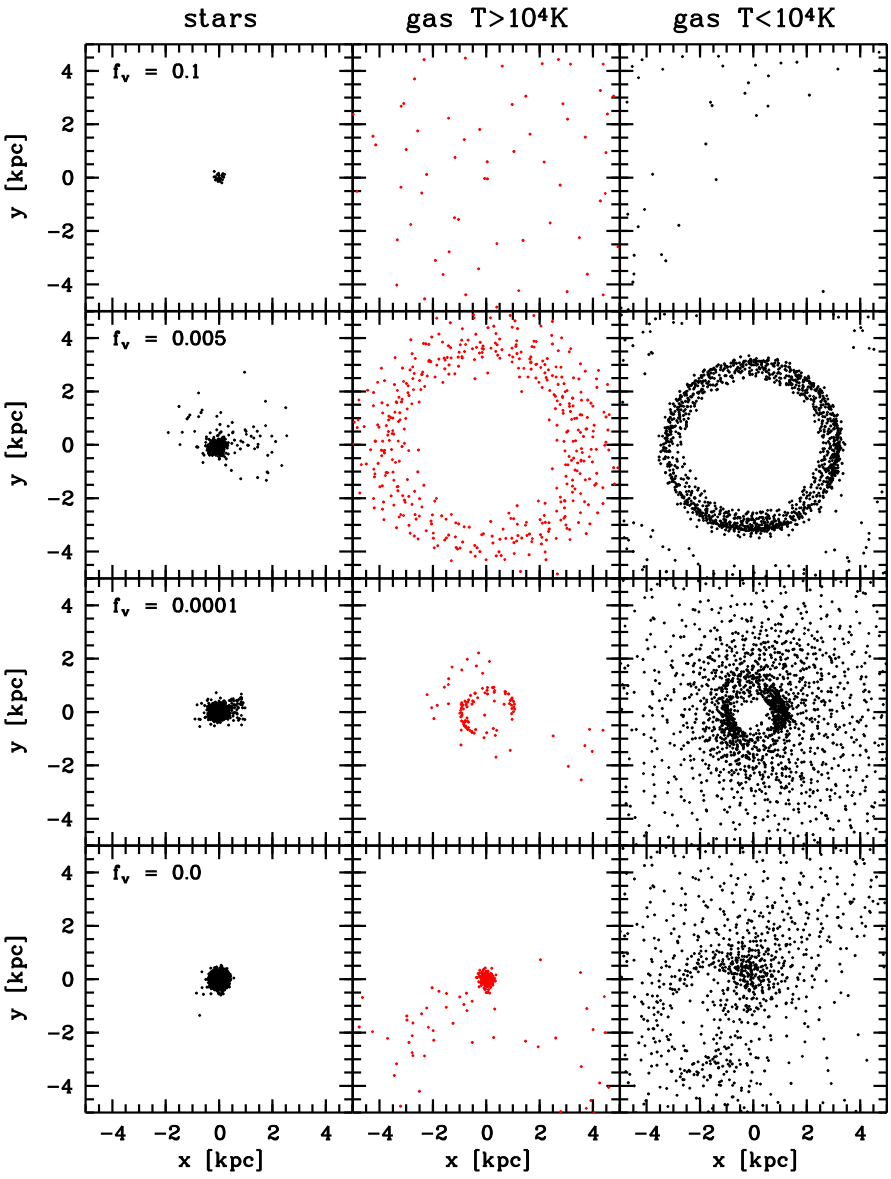

Figure 7.13: The spatial distribution of stars, hot and cool gas of the simulated dwarf after 5×10^8 yr, in function of $f_{\rm v}$.

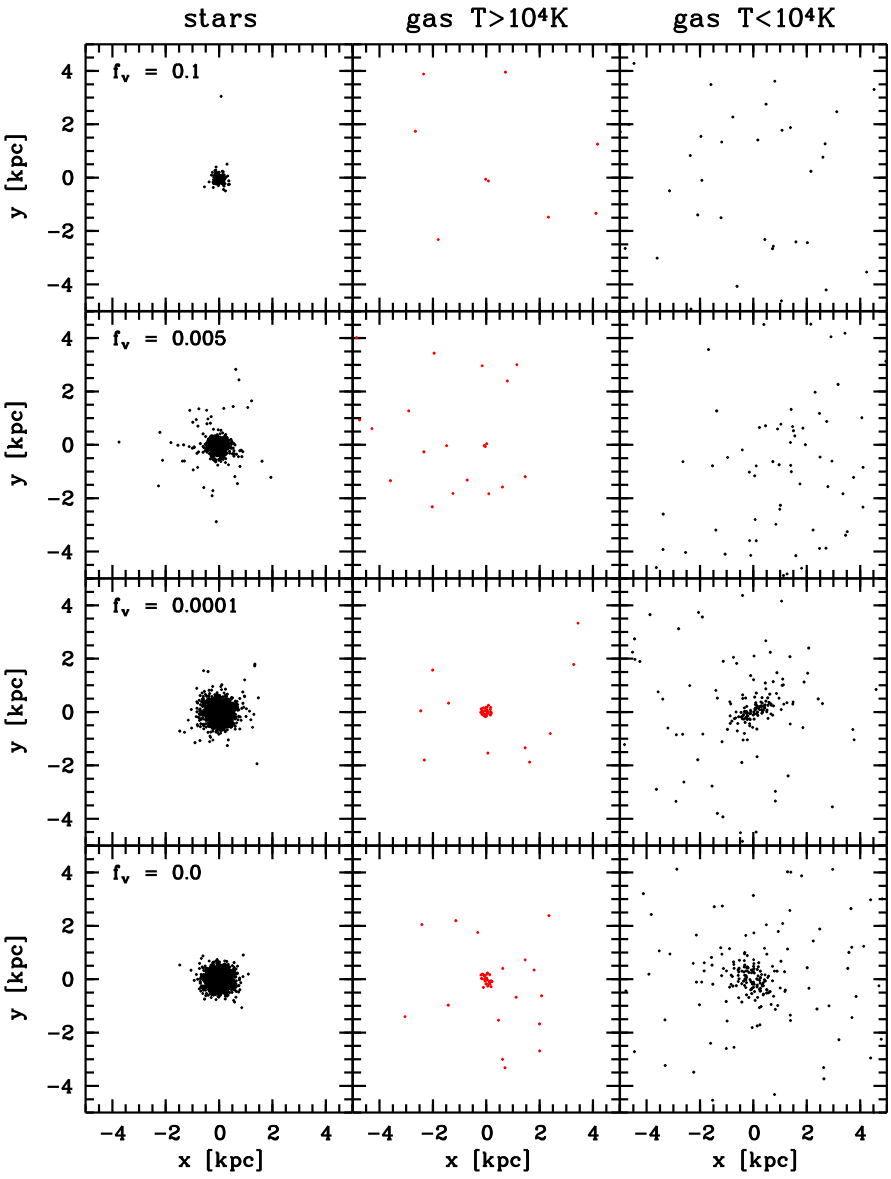

Figure 7.14: The spatial distribution of stars, hot and cool gas of the simulated dwarf after 2×10^9 yr, in function of $f_{\rm v}$.

Increasing the fraction of kinetic energy to 0.5 per cent of the feedback energy increases the efficiency of the galactic wind, and almost no stars are formed before most of the gas is blown out after 0.5 Gyr (Figures 7.12 and 7.13). Some gas falls back onto the galaxy at later stages, giving rise to very small starbursts. Only a small fraction of the initial gas mass is converted into stars. When a very strong kinetic feedback efficiency of 10 per cent is assumed, essentially all the gas is blown away by only a couple of stars.

From their detailed one-dimensional simulations of supernova evolution, Thornton et al. (1998) concluded that about 85 per cent of the energy returned to the surrounding ISM is in the form of kinetic energy. Our results clearly indicate that including such a high fraction of kinetic energy in galaxy formation simulations would prevent a dwarf galaxy from being formed. One has to bear in mind however, that our simulations do not resolve individual supernova events and that the spatial resolution is much coarser than in the Thornton et al. (1998) simulations. Moreover the increase of the thermal budget of the ISM surrounding a stellar particle eventually also imparts a kinetic effect on the ISM, through the formation of outward-expanding superbubbles. In their simulations of galaxy formation, Kawata & Gibson (2003) found that a kinetic feedback efficiency of $f_v = 0.002$ best reproduces the color-magnitude relation for elliptical galaxies, while Carraro et al. (2001) do not include kinetic feedback at all.

In Figure 7.24, the radial density profiles for stars, gas and dark matter are shown, in function of the kinetic feedback f_v. As in the case of varying total energy feedback $\epsilon_{\rm SN}$, the stronger the feedback, the more diffuse the stellar and dark matter distribution become. When $f_v = 0.005$, the early galactic wind is stronger than in the $f_v = 0.1$ case. Therefore, the dark matter distribution is most diffuse for the $f_v = 0.005$ case.

To summarize, we find that even including a small fraction of the feedback energy in the form of kinetic feedback has a very strong effect on the gas distribution and on the SFR. Star formation occurs in several bursts, separated by the lifetime of supernovae from the stellar population that formed during each burst. This leads to very few stars being formed.

Energy feedback: adiabatic period

Another way to avoid rapid radiative cooling of the gas heated by supernovae, is to include an adiabatic cooling period after the energy injection. The idea is that a supernova remnant consists of a hot, tenuous cavity which cannot cool efficiently because of the low density. In galactic simulations however, individual supernova remnants are not resolved and the density is smoothed out, leading to higher densities and larger cooling rates. To investigate the effect of including an adiabatic cooling phase in our simulations, in each timestep we simply switch off radiative cooling for those gas particles that are heated during that timestep. Several simulations were run, with weak, normal and strong feedback efficiency, and one including kinetic feedback.

Figure 7.15 shows the SFRs for the different simulations. The overall shape of the SFR is similar to that of simulations without an adiabatic cooling phase. However, the star formation now proceeds in a series of bursts, peaking around 0.5 Gyr. The amplitude of these bursts is also much smaller. The dense gas in the centre of the galaxy, which previously could cool very efficiently and continue forming stars, is now prevented from cooling and star formation is completely stopped even after a small star burst. In the simulations without an adiabatic cooling phase, a large and continuous starburst is needed to provide enough energy input to halt the star formation.

Because the heated gas is not allowed to cool, its increased pressure will push the surrounding cold gas out more efficiently, so that a galactic wind develops, even in the case of weak feedback efficiency. Hence, a smaller amount of gas is converted into stars, with only 10^7 $\mathrm{M}_\odot$ of stars formed after 2 Gyr in the case of $\epsilon_{\rm SN} = 0.1$. Somewhat more gas is able to stay within the galaxy boundary to fuel smaller star formation events (Figure 7.17).

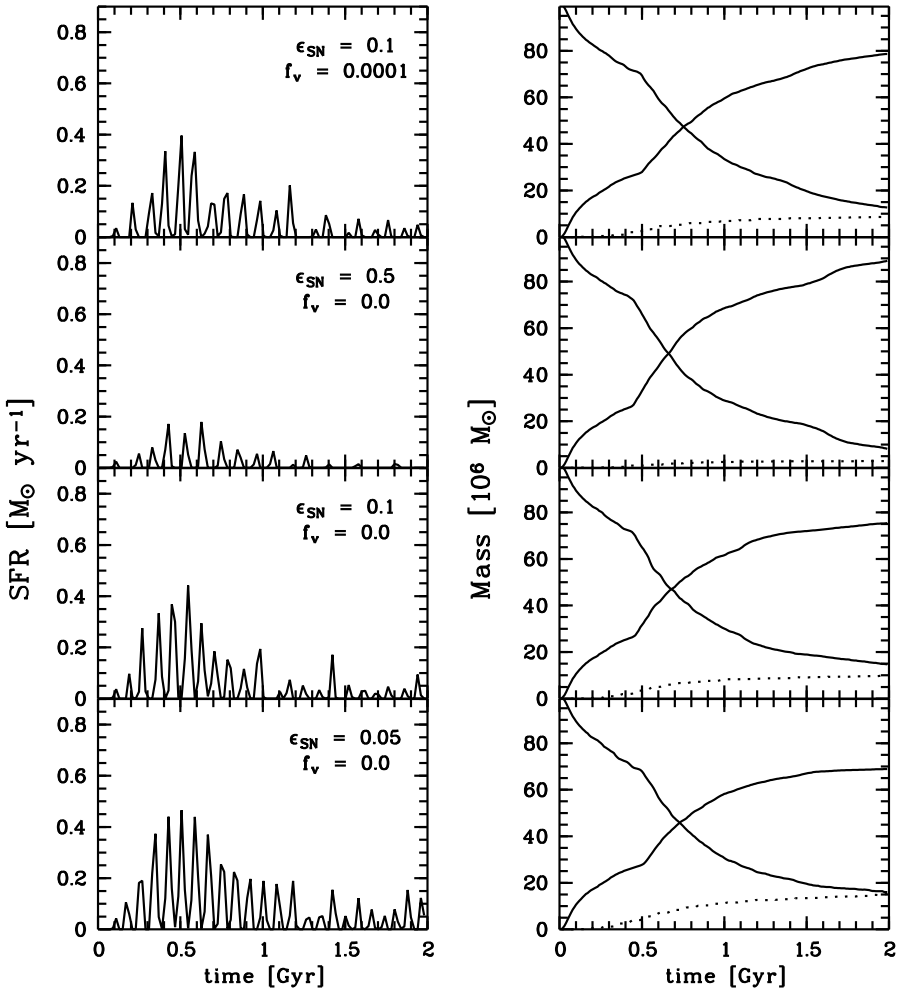

Figure 7.15: *Left panels:* The evolution of the SFR of the simulated dwarf, including an adiabatic period during energy feedback. In the lower three panels, the energy feedback efficiency is varied: $\epsilon_{\rm SN} = 0.05, 0.1, 0.5$ (going upwards). In the top panel, kinetic feedback is also included ($\epsilon_{\rm SN} = 0.1, f_{\rm v} = 0.0001$). *Right panels:* The time evolution of the gas (solid lines) and stellar (dotted lines) content.

When an adiabatic cooling phase is included, the influence of including kinetic feedback is much smaller. The separation between the subsequent bursts of star formation is somewhat longer, because the gas is more disrupted. Therefore it takes more time to fall back into the centre and reach the density needed to start star formation. The fraction of gas blown out in the galactic wind is also slightly higher when kinetic feedback is included.

Interestingly, if we compare the SFRs in the simulations including a kinetic feedback $f_v = 10^{-4}$, with and without an adiabatic cooling phase (Figures 7.12 and 7.15), the strength of the galactic wind is much larger if no adiabatic cooling phase is included. Star formation occurs in smaller bursts because the adiabatic cooling phase effectively stops star formation once the supernovae kick in. Therefore the

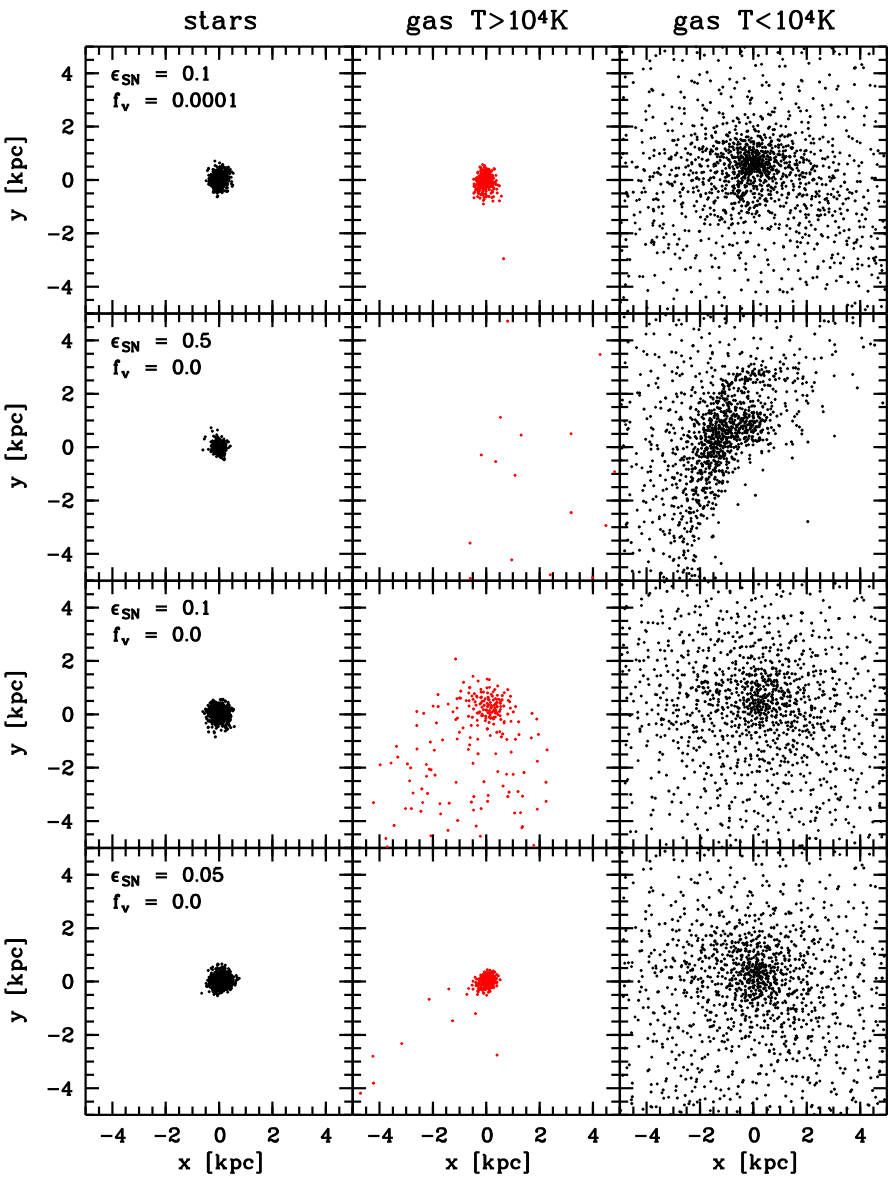

Figure 7.16: The spatial distribution of stars, hot and cool gas of the simulated dwarf after 5×10^8 yr, when an adiabatic cooling period is included. The feedback efficiency is the same as in Figure 7.15.

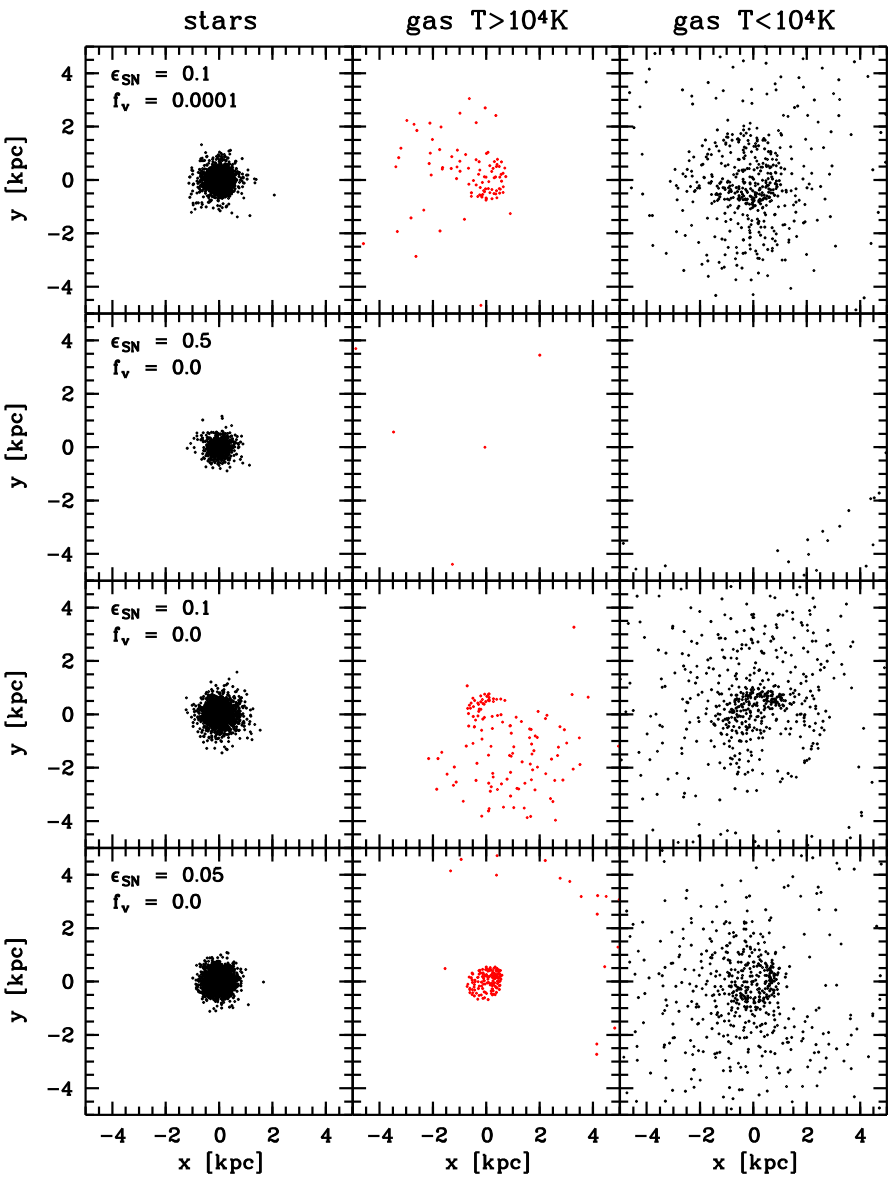

Figure 7.17: The spatial distribution of stars, hot and cool gas of the simulated dwarf after 2×10^9 yr, when an adiabatic cooling period is included. The feedback efficiency is the same as in Figure 7.15.

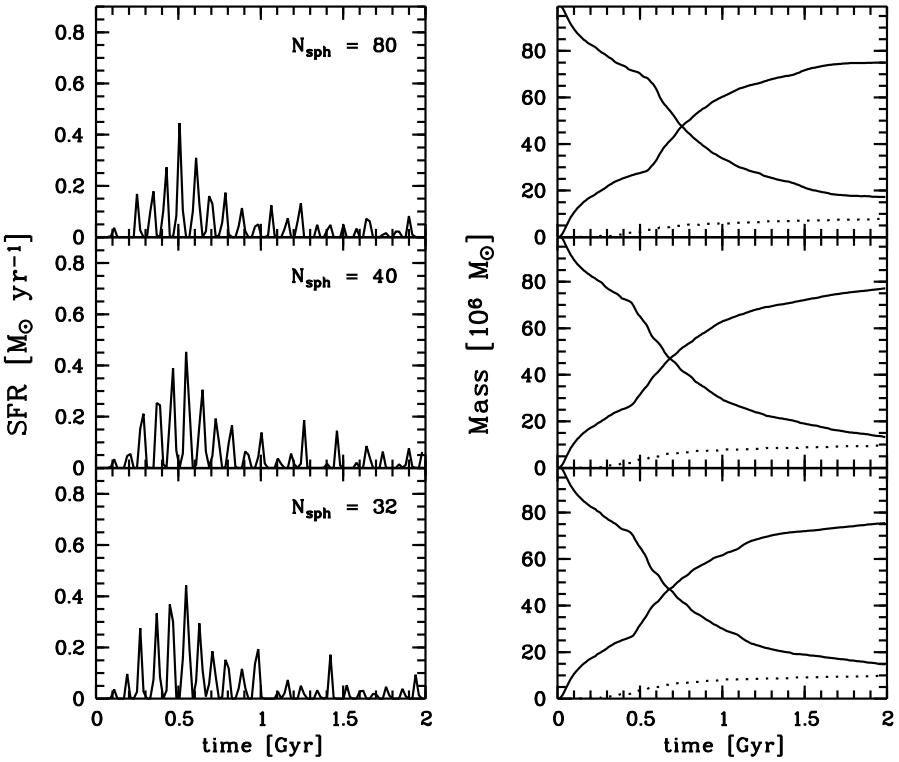

Figure 7.18: *Left panels:* The evolution of the SFR of the simulated dwarf, including an adiabatic period during energy feedback. The adiabatic feedback region is enlarged from 32 neighbour gas particles over 40 to 80 neighbour gas particles. The feedback efficiency is fixed at $\epsilon_{\rm SN} = 0.1$ and no kinetic feedback is included. *Right panels:* The time evolution of the gas (solid lines) and stellar (dotted lines) content.

total amount of kinetic energy injected during a burst is less, and the gravitational potential is able to prevent the gas from flowing out.

In Figure 7.25, we show the stellar, gas and dark matter density profiles for the different simulations. When including an adiabatic cooling period, the differences in radial profiles resulting from varying the feedback parameters $\epsilon_{\rm SN}$ and f_v are less pronounced. The dark matter distribution is not affected by varying the feedback parameters, but is much more diffuse than in simulations without feedback (see Figure 7.22), also approximating an exponential profile. Whereas the other simulations showed a concentration of the left-over gas towards the central region, the central parts of the galaxy are devoid of gas in the simulations with adiabatic cooling. In case of strong energy feedback, all gas has been expelled from the central 1 kpc.

The detailed star formation and feedback processes are not resolved in the simulations. Using the SPH smoothing kernel to distribute thermal energy over the neighbour gas particles will give the largest fraction to the nearest neighbours. The adiabatic cooling period however applies to all heated neighbour particles, regardless of the increase in thermal energy. In order to check that the results do not depend on the extend of the feedback region, we changed the number of neighbour gas particles from 32 to 40 neighbour gas particles. This does not significantly change the SFR, or the strength of the galactic wind

(Figure 7.18). Enlarging the feedback region to 80 neighbour particles gives slightly lower amplitudes for the star formation peaks, because although initially the same amount of gas particles are eligible for star formation, a larger feedback region prevents a larger amount of gas particles from cooling and forming stars.

7.4.4 Chemical evolution

Chemical evolution is an important ingredient in simulations of star formation. The cooling rate Λ is metallicity-dependent, especially in the temperature regime $10^4 - 10^6$ K (see Figure 7.1). Thus, as the first supernovae return enriched material to the surrounding gas, this gas will be able to cool more efficiently.

In the lower right panel of Figure 7.19, we show the SFH of a simulation including chemical evolution. The energy feedback parameter was fixed at $\epsilon_{\rm SN} = 0.1$. It is readily seen that including chemical enrichment allows the gas to cool efficiently and the effect of energy feedback becomes negligible. No galactic wind or bubbles form in the gas (lower panels of Figures 7.20 and 7.21), and star formation can continue, converting almost all gas into stars. The stellar, gas and dark matter density profiles at the end of the simulations (after 2 Gyr), shown in Figure 7.26, are also the same as in the simulations without energy feedback (Figure 7.22).

In Figure 7.27, we show the mean stellar metallicity in function of simulated time. Because no galactic wind is present in these simulations, the metals produced by SN II are incorporated in stars when they form from enriched gas. The metallicity rises monotonically during the first Gyr and then levels of at $Z = 2/3 Z_\odot$, which is much higher than observed for dEs.

Because we want to keep $\epsilon_{\rm SN}$ fixed, we need some mechanism to prevent the rapid cooling of metal-enriched gas. Therefore, we re-investigate the effects of including a fraction of kinetic energy feedback, and of including an adiabatic cooling period after supernova feedback.

Revisiting kinetic feedback

As in the simulations without chemical evolution, including kinetic feedback has a strong effect on the evolution of the dwarf galaxy. In this case, including a small fraction of the feedback energy in the form of kinetic energy ($f_v = 10^{-4}$), leads to two distinct star formation bursts (Figure 7.19). After the second, vigorous, burst of star formation, all the gas is carried away in a strong galactic wind. The total mass of stars formed is $\sim 1.5 \times 10^7$ M$_\odot$, comparable to the simulations without chemical evolution. Including stronger kinetic feedback results in a series of small starbursts, each time blowing a spherically symmetric superbubble in the gas (Figure 7.21) but never expelling all of the gas, so that star formation continues up to the end of the simulation. The total amount of stars formed is however quite low.

The resulting stellar density profile is exponential, and the central dark matter distribution is also flatter (Figure 7.26). Although in both cases the central 1 kpc is devoid of gas, in the case of strong kinetic feedback ($f_v = 0.005$), a starburst event has blown a superbubble in the gas, which will fall back onto the central regions once feedback ends (Figure 7.21).

The chemical evolution of the stellar population is shown in the left panel of Figure 7.27. With $f_v = 0.0001$, the metallicity rises to $Z = 1/3 Z_\odot$, still rather high for a dE. After the first star formation burst, star formation is halted because the gas is forced outward due to the kinetic feedback. This allows pristine gas to flow into the centre once the energy feedback ends, and stars formed from this gas will have low metallicities. When stronger kinetic feedback is implemented, the final mean stellar metallicity is lower, but this is mainly because fewer stars and hence fewer metals, are formed.

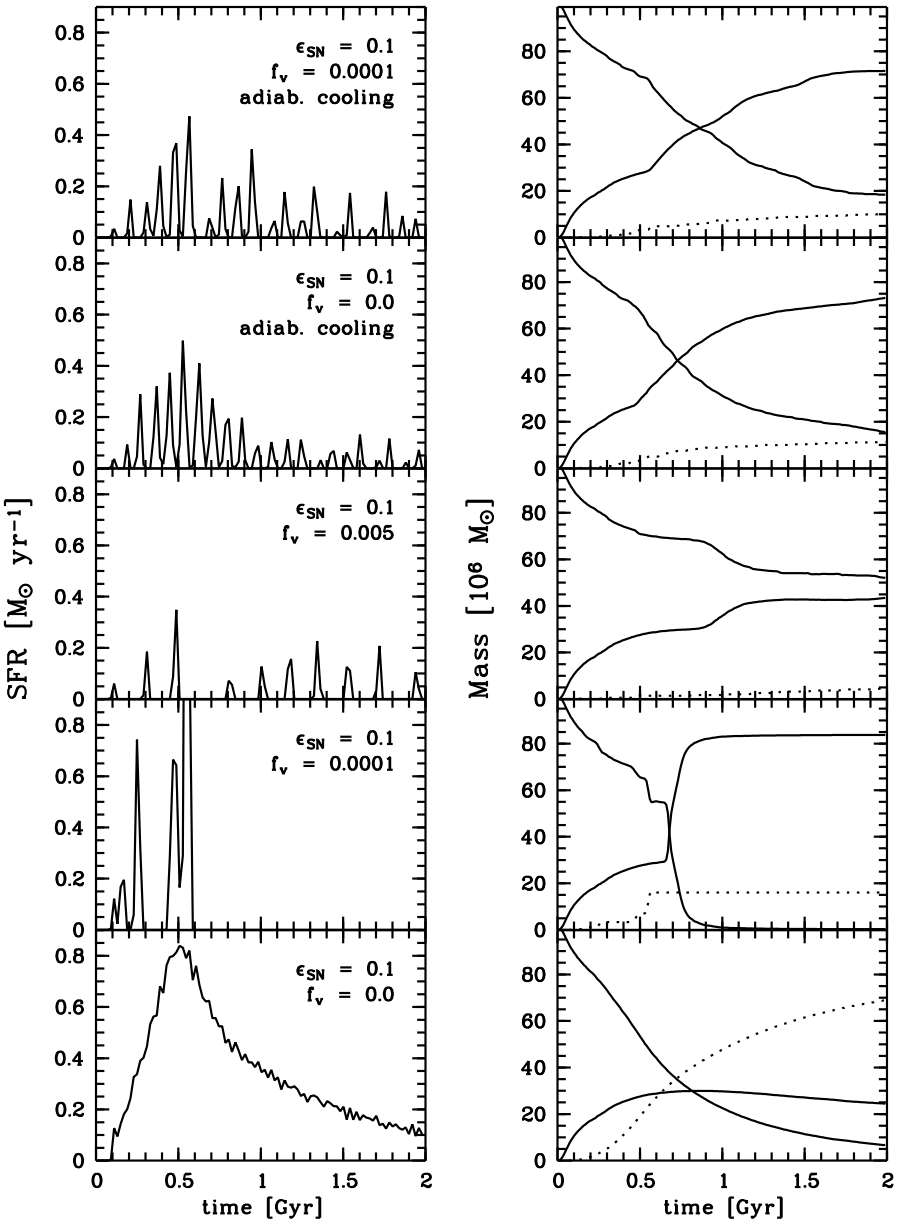

Figure 7.19: *Left panels:* The evolution of the SFR of the simulated dwarf, including chemical evolution. In all simulations, we fix the total energy feedback efficiency $\epsilon_{\rm SN} = 0.1$. In the lower three panels, the kinetic feedback efficiency is varied: $f_v = 0.0, 0.0001, 0.005$ (going upwards). In the two upper panels, an adiabatic cooling period is also included. *Right panels:* The time evolution of the gas (solid lines) and stellar (dotted lines) content.

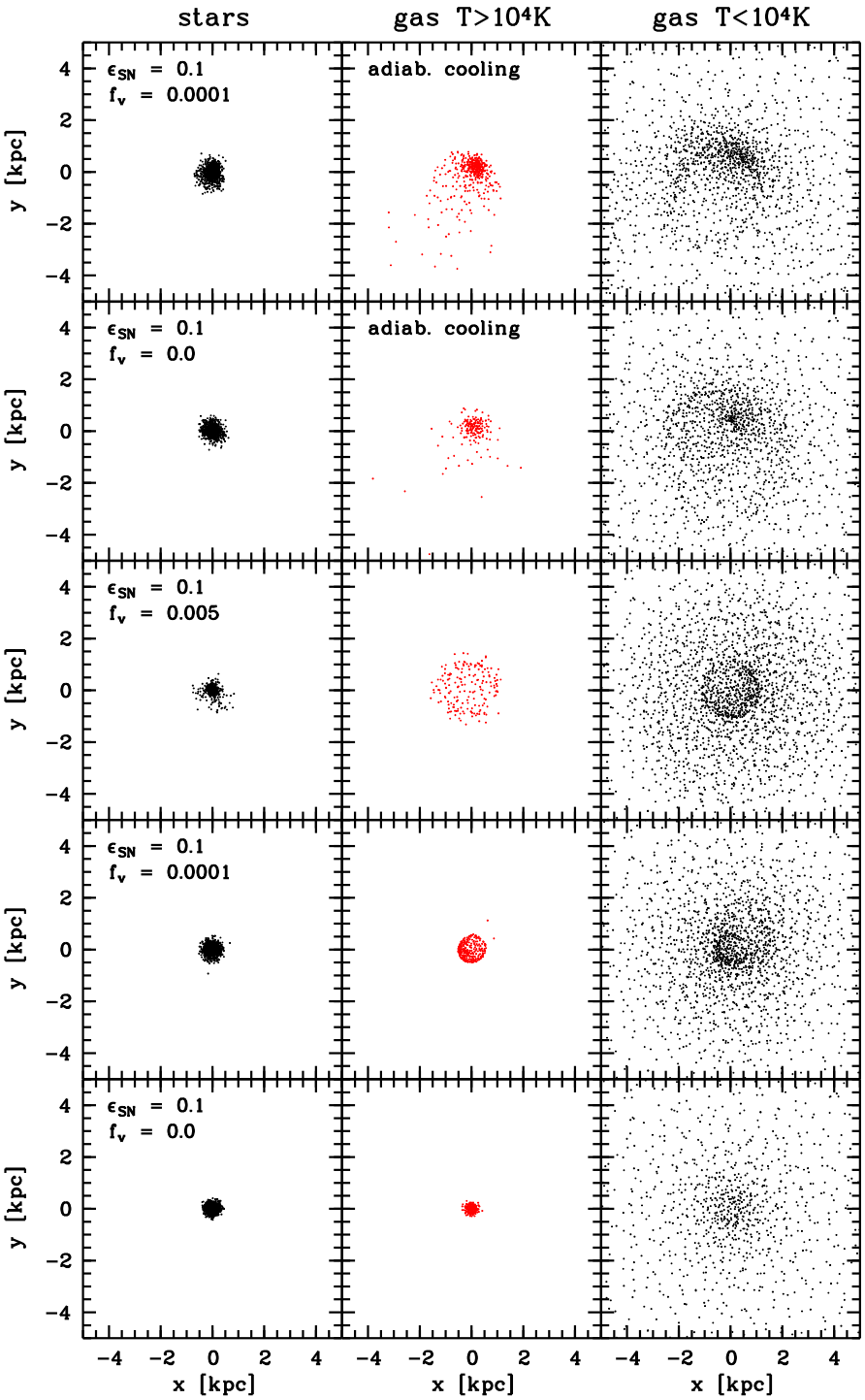

Figure 7.20: The spatial distribution of stars, hot and cool gas of the simulated dwarf after 5×10^8 yr, when chemical evolution is included. The feedback efficiency is the same as in Figure 7.19.

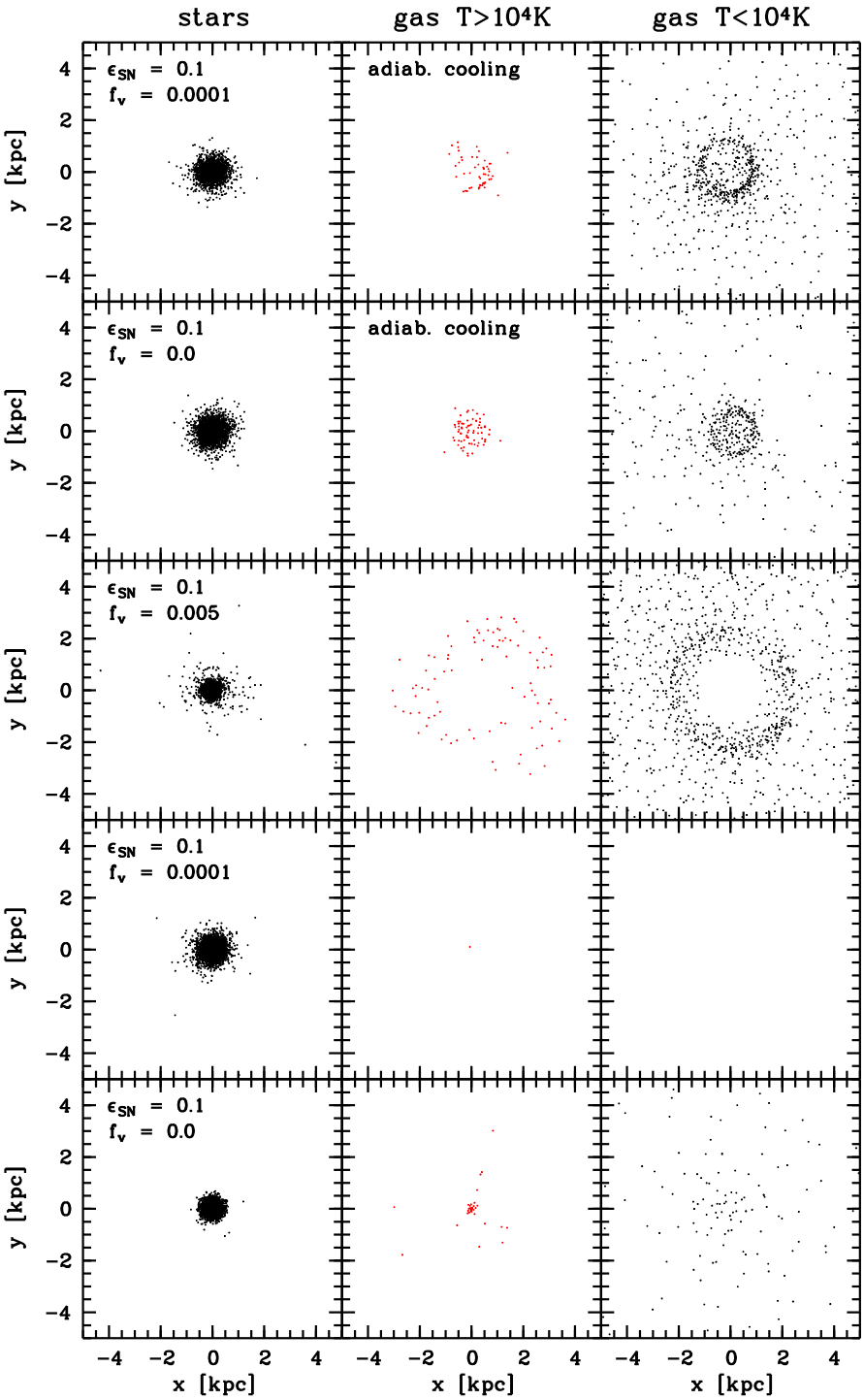

Figure 7.21: The spatial distribution of stars, hot and cool gas of the simulated dwarf after 2×10^9 yr, when chemical evolution is included. The feedback efficiency is the same as in Figure 7.19.

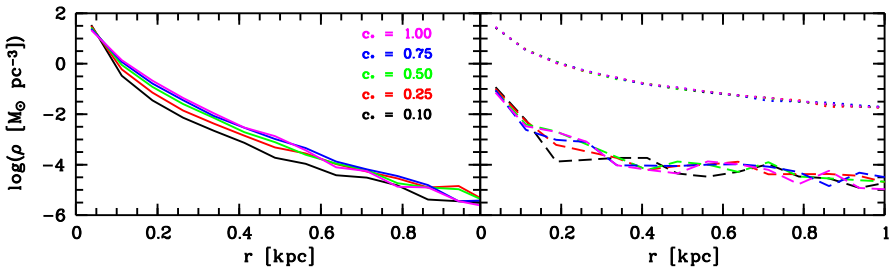

Figure 7.22: Radial density profiles in function of the star formation efficiency parameter c_*. *Left panel:* The stellar density profiles show a more centrally concentrated distribution for lower values of c_*. *Right panel:* The dark matter profiles (dotted lines) are not affected by the stellar or gas distribution. The radial gas density (dashed lines) are more scattered, but show a trend of more concentrated profiles for lower values of c_*. For lower c_*, the star formation proceeds in denser conditions.

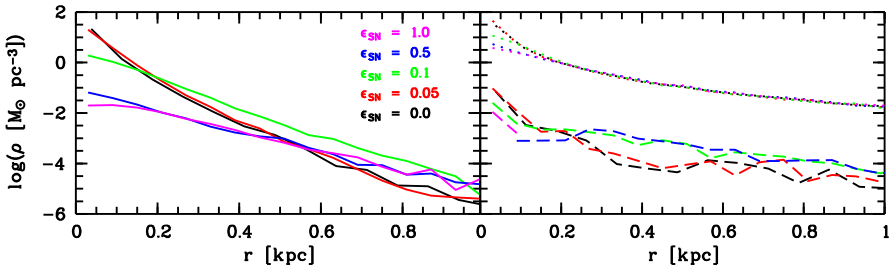

Figure 7.23: Radial density profiles in function of the energy feedback efficiency $\epsilon_{\rm SN}$. *Left panel:* The stellar density profiles. Including stellar feedback makes the stellar distribution more diffuse. For $\epsilon_{\rm SN} = 0.1$, the stellar density profile is approximately exponential. When strong or very strong feedback is assumed, the stellar density becomes quite low. *Right panel:* The dark matter profiles (dotted lines) are affected by the stellar winds. The stronger the feedback, and hence the more efficient and stronger the galactic wind, the more diffuse the dark matter distribution. The radial gas density (dashed lines) are more scattered, but also less centrally concentrated with increasing energy feedback efficiency. In case of very strong efficiency, only a small amount of gas is left in the centre of the galaxy.

In the right panel of Figure 7.27, we show the fraction of metals that is carried outside the galaxy's boundary by the galactic wind. Since kinetic energy feedback produces spherically symmetric galactic winds, the enriched material stays at the inner side of the shell. When the feedback stops, the enriched material flows back into the galactic centre where it is used for further star formation. In the simulations with strong kinetic feedback, no metals are ejected, whereas in the case of $f_v = 10^{-4}$, about 35 per cent of the metals is ejected.

Revisiting adiabatic cooling period

Another way to prevent the enriched gas from rapid cooling, is to include an adiabatic cooling period during supernova feedback. As in the simulations without chemical feedback, the SFH (upper panels of

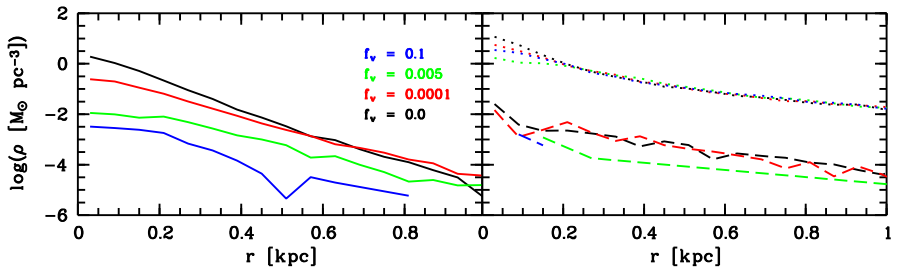

Figure 7.24: Radial density profiles in function of the kinetic feedback efficiency f_v, assuming a fixed feedback efficiency $\epsilon_{\rm SN} = 0.1$. *Left panel:* The stellar density profiles show that including kinetic feedback makes the stellar distribution more diffuse. Very few stars are formed if more than 0.5 per cent of the feedback energy is in kinetic form. *Right panel:* The dark matter profiles (dotted lines) are affected by the stellar winds. The stronger the feedback, and hence the more efficient and stronger the galactic wind, the more diffuse the dark matter distribution. The stronger the kinetic feedback, the more efficient the galactic wind in removing the gas, as seen in the radial gas density profiles (dashed lines).

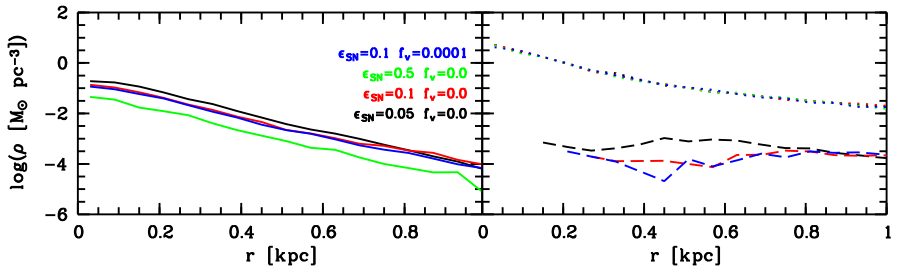

Figure 7.25: Radial density profiles in function of the energy feedback efficiency $\epsilon_{\rm SN}$ and kinetic feedback fraction f_v, when an adiabatic cooling period is implemented. *Left panel:* The stellar density profiles are all nearly exponential, with a central core. The stronger the feedback, the less stars are formed. *Right panel:* The dark matter profiles (dotted lines) are the same in all cases, and is also less cusped than in simulations without any feedback. The stellar wind is more spherically symmetric, and the inner parts of the galaxy are devoid of gas, as clearly seen in the radial gas density (dashed lines). In case of strong energy feedback ($\epsilon_{\rm SN} = 0.5$), no gas is left within the central 1 kpc.

Figure 7.19) shows a series of intermittent bursts. Part of the gas is blown away from the galaxy, but less efficient than in the case of kinetic feedback. Instead of a spherically symmetric wind blowing out all the gas, a superbubble develops that carries away only part of the gas. At the end of the simulation, a significant amount of gas is left inside the galaxy boundary, and some star formation still goes on.

When a superbubble breaks out of the galactic boundary, it creates a sort of chimney through which hot, enriched gas can escape freely. Up to 70 per cent of the produced metals is lost in the galactic winds (right panel of Figure 7.27). As a result, less metals are available for subsequent star formation and the metallicity of the galaxy is low, around $Z = 1/100 Z_\odot$ at the end of the simulation (left panel of Figure 7.27). This is somewhat lower than observed in dEs. If star formation continues in the gas remaining inside the galaxy, the metallicity could still increase.

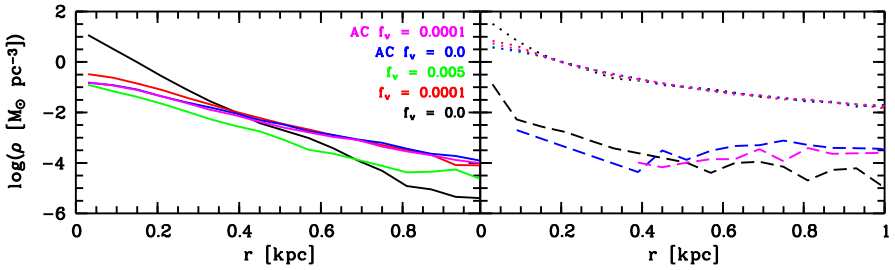

Figure 7.26: Radial density profiles for simulations including chemical evolution, after a simulation time of 2 Gyr. The total energy feedback is fixed at $\epsilon_{\rm SN} = 0.1$ and the kinetic feedback f_v is varied as indicated on the figure. AC stands for adiabatic cooling period. *Left panel:* The stellar density profiles. Note that, in the central 0.2 kpc, the results from the two AC simulations lie on top of each other. *Right panel:* The dark matter profiles (dotted lines) and the gas density profiles (dashed lines). In the simulations including kinetic feedback, the gas has been blown out to radii larger than 1 kpc.

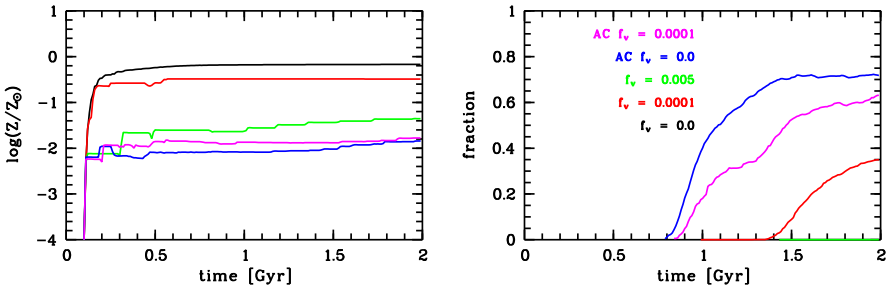

Figure 7.27: *Left panel:* Chemical evolution of the stellar component in the simulations with metal enrichment. The evolution of the mean metallicity Z in function of time is plotted. *Right panel:* Metal-enriched outflow. The fraction of produced metals that is carried outside the galaxy boundary in function of time for the different simulations. The different simulations are color-coded as indicated on the figure.

Including part of the feedback energy as kinetic energy in the simulations with an adiabatic cooling period does not alter the outcome much, compared to the simulation with only thermal feedback. The star formation during the first Gyr shows two periods of intermittent bursts instead of one, but overall the same amount of stars is formed and the same amount of gas is blown out in a superbubble. Also the final stellar density profiles are almost identical. The stellar distribution is slightly more diffuse than in the kinetic feedback $f_v = 10^{-4}$ simulation. The final metallicity is comparable to the adiabatic cooling simulation without kinetic feedback, but a smaller fraction of produced metals is blown out of the galaxy when the simulation ends.

7.5 Discussion

In order to simulate the formation of a dwarf elliptical galaxy, we investigated the implementation of star formation and supernova feedback in the numerical simulations. As a case study, we simulated the formation of a small galaxy of total mass $M_{\rm tot} = 10^9\,{\rm M}_\odot$, and a baryon fraction (initially only gas) of 10 per cent. We adopted a King distribution with concentration index $c = 2$ and tidal radius $r_t = 8.45\,$kpc. for the dark matter halo, and the $10^4\,$K gas was distributed homogeneously within this halo.

Radiative cooling is a necessary ingredient of the simulation, in order to allow the gas to cool as it sinks towards the centre of the gravitational potential.

Prescriptions for star formation are included based on physical assumptions, namely that star formation occurs in cold, dense, collapsing and Jeans-unstable regions. We follow the suggestion of Buonomo et al. (2000) to use the total local density in order to estimate the dynamical timescale, instead of using only the local gas density. The star formation is almost independent of the star formation efficiency parameter c_*, producing slightly more concentrated stellar distributions for lower values of c_*.

The implementation of stellar feedback is a necessary ingredient in dwarf galaxy formation simulations. If no feedback is included, almost all gas is eventually converted into stars, and the resulting galaxy is much too centrally concentrated. However, several methods exist to implement stellar feedback in N-body/SPH simulations. First, we investigated the effect of varying the stellar feedback efficiency $\epsilon_{\rm SN}$. The canonical value $\epsilon_{\rm SN} = 0.1$ is suggested by detailed one-dimensional simulations of supernova remnant evolution (Thornton et al., 1998). Including this stellar feedback as purely thermal feedback leads to an exponential radial density profile, as observed for dEs. Smaller values of $\epsilon_{\rm SN}$ have almost no effect compared to the simulations without feedback. Strong feedback on the other hand prevents star formation and only very few stars are formed. The dark matter distribution is also affected by the feedback, becoming less cusped as it responds to the loss of gas from the central region. The gas does not leave the galaxy in a spherically symmetric galactic winds, but rather through superbubbles and chimneys blown into the gas. Therefore, star formation can continue on one side of the galaxy, while gas is blown out on the other side.

In some simulations, a fraction f_v of the feedback is returned in kinetic energy. We found that including kinetic feedback has a strong influence on the SFR. The galactic winds are stronger, leading to separate bursts of star formation. Unless the kinetic feedback parameter f_v is quite small ($f_v \sim 10^{-4}$), the effect of kinetic energy prohibits star formation and the resulting galaxy is too diffuse.

Including an adiabatic cooling period for particles that are heated by stellar feedback prevents rapid cooling of those gas particles. In this case the star formation also occurs in a series of bursts, as star formation cannot occur in the heated regions. The adiabatic cooling period seems to lessen the effect of varying the feedback parameters $\epsilon_{\rm SN}$ and f_v. The stellar distribution is approximately exponential in all cases. The galactic wind seems to be more effective at expelling the gas from the central regions of the galaxy.

When metal enrichment is included, the enriched gas can cool much more efficiently, leading to shorter cooling timescales. Hence, the thermal energy returned is quickly radiated away and the SFH is the same as for simulations without energy feedback. Moreover, the chemical evolution is too efficient, leading to an almost solar mean metallicity, in contradiction with observations of dwarf galaxies. Therefore we re-investigated the methods to prevent overcooling: kinetic feedback and an adiabatic cooling period. It was found that including a small amount of kinetic feedback expels all the gas in a strong galactic wind, leaving a diffuse and gasless dE. Chemical enrichment is however quite effective and the resultant galaxy has a mean metallicity of about one-third solar. Alternatively, an adiabatic cooling period also keeps star formation under control. The galactic wind in this case is less strong, and some gas is still left at the end of our simulations. However, because the outflow is not spherically symmetric, chimneys

develop through which enriched gas can escape. The total metallicity is therefore much lower, about $1/100$ solar.

7.6 Conclusions

The implementation of star formation and stellar feedback in numerical simulations of galaxy formation has been investigated, paying special attention to the effects of the various parameters involved. Due to their low gravitational potential well, dwarf galaxies are sensitive to variations in the feedback parameters. If no feedback is assumed, the resulting galaxy is too centrally concentrated. The best results are obtained by using the established value $\epsilon_{\rm SN} = 0.1$ for the feedback efficiency. Including a small fraction of kinetic feedback or including an adiabatic cooling period is not necessary in simulations without chemical feedback.

When chemical feedback is implemented, thermal feedback is quickly radiated away by the enriched gas, and some mechanism needs to be invoked to prevent the star formation from being too efficient. Including a small fraction of kinetic energy feedback or including an adiabatic cooling period following heating by supernovae are both possible options, producing diffuse, metal-poor dwarf galaxies.

Although we are far from understanding all the mechanisms that are involved in star formation and feedback, it is clear that these processes are important ingredients in numerical simulations of galaxy formation. The interplay between cooling, energy feedback and chemical evolution is a complicated process because they influence each other to a great extend. Simulations that incorporate only energy feedback (and no chemical evolution) or only chemical evolution (and no energy feedback) are bound to miss a significant part of the overall picture.

7.6.1 Future work

There is still much room for improvement both for the simulations and for the analysis of the results.

First of all, in these simulations, the metallicity of a gas particle is calculated from its own metal/gas content. However, in the SPH idea, the metallicity of gas particles could be calculated by smoothing over the neighbour gas particles. One could also try to spread the metals over the neighbour particles at each timestep, to mimic a kind of metal mixing. Moreover, we only looked at the total metallicity. Using the tables in Section 7.2.3, the evolution of different elements can be followed. The age of the stars of different mass in the stellar populations could be taken into account during stellar feedback, instead of averaging the total feedback of a population. The effect of feedback from type Ia supernovae, and from intermediate-mass stars could be taken into account.

Secondly, simulations need to be performed with different galaxy masses, to distinguish between dwarf and giant formation.

Finally, the code could be linked to a population synthesis code, in order to produce observable quantities such as luminosity, surface brightness, spectral indices, velocity dispersions... in order to compare the simulation results to observed dEs, as in chapter 2.

Part III

Summary

Chapter 8

Samenvatting

8.1 Inleiding

Elliptische dwerggalaxieën (dwarf elliptical galaxies; dEs) zijn lichtzwakke, diffuse melkwegstelsels die weinig of geen gas bevatten en voornamelijk in groepen en clusters van melkwegstelsels aangetroffen worden. Het is de meest voorkomende galaxiesoort in het nabije universum. Ondanks dit numerieke overwicht begrijpen we echter nog steeds niet ten volle hoe deze stelsels gevormd worden en hoe ze evolueren. In de loop van de jaren is in elk geval gebleken dat dEs geen eenvoudige systemen zijn, zoals eerst werd aangenomen. In het *Koude Donkere Materie* beeld voor galaxievorming, worden steeds grotere structuren hiërarchisch opgebouwd. In deze theorie zijn dwerggalaxieën bij de eerste structuren die in het universum gevormd worden en vormen zij de fundamentele bouwstenen voor grotere sterrenstelsels, zoals onze Melkweg. Daarom is het bestuderen van de oorsprong en evolutie van dwerggalaxieën belangrijk voor het begrijpen van de vorming en evolutie van grotere sterrenstelsels.

Er zijn momenteel een drietal vormingsscenarios voor dEs in voege. Het *windmodel* veronderstelt dat dEs primordiale objecten zijn die niet versmolten zijn tot grotere galaxieën. In dit scenario leidt de eerste serieuze uitbarsting van stervorming tot een *galactische wind*, aangedreven door supernova explosies. Deze wind blaast al het gas uit de galaxie. Het verlies van een substantieel deel van het gas heeft een dynamisch effect op deze lichtgewicht stelsels, en leidt tot een diffuus object.
De overweldigende aanwezigheid van dEs in groepen en clusters doet echter vermoeden dat de omgeving een belangrijke rol speelt in de vorming en evolutie van dEs. Het *aanranding-* of *interactiemodel* beschouwt de omvorming van kleine spiraalstelsels in dEs door herhaaldelijke interacties met grotere stelsels in de groep of cluster. Het aanwezige interstellaire gas wordt op korte tijdsschaal uit de galaxie geblazen door de *ramdruk* van het hete, ijle intracluster medium, zodat een gasloze dwerg overblijft.
Tenslotte worden ook verschillende dwergstelsels waargenomen die noch bij de dEs, noch bij de gasrijke, stervormende onregelmatige dwergen (Irrs) thuishoren. Deze tussenliggende galaxiesoort lijkt zich in een overgangsfase tussen Irrs en dEs te bevinden. Het *uitdoofmodel* stelt dat de huidige Irrs evolueren naar dEs naarmate ze hun gasvoorraad opgebruiken door stervorming, al dan niet geholpen door een galactische wind of door ramdruk.

In de laatste twee decennia is er meer en meer onderzoek verricht over dEs, enerzijds dankzij de komst van 8-meter klasse telescopen die het mogelijk maken deze lichtzwakke galaxieën in detail waar te nemen, anderzijds doordat numerieke simulaties steeds realistischer worden dankzij de steeds toenemende rekenkracht van de hedendaagse computers. Recente waarnemingen tonen aan dat een significant deel van de als dE geclassificeerde dwergstelsels een interstellair medium bevatten. Het doel van dit werk is om zowel observationeel als numeriek het interstellair medium in dEs te bestuderen.

8.2 Waarnemingen

8.2.1 ESO Large Programme

De Gentse onderzoeksgroep speelde een grote rol in een ESO Large Programme omtrent de dynamica van dEs, waaraan 28 nachten waarnemingstijd met de Very Large Telescoop (VLT) te Chili werden toegekend. Er werden zowel optische beelden als nabij-infrarode spectra genomen van een 15-tal dEs in de Fornax Cluster en in drie groepen op het zuidelijke halfrond. Uit de beelden werden structurele parameters bepaald, terwijl de spectra, die de sterke Calcium II Triplet absorptielijnen (CaT) bevatten, gebruikt werden om de kinematica van deze galaxieën te bepalen.

In hoofdstuk 2 worden de structurele parameters van dEs uit onze en andere recent samengestelde datasets vergeleken met die van gewone elliptische galaxieën (Es). Het blijkt dat dEs niet dezelfde klassieke relaties volgen als de Es, hoewel er een continue overgang is van Es naar dEs. Deze overgang stemt overeen met voorspellingen van cosmologische numerieke simulaties van galaxievorming, waar het dynamisch effect van stellaire feedback expliciet in rekening wordt gebracht. Hoewel dit resultaat voor het windmodel als vormingsscenario van dEs pleit, mogen we toch het aanrandingsmodel niet uitsluiten. Waarnemingen van dEs met significante rotatie, en van spiraal- en schijfstructuren in dEs ondersteunen immers dit model.

8.2.2 Calcium II absorptielijnen

Naast kinematische informatie die gehaald wordt uit het verbredingsprofiel van de CaT-lijnen, vertelt de diepte van de CaT absorptie ons ook iets over de sterpopulaties in dEs. Voor individuele sterren en voor bolhopen zijn de CaT lijnen een uitstekende metalliciteitsschatter. Voor elliptische galaxieën ligt de situatie echter anders. Recent werd aangetoond dat de sterkte van CaT anticorreleert met de snelheidsdispersie σ in elliptische galaxieën, terwijl men voor andere metalliciteitsschatters een correlatie waarneemt. In hoofdstuk 3 tonen we dat de waargenomen anticorrelatie van CaT met σ zich doorzet tot in het regime van de dEs. Vergelijking van populatiesynthesemodellen met eerdere fotometrische en optische spectra wijzen op een metaal-arme sterpopulatie in dEs. De hoge CaT waarden voor 12 van de 15 dEs zijn echter niet in overeenstemming met voorspellingen voor metaal-arme sterpopulaties. Hoewel deze resultaten aantonen dat we de werking van het CaT nog niet helemaal doorgrond hebben, wijzen ze ook op het bestaan van chemisch verschillende sterpopulaties in morfologisch gelijke dEs.

8.2.3 Interstellair medium in dEs

Geïonizeerd interstellair medium

In twee van de dEs uit het Large Programme was eerder Hα emissie waargenomen, wat duidt op de aanwezigheid van geïonizeerd waterstof (H II). Aangezien de eerdere waarnemingen geen ruimtelijke informatie bevatten werden deze galaxieën ook waargenomen met een Hα filter. Beide emissiebeelden vertonen een centrale emissiepiek, maar in FCC046 wezen zes emissiewolkjes op mogelijk recente stervorming. Dit vermoeden werd nog versterkt door de H-Paschen absorptie die werd waargenomen in deze dE (hoofdstuk 3). Aangezien het windmodel voorspelt dat dEs oude sterpopulaties en geen gas bevatten, zijn dEs met een geïonizeerd interstellair medium interessante objecten. We verkregen dan ook waarnemingstijd op de VLT om het geïonizeerd waterstof in nog drie andere dEs waar te nemen. Deze waarnemingen worden beschreven in sectie 4.2 van hoofdstuk 4. De dEs bevatten enkele 100 tot 1000 $M_\odot$ aan geïonizeerd waterstof. Twee van deze dEs vertonen ook sterke aanwijzingen voor recente stervorming, in de vorm van complexe gasstructuren en individuele emissiewolken. Als de relatie tussen totale lichtkracht en emissielichtkracht voor normale elliptische galaxieën wordt doorgetrokken tot in

het regime van de dEs, dan blijkt dat de door ons waargenomen dEs een sterkere emissie hebben dan verwacht. Ze liggen eerder op de extentie van elliptische galaxieën die uitgestrekte emissie vertonen, wat aantoont dat de door ons waargenomen dEs gasrijker zijn dan verwacht wordt voor doorsnee-dEs. De precieze ionizatiemechanismen kunnen echter enkel via spectroscopie bepaald worden.

Neutraal interstellair medium

Tenslotte hebben we de Australian Telescope Compact Array (ATCA) gebruikt voor 21 cm radiowaarnemingen van twee dEs in de Fornax Cluster, om naar de aanwezigheid van neutraal waterstof (H I) te zoeken. In sectie 4.3 tonen we dat in beide galaxieën neutraal waterstof werd gedetecteerd. De H I massas (2×10^7 en 5×10^7 $M_\odot$), zijn vergelijkbaar met die van gasrijke Irrs met dezelfe helderheid.

8.3 Numerieke simulaties

8.3.1 De N-deeltjes/SPH code

Aangezien er in Gent geen code aanwezig was om de vorming en evolutie van galaxieën te simuleren, zijn we vertrokken van de publieke HYDRA code (hoofdstuk 5). Dit is een Lagrangiaanse *deeltjescode* die de beweging van deeltjes volgt onder invloed van de zwaartekracht en, voor gasdeeltjes, van hydrodynamische krachten. De zwaartekracht wordt geïmplementeerd door middel van een N-deeltjes adaptieve deeltje-deeltje deeltje-grid techniek, terwijl de hydrodynamische grootheden en krachten worden berekend met behulp van *uitgesmeerde deeltjes hydrodynamica* (smoothed particle hydrodynamics, SPH). Het Lagrangiaanse karakter van de code impliceert dat ze niet afhankelijk is van de geometrie van het bestudeerde probleem. Bovendien laat de deeltjesformulering toe om op een relatief eenvoudige manier processen als koeling, stervorming en feedback te implementeren.

8.3.2 Ramdruk

Het feit dat dEs voornamelijk waargenomen worden in groepen en clusters van galaxieën duidt erop dat de omgeving een belangrijke rol speelt in de evolutie van een dwerggalaxie. Het hete, ijle intracluster medium (ICM) oefent een ramdruk uit op het interstellaire medium (ISM) in de galaxieën. Aangezien dwerggalaxieën een ondiepe gravitationele potentiaalput bezitten, zijn ze gevoeliger aan deze ramdruk dan gewone galaxieën. In hoofdstuk 6 simuleren we gasrijke dEs die door een ICM bewegen. We tonen aan dat kleine dEs inderdaad onmiddellijk hun ISM verliezen. Massievere dEs daarentegen kunnen een deel van hun ISM bijhouden, zelfs over langere tijdsschalen, of na verschillende passages door het centrum van een middelzware galaxiecluster. De keuze voor de begincondities van het ISM speelt een belangrijke rol bij het voorspellen van deze tijdsschalen. Tenslotte zouden de verhoogde dichtheid en druk in het schokfront ervoor kunnen zorgen dat er tijdens de ramdruk fase, sterren gevormd worden uit het ISM. Deze tweede sterpopulatie zal dan jonger en metaal-rijker zijn dan de onderliggende, oude en metaalarme sterpopulatie en zo aanleiding geven tot de waargenomen verschillen van de chemische samenstelling van dEs.

8.3.3 Galactische winden

Geïsoleerde dEs worden verondersteld hun gas te verliezen door een galactische wind. De massaresolutie van hedendaagse numerieke simulaties kan stervorming nog niet in detail volgen, gesteld dat we al zouden weten hoe het stervormingsproces precies in zijn werk gaat. Daarom wordt stervorming geïmplementeerd door gasdeeltjes om te vormen tot sterdeeltjes als aan een aantal voorwaarden voldaan

is. Men veronderstelt bijvoorbeeld dat sterren gevormd worden in moleculaire wolken, voorgesteld door koude en dichte gasdeeltjes. Een *sterdeeltje* zal een sterpopulatie voorstellen van enkele duizenden sterren. Energie en zware elementen worden door deze sterdeeltjes teruggeven aan het omringende gas wanneer een deel van de sterren ontploft als supernova's. In hoofdstuk 7 onderzochten de verschillende parameters die deze processen reguleren. Aangezien dwerggalaxieën zeer gevoelig zijn voor feedback-processen, vormen ze een ideale test de voorschriften van de numerieke implementatie van stervorming te verfijnen. De simulaties tonen bovendien aan dat de galactische wind niet noodzakelijk heel efficiënt is in het verwijderen van het ISM uit een dE, en dat een deel van het gas overblijft om gedurende enkele gigajaren sterren te vormen.

8.4 Conclusies

We zijn natuurlijk nog ver verwijderd van het volledig begrijpen van de vorming en de evolutie an dEs. Het is echter wel duidelijk dat de klasse van de dEs niet noodzakelijk een homogene groep is, maar dat verschillende vormings- en evolutiescenario's uiteindelijk leiden tot morfologisch en kinematisch dezelfde objecten. Een mogelijke manier om toch te achterhalen waar een dE vandaankomt is via haar chemische evolutie.

Numerieke simulaties tonen aan dat in de verschillende voorgestelde vormingsscenarios voor dEs, het mogelijk is dat sommige stelsels een deel van hun ISM over lange tijdsspannes behouden. Meer en meer waarnemingen van gas in als dE geclassificeerde dwergen onderbouwen die stelling. Gedetailleerde waarnemingen van het ISM in dEs openen een nieuwe manier om deze belangrijke klasse van sterrenstelsels te bestuderen.

8.5 Verder onderzoek

8.5.1 Waarnemingen

Van de 15 dEs uit het Large Programme waarvoor we reeds fotometrie en nabij-infra-rode spectra hebben, worden momenteel optische spectra waargenomen met de VLT. Met behulp van deze spectra zullen we de leeftijden en metalliciteiten van deze dEs kunnen bepalen en zo hopelijk meer leren over de manier waarop ze gevormd zijn. Bovendien kunnen de metalliciteiten, geschat uit optische en nabij-infrarode spectra, met elkaar vergeleken worden.

Het Marie-Curie Training Network MAGPOP, waarvan ik de komende twee jaren deel van zal uitmaken, zal een dwerggalaxie-survey uitvoeren in de noordelijke hemelsfeer. Deze waarnemingen omvatten (onder andere) optische en nabij-infrarode fotometrie en spectroscopie.

8.5.2 Simulaties

We hebben nu de codes in handen om door ramdruk geïnduceerde stervorming te simuleren. Aangezien parameterruimte (totale dE massa, snelheid van de dE door het ICM, eigenschappen van het ICM) zeer uitgebreid is, is het nuttig deze simulaties op een parallelle computer uit te voeren. Tijdens een werkbezoek aan het Edinburgh Parallel Computing Centre, in kader van HPC-Europa, werden de uitbreidingen voor de seriële HYDRA code die in dit werk beschreven worden, geïmplementeerd in de parallelle versie. Gedurende de komende maanden zal de parameterruimte onderzocht kunnen worden.

Chapter 9

Summary

9.1 Introduction

Dwarf elliptical galaxies (dEs) are faint, diffuse galaxies. They are gas-less systems, mainly observed in groups and clusters of galaxies and constitute the most abundant class of galaxies in the nearby universe. Despite their plenitude, we still do not fully understand the mechanisms that govern the formation and evolution of these galaxies. In the course of the years it has become clear that dEs are not the simple systems they were assumed to be. In the *Cold Dark Matter* picture of galaxy formation, ever larger structure are formed by hierarchical merging. In this theory, dwarf galaxies are among the first objects formed and they are thought to be the fundamental building blocks of larger galaxies, such as our own Milky Way. Therefore, studying the formation and evolution of dEs is important for our understanding of the formation and evolution of large galaxies.

Currently, three formation scenarios for dEs are in vogue. The *wind model* posits that dEs are primordial objects having survived the hierarchical merging. In this scenario, a supernova-driven *galactic wind* develops after the first burst of star formation, sweeping out the gas from the galaxy. The loss of a substantial part of the gas has a dynamical effect on the low-mass system, leaving a diffuse object.
The overwhelming presence of dEs in groups and clusters suggests that the environment plays an important role in the formation and evolution of dEs. The *harassment model* considers the transformation of a small spiral galaxy into a dE through repeated interactions with giant cluster members. The interstellar medium is rapidly pushed out by the *ram pressure* of the hot, dilute intracluster medium, leaving a gas-less dwarf.
Finally, observations of transient galaxies belonging to neither the dEs, nor the gas-rich/starforming irregular dwarfs (Irrs), lead to the *fading model*. This model suggests that present-day Irrs can evolve into dEs, once the gas reservoir is used up in star formation (possibly helped by galactic winds or ram pressure), and the young stellar population fades.

During the last two decennia more and more studies about dEs have been conducted, inspired on the one hand by the coming of the 8-meter class telescopes, so that detailed observations of these faint galaxies is feasible, and on the other hand by the ever increasing computing power, so that numerical simulations are ever more realistic. Recent observations show that a significant part of galaxies classified as dE, contain an interstellar medium (ISM). The goal of this work is to investigate in detail the ISM in dEs, observationally as well as numerically.

9.2 Observations

The astronomical research group in Ghent has played an important role in an ESO Large Programme on the dynamics of dEs, consuming 28 nights of observing time with the VLT in Chile. Both optical imaging as near-infrared spectroscopy was obtained for a sample of 15 dEs in the Fornax Cluster and in three southern groups. From the imaging, structural parameters of the dEs were compiled, while the spectra, containing the strong Calcium II Triplet (CaT) absorption lines, were used to extract kinematical data.

In chapter 2, the structural parameters of dEs from our and other recently compiled dE samples are compared to those of normal elliptical galaxies (Es). It is shown that dEs do not follow the same classical relations for Es, although there is a continuous sequence going from Es down to dEs. This sequence coincides with predictions from cosmological simulations of galaxy formation, explicitly including the dynamical response of stellar feedback. Although this result pleas for the wind model as formation scenario for dEs, we cannot exclude the harassment model. Observations of dEs with significant rotation and of spiral and disk structures in dEs support the harassment theory.

The depth of the CaT absorption lines also tells us something about the stellar populations in dEs. For individual stars and for globular clusters, the CaT lines are excellent metallicity estimators. However, for elliptical galaxies the situation is quite different. Recent observations have shown that the strength of the CaT anti-correlates with the velocity dispersion σ, while other metallicity indicators are known to correlate with σ. In chapter 3 we show that the observed anti-correlation of CaT with σ continues down to the dE regime. Comparison with population synthesis predictions to earlier photometric and optical spectroscopic data point to a metal-poor stellar population in dEs. The large CaT values for 12 of our 15 dEs are in contradiction with them having a metal-poor stellar population. Although these results clearly show that we do not yet understand the behaviour of the CaT, they also show that morphologically similar dEs with chemically different stellar populations exist.

In two of the Large Programme dEs, Hα emission had been detected in an earlier survey, indicating the presence of ionized hydrogen (H II). Since these previous observations did not contain spatial information, Hα narrowband images were taken of these galaxies. Both contain a nuclear emission peak, but in FCC046 six emission blobs pointed to possible recent star formation. The observed H-Passchen absorption strengthened this suggestion (chapter 3). Since dEs are predicted to contain an old, metal-poor stellar population, we were granted time to observe three more dEs with detected H II. These observations are presented in section 4.2 of chapter 4. The dEs contain a few 100 to 1000 solar masses in ionized hydrogen. Two of them show evidence for recent star formation, in the form of complex gas structures and individual emission clouds. The exact ionization mechanisms can only be assessed via detailed spectroscopic observations.

Finally we used the Australian Telescope Compact Array (ATCA) to search for the presence of neutral hydrogen (H I) in two dEs. In section 4.3 we show that both galaxies contain H I. The H I masses of 2×10^7 and 5×10^7 $M_\odot$ are comparable to those of gas-rich Irrs of the same luminosity.

9.3 Numerical simulations

Because no code was available to simulate the formation and evolution of galaxies, we started from the publicly available HYDRA code (chapter 5). This is a Lagrangian particle code that follows the evolution of the particles under influence of gravitational and (in case of gas particles) hydrodynamical forces. The gravitational forces are implemented using an adaptive particle-particle particle-mesh technique, while the hydrodynamical forces are described using smoothed particle hydrodynamics. The Lagrangian character of the code implies that it is independent of the geometry of the problem under study. Moreover, the particle formalism allows star formation and feedback to be implemented in a relatively simple way.

The fact that dEs are predominantly observed in groups and clusters of galaxies suggests that the environment plays an important role in the evolution of a dwarf galaxy. The hot, dilute intracluster medium (ICM) induces a *ram pressure* on the interstellar medium (ISM) in the galaxy. Since dwarf galaxies have a shallow gravitational potential, they are more sensitive to ram pressure than normal galaxies. In chapter 6 we simulate the evolution of a gas-rich dE that moves through the ICM. We show that small dEs indeed lose their ISM instantaneously. Massive dEs however can retain part of their ISM, even over longer time spans. The choice of the initial conditions of the ISM plays an important role in the prediction of those timescales. Finally, the higher density and pressure in the shock front could induce star formation during the ram pressure phase. This second stellar population would then be younger and more metal-rich than the old, metal-poor underlying stellar population. This could lead to the observed differences in chemical composition of dEs.

Isolated dEs are presumed to have lost their gas in a galactic wind. The mass resolution of present-day numerical simulations cannot follow star formation in detail - presuming we should know all the details involved. Therefore star formation is implemented by converting gas particles into star particles if certain conditions are fulfilled. One assumes that star formation proceeds in molecular clouds, represented by cold and dense gas particles. A star particle actually represents a stellar population of a few thousand solar masses. The star particles feed back energy and heavy elements as part of the stars explode as supernovae. In chapter 7 we studied the parameters involved in the implementation of star formation and feedback processes in numerical simulations. Since dwarf galaxies are very sensitive to the feedback process, they are an ideal test bench in order to refine the numerical prescriptions used in modelling star formation.
The simulations show that the galactic wind is not necessarily efficient in removing the gas from the dwarf galaxy, and that part of the gas remains to sustain star formation over a time span of several gigayears.

9.4 Conclusions

We are of course still far away from the complete understanding of formation and evolution of dEs. However it is becoming clear that the dE class is not a homogeneous one. Several formation scenarios and evolutionary paths lead to morphologically and kinematically similar, but maybe chemically distinct objects.

Numerical simulations show that in all different scenarios, some dEs retain part of their ISM over long timescales. More and more observations of gas in dwarfs classified as dEs corroborate this theory. Detailed observations of the ISM in dEs could open a complete new window in the study of this important class of galaxies.

Chapter 10

Future projects

10.1 Observations

We have currently several proposals on dEs, dwarf spirals and BCDs that are accepted on the VLT, NTT and ATCA telescopes.

10.1.1 Stellar populations of dEs

Since the wind model predicts that dEs are old and metal-poor objects, while in the harassment model dEs will host a younger, more metal-rich (sub)population, it is clear that information on the ages, the metallicities and the chemical evolution of dEs is necessary to solve the problem of the origin of dEs.

We will obtain optical spectra of the dEs observed during the Large Program in which our research group was involved, with the objective to derive their ages and metallicities from comparison with population synthesis model spectra. We have been granted 21 hours of VLT+FORS2 time to observe 7 dEs in Southern groups (the NGC3285, NGC5044 and NGC5898 groups), during P75. Another 29 hours were granted for the 9 Fornax dEs during the next semester (P76). We will also request time for similar observations of Virgo dEs on the Russian 6m telescope with the same research team, including S. De Rijcke, H. Dejonghe (Ghent University, Belgium), P. Prugniel (Observatoire de Lyon, France), I. Ferreras (University College London, UK), W.W. Zeilinger (Vienna University, Austria), A. Pasquali (ETH Zurich, Switserland) and V. Debattista (University of Washington, USA). The questions we want to address are described below.

Ages and metallicities of dEs

Up to now, little is known about the ages and metallicities of the stellar populations of dEs. Early spectroscopic and photometric data on Fornax dEs confirm they are old and metal-poor objects (Held & Mould, 1994), as predicted by the wind model for dE formation. On the other hand, recent data on Virgo dEs show a larger range of metallicities, even up to solar (van Zee et al., 2004), as predicted by the harassment model. Moreover, the data suggest that round dEs are more metal-rich than flattened ones (Barazza & Binggeli, 2002). It remains unclear which mechanisms, internal or external, govern the evolution of dEs in the Fornax and Virgo clusters to produce morphological similar, but chemically distinct objects.

Comparing the observed spectra to recent population synthesis model spectra, we can compare the ages and metallicities of dEs in different environments (groups, Virgo and Fornax cluster) to the predictions from the different formation models.

The Calcium puzzle

As discussed in chapter 3, the strength of the Calcium II Triplet (CaT) absorption lines anti-correlates with velocity dispersion in ellipticals, in dwarf ellipticals and in bulges of spirals. This is surprising since other metallicity indicators, such as Fe and Mg are known to correlate with velocity dispersion. Moreover, the measured CaT strengths in Es are lower than predicted by population synthesis models, while we found the CaT in dEs to be stronger than expected for metal-poor objects. To complete the Calcium puzzle, it was recently discovered that for Es in different environments, systematic differences exist between the blue Ca4227 and the CaT lines (Cenarro et al., 2004).

Combining the optical and near-infrared spectra, we can compare the Calcium lines around 4227 Å and 8600 Å to investigate this Calcium puzzle.

The nuclei of dEs

Some dEs have an unresolved central intensity peak, and are therefore named *nucleated dEs* or dE.Ns. The origin of these nuclei is still unclear. The off-centered nuclei of some dEs suggest that they are formed by infall from globular clusters (Lotz et al., 2001), although instabilities can also trigger the displacement of the nucleus (De Rijcke & Debattista, 2004).

The spectra of the nucleated dEs of our sample are of sufficiently high signal-to-noise so that we can study the properties of the nucleus and the host galaxy separately. Thus we can compare the stellar populations of the nucleus and the host galaxy in dE.Ns. It will be the first time that such data is obtained for dEs outside the Local Group.

10.1.2 MAGPOP International Time

International time on the La Palma telescopes has been granted to a project from the MAGPOP Network. A sample of dwarfs, dEs, dIrrs and BCDs, will be studied in the Virgo Cluster and in the field. This project was initiated by R. Peletier (Univ. Groningen), and will be carried out by the MAGPOP network.

10.1.3 The faint end of the Tully-Fisher relation

Since in the harassment model, dEs stem from small late-type galaxies that are transformed into dEs through frequent interactions with giant cluster members. They are expected to still retain some signatures of their past, such as rotation or embedded stellar disks (De Rijcke et al., 2003a). Therefore, the properties of late-type dwarf galaxies can hold important information on the possible progenitors of dEs.

In the validation of cosmological models describing the formation and evolution of galaxies, the Tully-Fisher relation plays a prominent role (Verheijen, 2001). However, very little is known about the Tully-Fisher relation for dwarf spiral galaxies. From the scarce data available, they appear to deviate from the known Tully-Fisher relation for bright spirals (Pierini, 1999). Therefore we are planning to take BVI broadband photometry of 15 dwarf spirals with EMMI mounted on the ESO-NTT, which in combination with H I observations with the ATCA will allow us to investigate the properties of late-type dwarf galaxies.

This work is done in collaboration with P. Buyle and S. De Rijcke (Ghent University, Belgium).

10.2 Simulations

On the theoretical side, the N-body/SPH code described in this work will be used to simulate the formation of dEs in different environments, in order to quantify the effects of internal and external agents on the evolution of dEs. The code is based on the publicly available HYDRA code and includes star formation, supernova feedback and chemical evolution.

10.2.1 High performance computing

Up to now, detailed simulations of the formation of dEs (including star-formation, supernova feedback and chemical evolution) only considered isolated dEs (Mori et al., 1999; Carraro et al., 2001). However, it is assumed that the environment plays an important role in the evolution of dEs. On the one hand, the thermal pressure of the hot ICM will confine the ISM within the galaxy, thereby increasing the density and hence the star formation rate. On the other hand, the ram-pressure of the ICM can strip a light-weight dE from its ISM, thereby truncating the star formation process (Mori & Burkert, 2000). Including an ICM in the N-body/SPH simulations is not a trivial task, since the simulation box has to be "filled" with ICM particles, which drastically increases the number of simulated particles. As shown in chapters 7 and 6, the HYDRA code was adapted to include star formation and feedback, and to simulate ram-pressure stripping of dEs within an ICM (Michielsen et al., 2004b). To quantify the effects of the ICM on the evolution of dEs with different initial masses, a parameter space of ICM temperatures and densities, and dE velocities through the ICM will be explored. These simulations will be run on the parallel computer at the Edinburgh Parallel Computing Centre. During an HPC-Europa Transnational Access Research Visit to the Institute for Astronomy in Edinburgh, the extentions to the serial HYDRA code that are described in chapters 6 and 7 were incorporated in the OpenMP version of HYDRA (Rob Thacker, private communication), and access to the SUN supercomputer is provided during the coming months.

10.2.2 The metallicity-flattening relation for dEs

Barazza & Binggeli (2002) suggest that ellipticity is the driving parameter which governs metallicity in dEs. Such a metallicity-flattening relation for dEs is not implausible since the outflow of metal-enriched gas is preferentially occurring along the minor axis, rendering ellipticity a critical parameter for the metallicity of present-day dwarfs (De Young & Heckman, 1994). Using initial conditions of different ellipticities and different spin parameters we can numerically verify this conjecture. Sander Valcke will perform the simulations and analysis for his Master's thesis.

10.2.3 The evolution of BCDs

The possible evolutionary link between BCDs, dIrrs and dEs is still a matter of debate (van Zee et al., 2001). One of the proposed scenarios for dE formation is the fading of present-day BCDs into dEs. We will use the N-body/SPH code described in this work to follow the evolution of a BCD, and see if its properties evolve into something dE-like.

Detailed observations of the stellar and gas components of BCDs allow us to construct realistic initial conditions for the simulations. The dark matter distribution follows from dynamical modeling, which will be carried out by S. De Rijcke. To perform this modeling, we already obtained optical imaging and

spectra with FORS2, and near-infrared imaging of two BCDs with ISAAC, mounted on the VLT.ling, we already obtained optical imaging and spectra with FORS2, and near-infrared imaging of two BCDs with ISAAC, mounted on the VLT.

From the dynamical modeling of the BCD data, combined with published HI and Halpha maps and kinematics van Zee et al. (2001), we can construct realistic initial conditions for N-body/SPH simulations of the future evolution of BCDs, without assuming a priori that the outcome should resemble any present-day galaxy population such as dEs.ling of the BCD data, combined with published HI and Halpha maps and kinematics van Zee et al. (2001), we can construct realistic initial conditions for N-body/SPH simulations of the future evolution of BCDs, without assuming a priori that the outcome should resemble any present-day galaxy population such as dEs.

10.2.4 Modeling ram pressure stripping

Depending on the implementation of the hydrodynamical equations, ram-pressure stripping has been simulated using SPH, grid and sticky particle codes. In order to compare the strengths and weaknesses of each approach, I will collaborate with E. Roediger (University of Bremen, Germany) and B. Vollmer (Strassbourg University, France) who use grid and sticky particle codes respectively (Roediger & Hensler, 2005; Vollmer et al., 2001), to run simulations of ram-pressure stripping with exactly the same initial conditions.

Part IV

Appendices

Appendix A

The Fast Fourier Transform

In this appendix, we demonstrate that using the Fast Fourier Transform reduces the computational cost of evaluating the gravitational potential on a one-dimensional mesh with N cells from $O(N^2)$ to $O(N \log_2(N))$, with the only constraint that the number of cells needs to be a power of 2: $N = 2^m$. First we introduce the discrete Fourier transform and some of its properties. Then the Fast Fourier Transform algorithm is explained and we will see how it reduces the number of computations needed to evaluate the gravitational potential.

A.1 The discrete Fourier transform

Discrete Fourier transforms share many of the properties of continuous Fourier transforms. Later on, we will need the notions of an inverse discrete Fourier transform and a discrete Fourier convolution. Therefore, after giving its definition, we will prove two theorems connected to the discrete Fourier transform.

A.1.1 Definition

If $\{x_k | k = 0, \ldots, N-1\}$ is a set of N real numbers, the discrete Fourier transform of this set is defined as the set $\{\hat{x}_p | p \in \mathbb{Z}\}$:

$$\hat{x}_p = \frac{1}{\sqrt{N}} \sum_{k=0}^{N-1} x_k e^{-\frac{ipk2\pi}{N}}. \tag{A.1}$$

It is immediately clear that the discrete Fourier transform is periodic with period N, since

$$\hat{x}_{p+N} = \frac{1}{\sqrt{N}} \sum_{k=0}^{N-1} x_k e^{-\frac{ipk2\pi}{N}} e^{-ik2\pi} = \frac{1}{\sqrt{N}} \sum_{k=0}^{N-1} x_k e^{-\frac{ipk2\pi}{N}} = \hat{x}_p. \tag{A.2}$$

A.1.2 The discrete Fourier transform theorem

If the set of numbers $\hat{x}_p$ is defined by equation (A.1)*, then*

$$x_{k'} = \frac{1}{\sqrt{N}} \sum_{p=0}^{N-1} \hat{x}_p e^{\frac{ik'p2\pi}{N}}. \tag{A.3}$$

To prove this theorem, we insert the definition for the discrete Fourier transform in the right-hand side of equation (A.3) and rearrange the sums so that:

$$x_{k'} = \frac{1}{N}\sum_{p=0}^{N-1}\sum_{k=0}^{N-1} x_k e^{-\frac{ikp2\pi}{N}} e^{\frac{ik'p2\pi}{N}} \tag{A.4}$$

$$= \frac{1}{N}\sum_{k=0}^{N-1} x_k \sum_{p=0}^{N-1} e^{-\frac{i(k-k')p2\pi}{N}}. \tag{A.5}$$

The inner sum on the right-hand side of the last equation is the finite geometric series:

$$\sum_{p=0}^{N-1} \omega_N^{(k-k')p} \tag{A.6}$$

with base $\omega_N = \exp(-i2\pi/N)$. If $k = k'$, this sums to N. For $k \neq k'$, the sum of the finite geometric series is:

$$\sum_{p=0}^{N-1} \omega_N^{(k-k')p} = \frac{\omega_N^N - \omega_N^0}{\omega_N - 1} = \frac{1-1}{\omega_N - 1} = 0, \tag{A.7}$$

which proves the theorem.

In order to prove the discrete Fourier convolution theorem, we need to extend the set $\{x_k\}$ periodically, according to the rule

$$x_{k+mN} = x_k, \forall m \in \mathbb{Z}. \tag{A.8}$$

A.1.3 The discrete Fourier convolution theorem

If 3 sets of numbers $\{x_k\}, \{y_k\}, \{z_k\}; k = 0, \ldots, N-1$ *are related via*

$$z_k = \frac{1}{\sqrt{N}} \sum_{k'=0}^{N-1} y_{(k-k')} x_{k'}, \tag{A.9}$$

then their discrete Fourier transforms are related in the following way:

$$\hat{z}_p = \hat{y}_p \hat{x}_p. \tag{A.10}$$

To proof this theorem, we again take the discrete Fourier transform of both sides and rewrite

$$e^{-\frac{ikp2\pi}{N}} = e^{-\frac{i(k-k')p2\pi}{N}} e^{-\frac{ik'p2\pi}{N}}, \tag{A.11}$$

so that equation (A.9) reads:

$$\hat{z}_p = \frac{1}{\sqrt{N}}\sum_{k=0}^{N-1}\frac{1}{\sqrt{N}}\sum_{k'=0}^{N-1} y_{(k-k')} x_{k'} e^{-\frac{ikp2\pi}{N}}, \tag{A.12}$$

$$= \frac{1}{\sqrt{N}}\sum_{k=0}^{N-1}\frac{1}{\sqrt{N}}\sum_{k'=0}^{N-1} y_{(k-k')} e^{-\frac{i(k-k')p2\pi}{N}} x_{k'} e^{-\frac{ik'p2\pi}{N}} \tag{A.13}$$

Now write $k'' = k - k'$ and rearrange the sums, using the periodicity of the original dataset $\{x_k\}$:

$$\begin{aligned} \hat{z}_p &= \frac{1}{\sqrt{N}} \sum_{k''=0}^{N-1} y_{(k'')} e^{-\frac{i(k'')p2\pi}{N}} \frac{1}{\sqrt{N}} \sum_{k=0}^{N-1} x_{k'} e^{-\frac{ik'p2\pi}{N}} \\ &= \hat{y}_p \hat{x}_p, \end{aligned} \tag{A.14}$$

which proves the theorem.

Symbolically, we can denote the discrete Fourier convolution z_k in the following way:

$$z_k = (y * x)_k. \tag{A.15}$$

A.2 The Fast Fourier Transform

A.2.1 Introduction

Computing the discrete Fourier convolution of two sets $\{x_k\}$ and $\{y_k\}$ involves $O(N^2)$ computations. Therefore it rapidly becomes very costly to compute the discrete Fourier convolutions for increasing values of N.

The convolution theorem suggests a different way of computing the set $\{(y * x)_k | k = 0, \ldots, N-1\}$ as the set of inverse transforms $\{\hat{y}_p \hat{x}_p | p = 0, \ldots, N-1\}$. In other words, we first compute the discrete Fourier transforms of $\{x_k\}$ and $\{y_k\}$, then compute the products $\{\hat{y}_p \hat{x}_p\}$ and finally compute the inverse Fourier transforms to obtain $\{(y * x)_k\}$. However, the obvious way to calculate the discrete Fourier transform, using equation (A.1) involves $O(N)$ multiplications, for each of the N elements of the transformed set. Thus N times two transforms, a product and an inverse transform sum up to $O(3N^2 + N) = O(N^2)$ multiplications, which is as bad (even slightly worse) as computing the discrete Fourier convolution directly.

However, the advantage of using the Fourier formalism is that there exists an algorithm that makes the computation of the Fourier transform much more efficient, reducing the calculations from $O(N^2)$ to $O(N \log_2(N))$, provided that N is a power of 2 ($N = 2^m$).[1] This algorithm is known as the Fast Fourier Transform (FFT) and was brought to the attention of many people by Cooley & Tukey (1965), but apparently the ideas where already lined out in the 19th century by Gauss, who used a FFT to interpolate the trajectories of the planetoids Pallas and Juno!

A.2.2 The Fast Fourier Transform (FFT)

To concentrate on the essentials, we ignore the normalization factors $\sqrt{1/N}$ in what follows. At the end, these can be taken into account in N multiplications. Thus, suppose that $N = 2^m$, so that $m = \log_2(N)$, and $N = 2 \cdot 2^{m-1} = 2N_1$ for $m \geqslant 1$. In the following, we will also use:

$$\omega_N = e^{-\frac{i2\pi}{N}}, \tag{A.16}$$

so that the discrete Fourier transform reads:

$$\hat{x}_p = \sum_{k=0}^{N-1} x_k \omega_N^{kp}. \tag{A.17}$$

[1] more generally, one can reduce the computational cost to $O(N \log_p(N))$, provided that $N = p^m$, with p a prime number.

Now we rewrite the discrete Fourier transform of the set $\{x_k | k = 1, \cdots, N\}$ in terms of N_1 and we split it into a sum of even and odd k:

$$\begin{aligned}
\hat{x}_p &= \sum_{k=0}^{N-1} x_k \omega_N^{kp} \\
&= \sum_{k=0}^{2N_1-1} x_k \omega_{2N_1}^{kp} \\
&= \sum_{k=0}^{N_1-1} x_{2k} \omega_{2N_1}^{2kp} + \sum_{k=0}^{N_1-1} x_{2k+1} \omega_{2N_1}^{(2k+1)p} \\
&= \sum_{k=0}^{N_1-1} x_{2k} \omega_{N_1}^{kp} + \sum_{k=0}^{N_1-1} x_{2k+1} \omega_{N_1}^{kp} \, \omega_N^p. \qquad \text{(A.18)}
\end{aligned}$$

We consider this in more detail. Suppose $0 \leqslant p < N_1$, we can write:

$$\hat{x}_p = \hat{x}_{\mathsf{even},p} + \omega_N^p \hat{x}_{\mathsf{odd},p}. \qquad \text{(A.19)}$$

Here, the discrete Fourier transforms $\hat{x}_{\mathsf{even},p}$ and $\hat{x}_{\mathsf{odd},p}$ are defined over a subset of $N_1 = 2^{m+1}$ numbers. For the second half of the transformed domain, we have that

$$\hat{x}_{p+N_1} = \hat{x}_{\mathsf{even},p+N_1} + \omega_N^{p+N_1} \hat{x}_{\mathsf{odd},p+N_1}, \qquad \text{(A.20)}$$

and from the definition of ω_N (equation (A.16), it follows that

$$\omega_{N_1}^{k(p+N_1)} = \omega_{N_1}^{kp} \text{ and } \omega_N^{p+N_1} = -\omega_N^p. \qquad \text{(A.21)}$$

Finally, we can write the 2^m Fourier transforms as $(0 \leqslant p < N_1)$:

$$\begin{aligned}
\hat{x}_p &= \hat{x}_{\mathsf{even},p} + \omega_N^p \hat{x}_{\mathsf{odd},p} \qquad \text{(A.22)} \\
\hat{x}_{p+N_1} &= \hat{x}_{\mathsf{even},p} - \omega_N^p \hat{x}_{\mathsf{odd},p}. \qquad \text{(A.23)}
\end{aligned}$$

These two formulae are essentially the same, and show that we can calculate a transform of size $N = 2^m$ in terms of two transforms of size 2^{m+1}. This way of rearranging the discrete Fourier transform is known as the Fast Fourier Transform.

A.2.3 Timing the FFT

We can now prove that a FFT over a set of N numbers can be evaluated with $O(N \log_2(N))$ computations. Let $\mu(m)$ be the number of multiplications and $\alpha(m)$ be the number of additions necessary to perform the FFT. We will use induction to prove that $\mu(m) = m2^{m-1} + 2^m$ and $\alpha(m) = m2^m$. It is clear that $\mu(0) = \alpha(0) = 0$ since no evaluations need to be done for $N = 1$:

$$\hat{x} = x \qquad \text{(A.24)}$$

For $m = 1$, we have $N = 2, N_1 = 1$, hence the even and odd number sets are singletons: $\{x_{k,\mathsf{even}}\} = \{x_0\}$ and $\{x_{k,\mathsf{odd}}\} = \{x_1\}$; and the FFT is then given as:

$$\begin{aligned}
\hat{x}_0 &= x_0 + \omega_2^0 x_1 \\
\hat{x}_1 &= x_0 - \omega_2^0 x_1, \qquad \text{(A.25)}
\end{aligned}$$

Table A.1: Timing the FFT

m	N	N^2	$N\log_2(N)$	speed gain
3	8	64	24	2.7
6	64	4096	384	10.7
9	512	262144	4609	57
12	4096	$\sim 1.7\times 10^7$	$\sim 5\times 10^4$	344
15	32768	$\sim 10^9$	$\sim 5\times 10^5$	~ 2000
18	262144	$\sim 7\times 10^{10}$	$\sim 5\times 10^6$	~ 15000

thus $\mu(1)=1$ and $\alpha(m)=2$. Now if $\mu(m)=m2^{m-1}$ and $\alpha(m)=m2^m$, then to evaluate a FFT of length 2^{m+1} we need to evaluate 2 FFTs of length 2^m, perform 2^m multiplications with $\omega^p_{2^{m+1}}$, and finally perform 2^{m+1} additions. In total this amounts to

$$\begin{aligned}\mu(m+1) &= 2\cdot\mu(m)+2^m=(m+1)2^m\\ \alpha(m+1) &= 2\cdot\alpha(m)+2^{m+1}=(m+1)2^{m+1}.\end{aligned} \tag{A.26}$$

Taking into account the normalization factors, the FFT needs only $N+3/2\,N\log_2(N)$ calculations, which is $O(N\log_2(N))$ instead of $O(N^2)$ for the direct computation of the discrete Fourier transform. In Table A.2.3, a rough estimation of the timing of the FFT is compared to the direct evaluation of the discrete Fourier convolution. The speed gain is considerably, even for small numbers.

A.3 Applications of the FFT

The Fast Fourier Transformation has quite a lot of applications, varying from signal processing, over solving coupled differential equations, to multiplying large integer numbers, and of course for solving gravity in particle-mesh N-body codes. Finally, it is good to note that different algorithms exist to implement the FFT, but they all come down to the same thing: reducing computational cost.

Appendix B

Publication list

B.1 Publications in refereed journals

Michielsen, D., De Rijcke, S., Dejonghe, H., Zeilinger, W. W., Hau, G. K. T., 2003, Ap&SS, 284, 635–638 *Hα regions in FCC046 and FCC207.*

Michielsen, D., De Rijcke, S., Dejonghe, H., Zeilinger, W. W., Hau, G. K. T., 2003, ApJ, 597, L21–L24 *The puzzlingly large Ca II triplet absorption in dwarf elliptical galaxies.*

Michielsen D., de Rijcke S., Zeilinger W. W., Prugniel P., Dejonghe H., Roberts S., 2004, MNRAS, 353, 1293–1303 *Evidence for a warm interstellar medium in Fornax dwarf elliptical galaxies -II. FCC032, FCC206 and FCCB729.*

De Rijcke, S., Michielsen D., Dejonghe H., Zeilinger W. W., Hau, G. K. T., 2005, A&A, 438, 491 *The formation and evolution of dwarf elliptical galaxies -I. Structural and kinematical properties.*

Buyle P., De Rijcke S., Michielsen D., Baes M., Dejonghe H., 2005, MNRAS, 360, 853 *The H I content of Fornax dwarf elliptical galaxies: FCC032 and FCC336.*

B.2 Other publications

De Rijcke, S., Dejonghe, H., Zeilinger, W. W., Michielsen, D., Hau, G. K. T., 2004, Astr. Nach. Supp. Issue, 325, 57 *The evolution of dwarf elliptical galaxies in a dense cluster environment.*

Michielsen, D., De Rijcke, S., Dejonghe, H., 2004, Astr. Nach. Supp. Issue, 325, 122 *N-body/SPH study of the evolution of dwarf galaxies in a cluster environment.*

Michielsen, D., De Rijcke, S., Dejonghe, H., 2005, to appear in the Proceedings of the IAU Colloquium No. 198, 2005, eds. B. Binggeli and H. Jerjen. *N-body/SPH study of the evolution of dwarf elliptical galaxies in a cluster environment.*

Bibliography

Abadi M. G., Moore B., Bower R. G., 1999, MNRAS, 308, 947
Ram pressure stripping of spiral galaxies in clusters.

Acreman D. M., Stevens I. R., Ponman T. J., Sakelliou I., 2003, MNRAS, 341, 1333
Simulations of the effects of stripping and accretion on galaxy haloes in clusters.

Aguirre A., Hernquist L., Schaye J., Katz N., Weinberg D. H., Gardner J., 2001, ApJ, 561, 521
Metal enrichment of the intergalactic medium in cosmological simulations.

Andersen R.-P., Burkert A., 2000, ApJ, 531, 296
The self-regulated evolution of dwarf galaxies.

Arimoto N., Yoshii Y., 1986, A&A, 164, 260
Photometric and chemical evolution of galaxies based on an evolutionary method of population synthesis.

Arimoto N., Yoshii Y., 1987, A&A, 173, 23
Chemical and photometric properties of a galactic wind model for elliptical galaxies.

Armandroff T. E., Zinn R., 1988, AJ, 96, 92
Integrated-light spectroscopy of globular clusters at the infrared Ca II lines.

Barazza F. D., Binggeli B., 2002, A&A, 394, L15
A metallicity-flattening relation for dwarf elliptical galaxies.

Barazza F. D., Binggeli B., Jerjen H., 2002, A&A, 391, 823
More evidence for hidden spiral and bar features in bright early-type dwarf galaxies.

Barazza F. D., Binggeli B., Jerjen H., 2003, A&A, 407, 121
VLT surface photometry and isophotal analysis of early-type dwarf galaxies in the Virgo cluster.

Barnes J., Hut P., 1986, Nature, 324, 446
A hierarchical $O(NlogN)$ force-calculation algorithm.

Barth A. J., Ho L. C., Rutledge R. E., Sargent W. L. W., 2004, ApJ, 607, 90
POX 52: A dwarf Seyfert 1 galaxy with an intermediate-mass black hole.

Bekki K., 1998, ApJ, 496, 713
The fundamental plane and merger scenario. I. Star formation history of galaxy mergers and origin of the fundamental plane.

Bekki K., Couch W. J., 2003, ApJ, 596, L13
Starbursts from the strong compression of galactic molecular clouds due to the high pressure of the intracluster medium.

Bekki K., Couch W. J., Drinkwater M. J., 2001, ApJ, 552, L105
Galaxy threshing and the formation of ultracompact dwarf galaxies.

Bekki K., Couch W. J., Drinkwater M. J., Shioya Y., 2003, MNRAS, 344, 399
Galaxy threshing and the origin of ultra-compact dwarf galaxies in the Fornax cluster.

Bender R., Burstein D., Faber S. M., 1992, ApJ, 399, 462
Dynamically hot galaxies. I- Structural properties.

Bender R., Surma P., Döbereiner S., Möllenhoff C., Madejsky R., 1989, A&A, 217, 35
Isophote shapes of elliptical galaxies. II- Correlations with global optical, radio and X-ray properties.

Berczik P., 1999, A&A, 348, 371
Chemo-dynamical smoothed particle hydrodynamics code for evolution of star forming disk galaxies.

Bica E., Alloin D., 1987, A&A, 186, 49
Near-infrared spectral properties of star clusters and galactic nuclei.

Binggeli B., Barazza F., Jerjen H., 2000, A&A, 359, 447
Off-center nuclei in dwarf elliptical galaxies.

Binggeli B., Jerjen H., 1998, A&A, 333, 17
Is the shape of the luminosity profile of dwarf elliptical galaxies an useful distance indicator?

Binggeli B., Sandage A., Tarenghi M., 1984, AJ, 89, 64
Studies of the Virgo Cluster. I- Photometry of 109 galaxies near the cluster center to serve as standards.

Binney J., Merrifield M., 1998, Princeton University Press, Princeton, New Jersey
Galactic astronomy.

Binney J., Tremaine S., 1987, Princeton University Press, Princeton, New Jersey
Galactic dynamics.

Binette L., Magris C. G., Stasińska G., Bruzual A. G., 1994, A&A, 292, 13
Photoionization in elliptical galaxies by old stars.

Blakeslee J. P., Lucey J. R., Tonry J. L., Hudson M. J., Narayanan V. K., Barris B. J., 2002, MNRAS, 330, 443
Early-type galaxy distances from the Fundamental Plane and surface brightness fluctuations.

Buonomo F., Carraro G., Chiosi C., Lia C., 2000 MNRAS, 312, 371
Galaxy formation and evolution - II. energy balance, star formation and feedback.

Burkert A., 1995, ApJ, 447, L25
The structure of dark matter haloes in dwarf galaxies.

Burstein D., Bender R., Faber S. M., Nolthenius R., 1997, AJ, 114, 1365
Global relationships among the physical properties of stellar systems.

Buson L. M., Sadler E. M., Zeilinger W. W., Bertin G., Bertola F., Danzinger J., Dejonghe H., Saglia R. P., de Zeeuw P. T., 1993, A&A, 280, 409
The distribution of ionized gas in early-type galaxies.

Butcher H., Oemler A., 1978, ApJ, 219, 18
The evolution of galaxies in clusters. I- ISIT photometry of C1 0024+1654 and 3C 295.

Buyle P., De Rijcke S., Michielsen D., Baes M., Dejonghe H., 2005, MNRAS, 360, 853
The H I content of Fornax dwarf elliptical galaxies: FCC032 and FCC336.

Caldwell N., Bothun G. D., 1987, AJ, 94, 1126
Dwarf elliptical galaxies in the Fornax cluster. II - Their structure and stellar populations.

Calzetti D., Harris J., Gallagher J. S., Smith D. A., Conselice C. J., Homeier N., Kewley L., 2004, AJ, 127, 1405
The ionized gas in local starburst galaxies: Global and small-scale feedback from star formation.

Capaccioli M., Caon N., D'Onofrio M., 1992, MNRAS, 259, 323
Families of galaxies in the $\mu(e) - R(e)$ plane.

Carraro G., Chiosi C., Girardi L., Lia C., 2001, MNRAS, 327, 69
Dwarf elliptical galaxies: structure, star formation and colour-magnitude diagrams.

Carraro G., Lia C., Chiosi C., 1998, MNRAS, 297, 1021
Galaxy formation and evolution - I. The Padua tree-sph code (pd-sph).

Cayatte V., Kotanyi C., Balkowski C., van Gorkom J. H., 1994, AJ, 107, 1003
A very large array survey of neutral hydrogen in Virgo Cluster spirals. 3: Surface density profiles of the gas.

Cellone S. A., Buzzoni A., 2001, A&A, 369, 742
On the shape of luminosity profiles of dwarf galaxies as a distance indicator: The NGC 5044 Group revisited

Cellone S. A., Forte J. C., 1996, ApJ, 461, 176
Washington photometry of low surface brightness dwarf galaxies in the Fornax Cluster: Constraints on their stellar populations.

Cenarro A. J., Cardiel N., Gorgas J., Peletier R. F., Vazdekis A., Prada F., 2001, MNRAS, 326, 959
Empirical calibration of the near-infrared Ca II triplet - I. The stellar library and index definition.

Cenarro A. J., Gorgas J., Cardiel N., Vazdekis A., Peletier R. F., 2002, MNRAS, 329, 863
Empirical calibration of the near-infrared Ca II triplet - III. Fitting functions.

Cenarro A. J., Gorgas J., Vazdekis A., Cardiel N., Peletier R. F., 2003, MNRAS, 339, L12
Near-infrared line-strengths in elliptical galaxies: evidence for initial mass function variations?

Cenarro A. J., Sanchez-Blasquez, Cardiel N., Gorgas J., 2004, ApJ, 614, L101
Early-type galaxies in the Coma Cluster: A new piece in the Calcium puzzle.

Chiappini C., Matteucci F., Padoan P., 2000, ApJ, 528, 711
The chemical evolution of the Galaxy with variable initial mass functions.

Chiosi C., Bressan A., Portinari L., Tantalo R., 1998, A&A, 339, 355
A new scenario of galaxy evolution under a universal initial mass function.

Chiosi C., Carraro G., 2002, MNRAS, 335, 335 (CC02)
Formation and evolution of elliptical galaxies.

Cohen J. G., 1979, ApJ, 228, 405
Observations and interpretations of radial gradients of absorption features in galaxies.

Conselice C. J., Gallagher J. S., Wyse R. F. G., 2001, ApJ, 559, 791
Galaxy populations and evolution in clusters. I. Dynamics and the origin of low-mass galaxies in the Virgo Cluster.

Conselice C. J., Gallagher J. S., Wyse R. F. G., 2003, AJ, 125, 66
Galaxy populations and evolution in clusters. IV. Deep H I observations of dwarf elliptical galaxies in the Virgo Cluster.

Conselice C., O'Neil K., Gallagher J. S., Wyse R. F. G., 2003, ApJ, 591, 167
Galaxy populations and evolution in clusters. III. The origin of low-mass galaxies in clusters: Constraints from stellar populations.

Cooley J. W., Tukey J. W., 1965, Mathematics of Computation, 19, 297
An algorithm for the machine calculations of complex Fourier series.

Couchman H. M. P., 1991, ApJ, 368, L23
Mesh-refined P3M - A fast adaptive N-body algorithm

Couchman H. M. P., Thomas P. A., Pearce F. R., 1995, ApJ, 452, 797
Hydra: an Adaptive-Mesh Implementation of P3M-SPH

Dantas C. C., Capelato H. V., Ribeiro A. L. B., de Carvalho R. R., 2003, MNRAS, 340, 398
'Fundamental Plane'-like relations from collisionless stellar dynamics: a comparison of mergers and collapses.

David I. P., Forman W., Jones C., 1990, ApJ, 359, 29
The evolution of the interstellar medium in elliptical galaxies. I- The early wind phase.

de Avillez M. A., Berry D. L., 2001, MNRAS, 328, 708
Three-dimensional evolution of worms and chimneys in the Galactic disc.

Dekel A., Silk J., 1986, ApJ, 303, 39
The origin of dwarf galaxies, cold dark matter, and biased galaxy formation.

De Rijcke S., Debattista V. P., 2004, ApJ, 603, L25
The counterstreaming instability in dwarf elliptical galaxies with off-center nuclei.

De Rijcke S., Dejonghe H., Zeilinger W. W., Hau G. T. K., 2003a, A&A, 400, 119
Embedded disks in Fornax dwarf elliptical galaxies.

De Rijcke S., Zeilinger W. W., Dejonghe H., Hau G. T. K., 2003b, MNRAS, 339, 225
Evidence for a warm interstellar medium in the Fornax dwarf ellipticals FCC046 and FCC207.

De Rijcke S., Dejonghe H., Zeilinger W. W., Hau G. K. T., 2001, ApJ, 559, L21
The dynamics of the dwarf elliptical galaxy FS 76: Bridging the kinematic dichotomy between elliptical and dwarf elliptical galaxies.

De Young D. S., Heckman, T. M., 1994, ApJ, 431, 598
The effect of central starbursts on the interstellar medium of dwarf galaxies.

Djorgovski S., Davis M., 1987, ApJ, 313, 59
Fundamental properties of elliptical galaxies.

Dressler A., 1980, ApJ, 236, 351
Galaxy morphology in rich clusters - Implications for the formation and evolution of galaxies.

Dressler A., Faber S. M., Burstein D., Davies R. L., Lynden-Bell D., Terlevich R., Wegner G., 1987, ApJ, 313, L37
Spectroscopy and photometry of elliptical galaxies. - A large-scale streaming motion in the local universe.

Drinkwater M. J., Gregg M. D., Holman B. A., Brown M. J. I., 2001, MNRAS, 326, 1076
The evolution and star formation of dwarf galaxies in the Fornax Cluster.

Drinkwater M. J., Hardy E. 1991, AJ, 101, 94
Extreme blue compact dwarf galaxies in the Virgo Cluster.

Duc P.-A., Bournaud F., Masset F., A&A, 427, 803
A top-down scenario for the formation of massive tidal dwarf galaxies.

Faber S. M. & Jackson R. E., 1976, ApJ, 204, 668
Velocity dispersions and mass-to-light ratios for elliptical galaxies.

Falcón-Barroso J., Peletier R. F., Vazdekis A., Balcells M., 2003, ApJ, 588, L17
The near-infrared Ca II triplet-σ relation for bulges of spiral galaxies.

Farouki R., Shapiro S. L., 1980, ApJ, 241, 928
Computer simulations of environmental influences on galaxy evolution in dense clusters. I - Ram-pressure stripping.

Ferguson H. C., 1989, AJ, 98, 367
Population studies in groups and clusters of galaxies. II - A catalog of galaxies in the central 3.5 deg of the Fornax Cluster.

Ferguson H. C., Binggeli, B., 1994, A&ARv, 6, 67
Dwarf elliptical galaxies.

Ferguson H. C., Sandage A., 1990, AJ, 101, 765
Population studies in groups and clusters of galaxies. III- A catalog of galaxies in five nearby groups.

Ferrara A., Tolstoy E., 2000, MNRAS, 313, 291
The role of stellar feedback and dark matter in the evolution of dwarf galaxies.

Fish R. A., 1963, AJ, 68, 72
Significance of a luminosity concentration law in elliptical galaxies.

Fish R. A., 1964, ApJ, 139, 284
A mass-potential relationship in elliptical galaxies and some inferences concerning the formation and evolution of galaxies.

Forman W., Jones C., 1982, ARA&A, 20, 547 *X-ray-imaging observations of clusters of galaxies.*

Freedman W. L., Madore B. F., Gibson B. K., Ferrarese L., Kelson D. D., Sakai S., Mould J. R., Kennicutt R. C. Jr., Ford H. C. et al., 2001, ApJ, 553, 47
Final results from the Hubble Space Telescope key project to measure the Hubble constant.

Friedli D., Benz W., 1995, A&A, 301, 649
textslSecular evolution of isolated barred galaxies. II. Coupling between stars and interstellar medium via star formation.

Fontana A., Donnarumma I., Vanzella E., Giallongo E., Menci N., Nonino M., Saracco P., Cristiani S., D'Odorico S., Poli F., 2003, ApJ, 593, L9
The assembly of massive galaxies from near-infrared observations of the Hubble Deep Field South.

Forbes D. A., Ponman T. J., Brown R. J. N., 1998, ApJ, 508, L43
Dependence of the Fundamental Plane scatter on galaxy age.

Fujita Y., Nagashima M., 1999, ApJ, 516, 619
Effects of ram pressure from the intracluster medium on the star formation rate of disk galaxies in clusters of galaxies.

Gaetz T. J., Salpeter E. E., Shaviv G., 1987, ApJ, 316, 530
Gasdynamical stripping of elliptical galaxies.

García-Vargas M. L., Mollá M., Bressan A., 1998, A&AS, 130, 513
Calcium triplet synthesis.

Gavazzi G., Cortese L., Boselli A., Iglesias-Paramo J., Vílchez J. M., Carrasco L., 2003, ApJ, 597, 210
Capturing a star formation burst in galaxies infalling onto the cluster A1367.

Gavazzi G., Boselli A., van Driel W., O'Neil K., 2005, A&A, 429, 439
Completing H I observations of galaxies in the Virgo cluster.

Gebhardt K., Rich R. M., Ho L. C., 2002, ApJ, 578, L41
A 20,000 $M_\odot$ black hole in the stellar cluster G1.

Geha M., Guhathakurta P., van der Marel R. P., 2003, AJ, 126, 1794 (G03)
Internal dynamics, structure and formation of dwarf elliptical galaxies. II. Rotating versus nonrotating dwarfs.

Gerhard O. E., 1993, MNRAS, 265, 213
Line-of-sight velocity profiles in spherical galaxies: breaking the degeneracy between anisotropy and mass.

Gerritsen J. P. E., Icke V., 1997, A&A, 325, 972
Star formation in N-body simulations. I. The impact of the stellar ultraviolet radiation on star formation.

Gerssen J., van der Marel R. P., Gebhardt K., Guhathakurta P., Peterson R. C., Pryor C., 2002, AJ, 124, 3270
HST evidence for an intermediate-mass black hole in the globular cluster M15. II. Kinematic analysis and dynamical modeling.

Gnedin O. Y., Zhao H.-S., Pringle J. E., Fall S. M., Livio M., Meylan G., 2002, ApJ, 568, L23
The unique history of the globular cluster ω Centauri.

Gisler G. R., 1976, A&A, 51, 137
The fate of gas in elliptical galaxies and the density evolution of radio sources.

Goto T., Yamauchi C., Fujita Y., Okamura S., Sekiguchi M., Smail I., Bernardi M., Gomez P. L., 2003, MNRAS, 346, 601
The morphology-density relation in the Sloan Digital Sky Survey.

Gradshteyn I. S., Ryzhik I. M., 1965, Academic Press, New York
Table of integrals, series and products.

Graham A. W., Jerjen H., Guzmán R., 2003, AJ, 126, 1787
Hubble Space Telescope detection of spiral structure in two Coma Cluster dwarf galaxies.

Graham A. W., Guzmán R., 2003, AJ, 125, 2936
HST photometry of dwarf elliptical galaxies in Coma, and an explanation for the alleged structural dichotomy between dwarf and bright elliptical galaxies.

Grebel E. K., 2000, in Star formation from the small to the large scale, ESLAB symposium. Eds.: F. Favata, A. Kaas, and A. Wilson, p. 87
The star formation history of the Local Group.

Grebel E. K., Gallagher J. S., Harbeck D., 2003, ApJ, 125, 1926
The progenitors of dwarf spheroidal galaxies.

Gunn J. E., Gott J. R. I., 1972, ApJ, 176, 1
On the infall of matter into clusters of galaxies and some effects on their evolution.

Guzmán R., Lucey J. R., Bower R. G., 1993, MNRAS, 265, 731
The fundamental relations of elliptical galaxies.

Guzmán R., Graham A. W., Matkovic A., Vass I., Gorgas J., Cardiel N., 2003, "Star Formation Through Time", ASP Conf. Proc., Vol. 297, ed. Perez E., Gonzalez Delgado R. M., Tenorio-Tagle G.
The fundamental properties of dwarf elliptical galaxies in clusters.

Held E. V., de Zeeuw T., Mould J., Picard A., 1992, AJ, 103, 851
Internal dynamics of the dwarf elliptical NGC185.

Held E. V., Mould J. R., 1994, AJ, 107, 1307
Spectroscopy of dwarf elliptical galaxies in the Fornax cluster.

Hernquist L., 1992, ApJ, 400, 460
Structure of merger remnants. I- Bulgeless progenitors.

Hernquist L., Katz N., 1989, ApJS, 70, 419
TREESPH - A unification of SPH with the hierarchical tree method.

Hernquist L., Spergel D. N., Heyl J. S., 1993, ApJ, 416, 415
Structure of merger remnants. III. Phase-space constraints.

Hockney R. W., Eastwood J. W., 1987, Adam Hilger, Bristol
Computer simulations using particles.

Hubble E. P., 1925, ApJ, 62, 409
NGC6822, a remote stellar system.

Hubble E. P., 1926a, ApJ, 63, 236
A spiral nebula as a stellar system: Messier 33.

Hubble E. P., 1926b, ApJ, 64, 321
Extragalactic nebulae.

Hut, P., Makino, J., 1999, Science, 283, 501
Astrophysics on the GRAPE family of special-purpose computers.

Idiart T. P., Thevenin F., de Freitas Pacheco J. A., 1997, AJ, 113, 1066
The infrared Ca II triplet as a metallicity indicator of stellar populations.

Jerjen H., 2003, A&A, 398, 63
Surface brightness fluctuation distances for dwarf elliptical galaxies in the Fornax cluster.

Jerjen H., Binggeli B., Barazza F. D., 2004, AJ, 127, 771
Distances, metallicities and ages of dwarf elliptical galaxies in the Virgo Cluster from surface brightness fluctuations.

Jerjen H., Kalnajs A., Binggeli B., 2000, A&A, 358, 845
IC3328: A "dwarf elliptical galaxy" with spiral structure

Jones C., Forman W., 1999, ApJ, 511, 65 *Einstein Observatory images of clusters of galaxies.*

Katz N., 1992, ApJ, 391, 502
Dissipational galaxy formation. II - Effects of star formation.

Katz N., Weinberg D. H., Hernquist L., 1996, ApJS, 105, 19
Cosmological simulations with TreeSPH.

Kawata D., 1999, PASJ, 51, 931
Galaxy Formation from a low-spin density perturbation in a CDM universe.

Kawata D., 2001, ApJ, 558, 598 (K01)
Effects of type II and type Ia supernovae feedback on the chemodynamical evolution of elliptical galaxies.

Kawata D., Gibson B. K., 2003, MNRAS, 340, 908
GCD+: a new chemodynamical approach to modelling supernovae and chemical enrichment in elliptical galaxies.

Kay S. T., Pearce F. R., Frenk C. S., Jenkins A., 2002, MNRAS, 330, 113
Including star formation and supernova feedback within cosmological simulations of galaxy formation.

Kenney J. D. P., van Gorkom J. H., Vollmer B., 2004, AJ, 127, 3361
VLA H I observations of gas stripping in the Virgo Cluster spiral NGC 4522.

Kennicutt R. C., 1983, ApJ, 272, 54
The rate of star formation in normal disk galaxies.

Kim D., 1989, ApJ, 346, 653
Interstellar matter in early-type galaxies - Optical observations.

King I.R., 1966, AJ, 71, 64
The structure of star clusters. III. Some simple dynamical models.

Klypin A., Kravtsov A. V., Bullock J. S., Primack J. R., 2001, ApJ, 554, 903
Resolving the structure of cold dark matter halos

Knezek P. M., Sembach K. R., Gallagher J. S., 1999, ApJ, 514, 119
Evolutionary status of dwarf "transition" galaxies.

Kobayashi C., 2004, MNRAS, 347, 740
GRAPE-SPH chemodynamical simulation of elliptical galaxies - I. Evolution of metallicity gradients.

Kormendy J., 1977, ApJ, 218, 333
Brightness distributions in compact and normal galaxies. II- Structure parameters of the spheroidal component.

Kroupa P., 1998, MNRAS, 300, 200
The dynamical evolution of stellar superclusters.

Kroupa P., Tout C. A., Gilmore G., 1993, MNRAS, 262, 545
The distribution of low-mass stars in the Galactic disc.

Larson R. B., 1974, MNRAS, 169, 229
Effects of supernovac on the early evolution of galaxies.

Lea S. M., De Young D. S., 1976, ApJ, 210, 647
The dynamical interaction between galaxies and intracluster gas in clusters of galaxies.

Lia C., Portinari L., Carraro G., 2002, MNRAS, 330, 821
Star formation and chemical evolution in SPH simulations: a statistical approach.

Lotz J. M., Telford R., Ferguson H. C., Miller B. W., Stiavelli M., Mack J., 2001, ApJ, 552, 572
Dynamical friction in dE globular cluster systems.

Lotz J. M., Miller B. W., Ferguson H. C., 2004, ApJ, 613, 262
The colors of dwarf elliptical galaxy globular cluster systems, nuclei, and stellar halos.

Lucero D. M., Young L. M., van Gorkom J. H., 2005, AJ, 129, 647
Ram pressure stripping in the low-luminosity Virgo Cluster elliptical galaxy NGC 4476.

Macchetto F., Pastoriza M., Caon N., Sparks W. B., Giavalisco M., Bender, R., Capaccioli M., 1996, A&AS, 120, 463
A survey of the ISM in early-type galaxies. I. The ionized gas.

MacLow M., Ferrara, A., 1999, ApJ, 513, 142
Starburst-driven mass loss from dwarf galaxies: efficiency and metal ejection.

Marcolini A., Brighenti F., D'Ercole A., 2003, MNRAS, 456, 1329
Three-dimensional simulations of the interstellar medium in dwarf galaxies - I. Ram pressure stripping.

Marcolini A., Brighenti F., D'Ercole A., 2004, MNRAS, 352, 363
Three-dimensional simulations of the interstellar medium in dwarf galaxies - II. Galactic winds.

Marlowe A. T., Meurer G. R., Heckman, T. M., 1999, ApJ, 522, 183
The taxonomy of blue amorphous galaxies. II. Structure and evolution.

Martin C. L., 1998, ApJ, 506, 222
The impact of star formation on the interstellar medium in dwarf galaxies. II. The formation of galactic winds.

Mastropietro C., Moore B., Mayer L., Debattista V. P., Piffaretti R., Stadel J., 2004, submitted to MNRAS, astro-ph/0411648

Mayer L., Governato F., Colpi M., Moore B., Quinn T., Wadsley J., Stadel J., Lake G., 2001, ApJ, 559, 754
The metamorphosis of tidally stirred dwarf galaxies.

Mateo M. L., 1998, ARA&A, 36, 435
Dwarf galaxies of the Local Group.

Meylan G., Sarajedini A., Jablonka P., Djorgovski S. G., Bridges T., Rich R. M., 2001, AJ, 122, 830
Mayall II=G1 in M31: Giant globular cluster or core of a dwarf elliptical galaxy?

Michie R.W., 1963, MNRAS, 126, 127
On the distribution of high energy stars in spherical stellar systems.

Michie R. W., Bodenheimer P. H., 1963, MNRAS, 126, 269
The dynamics of spherical stellar systems, II.

Michielsen D., De Rijcke S., Dejonghe H., Zeilinger W. W., Hau G. K. T., 2003, Ap&SS, 284, 635
Hα regions in FCC046 and FCC207.

Michielsen D., De Rijcke S., Dejonghe H., Zeilinger W. W., Hau G. K. T., 2003, ApJ, 597, L21
The puzzlingly large Ca II triplet absorption in dwarf elliptical galaxies.

Michielsen D., De Rijcke S., Zeilinger W. W., Prugniel P., Dejonghe H., Roberts S., 2004, MNRAS, 353, 1293
Evidence for a warm interstellar medium in Fornax dEs. II- FCC032, FCC206 and FCCB729.

Michielsen D., De Rijcke S., Dejonghe H., 2004, ANS, 325, 122
N-body study of the dwarf galaxies in a dense cluster environment.

Mieske S., Hilker M., Infante L., 2002, A&A, 383, 823
Ultra compact objects in the Fornax cluster of galaxies: Globular clusters or dwarf galaxies?

Mihos J. C., Hernquist L., 1994, ApJ, 437, 611
Star-forming galaxy models: Blending star formation into TREESPH.

Miller G. E., Scalo J. M., 1979, ApJS, 41, 513
The initial mass function and stellar birthrate in the solar neighborhood.

Mollá M., García-Vargas M. L., 2000, A&A, 359, 18
Models for the interpretation of CaT and the blue spectral indices in elliptical nuclei.

Monaghan J. J., 1992, A&ARv, 30, 543
Smoothed particle hydrodynamics.

Moore B., Katz N., Lake G., Dressler A., Oemler A., Jr., 1996, Nature, 379, 613
Galaxy harassment and the evolution of clusters of galaxies.

Moore B., Lake G., Katz N., 1998, ApJ, 495, 139
Morphological transformation from galaxy harassment.

Mori M., Burkert A., 2000, ApJ, 538, 559
Gas stripping of dwarf galaxies in clusters of galaxies.

Mori M., Yoshii Y., Tsujimoto T., Nomoto K., 1997, ApJ, 478, L21
The evolution of dwarf galaxies with star formation in an outward-propagating supershell.

Mori M., Yoshii Y., Nomoto K., 1999, ApJ, 511, 585
Dissipative process as a mechanism of differentiating internal structures between dwarf and normal elliptical galaxies in a cold dark matter universe.

Mosconi M. B., Tissera P. B., Lambas D. G., Cora S. A., 2001, MNRAS, 325, 34
Chemical evolution using smooth particle hydrodynamical cosmological simulations - I. Implementation, tests and first results.

Mouri H., Taniguchi Y., 2003, ApJ, 585, 250
Orbital decay and tidal disruption of a star cluster: Analytical calculation.

Mulchaey J. S., 2000, ARA&A, 38, 289 *X-ray properties of groups of galaxies.*

Nagashima M., Yoshii Y., 2004, ApJ, 610, 23 (NY04)
Hierarchical formation of galaxies with dynamical response to supernova-induced gas removal.

Navarro J. F., Frenk C. S., White S. D. M., 1996, ApJ, 462, 563
The structure of cold dark matter halos.

Navarro J. F., White S. D. M., 1993, MNRAS, 265, 271
Simulations of Dissipative Galaxy Formation in Hierarchically Clustering Universes - Part One - Tests of the Code.

Nieto J.-L., Bender R., Davoust E., Prugniel P., 1990, A&A, 230, L17
The low-mass extension of the fundamental plane of elliptical galaxies.

Nulsen P. E. J., 1982, MNRAS, 198, 1007
Transport processes and the stripping of cluster galaxies.

Oh K. S., Lin D. N. C., 2000, ApJ, 543, 620
Nucleation of dwarf galaxies in the Virgo Cluster.

Osterbrock D. E., 1989, University Science books, USA
Astrophysics of gaseous nebulae and active galactic nuclei.

Padoan P., Nordlund Å., 2002, ApJ, 576, 870
The stellar initial mass function from turbulent fragmentation.

Padoan P., Nordlund Å., Jones B. J. T., 1997, MNRAS, 288, 145
The universality of the stellar initial mass function.

Pagel B. E. J., Tautvaišienė G., 1998, MNRAS, 299, 535
Chemical evolution of the Magellanic Clouds: analytical models.

Pasetto S., Chiosi C., Carraro G., 2003, A&A, 405, 931
Morphological evolution of dwarf galaxies in the Local Group.

Pedraz S., Gorgas J., Cardiel N., Sánchez-Blázquez, Guzmán R., 2002, MNRASL, 332, 59
Evidence of fast rotation in dwarf elliptical galaxies.

Peterson R., Caldwell N., 1993, AJ, 105, 1411 (PC93)
Stellar velocity dispersions of dwarf elliptical galaxies.

Phillips M. M., Jenkins C. R., Dopita M. A., Sadler E. M., Binette L., 1986, AJ, 91, 1062
Ionized gas in elliptical and S0 galaxies. I - A survey for Hα and forbidden N II emission.

Phillips S., Drinkwater M., Gregg M., Jones J., 2001, ApJ, 560, 201
Ultracompact dwarf galaxies in the Fornax Cluster.

Pierini D., 1999, A&A, 352, 49
Internal extinction, population incompleteness bias and the faint-end of the B-band Tully-Fisher relation.

Plummer H. C., 1911, MNRAS, 71, 460
On the problem of distribution in globular star clusters.

Poggianti B. M., et al., 2001, ApJ, 562, 689
A photometric and spectroscopic study of dwarf and giant galaxies in the Coma Cluster. III. Spectral ages and metallicities.

Portegies Zwart S. F., McMillan S. L. W., 2002, ApJ, 576, 899
The runaway growth of intermediate-mass black holes in dense star clusters.

Portnoy D., Pistinner S., Shaviv G., 1993, ApJS, 86, 95
Ram pressure stripping from elliptical galaxies. I - The mass contained in the Galaxy.

Press W. H., Teutolsky S. A., Vetterling W. T., Flannery B. P., 1992, Cambridge University Press, New York, US
Numerical recipes in C.

Quilis V., Moore B., Bower R., 2000, Sci, 288, 1617
Gone with the wind: The origin of S0 galaxies in clusters.

Raiteri C. M., Villata M., Navarro J. F., 1996, A&A, 315, 105
Simulations of Galactic chemical evolution I. O and Fe abundances in a simple collapse model.

Rakos K., Schombert J., Maitzen H. M., Prugovecki S., Odell A., 2001, AJ, 121, 1974
Ages and metallicities of Fornax dwarf elliptical galaxies.

Roediger E., Hensler G., 2005, A&A, 433, 875
Ram pressure stripping of disk galaxies. From high to low density environments.

Rutledge G. A., Hesser J. E., Stetson P. B., 1997, PASP, 109, 907
Galactic globular cluster metallicity scale from the Ca II Triplet II. Rankings, comparisons, and puzzles.

Ryden B. S., Terndrup D. M., Pogge R. W., Lauer T. R., 1999, ApJ, 517, 650
Detailed surface photometry of dwarf elliptical and dwarf S0 galaxies in the Virgo Cluster.

Sage L. J., Welch G. A., Mitchell G. F., 1998, ApJ, 507, 726
The missing interstellar medium of NGC 147 and M32.

Saglia R. P., Maraston C., Thomas D., Bender R., Colless M., 2002, ApJ, 579, L13
The puzzlingly small Ca II triplet absorption in elliptical galaxies.

Saito M., 1979, PASJ, 31, 181
Mass-anergy-mean density relationship of dust-poor stellar systems.

Salpeter E. E., 1955, ApJ, 121, 161
The luminosity function and stellar evolution.

Sandage A., Binggeli B., 1984, AJ, 89, 919
Studies of the Virgo Cluster. III. A classification system and an illustrated atlas of Virgo Cluster dwarf galaxies.

Sault R. J., Teuben P. J., Wright M. C. H., 1995, in Shaw R., Payne H. E., Hayes J. J. E., eds, ASP Conf. Ser. Vol. 77, Astronomical Data Analysis Software and Systems IV. ASP, San Fransisco, p.433

Schlegel D. J., Finkheiner D. P., Davis M., 1998, ApJ, 500, 525
Maps of dust infrared emission for use in estimation of reddening and cosmic microwave background radiation foregrounds.

Schmidt M., 1959, ApJ, 129, 243
The rate of star formation.

Schulz S., Struck C., 2001, MNRAS, 328, 185
Multi stage three-dimensional sweeping and annealing of disc galaxies in clusters.

Sérsic J.-L., 1968, Observatorio Astronomico, Cordoba
Atlas de galaxias australes.

Simien F., Prugniel, P., 2002, A&A, 384, 371
Kinematical data on early-type galaxies. VI.

Skillman E. D., Côté S., Miller B. W., 2003, AJ, 125, 593
Star formation in Sculptor Group dwarf irregular galaxies and the nature of "transition" galaxies.

Somerville R. S., Primack J. R., Faber S. M., 2001, MNRAS, 320, 504
The nature of high-redshift galaxies.

Somerville R. S., Moustakas L. A., Mobasher B., Gardner J. P., Cimatti A., Conselice C., Daddi E., Dahlen T., Dickinson M., Eisenhardt P., Lotz J., Papovich C., Renzini A., Stern D., 2004, ApJ, 600, L135
The redshift distribution of near infrared-selected galaxies in the Great Observatories Origins Deep Survey as a test of galaxy formation scenarios.

Spitzer Jr., L., 1978, John Wiley & sons, New York
Physical processes in the ISM.

Springer V., Hernquist L., 2002, MNRAS, 333, 694
Cosmological smoothed particle hydrodynamics simulations: the entropy equation.

Springel V., Yoshida N., White S. D. M., 2001, NewA, 6, 79
GADGET: a code for collisionless and gasdynamical cosmological simulations.

Sutherland R. S., Dopita, M. A.,1993, ApJS, 88, 253
Cooling functions for low-density astrophysical plasmas.

Takeda H., Nulsen P. E. J., Fabian A. C., 1984, MNRAS, 208, 261
Ram pressure stripping in a changing environment.

Terlevich E., Diaz A. I., Terlevich R., 1990, MNRAS, 242, 271
On the behaviour of the IR Ca II triplet in normal and active galaxies.

Thacker R. J., Couchman H. M. P., 2000, ApJ, 545, 728
Implementing feedback in simulations of galaxy formation: a survey of methods.

Thacker R. J., Tittley E. R., Pearce F. R., Couchman H. M. P., Thomas P. A., 2000, MNRAS, 319, 619
Smoothed Particle Hydrodynamics in cosmology: a comparative study of implementations.

Thomas D., Maraston C., Bender R., 2003, MNRAS, 343, 279
New clues on the calcium underabundance in early-type galaxies.

Thomas P. A., Couchman H. P. M., 1992, MNRAS, 257, 11
Simulating the formation of a cluster of galaxies.

Thornton K., Gaudlitz M., Janka H.-Th., Steinmetz M., 1998, ApJ, 500, 95
Energy input and mass redistribution by supernovae in the interstellar medium.

Tonry J. L., Dressler A., Blakeslee J. P., Ajhar E. A., Fletcher A. B., Luppino G. A., Metzger M. R., Moore C. B., 2001, ApJ, 546, 681
The SBF survey of galaxy distances. IV. SBF magnitudes, colors and distances.

Trujillo I., Aguerri J. A. L., Gutiérrez C. M., Caon N., Cepa J., 2002, ApJ, 573, L9
A correlation between light concentration and cluster local density for elliptical galaxies.

Trujillo I., Burkert A., Bell E. F., 2004, ApJ, 600, L39
The tilt of the Fundamental Plane: Three-quarters structural nonhomology, one-quarter stellar population.

Tsujimoto T., Nomoto K., Yoshii Y., Hashimoto M., Yanagida S., Thielemann F. K., 1995, MNRAS, 277, 945
Relative frequencies of Type Ia and Type II supernovae in the chemical evolution of the Galay, LMC and SMC.

Tully R. B., Fouque P., 1985, ApJS, 58, 67
The extragalactic distance scale. I- Corrections to fundamental observables.

van der Marel R. P., Franx M., 1993, ApJ, 407, 525
A new method for the identification of non-Gaussian line profiles in elliptical galaxies.

van Zee L., Barton E. J., Skillman E. D. 2004, AJ, 128, 2797
Stellar populations of dwarf elliptical galaxies.: UBVRI photometry of dwarf elliptical galaxies in the Virgo Cluster.

van Zee L., Salzer J. J., Skillman E. D. 2001, AJ, 122, 121
Kinematic constraints on evolutionary scenarios for blue compact dwarf galaxies. I. Neutral gas dynamics.

van Zee L., Skillman E. D., Haynes M. P., 2004, AJ, 128, 121
Rotationally supported Virgo Cluster dwarf elliptical galaxies: Stripped dwarf irregular galaxies?

Vazdekis A., Casuso E., Peletier R. F., Beckman J. E., 1996, ApJS, 106, 307
A new chemo-evolutionary population synthesis model for early-type galaxies. I. Theoretical basis.

Vazdekis A., Peletier R. F., Beckman J. E., Casuso E., 1997, ApJS, 111, 203
A new chemo-evolutionary population synthesis model for early-type galaxies. II. Observations and results.

Vazdekis A., Cenarro A. J., Gorgas J., Cardiel N., Peletier R. F., 2003, MNRAS, 340, 1317
Empirical calibration of the near-infrared Ca II triplet - IV. The stellar population synthesis models.

Verheijen M. A. W., 2001, ApJ, 563, 694
The Ursa Major cluster of galaxies. V. H I rotation curve shapes and the Tully-Fisher relations.

Verheijen M. A. W., Sancisi R., 2001, A&A, 370, 765
The Ursa Major cluster of galaxies. IV. H I synthesis observations.

Vollmer B., 2003, A&A, 398, 525
NGC4654: Gravitational interaction or ram pressure stripping?

Vollmer B., Beck R., Kenney J. D. P., van Gorkom J. H., 2004, AJ, 127, 3375
NGC 4569: Recent evidence for a past ram pressure stripping event.

Vollmer B., Cayatte V., Balkowski C., Duschl W. J., 2001, ApJ, 561, 708
Ram pressure stripping and galaxy orbits: The case of the Virgo Cluster.

Worthey G., 1998, PASP, 110, 888
Abundance ratio trends and nucleosynthesis in elliptical galaxies and spheroids.

Yoshii Y., Arimoto N., 1987, A&A, 188, 13 (YA87)
Spheroidal systems as a one-parameter family of mass at their birth.

Young C. K., Currie M. J., 1994, MNRAS, 268, L11
A new extragalactic distance indicator based on the surface brightness profiles of dwarf elliptical galaxies.

Young C. K., Currie M. J., 1995, MNRAS, 273, 1141
Distances to 64 Virgo dwarf elliptical galaxies and the depth in their spatial distribution.

Young C. K., Currie M. J., 1998, A&A, 333, 795
Distance indicators based on the luminosity-profile shapes of early-type galaxies-a reply.

Young C. K., Currie M. J., 2001, A&A, 369, 736
Surface-brightness profiles of dwarf galaxies in the NGC 5044 Group: Implications for the luminosity-shape and scalelength-shape relationships as distance indicators.

Young L. M., Lo K. Y., 1996, ApJ, 464, L59
Molecular clouds in the dwarf elliptical galaxy NGC205.

Young L. M., Lo K. Y., 1997, ApJ, 476, 127
The neutral interstellar medium in nearby dwarf galaxies. II. NGC 185, NGC 205, and NGC 147.